Title
Design and Control of a Floating Wave-Energy Converter Utilizing a Permanent Magnet Linear Generator

Author
Tom, Nathan Michael

Publication Date
2013

Peer reviewed|Thesis/dissertation

Design and Control of a Floating Wave-Energy Converter Utilizing a Permanent Magnet Linear Generator

By

Nathan Michael Tom

A dissertation submitted in partial satisfaction of the

requirements for the degree of

Doctorate of Philosophy

in

Engineering - Mechanical Engineering

in the

Graduate Division

of the

University of California, Berkeley

Committee in Charge:

Professor Ronald W. Yeung
Professor Ömer Savaş
Professor Dennis K. Lieu
Professor Per-Olof Persson

Fall 2013

Abstract

Design and Control of a Floating Wave-Energy Converter

Utilizing a Permanent Magnet Linear Generator

by

Nathan Michael Tom

Doctor of Philosophy in Engineering - Mechanical Engineering

University of California, Berkeley

Professor Ronald W. Yeung, Chair

This thesis considers the design, optimization, and control of a coupled cylindrical floater and permanent magnet linear generator for wave-energy conversion. The investigation begins with the construction of the time-domain equation of motion for a generic floating body. The construction of a physical cylindrical floater is followed by a description of the experiments completed to verify free-motion and wave-exciting force predictions. The time-domain equation of motion was compared against experiments where it was found that corrective terms needed to be added due to the presence of viscosity. Initial low motion amplitudes lead to evaluation of the hydrodynamic performance between a floater with a flat and rounded-hemispherical bottom. Experimental results demonstrated that motion amplitudes can be over predicted by a factor of 2 when neglecting the effects of viscosity.

Second, modifications to the design, fabrication process, and material of a permanent magnet linear generator (PMLG) will be discussed with the aim of increasing both power output and mechanical-to-electrical conversion efficiency. In order to evaluate the performance of the power-take-off unit a dry-bench test was completed which consisted of driving the armature of the PMLG at various frequencies with a fixed motion amplitude. The force signature from the bench test was used to extract the spring, damping, and inertia force coefficients due to the influence of the PMLG. The force coefficients were obtained for various speeds, resistive loads, and magnet coil gap widths. The floater equation of motion was modified to accommodate the influence of the PMLG to predict the coupled system performance. As the damping coefficient was the dominant contribution to the PMLG reaction force, the optimum non time-varying damping values were presented for all frequencies, recovering the well known impedance matching at the coupled resonance frequency. Model-scale tests of the coupled floater-generator system were performed at the UC-Berkeley Model Testing Facility to verify the optimum conditions for energy extraction.

In an effort to further maximize power absorption, nonlinear model predictive control (NMPC) was applied to the model-scale point absorber. The NMPC strategy was set up as a nonlinear optimization problem utilizing the Interior Point OPTimizer (IPOPT) package to obtain the optimal time-varying generator damping from the PMLG. This was accompa-

nied by a latching damper that was allowed to periodically slow the floater velocity in an effort to increase power absorption. The emphasis on this work has been on sub-optimal strategies that limit the power-take-off unit to behave as a generator, thereby minimizing energy return to the waves. It was found that the ideal NMPC strategy required a PTO unit that could be turned on and off instantaneously, leading to sequences where the generator would be inactive for up to 60% of the wave period. Experimental validation of the NMPC included repeating the dry bench test in order to characterize the time-varying performance of the PMLG. This was achieved through the use of mechanical relays to control when the electromagnetic conversion process would be active. After the time-varying performance of the PMLG was characterized the experimental set-up was transferred to the wave tank. The on/off sequencing of the PMLG was tested under regular and irregular wave excitation to validate NMPC simulations using the control inputs obtained from running the controller offline. Experimental results indicate that successful implementation was achieved and the absorbed power was indeed maximized.

Dedication

To my family and all of the individuals who have supported my intellectual growth and who believed in my abilities. Without their encouragement and unwavering faith I would not be where I am today.

"For most of history, man has had to fight nature to survive; in this century he is beginning to realize that, in order to survive, he must protect it."
Jacques-Yves Cousteau

"The sea is everything. It covers seven tenths of the terrestrial globe. Its breath is pure and healthy. It is an immense desert, where man is never lonely, for he feels life stirring on all sides. The sea is only the embodiment of a supernatural and wonderful existence. It is nothing but love and emotion; it is the Living Infinite."
Jules Verne, 20,000 Leagues Under the Sea.

Acknowledgements

I would like to first thank my research advisor, Professor Ronald W. Yeung, of Hydromechanics and Ocean Engineering at UC Berkeley. I cannot thank him enough for his assistance and guidance throughout the course of my academic and research program. Without taking Professor Yeung's undergraduate course on ocean-environment mechanics, I would not have been exposed to the opportunities available in the marine field. Furthermore, I will be forever indebted to Professor Yeung for supporting my petition to enter the Ph.D. track after completing the UC Berkeley Mechanical Engineering 5th year Master's program. It is his love and knowledge of the field that have sparked my own interest in continuing my formal education and career in this field. I would also like to congratulate Professor Yeung as the inaugural faculty holder of the American Bureau of Shipping Endowed Chair in Ocean Engineering.

I would also like to thank Professor Ömer Savaş and Professor Per-Olof Persson for serving on both my qualifying and thesis committee. Many thanks are due also to Professor Dennis K. Lieu, not only for serving on my thesis committee, but for the useful meetings and discussions on the power-take-off design. There are also many members of the UC Berkeley technical staff I would like to thank for their advice and guidance through the years. Specifically, I would like to thank Tom Clark, the Assistant Development Engineer, and Rene Viray, the Computer Systems Administrator of the ME department, without their consultation, I would not have been able to complete my work. Furthermore, I would like to thank Gordon Long and Mick Franssen from the ME student machine shop who provided support and guidance in the construction and development of all the experimental apparatus. In addition, I would like to acknowledge Professor Francesco Borelli, Sergey Vichik, and Anthony Kelman for providing the Berkeley Library for Optimization Modeling (BLOM).

Furthermore, the work that I have completed during the completion of my program would not have been possible without the support of the various ocean engineering students throughout the years. Last but not the least, I want to thank my family and all of the individuals who have always provided their encouragement throughout my graduate career.

Acknowledgement for partial support is made to KAUST/UC-Berkeley Grant #25478 and to the Office of Naval Research, under Grant No. N00014-09-1-1086.

Design and Control of a Floating Wave-Energy Converter Utilizing a Permanent Magnet Linear Generator © 2013

by Nathan Tom

Contents

List of Figures

List of Tables

Nomenclature

$\ddot{\zeta}_3(t)$	Time varying (vertical) acceleration of floater or armature
ΔB_g	Change in generator damping per time step
Δt	Time step
$\dot{\zeta}_3(t)$	Time varying (vertical) velocity of floater or armature
η_{el}	Mechanical-to-electrical efficiency
η_{mech}	Mechanical efficiency of absorbed power
η_{PTO}	Power Take-Off (PTO) efficiency
$\forall$	Displaced volume of floater
$\hat{n}$	Unit normal
Λ	Scale factor
λ	Wavelength of incident waves
Λ_{2D}	Shape-effect factor for 2D geometry
λ_{33}	Heave-motion radiation damping coefficient
Λ_{3D}	Shape-effect factor for 3D geometry
λ_f	Flux linkage
λ_m	Magnetic wavelength
λ_T	Total hydrodynamic damping
λ_{vis}	Linear viscous damping coefficient of floater
$\mathcal{A}_3$	Floater complex amplitude of heave motion
$\mathcal{L}$	Lagrange function
μ	Magnetic permeability
μ_0	Permeability of air
μ_{33}	Heave-motion added mass
μ_g	Generator inertia

μ_r	Relative permeability
μ_T	Total added mass
ν	Kinematic viscosity
ω	Vorticity
ω_n	Undamped natural frequency
$\overline{\dot{W}}$	Time averaged mechanical power input to PMLG
$\overline{C}_w$	Non-dimensional experimental capture width
$\overline{P}$	Time averaged absorbed power
$\overline{P}_{load}$	Time averaged power over one period per phase
Φ	Total velocity potential
ϕ_0	Incident wave potential
ϕ_3	Radiation potential for heave motion
ϕ_7	Diffraction potential
Φ_m	Magnetic flux
ρ	Mass density of fluid
ρ_{Fe}	Resistivity of the used material
σ	Wave angular frequency
σ_M	Normal stress
σ_S	Shear stress
$\sum E$	Cumulative absorbed energy
v	Volume
Θ	Lagrange dual problem
θ	Phase lag between wave elevation and heave motion
$\tilde{f}$	Ratio of generator damping to hydrodynamic damping
ε	Random phase angle

φ	Heave wave-exciting force phase angle
$\vec{B}_m$	Magnetic flux density
$\vec{B}_r$	Residual magnetic flux density
$\vec{E}$	Electrical field intensity
$\vec{F}_l$	Lorentz force
$\vec{H}_{ci}$	Intrinsic coercivity
$\vec{H}_m$	Magnetic intensity
$\vec{J}_m$	Current density at a field point
$\vec{K}$	Electric loading
$\vec{l}$	Electrical conductor length
$\vec{U}$	Velocity vector $(u,\ v,\ w)$
ζ	Damping ratio
$\zeta_3(t)$	Time varying (vertical) displacement of floater or armature
$\zeta_o(t)$	Time varying wave elevation
A	Incident-wave amplitude
a	Radius of floater
A_r	State matrix for radiation force
A_{sys}	State matrix describing system dynamics
A_{wp}	Waterplane area of floater
B	Input matrix for f_{gen}
B_{coil}	Coil flux density
b_{Fe}	Width of lamination
B_{gap}	Air-gap flux density
B_g	Generator damping
B_g^*	Constant and continuous damping coefficient
$B_L(t)$	Latching damper

B_r Input matrix for radiation force

C_r Output matrix for radiation force

C_w Capture width

D Diameter of floater $= 2a$

d Draft of cylinder

$d^* - J^*$ Duality gap

D_r Feedthrough matrix for radiation force

F Magnetic motive force (mmf)

$F|_\infty$ Force time history due to eddy currents, hysteresis, cogging effects

$F|_f$ Force time history due to friction

F_3 Hydrodynamic heaving force

$f_e(t)$ Time varying wave-exciting force

$f_{gen}(t)$ Time varying generator force

F_g Generator force

$f_h(t)$ Time varying hydrostatic force

$f_L(t)$ Time varying latching force

$f_r(t)$ Time varying radiation force

g Gravitational acceleration

g_i Inequality constraints

H Wave height $= 2A$

h Water depth

$H_{1/3}$ Wave spectrum significant wave height

h_j Equality constraints

H_p Number of discrete steps per time horizon

h_T Tank depth

i Conductor current

J	Objective function
K	Floater spring constant, $\pi\rho g a^2$
k	Wave number, also $= m_o$
K_e	Heave wave-exciting force kernel
K_g	Generator spring constant
K_r	Impulse response function
K_{sp}	External spring constant
K_v	Speedance
L_c	Coil inductance
l_f	Length of flux path
L_s	Separation distance between wave probes
M	Floater mass plus infinite frequency added mass
m	Mass of floater
m_b	Moving mass during bench test
N	Number of wires
P	Instantaneous absorbed power
P_{coil}	Power consumed by coil resistance
P_{el}	Time averaged power over one period for permanent magnet linear generator
P_{fric}	Friction coefficient
P_g	Magnetic coil gap width permeance
P_{load}	Power consumed by load resistance
P_{me}	Time averaged mechanical power input to PMLG
P_{ml}	Magnetic leakage permeance
P_m	Magnet permeance
P_s	Stator permeance
P_w	Power contained per unit wave crest

$PL_{cog+eddy}$ Time averaged power loss due to eddy currents, hysteresis, cogging effects

PL_{coil} Time averaged power loss due to coil resistance

PL_e Theoretical power loss due to eddy currents

PL_{fric} Time averaged power loss due to friction

PL_h Theoretical power loss due to hysteresis

Q Electrical Charge

Q_p Penalty term associated with ΔB_g

R Load resistance

r Coil resistance

R_m Reluctance

S Cross sectional area

S_B Equilibrium surface of the body

S_p Wave spectrum

S_w Input matrix for ζ_o

Ss Number of steps in 5 min simulation

T Period of wave and response

t Time

t_c Causal time shift

T_h Time horizon

T_{opt} Time for completion of optimization

T_p Wave spectrum peak period

T_{shift} Time a wave crest traveled between reference points

u_i Lagrange multiplier for inequality constraints

V Voltage potential

V_{ap} Applied Voltage potential

V_e Induced voltage

V_g	Group velocity of incident wave
v_i	Lagrange multiplier for equality constraints
V_p	Phase velocity of incident wave
w_{gap}	Magnet coil gap width
w_p	Wire pitch
w_T	Tank width
x	Horizontal axis
X_3	Heave wave-exciting force per unit amplitude of incident wave
X_r	Vector of states for radiation force
X_{sys}	Vector of states describing floater dynamics
Z	Free surface elevation
z	Vertical axis
GS	Generator span
MS	Magnet span
np	Number of poles
ns	Number of slots
PS	Pole span
r	Corner radius
Sp	Spacing
SS	Slot span
TS	Tooth span

Chapter 1

Introduction

As the price of oil rises and other traditional electrical generation processes become increasingly unfavorable, in terms of long-term sustainability and associated CO2 emissions, a new source of energy is required. In recent years, the extraction of energy from the ocean, particularly surface waves, has become an increasingly favorable alternative to meet the world's energy demand. Within this category of alternative energy resource, an amazing collection of ideas exist and continue to be developed. Generally, there are four classifications of conversion methods: the point absorber (using the wave-excited resonant, periodic motion of a device), the terminator (using oscillation of a water column), an attenuator (using the differential motion of a wave surface), and over topping into a shore barrier. The distinctions among these are well described in [1, 2].

A single wave energy converter would not suffice to generate the power levels strong enough to connect directly into the electrical grid, as with most other renewable energy technologies, thus the construction of a wave farm is required. The wave farm will create additional difficulties because of mutual interference patterns [3] though preliminary analysis has shown that a larger number of converters will help to reduce power fluctuations [4]. Furthermore, it has been postulated that an array of small compact point absorbers, rather than a large single unit, will have greater extraction efficiency per unit absorber over a broader range of wave frequencies [5].

The point-absorber [6] concept has been under investigation by both industrial and academic groups in varying stages of development from model-to-prototype scales [7, 9, 8, 10, 11, 12, 13, 14]. These projects have target power goals that range from small marine surveillance systems, aquaculture, to utility grid production. With point absorbers, it has been found that the utilization of linear(-motion) generators using electro-magnetic principles eliminate the need for additional conversion methods such as crank gearing and drives [15, 16, 17, 18], though the use of a hydraulic power-take-off is also of contemporary interest [19]. A large number of devices currently under investigation use a permanent magnet linear generator (PMLG) to produce electricity. The introduction of the permanent magnet system requires an understanding of the coupling behavior of the electromagnetic properties of the linear generator and the hydrodynamics of the floating body. Numerical simulations and experimental tests have shown that the coupling is not a simple procedure and mere changes to the geometry of the generator cannot be easily carried over to increase efficiency and power output. The coupled point absorber and PMLG concept has been under investigation in the Computational Marine Mechanical Laboratory at the University of California at Berkeley since 2008 [20, 21].

The incoming waves drive the heaving motion of the floater, which is connected to the armature, the moving part of the linear generator, and with the proper design energy loss caused by pitch motion can be reduced. An axisymmetric floater design is highly desirable

as the expected response for a wave front is invariant to the directional heading; however, this floater design can only capture up to 50% of the incoming wave power when constrained to one degree of freedom motion. It is possible to obtain 100% capture efficiency if a asymmetric floater is used [22, 23] though performance degradation will occur in oblique seas. It is also necessary to understand the effects of viscosity on the maximum extractable power. High viscous forces, due to floater shape, act as an additional power sink even before considering the efficiency of the energy conversion process [24, 25]. An extensive amount of research has gone into predicting viscous effects in the presence of a free surface [26, 27] and it continues to be a contemporary topic of investigation. Thus, inviscid estimates on the maximum absorbed power [28] may be severely optimistic.

One of the most critical elements for wave energy conversion is the PTO damping which is directly related to energy extraction. It has been found that in irregular sea states there is a PTO damping range resulting in the greatest amount of absorbed energy [29, 30]. Thus, it is theoretically ideal to actively control the PTO properties in an effort to optimize the extracted power in various sea states. The application of state constrained optimization to energy extraction [31] has recently been gaining interest as it allows one to better estimate the performance of real systems. For example, the maximum inviscid capture width [41] requires unconstrained motion, which can lead to physically unrealistic excursion amplitudes. The use of model predictive control (MPC) [32] has been identified as a strategy with strong potential as it can optimize over any number of state constraints, such as the amplitude of motion or PTO power capacity [33]. Previous works have used MPC as a reference tracking application directing the floater to follow an optimum velocity profile in an effort to absorb the greatest amount of energy from an irregular wave train [34]. In addition, MPC has been used to optimize the accumulated energy over a given time horizon [35, 36]. In these cases, the flow of energy in the system is reversible while a penalty term was introduced in an attempt to account for conversion losses. Nonlinear model predictive control has also been used to account for the non-linear dynamics created by the introduction of mooring lines [37] as well as for the optimization of a time-varying PTO damper [38, 39]. However, the results from [38] include an additional active control force in addition to a time-varying PTO damper that allows for energy flow reversal; whereas [39] relies on the time-varying PTO damping as the only control input preventing a reverse in energy flow. However, results from both sources suggest a damping input following a strongly bang-bang time history. The time-line of these publication have significant overlap and given the present author was unaware of the work presented in [38], research concepts in this work should be considered to have been developed independently.

This thesis will investigate the coupled floater and PTO system in an attempt to identify areas that can lead to improved energy capture. These improvements include the effects of two floater shapes on the viscous damping and overall motion. Further investigation into the PMLG will focus on increasing efficiency and power output through modifications made in the construction and material of the armature and stator components. Finally, control of the coupled system will be explored in order to increase the capture efficiency and broaden the effective frequency range of the device.

In Chapter 2 the time-domain heave equation of motion is constructed after performing a force balance on the floater. The use of the Cummins decomposition [40] allows the hydrodynamic radiation and wave exciting-forces to be represented in the time domain through the use of convolution kernels. The potential theory used to calculate the hydrodynamic coefficients for an arbitrary floating body are presented. The components of the total velocity potential are described and their subsequent force contributions identified.

In Chapter 3 the heave equation of motion under sinusoidal excitation is constructed providing the heave response amplitude operator. The design, construction, and testing of a flat bottom floater is described while experimental results for the response amplitude operator and wave exciting force are compared against theory. A linear state space equation of motion is constructed in order to validate the simulated performance of the floater with experimental trials. In addition, the construction and testing of a rounded bottom floater is presented in an effort to reduce the floater's viscous damping.

In Chapter 4 the electro-magnetic theory that describes the power conversion process is reviewed. The evolution in the design and construction of the current permanent magnet linear generator is discussed with focus on increasing both power output and conversion efficiency. The experimental results from a dry bench test are presented to validate the performance gains of the power-take-off unit.

In Chapter 5 the cylindrical floater and PMLG are combined leading to the coupled system's heave response amplitude operator. The theoretical optimum condition for passive energy harvesting is presented, requiring the floater and PMLG impedance be matched at resonance. The optimal tuning of the generator damping for frequencies off resonance, assuming it is constant and continuous, is also discussed. Results from testing the coupled system at the Richmond Field Station Model Testing Facility are presented, providing evidence that helps confirm the optimum conditions for energy extraction while setting the current maximum threshold of the UC Berkeley design.

In Chapter 6 the basics of model predictive control and constrained optimization are presented to familiarize the reader. The construction of the non-linear program and the time-varying state space matrices are presented while the choice solver is described. The performance gains from applying the NMPC controller, in both regular and irregular waves, are compared against a passive energy harvester, with a fixed linear damping coefficient [41] with no controller. Sensitivity of the NMPC to environmental conditions as well as the non-linear solver characteristics are presented to evaluate the robustness of the controller. In order to extend the current work past [38], the control of a variable PTO damper will also be combined with a latching damper [42].

In Chapter 7, the on/off sequencing of the PMLG, as presented in Chapter 6, is experimentally investigated. First, the chosen controller hardware and software is applied to a revised dry-bench test. The dry-bench test results indicate that the use of mechanical relays, activated by a digital signal, are successful at eliminating the electro-magnetic power conversion process, thereby dramatically reducing the PMLG's influence on the floater dynamics. The control system is transferred to the model testing facility to verify that the predicted increases in power absorption are achieved under regular and irregular wave excitation.

1.1 Ocean-Wave Power Potential

Estimations of US wave resources have been made by the Electric Power Research Institute (EPRI) in 2003 [43]. Using 20 years of data of wave amplitude and frequency, gathered by the National Oceanic and Atmospheric Administration (NOAA) and the Scripps Institution of Oceanography, they concluded that about 2,100 TWh/yr is available. This is a significant resource given the Energy Information Administration (EIA) estimates that in 2009 US hydroelectric generation was 270 TWh [44], about a tenth of the offshore wave energy flux. However, because of societal, practical, political, and environmental limitations, only part of these resources are economically viable. Even so, the global wave power resource in deepwater (i.e. greater than 50 m depth) is estimated to be about 2.11 TW [45]. If 5% of this resource is captured it would be on the same order of magnitude as the world's 2009 electricity consumption [46]. With future improvements, however, more and more wave power can be extracted. Wave energy has the highest power density watt per unit area perpendicular to the direction of propagation among renewable energy sources. The power of ocean waves is preferably expressed in kW/m wave crest front and, in deep water, can be shown to be proportional to the wave amplitude A squared and the period of the wave T [47]. For most of the US West coast between 25 to 40 kW/m intensity is available, on a yearly-averaged basis. If fact, in California both Eureka and Ocean Beach are two sites that have been discussed [48] for wave energy development, as well as Portland, Oregon [49], as these locations are near population centers, which would reduce transmission-line losses and installation costs.

As can be seen, clean technologies, such as ocean wave energy, present the opportunity to stem the world's current dependence on fossil fuels and can be the next engine of economic growth. Properly controlled, wave energy is practically inexhaustible and easily forecastable from satellites. Compared with other renewable energy sources, it also presents limited environmental impacts. Thus, granted that technological hurdles are overcome, pushing clean technology into the mainstream, and driving rapid growth and expansion represent the next challenges in this energy transition of historical proportion.

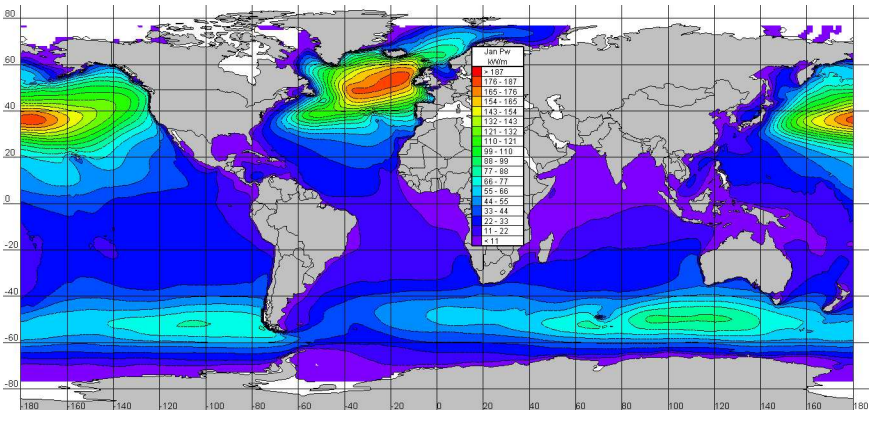

Figure 1.1: Global wave energy resources in January (kW/m) [50].

Chapter 2

Hydrodynamics of the Floater

2.1 Time-Domain Heave Equation of Motion

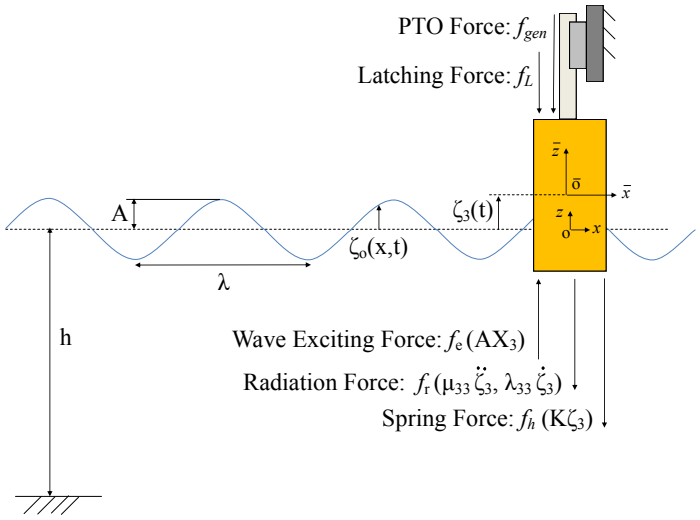

Figure 2.1: Schematic of the physical system under investigation.

After performing a force balance on the floater in Fig. 2.1, while accounting for the hydrodynamic, gravitational, and generator forces, the equation of motion for the heaving floater is given by:

$$m\ddot{\zeta}_3(t) = f_e(t) + f_r(t) + f_h(t) + f_{gen}(t) + f_L(t) \quad , \tag{2.1}$$

where $m\,(=\rho\forall)$ and $\ddot{\zeta}_3(t)$ are the mass and heave acceleration of the body, respectively. The floater mass is equal to the product of the fluid density, ρ, and displaced volume, $\forall$. Furthermore, $f_e(t)$, $f_r(t)$, $f_h(t)$, $f_{gen}(t)$, and $f_L(t)$ are the wave exciting, wave radiation, restoring, generator, and latching forces. The restoring force is represented by:

$$f_h(t) = -K\zeta_3\,(t) = -\rho g A_{wp}\zeta_3\,(t) \quad , \tag{2.2}$$

where K is the floater spring constant, g is the gravitational acceleration, and A_{wp} is the waterplane area, which can be constant or a function of $\zeta_3(t)$. The wave radiation force [40] can be written as the following:

$$f_r(t) \;\; = \;\; -\mu_{33}(\infty)\ddot{\zeta}_3(t) - \lambda_{33}(\infty)\dot{\zeta}_3(t) - \int_{-\infty}^{t} K_r(t-\tau)\dot{\zeta}_3(\tau)d\tau \quad , \tag{2.3}$$

where $\mu_{33}(\infty)$ and $\lambda_{33}(\infty)$ are the infinite frequency hydrodynamic radiation coefficients commonly known as the added mass and wave damping while $\lambda_{33}(\infty)$ normally vanishes. K_r is a causal function known as the radiation impulse response function and can be calculated from the inverse Fourier transform of the hydrodynamic radiation coefficients.

The wave exciting force is described in the time domain by the following:

$$f_e(t) = \int_{-\infty}^{\infty} K_e(t-\tau)\zeta_0\left(0,\tau\right) d\tau \tag{2.4}$$

where $\zeta_0\left(x,t\right)$ is the incident wave elevation, thus $\zeta_0\left(0,t\right)$ will be the wave elevation at the floater origin. K_e is the excitation kernel function which is found from the inverse Fourier transform of the frequency dependent complex hydrodynamic wave exciting force, X_3. It should be noted that the excitation kernel function can be non-causal [51].

After inserting Eqn. (2.2), Eqn. (2.3), Eqn. (2.4) into Eqn. (2.1) the resulting equation of motion is given by:

$$\begin{aligned}(m+\mu_{33}(\infty))\ddot{\zeta}_3(t) + (\lambda_{33}(\infty)+\lambda_{vis})\dot{\zeta}_3(t) \quad &+ \quad \rho g A_{wp}\zeta_3(t) + \int_{-\infty}^{t} K_r(t-\tau)\dot{\zeta}_3(\tau)d\tau \\ &= \quad \int_{-\infty}^{\infty} K_e(t-\tau)\zeta_0\left(0,\tau\right) d\tau \quad [+f_{gen}(t) + f_L(t)] \quad .\end{aligned} \tag{2.5}$$

It should be noted that a corrective linear viscous damping term, λ_{vis}, could be included to limit unrealistic inviscid amplitudes of motion. However, this assumption would lead to the inaccurate use of the impulse response function, as it is calculated under the inviscid assumption. It was decided that given the importance of viscous contributions to motion response [25] a viscous term will be included for modeling purposes. The f_{gen} and f_L contributions will be discussed in greater detail in Chapter 6 and will be ignored for the time being.

2.2 Calculation of Hydrodynamic Coefficients

In order to calculate μ_{33}, λ_{33}, and X_3 the fluid flow about the floater will be considered invsicid, incompressible, and irrotational which require the following conditions:

$$\nu = 0 \quad , \tag{2.6}$$

$$\nabla \cdot \vec{U} = 0 \quad , \tag{2.7}$$

$$\vec{\omega} = \nabla \times \vec{U} = 0 \quad , \tag{2.8}$$

where ν is kinematic viscosity, $\vec{U}$ is the velocity field, and $\vec{\omega}$ is vorticity. The irrotational condition allows the flow to be expressed in terms of a scalar function, $\Phi\left(x,y,z,t\right)$, known

as the velocity potential. The velocity potential is related to the velocity field through the following relations:

$$\nabla\Phi = \vec{U} = (u, v, w) \quad , \tag{2.9}$$

$$u = \frac{\partial\Phi}{\partial x} \quad , \quad v = \frac{\partial\Phi}{\partial y} \quad , \quad w = \frac{\partial\Phi}{\partial z} \quad . \tag{2.10}$$

Inserting Eqn. (2.9) into Eqn. (2.7) leads to:

$$\nabla^2\Phi = 0 \quad , \tag{2.11}$$

where ∇^2 is the Laplacian operator and arises in many areas of engineering and physics.

2.2.1 Free Surface Boundary Conditions (FSBC)

Floating body problems are unique in that there exists an interface between the working fluid and surrounding air called the free surface. At the free surface boundary conditions must be met in order to maintain continuity. This can be difficult at times given the free surface elevation itself can be an unknown that must be calculated.

Kinematic Boundary Condition

The kinematic boundary condition for any geometric surface can be written as:

$$\vec{U} \cdot \hat{n} = \Phi_{\hat{n}} \quad , \tag{2.12}$$

which after expanded:

$$Z_x\left(x, y, t\right)\Phi_x\left(x, y, Z\left(x, y, t\right), t\right) + Z_y\Phi_y - \Phi_z + Z_t = 0 \quad , \tag{2.13}$$

where $z = Z\left(x, y, t\right)$ defines the free surface.

Dynamic Boundary Condition

The dynamic boundary condition ensures that the pressure at the water-air interface is equal. In order to satisfy this condition Euler's Integral is used and working in gauge pressure provides:

$$\Phi_t\left(x, y, Z\left(x, y, t\right), t\right) + \frac{1}{2}\left|\nabla\Phi\right|^2 + gZ = 0 \quad . \tag{2.14}$$

2.2.2 Linearization of F.S.B.Cs

In order to linearize the free surface boundary conditions, it will be assumed that $|\nabla\Phi|$ is small compared to a characteristic speed of the problem. This assumption allows one to write:

$$\Phi_t\left(x, y, Z\left(x, y, t\right), t\right) = \Phi_t\left(x, y, 0, t\right) + Z\Phi_{tz} + ... \tag{2.15}$$

thereby discarding $Z\Phi_{tz}$ and other higher order terms leads to the simplification of the linearized free surface boundary conditions:

$$\Phi_t(x,y,0,t) + gZ(x,y,t) = 0 \quad , \tag{2.16}$$
$$\Phi_z(x,y,0,t) - Z_t(x,y,t) = 0 \quad . \tag{2.17}$$

The linearized free surface boundary conditions can then be combined as:

$$\Phi_{tt} + g\Phi_z(x,y,0,t) = 0 \quad . \tag{2.18}$$

It is generally sufficient that in deep water, when the wavelength, λ, to water depth, h, ratio is less than a half, $\lambda/h < 1/2$, linearization can be applied when the wave slope, the wave height, H, to wavelength ratio is sufficiently small, $H/\lambda < 1/20$.

2.2.3 Complete Velocity Potential

The total velocity potential Φ can be written as:

$$\Phi(x,y,z,t) = \Re\left\{A\left[\phi_0(x,y,z) + \phi_7(x,y,z)\right]e^{-i\sigma t}\right\} + \Re\left\{\phi_3(x,y,z)\,\dot{\zeta}_3(t)\right\} \quad . \tag{2.19}$$

The incident wave potential ϕ_0 for a rightward moving regular wave, in water depth h, is given by:

$$\phi_0(x,z,t) = \frac{-ig\cosh(k[z+h])}{\sigma\cosh(kh)}e^{i(kx-\sigma t)} \quad , \tag{2.20}$$
$$\zeta_0(x,t) = \Re\left\{Ae^{i(kx-\sigma t)}\right\} \quad . \tag{2.21}$$

where ζ_0 is the wave elevation which satisfies the dynamic boundary condition, Eqn. (2.16), k is the wave number, σ is the wave angular frequency, and A is the wave amplitude.

ϕ_7 is the unknown diffraction potential and must be solved to meet the no - flux boundary condition on the floater:

$$\nabla^2\phi_0 = \nabla^2\phi_7 = 0 \quad , \tag{2.22}$$
$$\frac{\partial\phi_0}{\partial\hat{n}}|_{S_B} = -\frac{\partial\phi_7}{\partial\hat{n}}|_{S_B} \quad , \tag{2.23}$$

where S_B is the equilibrium wetted surface of the body and $\hat{n}$ is the unit normal to the body surface.

ϕ_3 is the radiation potential associated with the time dependent heaving motion of the floater. The radiation potential must satisfy the following conditions:

$$\nabla^2\phi_3 = 0 \quad , \tag{2.24}$$
$$\frac{\partial\phi_3}{\partial\hat{n}}|_{S_B} = n_3 \quad , \tag{2.25}$$

where the time history of floater displacement assumed to be periodic:

$$\zeta_3(t) = \Re\left\{\mathcal{A}_3 e^{-i\sigma t}\right\} \quad , \tag{2.26}$$

and $\mathcal{A}_3$ is a complex amplitude and θ is the angle of response relative to the incoming wave such that:

$$\mathcal{A}_3 = |\mathcal{A}_3| e^{-i\theta} \ . \tag{2.27}$$

2.2.4 Dispersion Relation

The incident wave potential, Eqn. (2.20), must satisfy the combined free surface boundary condition of Eqn. (2.18) which leads to the dispersion relation:

$$\frac{\sigma^2}{g} = k \tanh(kh) \quad , \tag{2.28}$$

providing a relationship between the frequency and wave number of dispersive water waves.

2.2.5 Hydrostatic-dynamic Forces: Frequency Domain

The hydrodynamic forces can be calculated by integrating the pressure, given by the Bernoulli equation for unsteady potential flow, along the floater's outer surface:

$$F_3 \quad = \quad \int_{S_B} p n_3 dS = \int_{S_B} \left[-\rho g z - \rho \frac{\partial \Phi}{\partial t}\right] n_3 dS \quad , \tag{2.29}$$

where p is pressure, n_3 is the unit normal in the vertical direction. The hydrostatic force emerges from the non-time-varying component of Eqn. (2.29) given by:

$$\int_{S_B} -\rho g z n_3 dS = \rho g \forall - \rho g A_{wp} \zeta_3(t) \quad . \tag{2.30}$$

The hydrodynamic portion of Eqn. (2.29) can be expanded to show the contributions from $\phi_0,\ \phi_7,\ \phi_3$. Examining the contributions from the incident and diffraction potentials leads to:

$$\int_{S_B} -\rho \frac{\partial \Phi}{\partial t} n_3 dS = -\int_{S_B} \rho A \left[\phi_0 + \phi_7\right](-i\sigma) e^{-i\sigma t} n_3 dS \quad , \tag{2.31}$$

where the complex wave-exciting force per unit wave amplitude, X_3, is defined as:

$$X_3 = \rho \int_{S_B} \left[\phi_0 + \phi_7\right](i\sigma) n_3 dS \quad , \tag{2.32}$$

this allows Eqn. (2.31) to be written as:

$$\int_{S_B} -\rho \frac{\partial \Phi}{\partial t} n_3 dS = A X_3 e^{-i\sigma t} \quad . \tag{2.33}$$

The contribution from the radiation potential produces the added mass, μ_{33}, and wave radiation damping, λ_{33}. Accounting for the contribution from the radiation potential:

$$\int_{S_B} -\rho \frac{\partial \Phi}{\partial t} n_3 dS = -\int_{S_B} \rho \phi_3 \mathcal{A}_3 \left(-i\sigma\right)^2 e^{-i\sigma t} n_3 dS \quad . \tag{2.34}$$

Simplifying the contribution from ϕ_3 using added mass and wave radiation damping provides:

$$\int_{S_B} \rho \phi_3 n_3 dS = \mu_{33} + \frac{\lambda_{33}}{-i\sigma} \quad , \tag{2.35}$$

$$\int_{S_B} -\rho \frac{\partial \Phi}{\partial t} n_3 dS = -\left(\mu_{33} + \frac{\lambda_{33}}{-i\sigma}\right) \mathcal{A}_3 \left(-i\sigma\right)^2 e^{-i\sigma t} \quad . \tag{2.36}$$

Collecting the hydrostatic and hydrodynamic contributions, while noting that $m = \rho \forall$ as the floater is neutrally buoyant, leads to the following [52]:

$$F_3 = f_h\left(t\right) + f_e\left(t\right) + f_r\left(t\right) = -\rho g A_{wp} \zeta_3(t) + A X_3 e^{-i\sigma t} + \mu_{33} \sigma^2 \mathcal{A}_3 e^{-i\sigma t} + i\sigma \lambda_{33} \mathcal{A}_3 e^{-i\sigma t} \quad , \tag{2.37}$$

The values of μ_{33}, λ_{33}, and X_3 were obtained from [54], using the geometric parameters described in Table 3.1, but can also be obtained from other codes, such as WAMIT [53].

Chapter 3

Heave Response Amplitude Operator

In the frequency domain for an incident wave of amplitude A, and frequency σ, the heave response of the cylinder is given by $\zeta_3(t)$:

$$\zeta_0(x,t) = \Re\left\{Ae^{i(kx-\sigma t)}\right\} \quad , \tag{3.1}$$

$$\zeta_3(t) = \Re\left\{\mathcal{A}_3 e^{-i(\sigma t-\theta)}\right\} \quad , \tag{3.2}$$

Inserting this representation into Eqn. (2.5), using Eqn. (2.37), and ignoring external forces leads to the response amplitude operator (RAO):

$$\left\{\left[\rho g\pi a^2 - \sigma^2\left(m+\mu_{33}(\sigma)\right)\right] - i\sigma\left(\lambda_{vis}(\sigma)+\lambda_{33}(\sigma)\right)\right\}\mathcal{A}_3 = AX_3(\sigma) \quad , \tag{3.3}$$

$$\frac{\mathcal{A}_3}{A} = \frac{X_3(\sigma)}{\left[\rho g\pi a^2 - \sigma^2\left(m+\mu_{33}(\sigma)\right)\right] - i\sigma\left(\lambda_{vis}(\sigma)+\lambda_{33}(\sigma)\right)} \quad , \tag{3.4}$$

$$\left|\frac{\mathcal{A}_3}{A}\right|^2 = \frac{|X_3(\sigma)|^2}{\left[\rho g\pi a^2 - \sigma^2\left(m+\mu_{33}(\sigma)\right)\right]^2 + \left[\sigma\left(\lambda_{vis}(\sigma)+\lambda_{33}(\sigma)\right)\right]^2} \quad . \tag{3.5}$$

It is common to further non-dimensionalize Eqn. (3.5) to take into account the possible geometric scaling of the floater's dimensions. Following the definitions in Table 3.2 provides:

$$\left|\frac{\mathcal{A}_3}{A}\right| = \frac{|\overline{X}_3(\sigma)|}{\sqrt{\left[1-\overline{\sigma}^2\left(\overline{d}+\overline{\mu}_{33}(\sigma)\right)\right]^2 + \left[\overline{\sigma}^2\left(\overline{\lambda}_T(\sigma)\right)\right]^2}} \quad , \tag{3.6}$$

where $\lambda_T = \lambda_{33}+\lambda_{vis}$. The phase shift, θ, in the motion of $\zeta_3(t)$ relative to the wave elevation is defined by:

$$\theta(\sigma) = arg\left(\frac{\mathcal{A}_3}{A}\right) \quad , \tag{3.7}$$

the results are plotted along with the RAO in Fig. 3.1.

The large peak in the response amplitude operator occurs at the the resonant frequency of the floater which is defined as:

$$\sigma_{res} = \sqrt{\frac{K}{m+\mu_{33}(\sigma_{res})}} \quad . \tag{3.8}$$

At the resonant frequency the spring and inertia terms cancel and the floater motion is shifted out of phase with the wave elevation by $\pi/2$. For a single floating body, this condition produces the greatest amount of motion for a given incident wave amplitude. However, under the inviscid assumption, the wave damping is insufficient in predicting the motion response of the floater. From Fig. 3.1a, a 1-in amplitude wave would lead to approximately 4 ft of motion, which is unrealistic and would require the floater to leave the fluid completely. Including a viscous damping multiplier, to increase the wave damping magnitude, can lead to motion estimates that may be reproducible in experiments as found in Fig. 3.1b.

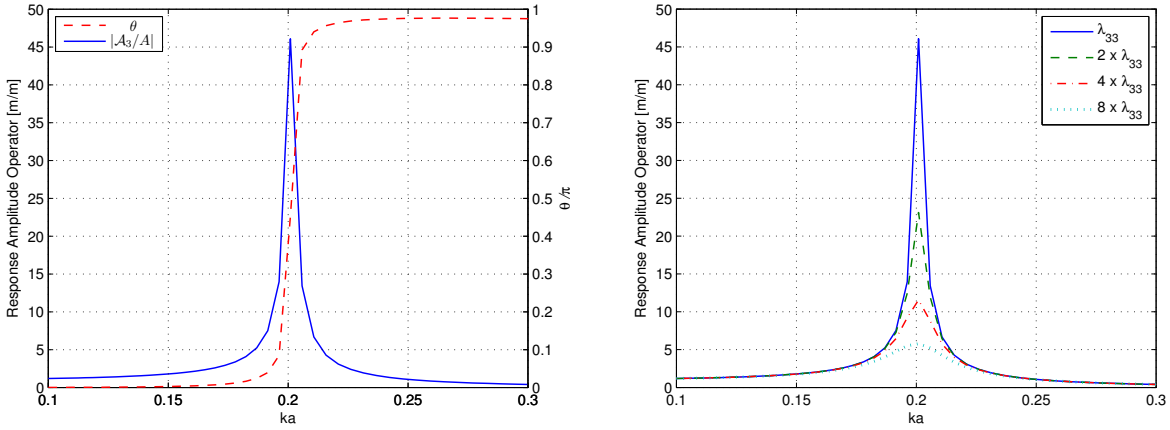

(a) Response amplitude operator and phase angle. (b) Response amplitude operator with λ_{33} multiplier.

Figure 3.1: Response amplitude operator as calculated using data directly from [54].

Table 3.1: Geometric parameters used to solve for μ_{33}, λ_{33}, and X_3.

$D = 2\text{a} = 0.273$ m $\quad d = 0.6126$ m	$\forall = 0.0356$ m^3
$d/D = 2.244$	r(corner radius)$/D = 0.035$
σ_{res} (target) $= 3.695$ rad/s	$T_{res} = 1.7$ s
(Tank width, w_T)$/D = 8.938$	(Tank depth, h_T)$/w_T = 0.612$

Table 3.2: Definition of the normalized parameters consistent with [54].

Parameter	**Normalized form**	**Parameter**	**Normalized form**
Wave-exciting force X_3	$\overline{X}_3 = \frac{X_3}{\pi\rho g a^2}$	Angular frequency σ	$\overline{\sigma} = \sigma\sqrt{\frac{a}{g}} = \sqrt{ka}$
Radius a	$\overline{a} = a/H$	Draft d	$\overline{d} = d/a$
Added-mass μ_{33}	$\overline{\mu}_{33} = \frac{\mu_{33}}{\pi\rho a^3}$	Damping λ_{33}	$\overline{\lambda}_{33} = \frac{\lambda_{33}}{\pi\rho\sigma a^3}$

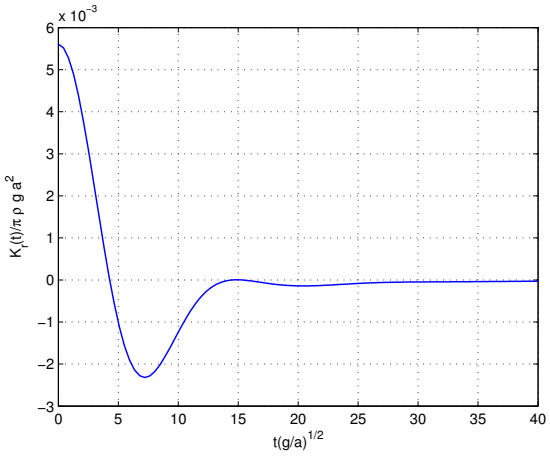

(a) $K_r(t)$.

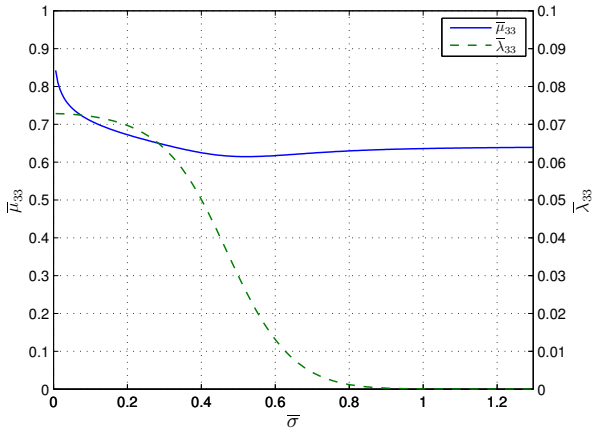

(b) Non-dimensional frequency dependent added mass and wave damping.

Figure 3.2: Non-dimensional time and frequency domain hydrodynamic radiation coefficients.

3.1 Time-Domain Hydrodynamic Coefficients

3.1.1 Calculation of K_r

As previously stated the radiation impulse response function can be calculated by taking the inverse Fourier transform of the hydrodynamic radiation coefficients as found by:

$$K_r(t) = -\frac{2}{\pi}\int_0^\infty \sigma[\mu_{33}(\sigma) - \mu_{33}(\infty)]\sin\sigma t d\sigma \ , \tag{3.9}$$

$$K_r(t) = \frac{2}{\pi}\int_0^\infty [\lambda_{33}(\sigma) - \lambda_{33}(\infty)]\cos\sigma t d\sigma \ . \tag{3.10}$$

Equation (3.10) converges significantly faster than Eqn. (3.9) and is used in this analysis. The geometric properties used to calculate the frequency dependent added mass, wave damping, and complex wave exciting force can be found in Table 3.1. The frequency dependent added mass, wave damping, and wave exciting force were obtained from [54] at a spacing of 0.05 between 0.05-11 rad/s, Fig. 3.2.

3.1.2 Calculation of K_e

The wave exciting force is described in the time domain by Eqn. (2.4), where K_e can be calculated from the inverse Fourier transform of the complex wave exciting force:

$$2\pi K_e(t) \quad = \quad \Re\left\{\int_{-\infty}^{\infty} X_3(\sigma)e^{i\sigma t}d\sigma\right\} \quad . \tag{3.11}$$

$$\tag{3.12}$$

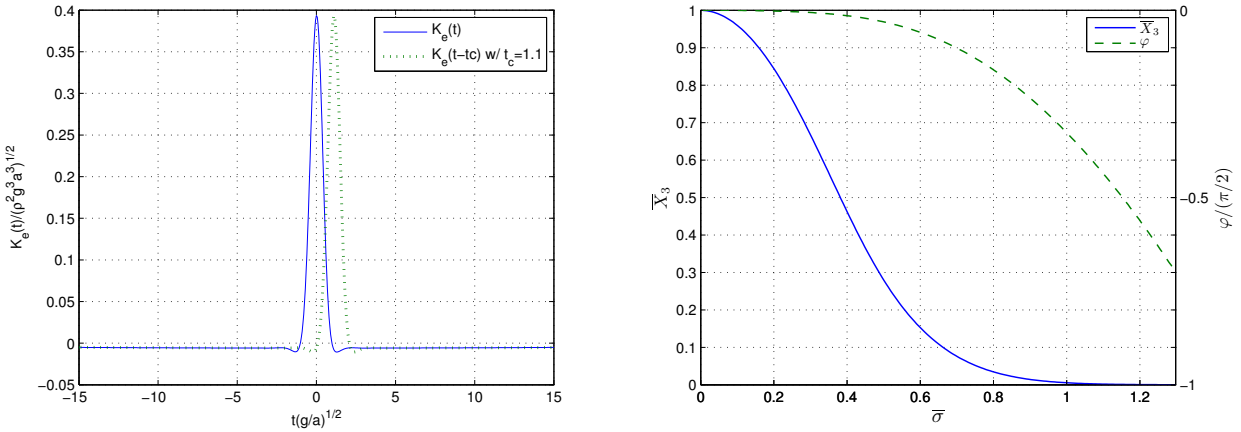

(a) $K_e(t)$, where t_c is a causal time shift.

(b) Non-dimensional heave wave exciting force and phase angle.

Figure 3.3: Non-dimensional time and frequency domain wave exciting force coefficients.

Since K_e is real, $X_3(-\sigma) = X_3^*(\sigma)$, and thus,

$$2\pi K_e(t) = \int_0^\infty [X_3(\sigma)e^{i\sigma t} + X_3^*(\sigma)e^{-i\sigma t}]d\sigma \quad , \tag{3.13}$$

$$K_e(t) = \frac{1}{\pi}\int_0^\infty [\Re(X_3(\sigma))\cos\sigma t - \Im(X_3(\sigma))\sin\sigma t]d\sigma \quad . \tag{3.14}$$

As seen from Fig. 3.3a, K_e is non-causal implying that a heaving force will be felt by the floater before any change in wave elevation is measured at the floater origin.

Heave Exciting-Force Approximation

An approximation to the wave-exciting force X_3 is given by the Froude-Krylov force, which assumes the floater's characteristic length is small compared to the wavelength, $ka << 1$. In this case the presence of the floater is consider to have little effect on the incident wave and neglects the diffraction potential in Eqn. (2.32). The Froude-Krylov approximation for a heaving cylindrical floater is given by:

$$\overline{X}_3(k) \approx \frac{2J_1(ka)}{ka}\left(\frac{e^{-kd}}{1+e^{-2kh}} + \frac{e^{kd}}{1+e^{2kh}}\right) \quad , \quad ka << 1 \quad , \tag{3.15}$$

$$\tag{3.16}$$

with J_1 being the first order Bessel function.

3.2 Floater Construction: Flat Bottom

After obtaining the hydrodynamic coefficients it was desired to verify the predictions with experimental data. In order to complete this the first step was to construct a truncated cylindrical floater. The geometric characteristics of the floater, a truncated cylinder, were chosen to reach a resonance period of 1.7 s [21] calculated from the frequency dependent hydrodynamic coefficients. The main body of the floater is a cylindrical PVC tube with a bottom waterproof wooden cap. Its internal and external diameters are 0.254 m (10 in) and 0.27305 m (10.75 in) respectively. The cylindrical geometry ensures no specific direction of incident waves is necessary for functionality in the ocean. The mass of the floater is directly linked to the draft. In the experimental tests, variations in draft are accomplished by adjusting the amount of ballast that is evenly distributed inside the cylinder. The resonance frequency stands far from the first cut-off frequency of the tank due to the walls of the tank.

3.2.1 Interferences from the tank walls

The walls of the tank, that would not be present in a wide ocean, can spawn unwanted interferences in the response of the device. If a cut-off frequency due to the walls is reached, resonance as defined by Eqn. 3.8 may not show up. It is crucial to design the floater's resonance far from this cut-off frequency. The cut-off frequencies due to the walls were shown to be [55, 56]:

$$\frac{kw_T}{2\pi} = \mathrm{n} \quad , \tag{3.17}$$

where n is an integer and w_T is the tank width. In order to target a resonance frequency smaller than the first cut-off frequency requires:

$$\frac{kw_T}{2\pi} \leq 1 \quad , \tag{3.18}$$

$$ka \leq 2\pi \frac{a}{w_T} \quad . \tag{3.19}$$

The diameter $D = 2a$ and the draft d of the floater are determined by iterations. A given initial diameter D implies that ka has to be smaller than a certain value. The chosen ka at resonance must be far from the cut-off frequency. The draft d is then determined to achieve the desired resonance frequency.

3.2.2 Floater Interior Support Structure

The framing of the floater's interior, Fig. 3.4, is constructed from a low-carbon steel hollow square beam with side lengths of 5.08 cm (2 in) and 0.3048 cm (0.12 in) thick. There are four levels of perpendicular threaded rods that are 24.13 cm (9.5 in) long, 1.27 cm (1/2 in) in diameter, with 13 threads per inch. The square beam prevents excessive bending due to the cantilever geometry of the experimental set-up, see Fig. 3.4. Rubber stoppers are placed at the ends providing a compressible surface to create a tight fit between the inner wall of

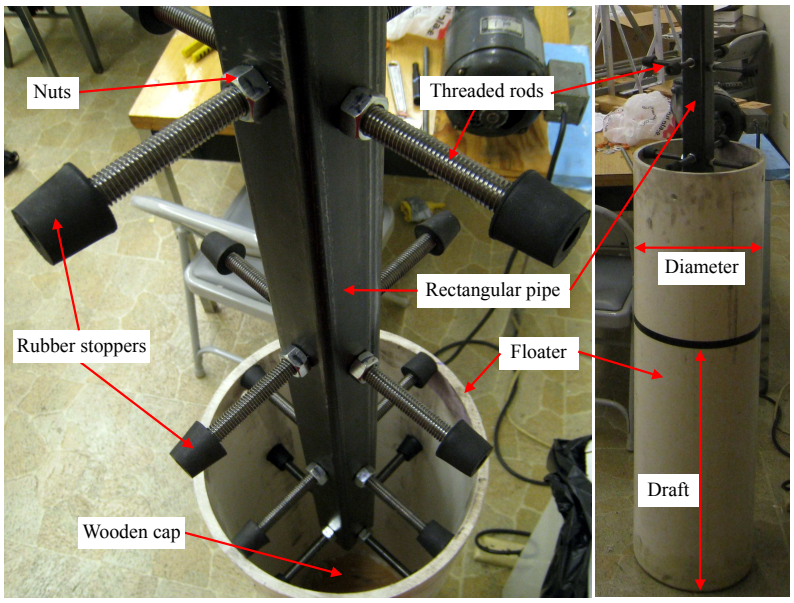

Figure 3.4: Left - Floater interior with support structure, Right - Floater side profile

the cylinder and the threaded rods. The fifth level of threaded rods is bolted directly to the floater.

3.2.3 Floater Heaving Support Structure

For this investigation the floater is restricted only to heave motion. Therefore a support structure is required to eliminate surge and pitch motion. The square beam is connected to cylindrical rods protruding from a solid steel slider. This slider contains two sets of concentric ball bearings that allow for linear travel along two heave rods. The heave rods are held in place by a rectangular steel frame that can be clamped or lashed to the carriage truss frame, thereby constraining surge and pitch motion. To provide additional rigidity, low-carbon steel rectangular bars connected in an L shape are linked to the square beam at the top of the floater and surround the slider. A schematic of the heave support structure can be found in Fig. 3.6.

3.3 Wave Tank Experiments

In order to verify the hydrodynamic performance of the floater experimental tests were completed at the UC Berkeley Richmond Field Station (RFS) Model Testing Facility which holds a wave tank of 68 m X 2.44 m X 1.8 m with a flap-type wavemaker, see Fig. 3.5. Tests of the floater in the fixed position and freely floating (without the generator) were conducted.

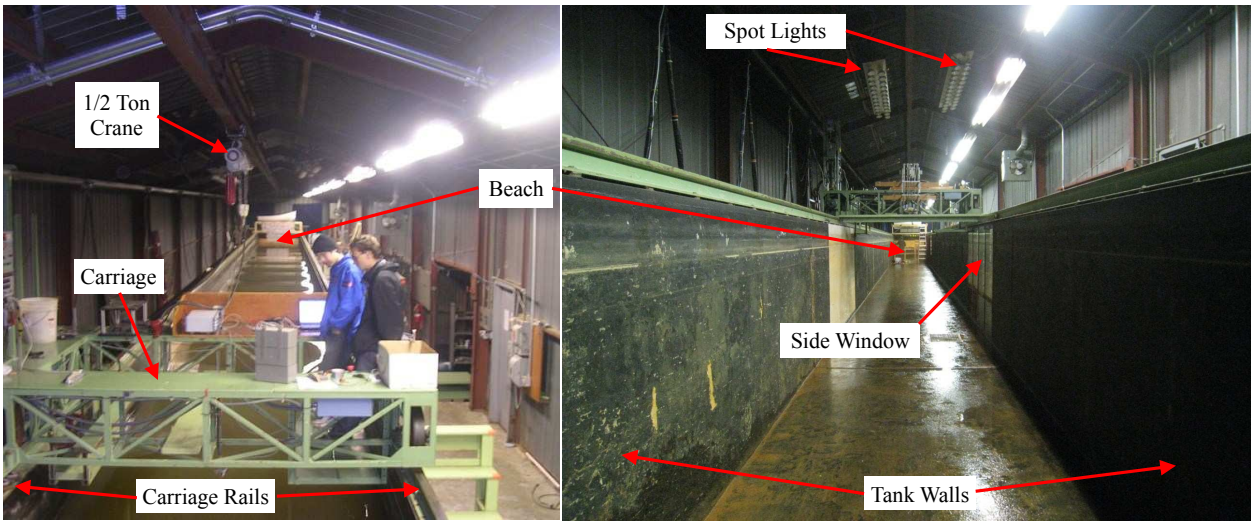

Figure 3.5: Wave Tank at Richmond Field Station. Author of [21] in black jacket and dissertation author in blue jacket in left photo

The floater in the fixed position will allow for the measurement of the wave-exciting force and when freely floating provides the response amplitude operator.

3.3.1 Experimental Instrumentation

It is necessary to obtain accurate measurements of environmental conditions and motion response for parameter estimation, see Sec. 3.4. The RFS facility provides the following instrumentation for use by investigators:

- Celesco SP1 String Pot[1]
- Custom strain gauge force blocks and Interface signal conditioners[2]
- Capacitance wave probes and amplifier box
- Custom Circuit Board for wavemaker control [57]
- Measurement Computing USB-1208FS data acquisition units[3]

3.3.2 Experimental Hydrodynamic Measurements

Response Amplitude Operator

In order to quantify the motion amplitudes of the floater the experimental response amplitude operator was measured, see Fig. 3.7a. The experimental set-up consists of a linear

[1] `http://www.celesco.com/datasheets/index.htm`
[2] `http://www.interfaceforce.com/dma-din-rail-mount-signal-conditioner-p-96.html`
[3] `http://www.mccdaq.com/usb-data-acquisition/USB-1208FS.aspx`

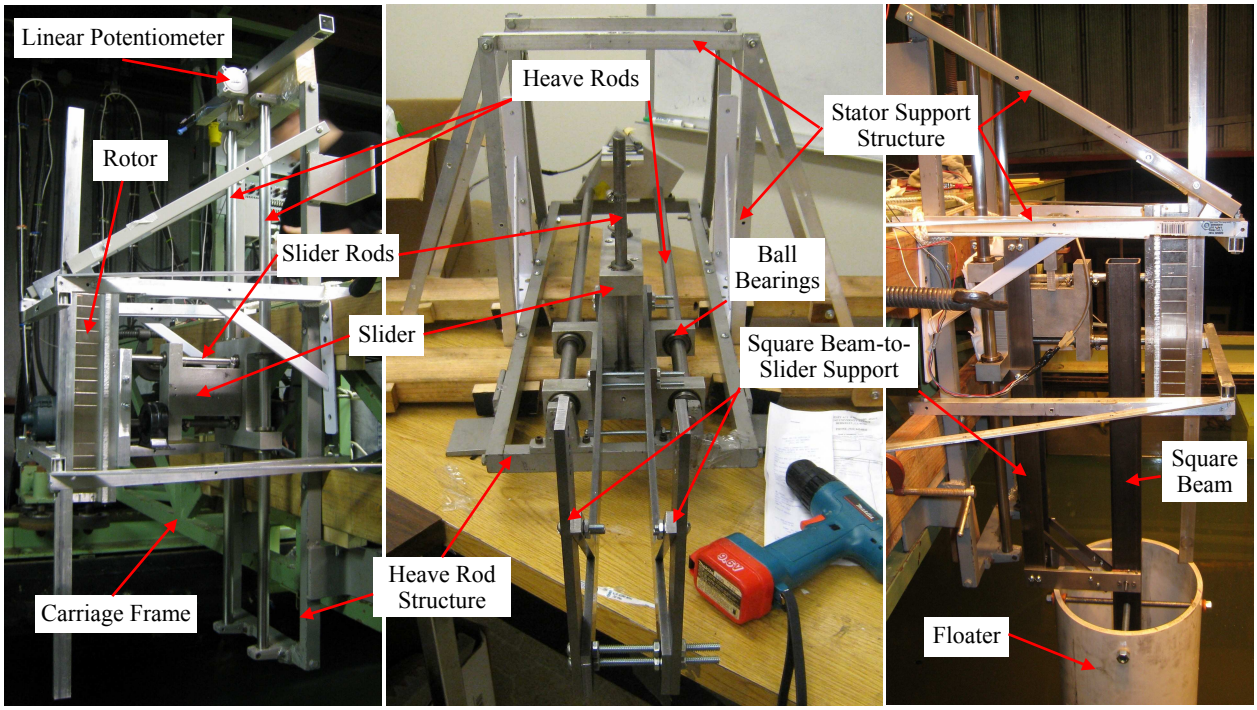

Figure 3.6: Experimental set-up for free motion tests.

potentiometer to measure the wave induced motion of the floater and wave probes for incident wave elevation. The floater free motion tests saw discrepancies between theory and experiment as seen in Fig. 3.7b. As shown in Fig. 3.1, the inviscid RAO greatly over predicts floater motion. In order to provide a better comparison between the measured and predicted RAO a corrective $\lambda_{vis|exp}$ term was included which was obtained from experimental results and described in further detail in Sec. 3.4.1. The addition of $\lambda_{vis|exp}$ led to a maximum RAO that was on the same magnitude as experiments but failed to capture the measured resonance frequency. After the addition of a small corrective added mass term, $\mu_{33|a}$, there was good agreement in the low frequency and resonance regions, but broke down at higher frequencies.

Wave-Exciting Force

Proper modelling of the wave-excitation force is imperative as this drives the floater's motion. X_3 is defined as the force, per unit wave amplitude, felt by the floater while fixed at its calm water line. A restraining block was rigidly attached to the heave rods, see Fig. 3.9, to prevent floater motion. The restraining block was connected to the slider through a force block which is in-line with the vertical axis thereby measuring only the heave exciting force; however, due to the cantilever beam support for the floater an additional force may have been recorded due to a moment generated by the surge force, X_1.

The convolution integral in Eqn. (2.4) for calculating $f_e(t)$ can be completed quickly by using the Fast Fourier Transform (FFT):

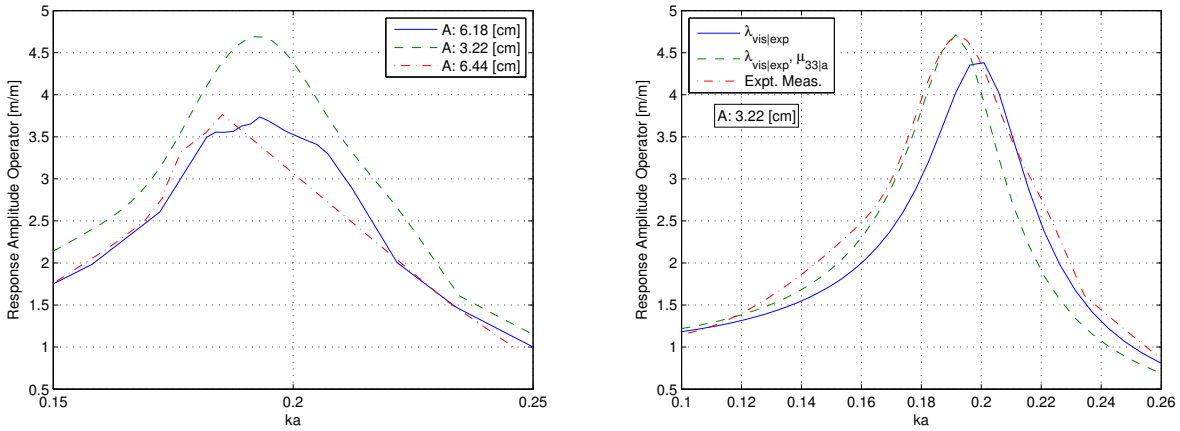

(a) Experimental RAO with varying wave amplitude. (b) Measured RAO versus [54] with experimental corrections.

Figure 3.7: Response amplitude operator for flat bottom floater.

$$f_e(t) = \mathcal{F}^{-1}\{\mathcal{F}\{K_e\} \cdot \mathcal{F}\{\zeta_o(0,t)\}\} \quad , \tag{3.20}$$

where $\mathcal{F}$ denotes FFT. The hydrodynamic analysis is performed under the linear wave approximation, therefore it is important to check the wave height to wave length ratio, H/λ. From Fig. 3.9, it appears that potential theory adequately models the heave wave-exciting force in both the frequency and time domain. The Froude Krylov approximation significantly over predicts the exciting force over the tested frequency range.

3.4 Experimental Hydrodynamic Coefficient Estimates

3.4.1 Frequency-Domain Solution

In this section it will be assumed that the floater's heave motion is time harmonic. Values of X_3 can be obtained from [54] or experimental measurements. At resonance the spring and inertia terms cancel simplifying the denominator of Eqn. (3.5):

$$|\frac{\mathcal{A}_3}{A}|^2 = \frac{|X_3(\sigma)|^2}{[\sigma(\lambda_{vis} + \lambda_{33}(\sigma_{res}))]^2} \quad , \tag{3.21}$$

$$\lambda_{vis} + \lambda_{33}(\sigma_{res}) = \frac{|X_3(\sigma_{res})|}{\sigma_{res}|\frac{\mathcal{A}_3}{A}|} \quad , \tag{3.22}$$

$$\mu_{33}(\sigma_{res}) = \frac{K}{\sigma_{res}^2} - m \quad . \tag{3.23}$$

Therefore, at the resonance frequency estimates on the floater's damping can be made from wave-exciting force and RAO measurements. As seen from Fig. 3.7b, the inviscid hydrody-

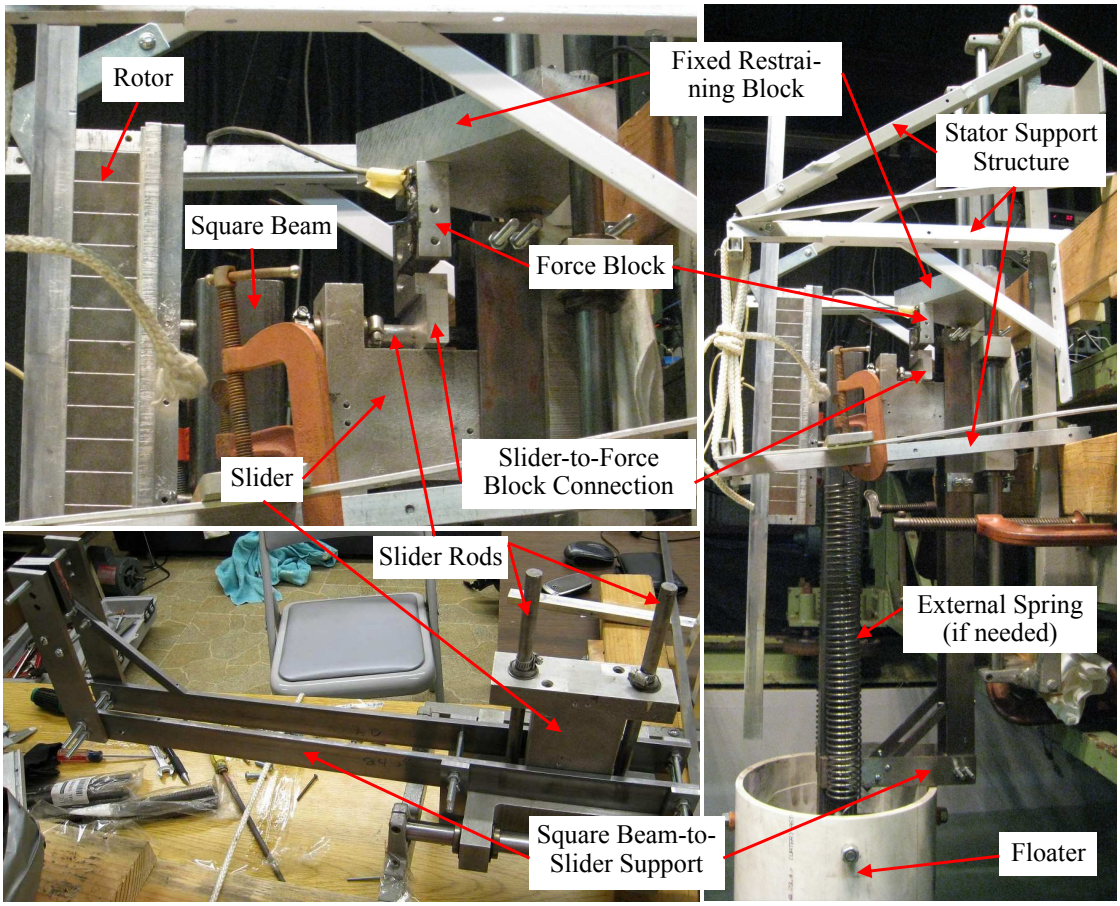

Figure 3.8: Wave exciting force experimental floater set-up

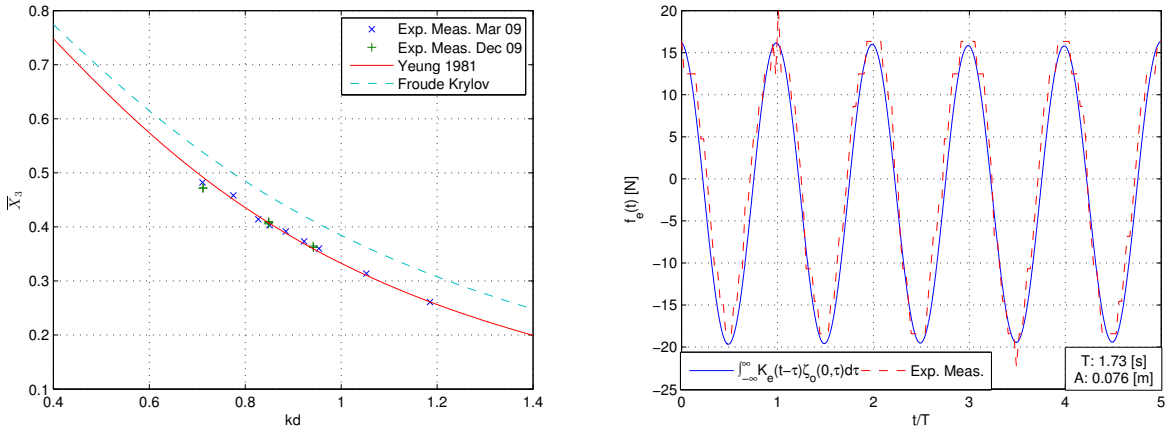

(a) Experimental frequency domain wave-exciting force.

(b) $f_e(t)$ from measurements and Eqn. (3.20) with $H/\lambda = 0.034$.

Figure 3.9: Experimental wave-exciting force measurements. For figure (b), the wave elevation and exciting force measurements were not taken at the same location. The results from Eqn. (3.20) were time-shifted to account for the separation distance.

namic coefficients need a correction factor to have a better agreement with experiments. In an attempt to quantify these corrections, the following values were calculated and included in Eqn. 3.6:

$$\lambda_{vis|exp}\left(\sigma_{res}\right) = \frac{\left|X_3\left(\sigma_{res}\right)\right|}{\sigma_{res}\left|\frac{A_3}{A}\right|} - \lambda_{33}\left(\sigma_{res}\right) \quad , \tag{3.24}$$

$$\mu_{33|a}\left(\sigma_{res}\right) = \frac{K}{\sigma_{res}^2} - m - \mu_{33}\left(\sigma_{res}\right) \quad . \tag{3.25}$$

where $\lambda_{33}\left(\sigma_{res}\right)$ and $\mu_{33}\left(\sigma_{res}\right)$ were obtained from [54]. It should be noted that the corrective values did not vary with frequency as they were calculated at resonance.

$\lambda_T\left(\sigma_{res}\right)$ and $\mu_{33}\left(\sigma_{res}\right)$ calculated from experimental values are presented in Table 3.3. Furthermore, the effects of a non-linear damping are apparent in Fig. 3.7a. The larger amplitudes of motion achieved with greater incident wave heights have lead to an increased

Table 3.3: Experimental Measurements from Fig. 3.7.

	σ_{res}	RAO	X_3	$\lambda_T\left(\sigma_{res}\right)$	$\mu_{33}\left(\sigma_{res}\right)$
A: 3.22 cm	3.67	4.68	228.2	13.29	6.77
A: 6.18 cm	3.67	3.73	228.0	16.63	6.75
A: 6.44 cm	3.68	3.69	227.2	16.34	6.59

amount of shed vortices beneath the floater. In this case, the RAO is dependent on the wave height whereas it should be invariant under linear potential theory.

3.4.2 Time-Domain Modeling: Free Decay

The floater's heave motion can be approximated by a general spring-mass-damper system, whose equation of motion is written as:

$$\frac{d^2\zeta_3}{dt^2} + 2\zeta\omega_n\frac{d\zeta_3}{dt} + \omega_n^2\zeta_3 = 0 \tag{3.26}$$

$$\frac{d^2\zeta_3}{dt^2} + \frac{\lambda_T}{M}\frac{d\zeta_3}{dt} + \frac{K}{M}\zeta_3 = 0 \tag{3.27}$$

where ζ, ω_n, and M are the damping ratio, undamped angular frequency, and virtual mass of the system. The virtual mass includes the body mass, m, and the infinite frequency added mass, $M = m + \mu_{33}(\infty)$. From inspection of Eqn. 3.26 and Eqn. 3.27 the following relationships are found:

$$\omega_n = \sqrt{\frac{K}{M}} = \sqrt{\frac{K}{m+\mu(\infty)}} \tag{3.28}$$

$$\lambda_T = 2\zeta\omega_n M = 2\zeta\sqrt{KM} \tag{3.29}$$

It is of interest to estimate the damping coefficient of the floater to validate possible reductions in hydrodynamic damping due to bottom re-shaping [25, 62, 63]. This characterization can be performed in the time domain by using logarithmic decrement. The logarithmic decrement analysis will be applied to experimental free decay tests, Fig. 3.10. A free decay test provides the time history of heave position, measured by the linear potentiometer, after release of the floater from the following initial conditions, $\zeta_3(0) = C$ and $\dot{\zeta}_3(0) = 0$, where C is the offset amplitude. From the free decay time history the reduction in oscillation amplitude and time between successive positive peaks can be measured. Finally, λ_T and $\mu_{33}(\infty)$ can be estimated from Eqns. (3.28) & (3.29). The logarithmic decrement results applied to Fig. 3.10a can be found in Table 3.4. The average values from the maximum peaks provide $\mu_{33}(\infty)$ and λ_T of 6.36 kg and 13.5 kg/s respectively.

3.4.3 State-Space Representation of Radiation Impulse Response Function

The convolution integral found in Eqn. (2.3) is inconvenient for control implementation. Therefore it is desired to represent Eqn. (2.3) as a set of ODEs to be used in a linear state-space form. This can be achieved by using the Matlab function, **imp2ss**, to generate the following approximation:

$$\dot{X}_r(t) = A_r X_r(t) + B_r\dot{\zeta}_3(t)\,;\;\; X_r(0) = 0 \tag{3.30}$$

$$\int_{-\infty}^{t} K_r(t-\tau)\,\dot{\zeta}_3(\tau)\,d\tau \approx C_r X_r(t) + D_r\dot{\zeta}_3(t) \tag{3.31}$$

$$X_r \in \mathbb{R}^{n\times 1}\;,\; A_r \in \mathbb{R}^{n\times n}\;,\; B_r \in \mathbb{R}^{n\times 1}\;,\; C_r \in \mathbb{R}^{1\times n}\;,\; D_r \in \mathbb{R}^{1\times 1} \tag{3.32}$$

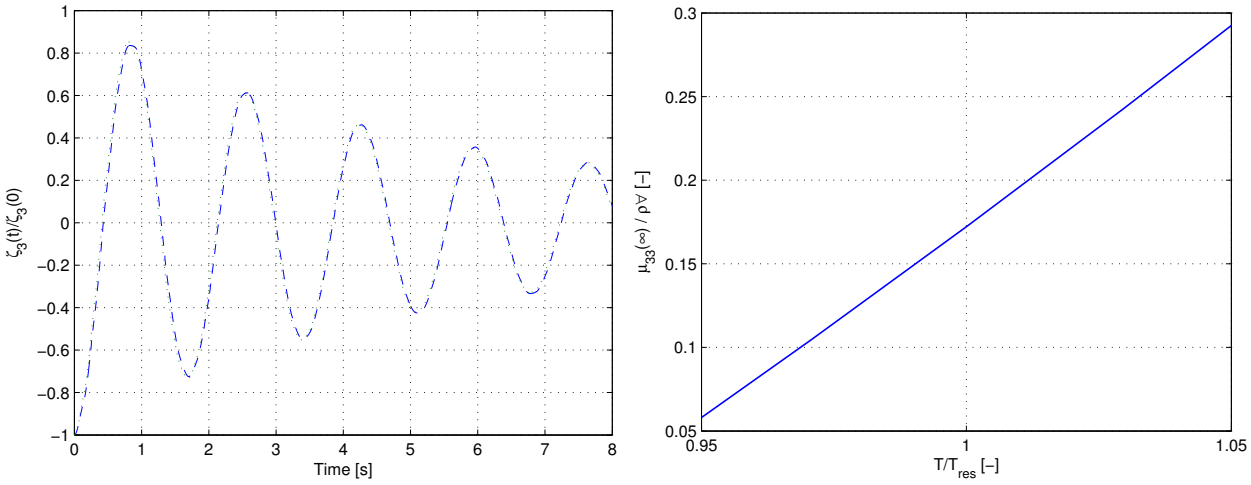

(a) Free decay test for FB floater, $\zeta_3(0) = 0.27$ m.

(b) Estimated $\mu_{33}(\infty)$ for FB Floater.

Figure 3.10: Time Domain Characterization. Note: $m_{FB} = 35.87$ kg.

Table 3.4: Logarithmic Decrement Measurements from Fig. 3.10a.

n	1	2	3	4
$\frac{\zeta_3(t+(n-1)T)}{\zeta_3(t+nT)}\|_{Neg}$	1.38	1.32	1.29	1.27
$\frac{\zeta_3(t+(n-1)T)}{\zeta_3(t+nT)}\|_{Pos}$	1.36	1.33	1.30	1.24
$\delta\|_{Neg}$	0.0512	0.0439	0.0412	0.0383
$\delta\|_{Pos}$	0.0495	0.0449	0.0408	0.0347
$\mu_{33}(\infty)\|_{Neg}$	5.61	5.64	5.65	5.66
$\mu_{33}(\infty)\|_{Pos}$	6.35	6.36	6.38	6.40
$\lambda_T\|_{Neg}$	15.81	13.55	12.71	11.84
$\lambda_T\|_{Pos}$	15.4	14.00	12.7	10.82

The detailed theory behind this realization theory can be found in [58, 59, 60]. A balanced model reduction was used to find the lowest number of states that could be used to accurately represent K_r. As seen from the error between Eqn. (3.9) and the reduced state-space models, Fig. 3.11b, the number of states can be reduced to 3 without a substantial loss in accuracy.

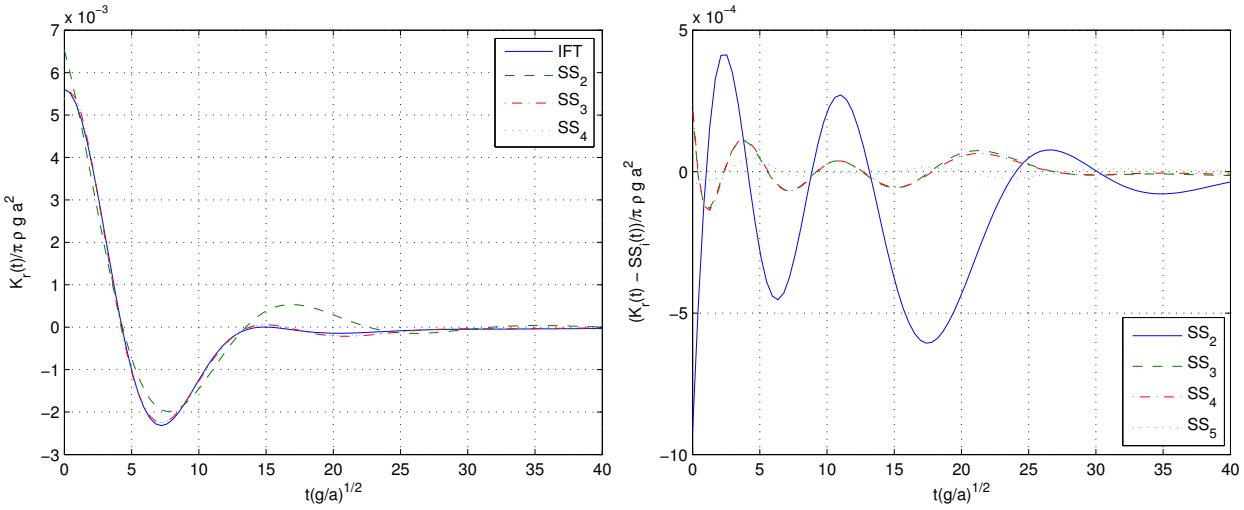

(a) Time History of $K_r(t)$.

(b) Error of $K_r(t)$ approximations.

Figure 3.11: $K_r(t)$ from Inverse Fourier Transform (IFT) vs reduced state space model of order i, SS_i, from imp2ss.

3.4.4 State-Space Representation of Wave-Exciting Force Kernel

It may be desired to represent Eqn. (2.4) in state-space form, similar to the radiation impulse response function. However, as seen from Fig. 3.3a, K_e is non-causal and more difficult to approximate in the form of Eqn. (3.31). A time shift, t_c, could be included that approximates K_e as a causal function, but creates a delay in the response which is not desired in this investigation. However, this work will not implement any wave elevation prediction methods and the time series of waves is assumed known. Since the wave input will be known, Eqn. (2.4) will be computed with the Fast Fourier Transform (FFT) and used as a direct input for simulations.

3.4.5 State-Space EOM

The time-invariant state-space matrices [61], with sinusoidal wave excitation, can now be constructed as follows:

$$X_{sys} = \underbrace{\begin{bmatrix} x_{r|1} \\ \vdots \\ x_{r|n} \\ \zeta_3 \\ \dot{\zeta}_3 \end{bmatrix}}_{\mathbb{R}^{n+2\times 1}} \quad A_{sys} = \underbrace{\begin{bmatrix} A_r & 0 & B_r \\ 0 & 0 & 1 \\ -\frac{C_r}{m+\mu_{33}(\infty)} & -\frac{\rho g \pi a^2}{m+\mu_{33}(\infty)} & -\frac{D_r+\lambda(\infty)+(\lambda_{vis})}{m+\mu_{33}(\infty)} \end{bmatrix}}_{\mathbb{R}^{n+2\times n+2}} \quad S_w = \underbrace{\begin{bmatrix} 0 \\ 0 \\ \vdots \\ \frac{A|X_3(\sigma)|\Re(e^{i\varphi})}{m+\mu_{33}(\infty)} \end{bmatrix}}_{\mathbb{R}^{n+2\times 1}} \tag{3.33}$$

where $x_{r|n}$, ζ_3, $\dot{\zeta}_3$ correspond to the radiation states, floater position, and floater velocity. The heave equation of motion in state-space form can now be written as:

$$\dot{X}_{sys}(t) = A_{sys} X_{sys}(t) + S_w \zeta_o(t) \ . \tag{3.34}$$

Free Decay Simulations

Equation (3.27) combines the viscous and wave damping contributions making them indistinguishable as no information was gathered on the radiated waves from free decay motion. Therefore, model simulations will include the inviscid wave damping while the viscous contribution will be tuned from the estimates provided by logarithmic decrement for time domain matching.

The initial values of $\mu_{33}(\infty)$ and λ_{vis} were fine tuned in Eqn. 3.34 to simulate the heave time history, $\zeta_{3|s}$, see Fig. 3.12. Simulations were run using the built-in Matlab 4th order Runge-Kutta scheme with fixed time step, Δt. The experimental and simulated time histories match well with deviations appearing after 6 s as the simulations begin to decay faster. This is likely due to the non-linear nature of the drag component evident from [62, 63]. However, given that the time domain control strategies, described in Chapter 6, require between 2 - 3 s of accurate motion predictions, this characterization appears to be sufficient.

3.5 Reduction of λ_T by Floater Shape Change

3.5.1 Viscous Effects due to Vortex Shedding

The sharp corners of a flat bottom (FB) floater, shown in Fig. 3.15, shed a large amount of vorticity, causing large viscous damping. Altering the bottom shape of the floater to decrease the hydrodynamic damping should amplify the floater motion and improve power

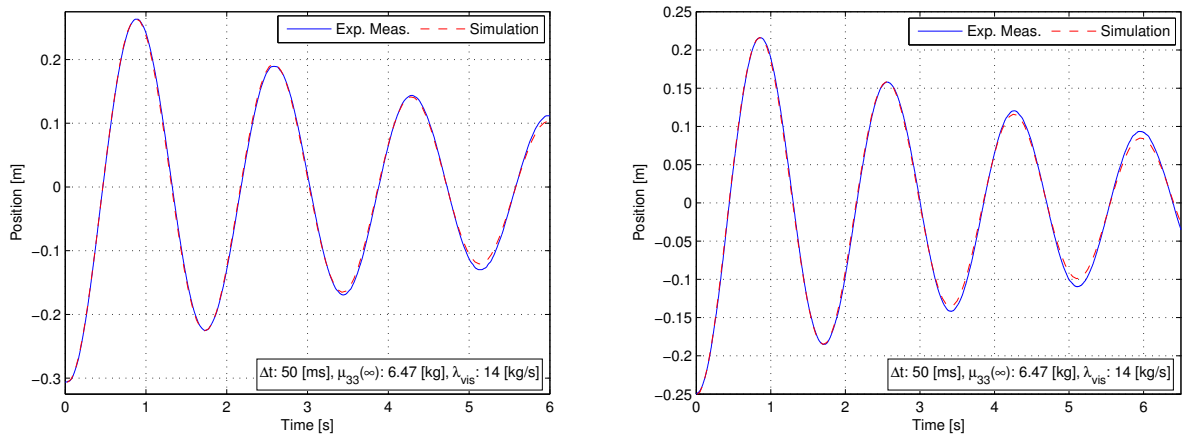

(a) Free Decay Measurement 12-09-09.

(b) Free Decay Measurement 07-22-10.

Figure 3.12: Free Decay Simulations.

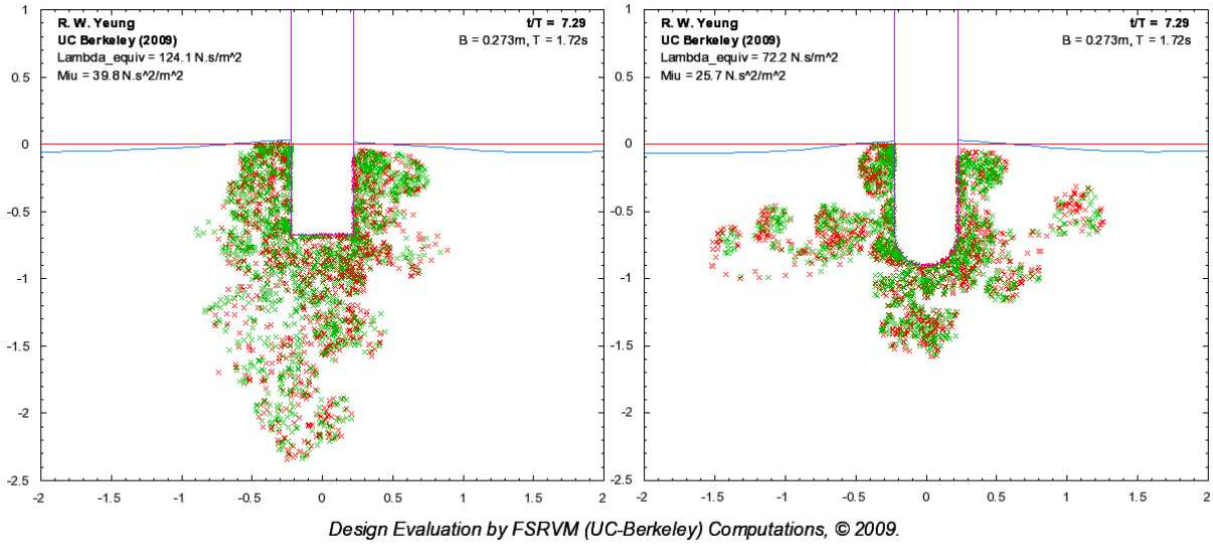

Figure 3.13: Vortex-blob patterns from FSRVM [64] for prescribed heave oscillation: a comparison between 2D RB and FB shapes: Red and green crosses represent clockwise and counter-clockwise vorticity, respectively. Simulation parameters are comparable to the 3D geometry, Fig. 3.15: $(\mathrm{d/B}) = 2.24$, $\mathcal{A}_3 = 6$ in, $\sigma = 3.65$ rad/s. The hydrodynamic coefficients μ_{33} and λ_T for each shape are shown in the upper left corner of each plot.

extraction.

Under prescribed motion, the hydrodynamic heaving force on a floating body can be approximated by the following inertia and damping terms:

$$F_3(t) \cong -\mu_{33}\ddot{\zeta}_3(t) - \lambda_{33}\dot{\zeta}_3(t) \tag{3.35}$$

Within inviscid-fluid theory, F_3 would be dominated by μ_{33} with only a small contribution coming from λ_{33}; however, as noted in [24], the total (real-fluid) hydrodynamic damping is significantly greater than that predicted by inviscid theory. As per [25, 62], which utilized the two-dimensional viscous-fluid algorithm, FSRVM [64], μ_{33} is slightly reduced with viscosity present, whereas λ_T is significantly larger particularly for cylinders with shallower drafts. Quantitatively, it was observed that a floater with a semi-circular bottom (RB) could experience a decrease in hydrodynamic damping by as much as 50% when compared to a flat-bottom geometry. These results were reported for two-dimensional geometries, but can provide some guidance towards reshaping the floater geometry. A shape-effect factor, for a vertical cylinder bottom, may be defined as:

$$\Lambda_{3D} \equiv \lambda_T^{(q1)}/\lambda_T^{(q2)} < \Lambda_{2D} \quad , \tag{3.36}$$

with RB designated as $q1$ and FB as $q2$, the Fourier-analyzed damping coefficients from FSRVM simulations, for the conditions and geometry shown in the legend of Fig. 3.13, are listed in Table 3.5.

The vortical flow patterns corresponding to these computations are shown in Fig. 3.13. This static display does not provide the interacting effects among the many vortices (O(50,000)). In a video animation, the rounded-bottom floater yields vortex clusters of opposing signs that annihilate more readily than those of the flat-bottom case; this latter geometry tends to spread the vorticity into a larger field. This is the source for the significant reduction in damping when the shape is changed.

3.5.2 Floater Construction: Rounded Bottom (RB)

In order to verify the reduction in viscous damping a hollow plastic hemispherical cap was attached to the existing flat bottom (FB) floater pictured in Fig. 3.14. It was chosen to modify the FB floater in order to take advantage of the existing support structure inside the cylindrical body. The hollow plastic cap does not fully match the mathematical profile given by, $\forall = 2/3\pi r^3$, but has been assumed so for modelling purposes. Before mounting

Table 3.5: 2D Hydrodynamic damping from FSRVM.

λ_T^{RB}	72.2 N-s/m
λ_T^{FB}	124.1 N-s/m
Λ_{2D}	58.2 %

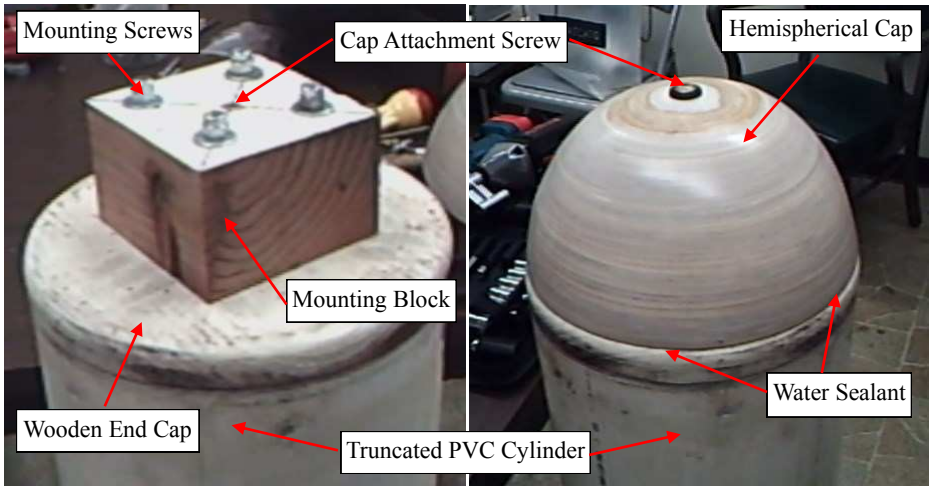

Figure 3.14: Left - Flat bottom profile with attachment block, Right - Rounded bottom profile, courtesy of Professor Ronald W. Yeung

the hemispherical cap, a wood block measuring 10 cm x 10 cm x 7.6 cm was cut to provide a foundation for the attachment screw. The mounting block was attached to the wooden end cap of the FB floater through four mounting screws. The hemispherical cap was centered over the end cap and a single attachment screw, with rubber washer, was driven into the mounting block. Finally, water proof sealant was applied to the outer edges of the hemisphere and at the mounting screw insertion point to create a waterproof seal. It was decided to keep the hollow center of the hemisphere free of water to provide extra buoyancy that might be needed to reach a desired draft, without the use of external springs.

3.6 Rounded Bottom Floater Experimental Hydrodynamics

3.6.1 Free Decay Tests of RB Floater

The RB geometry could not be used with [54]; therefore, free decay tests were used to calculate the natural period of the modified floater. It was desired to maintain a resonance period of 1.7 s in order for comparisons to be made against the FB floater. After the RAO experimental instrumentation was installed at the RFS wave tank, ballast was added/removed until the natural period of free decay oscillations matched with the FB floater. The tests also provided time histories which could be used with the logarithmic decrement procedure, described in Section 3.4.2, to confirm if the expected reduction in hydrodynamic damping was achieved.

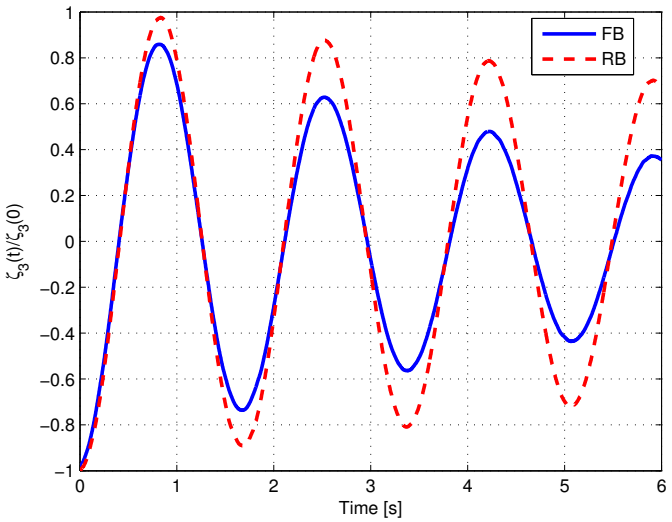

(a) Free decay tests of FB and RB floaters.

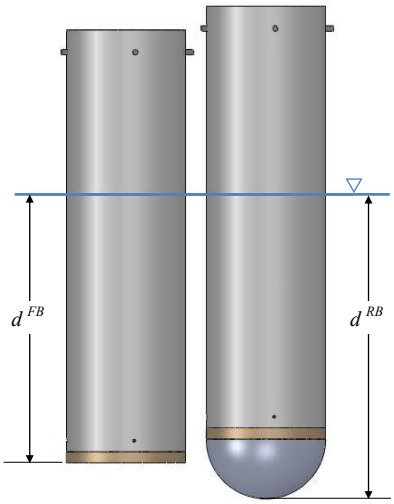

(b) Profile view of FB and RB floaters.

Figure 3.15: FB and RB comparisons.

Table 3.6: Geometric parameters used during the tank tests for FB and RB floaters.

D(dia) = 2a = 0.273 m $\quad d$(draft) = 0.706 m	$\forall = 0.0382$ m^3
$d/D\|_{FB} = 2.243$	$d/D\|_{RB} = 2.586$
σ_{res} (target) = 3.695 rad/s	$T_{res} = 1.7$ s
(Tank width, w_T)$/D = 8.938$	(Tank depth, H_T) / $w_T = 0.612$

Time History Comparison of Free Decay Tests

After the period of oscillation was matched between the RB and FB floaters, see Fig. 3.15a, a draft of approximately 0.7 m was achieved, see Table 3.6. The RB draft, as measured from the calm water-line to the tip of the hemispherical cap, is approximately 13% greater than the FB; however, the displaced volume increased by only 6 % due the decreasing cross sectional area at the bottom of the floater, see Fig. 3.15b. It is expected that the RB geometry not only leads to a decrease in the hydrodynamic damping, but also in the added mass and will be verified in the next section.

Free Decay Hydrodynamic Damping Estimates

The hydrodynamic damping estimates for the FB and RB floaters, for the time histories displayed in Fig. 3.15a, can be found in Table 3.7. The tables indicate that a substantial reduction in λ_T, approximately 55%, was achieved; however, since no information on the

Table 3.7: Logarithmic Decrement Measurements from Fig. 3.15a

(a) RB Logarithmic Decrement Results.

n	1	2	3
$\frac{\zeta_3(t+(n-1)T)}{\zeta_3(t+nT)}\|_{Neg}$	1.12	1.10	1.12
$\frac{\zeta_3(t+(n-1)T)}{\zeta_3(t+nT)}\|_{Pos}$	1.11	1.11	1.12
$\zeta\|_{Neg}$	0.0184	0.0153	0.0182
$\zeta\|_{Pos}$	0.0171	0.0169	0.0183
$\mu_{33}(\infty)\|_{Neg}$	2.97	2.97	2.97
$\mu_{33}(\infty)\|_{Pos}$	3.08	3.08	3.08
$\lambda_T\|_{Neg}$	5.68	4.73	5.63
$\lambda_T\|_{Pos}$	5.29	5.24	5.66

(b) FB Logarithmic Decrement Results.

n	1	2	3
$\frac{\zeta_3(t+(n-1)T)}{\zeta_3(t+nT)}\|_{Neg}$	1.33	1.30	1.29
$\frac{\zeta_3(t+(n-1)T)}{\zeta_3(t+nT)}\|_{Pos}$	1.37	1.31	1.29
$\zeta\|_{Neg}$	0.0454	0.0423	0.0409
$\zeta\|_{Pos}$	0.0497	0.0432	0.0401
$\mu_{33}(\infty)\|_{Neg}$	5.87	5.88	5.89
$\mu_{33}(\infty)\|_{Pos}$	6.22	6.25	6.26
$\lambda_T\|_{Neg}$	14.05	13.09	12.66
$\lambda_T\|_{Pos}$	15.46	13.44	12.49

radiated waves is available one cannot differentiate between wave and viscous damping. Furthermore, the added mass has also decreased by approximately 50%, which can be expected due to the increase in floater weight requiring a lower added mass to maintain the same resonance period. In addition, the hydrodynamic damping from the FB floater has a decreasing trend with oscillation number whereas the RB floater remains roughly constant. This helps strengthen the argument for a non-linear viscous damping that is a function of the motion amplitude.

RB Free Decay Simulations

The hydrodynamic code in [54] was not intended to handle the bottom geometry of the RB floater. Therefore, it was decided that when attempting to simulate the floater motion the FB impulse response function would be kept, while $\mu_{33}(\infty)$ and λ_{vis} would be tuned from experimental measurements. This was considered to be a sufficient approximation as the cross sectional area was unaltered, therefore the amount of displaced fluid resulting from floater motion, which is related to the wave damping, would be the same. Similar to Sec. 3.4.5, the logarithmic decrement procedure combines the viscous and wave damping contributions. Therefore, model simulations will include the inviscid wave damping while the viscous contribution will be tuned from the estimates provided by logarithmic decrement for time domain matching. The values of $\mu_{33}(\infty)$ and λ_{vis} were fine tuned in Eqn. 3.34 to simulate the heave time history $\zeta_{3|s}(t)$, see Fig. 3.16. The simulations were again run using the built in Matlab 4th order Runge-Kutta scheme with a fixed time step. The experimental and simulated time histories match better over the duration of the simulation than compared

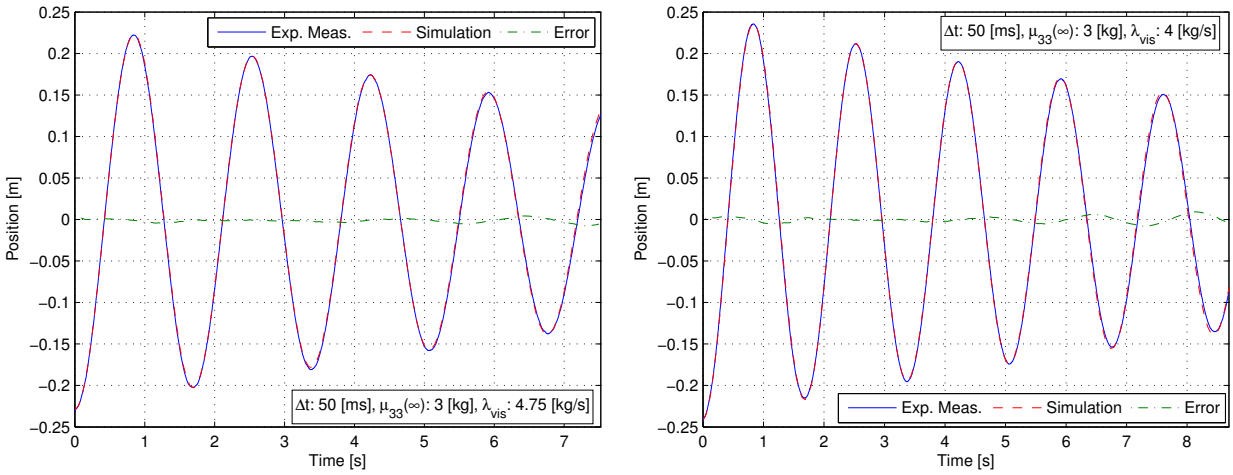

(a) (b)

Figure 3.16: Comparison of RB hydrodynamic model to free decay experimental measurements.

to the flat bottom, with the values of $\mu_{33}(\infty)$ and λ_{vis} close to those presented in Table 3.7. At this point the resulting hydrodynamic coefficient characterization from free decay tests appears to be sufficient for the rounded bottom floater.

3.6.2 Free Motion Test

After determining the appropriate draft of the RB floater, while maintaining a 1.7 s resonance period, the free motion test was repeated as described in Section 3.3.2. The results of the RB free motion test compared with the FB floater can be found in Fig. 3.17. It was found that the RAO at resonance increased by a factor of 2 when compared to the FB floater again indicating that a substantial reduction in hydrodynamic damping was achieved. Furthermore, due to the large response at resonance a much smaller wave amplitude was used to prohibit the RB floater from hitting the heave rod end stops. Therefore, sensitivity of the RAO to wave amplitude was not investigated.

3.6.3 Wave-Exciting Force Test

The wave-exciting force test was repeated so frequency domain hydrodynamic damping estimates could be made. Given the increased draft of the RB floater it is expected that X_3 will have decreased since the oscillating pressure due to the waves decreases when moving below the free surface. As seen from Fig. 3.17b, the non-dimensional wave-exciting force decreased approximately by 4%. Therefore, future estimates on the wave exciting force for the RB floater will simply be the scaled values from the FB floater.

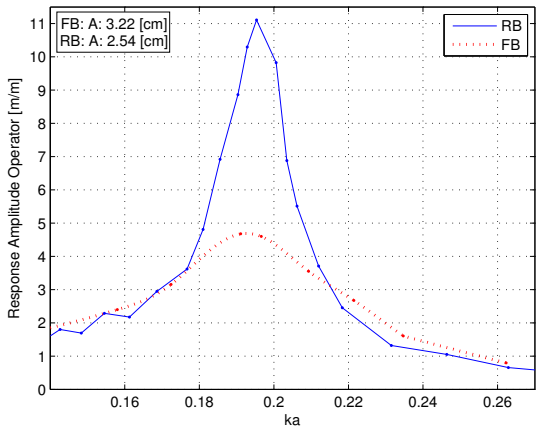

(a) Free motion tests of FB and RB floaters.

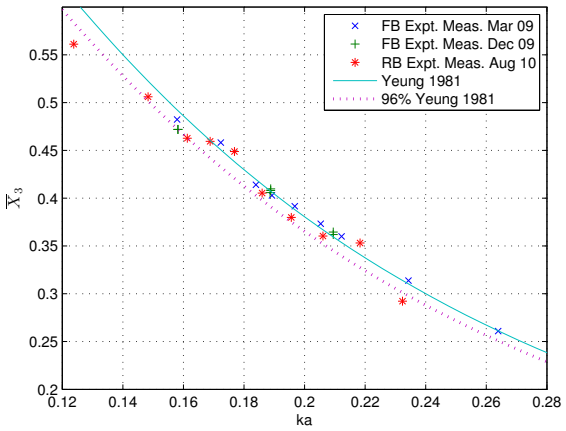

(b) Wave-exciting force of FB and RB floaters.

Figure 3.17: Comparison of hydrodynamic performance between FB and RB floaters.

3.6.4 Free Motion Hydrodynamic Damping Estimates

With measurements from the free motion and wave exciting force tests, estimates on the hydrodynamic damping at resonance can be made from Eqn. (3.22). The calculated values for $\lambda_{T|res}$ for both floaters can be found in Table 3.8. The calculations show that the hydrodynamic damping and added mass of the RB floater decreased by approximately 50% and are consistent with the values found in Table 3.7. These results are below the 2D bound that was set in Table 3.5 and should lead to an increase in the maximum capture width as the decrease in hydrodynamic damping exceeded that of the wave-exciting force.

Table 3.8: Experimental Measurements from Fig. 3.17.

	σ_{res}	RAO	X_3	$\lambda_T(\sigma_{res})$	$\mu_{33}(\sigma_{res})$
FB A: 3.22 cm	3.67	4.68	228.2	13.29	6.77
RB A: 2.54 cm	3.70	11.1	215.8	5.50	3.6

Chapter 4

Power Take-Off

In order to convert the floater's motion into useful energy a power-take-off unit is required. For this research a permanent magnet linear generator (PMLG) was developed in house for this purpose [20, 21, 24, 25]. A PMLG normally consists of two components moving relative to one another. The moving component of the device is typically called the armature and is directly attached to the floater. The fixed component is commonly called the stator and will be connected to the supporting structure.

For development at UC Berkeley the armature consists of rare earth permanent magnets, poles, which generate a changing magnetic field as it moves through the stator. The stator holds the copper windings that carry the induced current, produced to counteract the changing magnetic field, to the applied electrical load. Before describing the construction of the UC Berkeley PMLG it is important to review the electro-magnetic theory used in the design.

4.1 Basic Electro-Magnetic (EM) Theory [65, 66]

Electro-Magnetic Devices are governed by Maxwell Equations.

4.1.1 Magnetic Intensity

The magnetic intensity, $\vec{H}_m$, is a vector quantity that is a measure of a magnetic field's strength at a given point in space. When a current moves along an electrical conductor a magnetic field will be generated which can be represented mathematically by the Biot-Savart Law:

$$\vec{H}_m = \oint \frac{i\vec{dl} \times \hat{n}}{4\pi|\vec{r}|^2} \quad , \tag{4.1}$$

where i, $\vec{l}$, $\hat{n}$, and $|\vec{r}|$ are current, electrical conductor length, unit normal, and distance to the field point from the electrical conductor. Thus, magnetic intensity is generally proportional to the applied current and inversely proportional with square of the distance.

4.1.2 Magnetic Properties of a Material

The flux density, $\vec{B}_m$, that passes through an object for a given magnetic intensity is related to a material property called permeability, μ,

$$\vec{B}_m = \mu\vec{H}_m \quad . \tag{4.2}$$

The relationship between $\vec{B}_m$ and $\vec{H}_m$ is only approximated as linear. In reality the flux density will begin to saturate at different levels based on the material. Often a material's permeability is compared to that of air or free space, μ_o, generally referred to as the relative permeability, $\mu_r = \mu/\mu_o$. Near saturation a much larger change in $\vec{H}_m$ is required before a change in $\vec{B}_m$ will be observed.
The magnetic flux through a surface is given by:

$$\Phi_m = \int_S \vec{B} \cdot d\vec{S} \quad , \tag{4.3}$$

where S refers to cross sectional area of interest.

4.1.3 Ampere's Law

The first of Maxwell's Laws is Ampere's Law, which provides a relationship between current density and magnetic intensity. At a point in static magnetic fields:

$$\nabla \times \vec{H}_m = \vec{J}_m \quad , \tag{4.4}$$

where J_m is the current density at the field point. At this point Stokes' Theorem can be applied to generate the integral form of Ampere's Law:

$$\oint \vec{H}_m \cdot d\vec{l} = \int_S \left(\nabla \times \vec{H}_m \right) \cdot d\vec{S} = \int_S \vec{J}_m \cdot \vec{S} \quad . \tag{4.5}$$

4.1.4 Faraday's Law

The electrical field intensity and the magnetic flux density are related by the following:

$$\nabla \times \vec{E} = -\frac{\partial \vec{B}_m}{\partial t} \quad , \tag{4.6}$$

which is known as Faraday's Law and after applying Stoke's Theorem provides:

$$\oint \vec{E} \cdot d\vec{l} = \int_S \left(-\frac{\partial \vec{B}_m}{\partial t} \right) \cdot d\vec{S} \quad . \tag{4.7}$$

The drop in voltage potential, V, along a closed loop is given by:

$$\oint \vec{E} \cdot d\vec{l} = V \quad , \tag{4.8}$$

where the electrical charges travel along conductors moving from higher to lower potentials. Now, combining Eqn. (4.7) and Eqn. (4.8):

$$V = \oint \vec{E} \cdot d\vec{l} = \int_S \left(-\frac{\partial \vec{B}_m}{\partial t} \right) \cdot d\vec{S} \quad . \tag{4.9}$$

If the cross-sectional area of the conductor, is constant and perpendicular to the the magnetic flux density, the above equation can be simplified to:

$$V = -\frac{dB_m}{dt}S = -\frac{d\Phi_m}{dt} \quad , \tag{4.10}$$

which relates the induced voltage to the time rate of change in the magnetic flux through a device.

4.1.5 Gauss' Law

Gauss' Law states that the divergence of the magnetic flux density must be zero, which can be written as:

$$\nabla \cdot \vec{B}_m = 0 \quad . \tag{4.11}$$

Utilizing the divergence theorem allows one to write:

$$\oint \vec{B}_m \cdot d\vec{S} = \int \left(\nabla \cdot \vec{B}_m\right) d\mathrm{v} = 0 \quad . \tag{4.12}$$

The result of Gauss' Law, similar to Kirchoff's Current Law, requires that the magnetic flux density be conserved in your device.

4.1.6 Magnetic Motive Force

The corollary of the electromotive force in electronics is the magnetic motive force (mmf), F. The mmf is the differential drop in magnetic potential over a path in space and can be found from Ampere's Law:

$$\oint \vec{H}_m \cdot d\vec{l_f} = i = F \quad . \tag{4.13}$$

The mmf can then be used to calculate the H_m which is related to the B_m by the permeability of the conducting material. This can be achieved by defining reluctance, R_m, as:

$$R_m = \left[\frac{l_f}{\mu S}\right] \quad , \tag{4.14}$$

where l and S are the length the flux density travels and cross sectional area of the magnetic conducting material. This allows one to write:

$$F = R_m \Phi_m \quad , \tag{4.15}$$

which is an analog of Ohm's Law for magnetic devices.

4.2 Generator Design

With a refresher of the basic EM theory, the design of the UC Berkeley permanent magnet linear generator will be described with additional EM and generator theory highlighted in the appropriate section. As described in [20, 21, 24], the generator was chosen to be three phase, as this would be the most likely choice for full-scale deployment. The initial model-scale design [21] consisted of 16 poles and 15 slots with a 1 ft generator span (GS). There were two distinct geometrical inadequacies from this design. The first arises from the armature length, also 1 ft, which left part of the stator unexposed to the permanent magnets during the floater's periodic motion. Thus, the phases, at either ends of the stator, will be inactive for greater periods as seen from the voltage time histories presented in [21]. In order to correct for this the armature was modified so its span would provide 7.125 in (0.181 m) of overlap with the stator.

4.2.1 Pole-Slot Configuration

Second, the armature geometry provided no spacing between adjacent magnets, refer to Fig. 3.8. This pole-slot configuration will lead to aggravated cogging forces. Cogging forces occur due to the interaction between the permanent magnets and the stator teeth with periodocity that is a function of the generator geometry [67, 68]. It is often called the 'no-current' force as it would be felt when moving the armature through the stator and disconnecting each phase from its corresponding load. The cogging force acts as a restoring force that pushes or pulls the magnets and coils to the nearest equilibrium position or lowest energy state. A large cogging force magnitude can lead to significant vibrations and 'jerkey' armature movement. This effect is most prevalent at lower speeds when the armature's inertia has difficulty dampening the cogging force magnitude. The number of cogging points expected, in one rotation of a rotary generator, is the lowest common multiple between the number of poles and slots. For a linear generator, this would correspond to one generator span worth of movement, or half a period, of the armature in either direction. Thus, the 16 pole - 15 slot configuration from [21, 24] is expected to have 240 cogging points, which was initially chosen as the cogging force magnitude decreases with the number of occurrences.

As stated in [24], the dominating power loss of the generator was originally thought to be a result of cogging forces. Therefore a revised armature geometry, based on [69], was constructed to eliminate or reduce cogging losses. The theoretical pole and slot spans for minimizing cogging losses are given by the following formula (see Fig. 4.1 for definitions):

$$\mathrm{PS} = \mathrm{GS}/\mathrm{np}, \tag{4.16}$$

$$\mathrm{SS} = \mathrm{GS}/\mathrm{ns}, \tag{4.17}$$

$$\mathrm{Sp} = \mathrm{n} * (\mathrm{PS} - \mathrm{SS}), \tag{4.18}$$

$$\mathrm{TS} = \mathrm{SS} - \mathrm{Sp}, \tag{4.19}$$

$$\mathrm{MS} = \mathrm{PS} - \mathrm{Sp}, \tag{4.20}$$

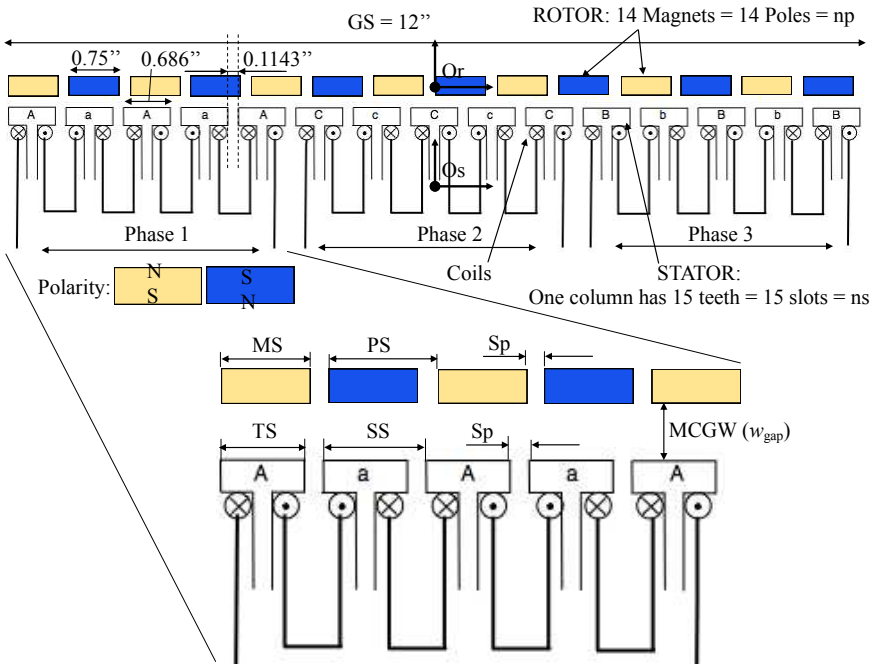

Figure 4.1: Schematic of the pole-slot configuration for one side of PMLG.

where, np is the number of poles, ns is the number of slots, and n is an integer number. The spacing between the existing stator teeth was closest to n=2. Furthermore, in order to maintain a magnet span of 1.9 cm, used in [21, 24], the generator was converted to a 14 pole - 15 slot configuration. The theoretical magnet span, slot span, and spacing can be found in Table 4.1 for a 15-slot and 14-pole configuration. There are no additional cogging effects when extending the armature span past the stator as long as the magnet and gap spacing from Table 4.1 are maintained.

4.2.2 Stator Construction

The first generation stator is attributed to [20, 21], but is briefly described for benefit of the reader. The first generation stator consists of two facing columns of 15 teeth that are

Table 4.1: Theoretical span and spacing (in) for minimal cogging force.

Slot Span (SS)	Pole Span (PS)	Spacing (Sp) (n=1)
0.800	0.857	0.057
Tooth Span (TS)	Magnet Span (MS)	Spacing (n=2)
0.686	0.743	0.1143

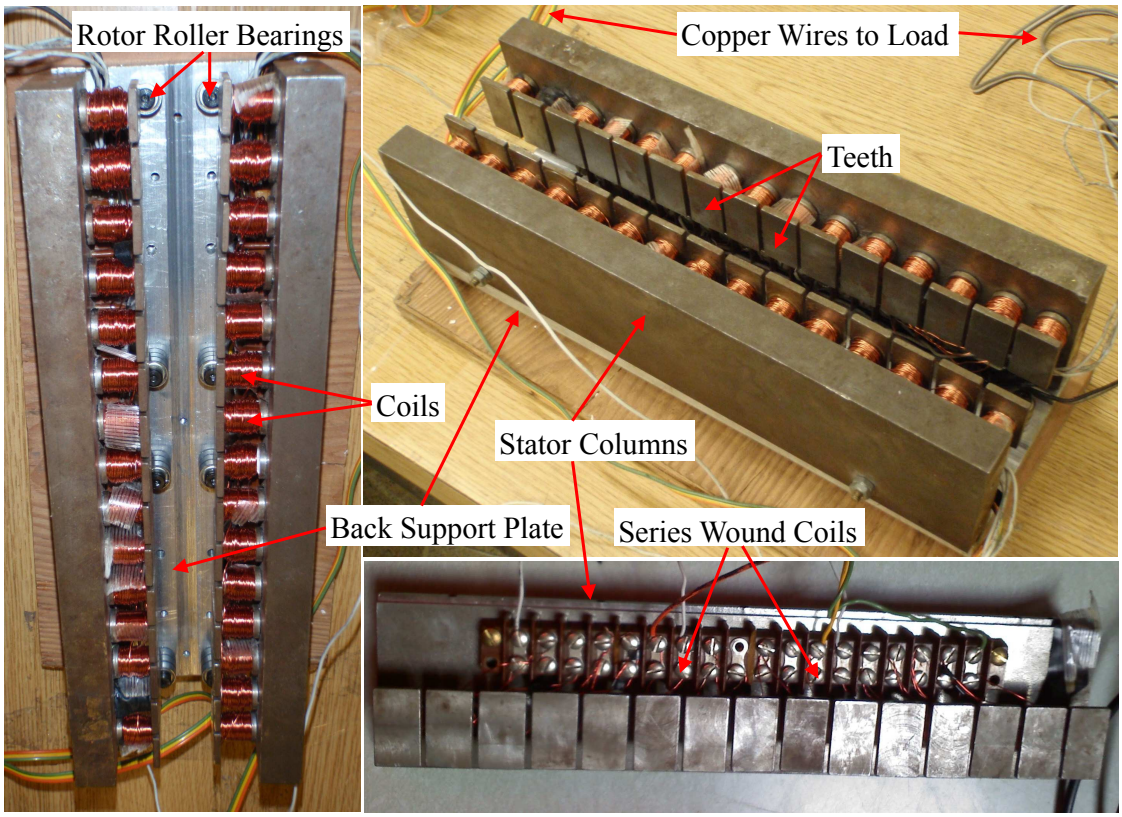

Figure 4.2: 1st generation stator constructed by [20, 21].

attached to a back support plate for ease of construction and modification, see Fig. 4.2. The stator columns are constructed separately from the teeth and were each made from a single piece of 1018 steel. The teeth were constructed from C1215 steel and were super glued to the stator columns. The base steel was chosen for its high permeability while the difference in steel grade was due to the ease of machining required when lathing each individual tooth. Each tooth is composed of two distinct portions: a thin frontal panel and a solid cylinder. The frontal panels measure 1.26 in x 0.69 in x 0.13 in where the solid cylinder has a radius of 0.375 in extending for 0.7 in. The cylindrical body of the tooth was chosen for ease of machining and the individual construction of each tooth allowed for faster coil winding. The frontal panel span (width) matches the spacing required to reduce the cogging force magnitude and prevents the coils from sliding off the tooth.

Each tooth was wound with 24 gauge copper magnet wire approximately 100 times around the cylindrical base. As noted in Fig. 4.1, each 5 adjacent teeth are wound in series with alternating winding directions. In this configuration, approximately 0.375 in of wire is perpendicular to the direction of the armature motion, which is the length component used when calculating the back electromagnetic force constant.

4.2.3 Armature Construction

The armature (rotor) houses the rare earth permanent magnets which hold a residual magnetism. The permanent magnets are used to generate a magnetic field in the absence of an applied current, Eqn. 4.1. A material that holds a residual magnetic field after $\vec{H}_m$ is removed is known as a hard magnetic material. In these materials a modified $B_m - H_m$ is used to account for $\vec{B}_r$, the residual flux density,

$$\vec{B}_m = \mu \vec{H}_m + B_r \quad . \tag{4.21}$$

The residual magnetism is due to the alignment of the magnetic domains resulting from the application of a sufficiently high $\vec{H}_m$. Once aligned the required magnetic intensity to flip the domains is know as the intrinsic coercivity, H_{ci}. It is highly desirable for permanent magnets to have a high H_{ci} to prevent demagnetization that may be caused by the current generated in the stator coils.

The permanent magnets were manufactured by K&J Magnetics Inc.[1] to grade N42 NdFeB, which is comprised of a mixture of Neodymium (Nd), Iron (Fe), and Boron (B), with a Nickel plated exterior which has a relative permeability of 1.05 [70]. The magnets measure 2 in (5.08 cm) x 0.75 in (1.905 cm) x 0.25 in (0.635 cm) with the magnetization through its thickness. The magnets are held in a slotted aluminium rectangular block with a square end face and side length of 1.5 in (3.81 cm) and extends for approximately 3 ft (0.914 m). The slot measures 0.25 in wide and 0.25 in deep extending the length of rectangular magnet support block. An aluminium top bar measuring 0.5 in by 0.5 in also measuring 3 ft long is used as a guide for the armature as it moves through the stator between the rollers. A slot was machined into the top guide bar, with the same dimensions as in the lower magnet support, in order to cap the top and bottom of the magnets leaving approximately 1.5 in of the magnet height exposed to air, see Fig. 4.3. The top guide and bottom magnet support are connected by aluminium end stops that include top and bottom threads allowing tightening screws. Adjacent magnets are separated by Delrin plastic non-magnetic spacers and placed with alternating polarity, see Fig. 4.1.

4.2.4 Stator and Armature Attachment to Support Structure

As briefly described in Fig. 3.7 and shown again in Fig. 4.4, the armature is supported by the slider rods protruding from the linear bearing slider that sits between the heave rods. The slider rod height can be manually adjusted ensuring the magnets and teeth are properly aligned. The magnet support block of the armature is then tightened to the slider rods by 4 set screws. As described earlier, the linear bearing slider will also attach to the floater and whose motion will be excited by the wave exciting force.

The current stator support structure, constructed in [21], is comprised of a two tier truss system. The truss system consists predominantly of 1 in x 1 in square aluminium tubing

[1] http://www.kjmagnetics.com/

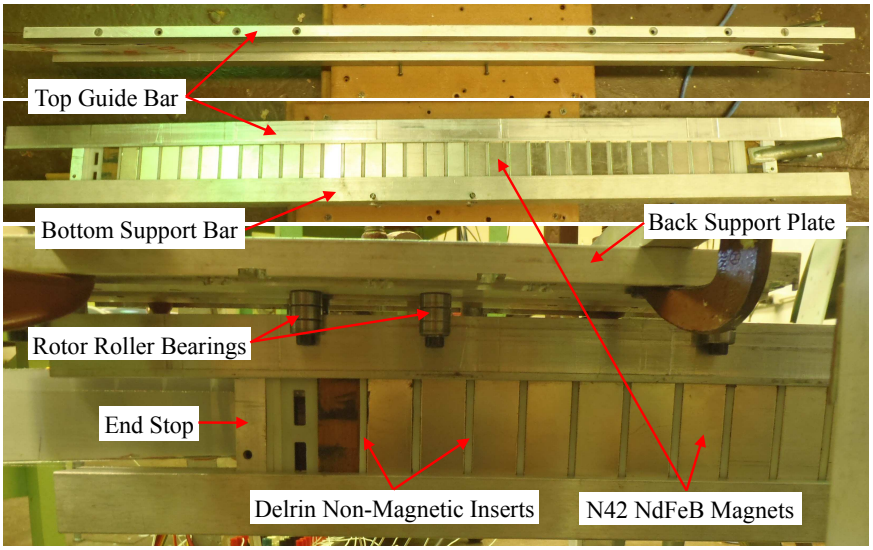

Figure 4.3: Modified armature. Top photo contains a top-down view of armature, middle photo contains a side view of armature, and the bottom photo is a zoomed side view of armature when attached to support structure.

for rigidity. The stator is aligned along the direction of slider motion and is attached to the horizontal square tubes through the use of C-clamps that are parallel to the plane of the heave rods. The stator support structure is connected to the heave rod steel frame and the unit as a whole remains stationary during experimentation.

4.3 Generator Modeling

An estimation of the air-gap flux density can be provided by [71], after modification due to variations in generator geometry, providing the following expression:

$$B_{gap} = B_r \frac{l_m/\mu_r}{l_m/\mu_r + g_{eff}} \frac{4}{\pi} \sin\left(\frac{\text{MS}}{\text{PS}} \frac{\pi}{2}\right) \tag{4.22}$$

where l_m is the magnet length in the direction of magnetization, $g_{eff} = 2w_{gap}$ the effective air-gap length, and w_{gap} is the perpendicular distance between the magnet and stator faces, Fig. 4.1. The air-gap flux density from Eqn. (4.22) is estimated to be approximately 0.42 Tesla, which is not considered very large. However, Eqn. (4.22) does not take into account variations that arise from the armature's position relative to the stator or geometries sufficiently different than considered in [71]. Therefore the use of finite element methods (FEM) is commonly used for calculating the electro-magnetic properties specific to a given geometry, see [8, 67, 72], though not explored in this work. Alternatively, a Gauss meter can be used during prototype testing to check analytical calculations.

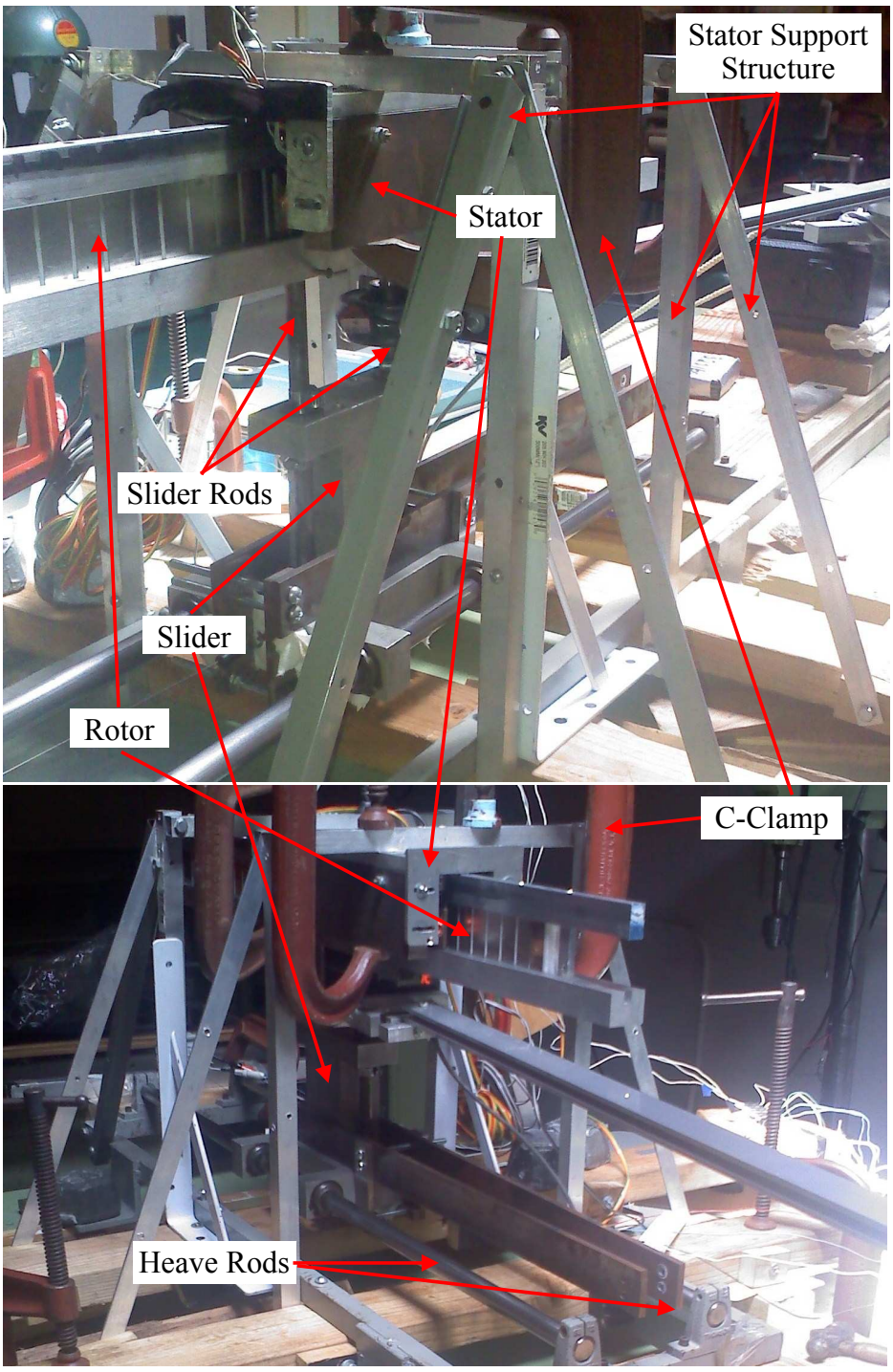

Figure 4.4: 1st generation stator attached to support structure.

An alternative method for estimating the magnetic flux density in the magnet-coil gap of the generator can be completed using lumped magnetic circuit analysis [73]. In this process the magnets are represented as a flux source, similar to a current source in electric circuits, in series and parallel with various magnetic permeances, which are the inverse to reluctance. It is of interest in determining the flux, Φ_m, that exits the magnet into the rest of the magnetic circuit as this will help estimate the magnetic flux density in the air gap. In order to simplify the analysis the superposition principle will be used by ignoring one current source, as seen in Fig. 4.5, and then doubling the result.

The magnetic flux travels out from the permanent magnet, across the magnet-coil gap, through the electric steel, back through the magnet-coil gap into the second magnet, and repeating on the opposite stator side. An extra permeance is included to model the magnetic leakage that occurs due to the generator geometry. The idealized flux lines pass from the permanent magnetic to the stator; however, the flux lines may curve back onto adjacent magnets or take a radial path thereby increasing the distance the flux must travel. The presence of leakage decreases the flux density in the magnet coil gap and the efficiency of generator. Magnetic leakage becomes more prevalent as the ratio of the magnet and the magnet-coil gap length decreases, where anything below a ratio of one is considered large. Completing the magnetic circuit analysis in Fig. 4.5 provides the following estimate on B_{gap}:

$$P_r = \frac{P_g P_s}{2P_s + P_g} \quad , \tag{4.23}$$

$$P_t = \frac{(P_{ml} + P_r) P_m}{2P_m + P_{ml} + P_r} \quad , \tag{4.24}$$

$$\Phi_m = \Phi_o \frac{P_t}{P_t + P_m} = B_r A_m \frac{P_t}{P_t + P_m} \quad , \tag{4.25}$$

$$B_{gap} = \frac{\Phi_o}{A_g} \frac{P_t}{P_t + P_m} = B_r \frac{A_m}{A_g} \frac{P_t}{P_t + P_m} \quad , \tag{4.26}$$

where A_m is the area of the magnet perpendicular to the direction of magnetization and A_g is the area of the magnet coil gap perpendicular to the flux density. When neglecting magnetic leakage the expected B_{gap} is approximately 0.4 Tesla which is close to the value provided by Eqn. (4.22). If a magnetic leakage term, on the same order as the magnet coil gap permeance, is included the air-gap flux density will drop to 0.25 Tesla.

4.3.1 Electromagnetic Forces

The Lorentz Force allows one to calculate the repulsive force felt by an electric charge, Q, moving in a magnetic field and is given by:

$$\vec{F_l} = Q\vec{U} \times \vec{B}_m \quad . \tag{4.27}$$

Thus, the differential force felt by a wire conductor can be calculated from:

$$d\vec{F_l} = dQ \left(\vec{U} \times \vec{B}_m \right) = (idt) \left(\vec{U} \times \vec{B}_m \right) = i \left(d\vec{l} \times \vec{B}_m \right) \quad . \tag{4.28}$$

If the exposed portion of the wire is straight and perpendicular to the magnetic field, the integration of Eqn. (4.28) provides:

$$F_l = B_m l i \tag{4.29}$$

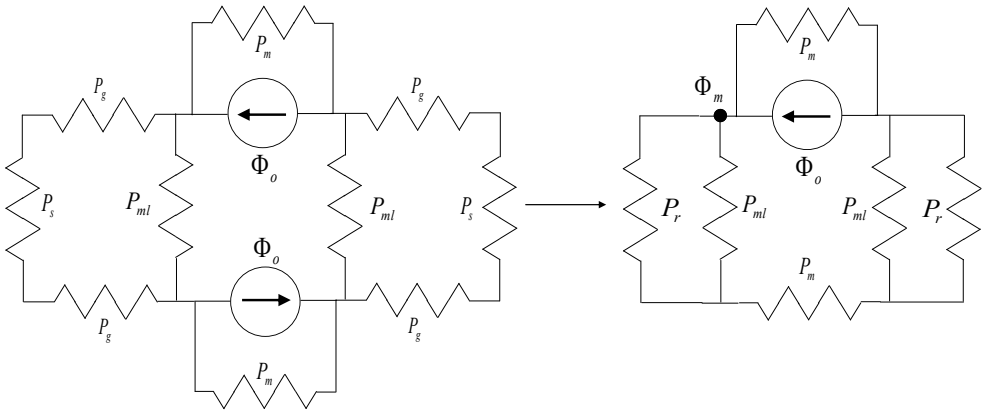

Figure 4.5: Lumped magnetic circuit consisting of four stator slots and two armature poles. The inclusion of four stator slots is due to the symmetry of the generator as it consists of two stator sides. P_m, P_g, P_{ml}, and P_s are the magnet, magnet coil gap, magnetic leakage, and stator steel permeanances.

Furthermore, following [65, 74, 75], an estimate on the normal and shear stresses associated with electromagnetic forces are given by:

$$\sigma_S = B_m \hat{K} \quad , \tag{4.30}$$

$$\hat{K} = i/w_p \quad , \tag{4.31}$$

$$\sigma_M = \frac{B_m^2}{2\mu_0} \quad , \tag{4.32}$$

where $\hat{K}(A/m)$ is the electric loading, i is current in the conductor, and w_p is the pitch of the wire winding $(turns/m)$. Furthermore, under most engineering applications it can be shown [65] that the $B_{gap} \propto 1/w_{gap}$ which makes $\sigma_M \propto 1/w_{gap}^2$. Thus as w_{gap} is decreased the normal force between armature and stator increases non-linearly. The normal force is of interest in terms of structural support and power loss. The normal stress can be on the order of 100 kN/m^2 [74] making it imperative that a bearing system be strong enough to prevent the magnets and stator from touching. Failure to withstand the attractive pull can lead to impact forces that can break the magnets or cut coil windings. In [21] and this work poor monitoring of the magnet configurations lead to such instances. In addition, the increase in the normal force will result in larger power losses due to friction between the armature and bearings.

4.3.2 Coil Voltage

In permanent magnet brushless motors the armature speed is controlled by the current generated in the stator coils as shown from Eqn. (4.33). The desired current is normally

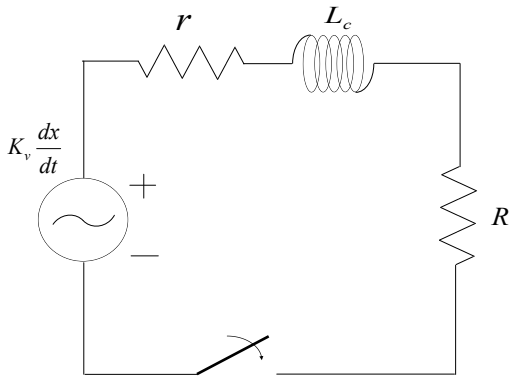

Figure 4.6: Approximated electrical circuit diagram for one phase.

achieved by applying a voltage to the coil ends and is given by:

$$V_{ap} = ir + L_c\frac{di}{dt} + K_v\frac{dx}{dt} \quad , \tag{4.33}$$

$$K_v = \frac{d\lambda_f}{dx} = N\frac{d\Phi}{dx} \quad , \tag{4.34}$$

where r, L_c, λ_f, and K_v are the coil resistance, coil inductance, flux linkage, and speedance or back EMF constant. For N wires moving in a uniform magnetic field, Eqn. (4.34) can be simplified to $K_v = NlB_m$. A generator exploits the back EMF created from the armature's motion to induce a voltage drop across the coil. This leads to a slightly modified equation which also includes the load resistance, R:

$$0 = i\,(r + R) + L_c\frac{di}{dt} - NBl\dot{\zeta}_3(t) \quad . \tag{4.35}$$

Now, let's consider the PMLG where the stator is stationary and the magnetic flux is changing with armature position. The flux passing through a single tooth can be described by:

$$\Phi_{coil}\,(t) = B_{gap}A_s \sin\left(\frac{2\pi}{\lambda_m}\zeta_3\,(t)\right) \quad , \tag{4.36}$$

where A_s is the cross sectional area of the tooth and λ_m is the magnetic wavelength. The magnetic wavelength is twice the pole span (pitch) as the polarity of the magnets repeat after passing two poles. Taking the time derivative of Eqn. (4.36):

$$\dot{\Phi}_{coil}\,(t) = B_{gap}A_s\frac{2\pi}{\lambda_m}\cos\left(\frac{2\pi}{\lambda_m}\zeta_3\,(t)\right)\dot{\zeta}_3\,(t) \quad . \tag{4.37}$$

By matching terms in Eqn. (4.37) and the speedance contribution in Eqn. (4.33), allows one to write:

$$K_v = NB_{gap}A_s\frac{2\pi}{\lambda_m}\cos\left(\frac{2\pi}{\lambda_m}\zeta_3\,(t)\right) = \hat{K}_v\cos\left(\frac{2\pi}{\lambda_m}\zeta_3\,(t)\right) \quad . \tag{4.38}$$

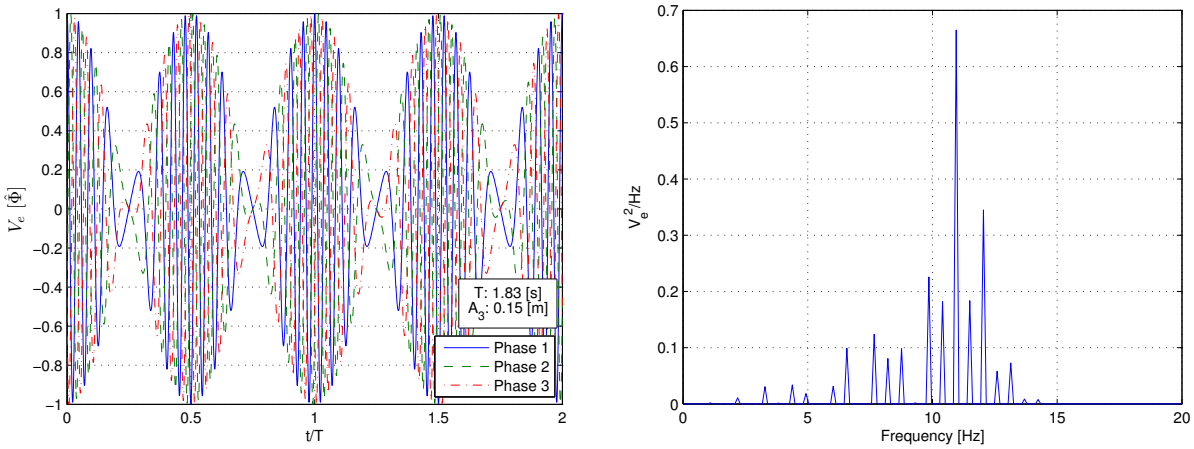

(a) Normalized induced voltage from armature motion, with each phase time-shifted by $2\pi/3$.

(b) Power spectral density of normalized induced voltage where only one phase is shown due to the constant phase shift.

Figure 4.7: Theoretical induced voltage performance of generator.

If the motion of the armature is assumed to be sinusoidal then Eqn. (4.37) can be simplified as follows:

$$\zeta_3(t) = \mathcal{A}_3 \sin(\sigma t) \quad , \tag{4.39}$$

$$\begin{aligned} \dot{\Phi}_{coil}(t) &= \frac{2\pi N B_{gap} A_m \mathcal{A}_3 \sigma}{\lambda_m} \cos(\sigma t) \cos\left(\frac{2\pi \mathcal{A}_3}{\lambda_m} \sin(\sigma t)\right) \quad , \\ &= \hat{\Phi} \cos(\sigma t) \cos\left(\frac{2\pi \mathcal{A}_3}{\lambda_m} \sin(\sigma t)\right) \quad , \end{aligned} \tag{4.40}$$

$$V_e = -\dot{\Phi}_{coil}(t) = -\hat{\Phi} \cos(\sigma t) \cos\left(\frac{2\pi \mathcal{A}_3}{\lambda_m} \sin(\sigma t)\right) \quad , \tag{4.41}$$

where Eqn. (4.41) is a result from Faraday's Law.

4.4 Three Phase Approximation

It is desired to construct a three phase generator which requires modifying Eqn. (4.35) to take into account the effect of one coil on its neighbours. Before proceeding a simplification will be made such that the 5 teeth wound in series will be represented as a single coil, thus one phase. The voltage drop across each phase is given by:

$$V_j = i_j r_j + \frac{d}{dt}\lambda_j \quad , \tag{4.42}$$

$$\lambda_j = \sum_{k=1}^{3} L_{c|jk} i_k + \lambda_{f|j} \quad . \tag{4.43}$$

where r_j, $\lambda_{f|j}$, and $L_{c|jk}$ are the phase resistance, flux linkage, and inductance ($j = k$ and $j \neq k$ denote self and mutual inductance). If Eqn. (4.42) is written out for phase 1:

$$V_1 = i_1 r_1 + L_{c|11}\frac{d}{dt}i_1 + L_{c|12}\frac{d}{dt}i_2 + L_{c|13}\frac{d}{dt}i_3 + \frac{d\lambda_{f|1}}{dt} \quad , \tag{4.44}$$

$$= i_1 r_1 + L_{c|11}\frac{d}{dt}i_1 + L_{c|12}\frac{d}{dt}i_2 + L_{c|13}\frac{d}{dt}i_3 + V_e \quad . \tag{4.45}$$

As seen from Eqn. (4.44) the voltage drop is not independent of the other phases. The mutual inductance takes into account of the induced voltage resulting from the magnetic fields generated by adjacent phases. If the coils of the generator are exact copies, then the centerline symmetry provides mutual inductances that are equivalent, such as $L_{12} = L_{32}$. The calculation of both self and mutual inductances is no trivial matter and generally requiring the use of FEM methods [8, 68]. Due to the relatively low speeds of the armature the self and mutual inductances will be assumed negligible and therefore:

$$V_1 \approx i_1 r_1 + V_e \quad . \tag{4.46}$$

4.5 Generator Dry Bench Test

The reaction force from the PMLG will be assumed to be in the following form:

$$F_g(t) = -\mu_g \ddot{\zeta}_3(t) - B_g \dot{\zeta}_3(t) - K_g \zeta_3(t) \quad , \tag{4.47}$$

where K_g, B_g, μ_g are the spring, damping, and inertia coefficients of the PTO. A bench test of the generator was completed to establish the values of the coefficients from Eqn. (4.47) at different frequencies, resistive loads, and magnet-coil gap widths. The bench test consists of horizontally driving the armature of the generator with a combination of a variable-speed motor and gearbox with the amplitude of motion set at $|A_3| = 15.24$ cm, which is half of the length of the stator. The results in this work will be made from data recorded while running a modified bench test initially described in [21], see Fig. 4.8.

4.5.1 Bench Test Experimental Apparatus

The mechanism driving the armature through the stator is a combination of a variable speed motor[2] and gearbox[3], Fig. 4.9. The motor output shaft is connected to the gearbox input shaft through a timing belt system. The timing belt pulleys have a pitch-diameter ratio of 1.5 increasing the rotational speed from motor to gearbox. The gear box is a 1:40 speed reducer which leads the output shaft to rotate at roughly 1/26 the speed of the motor. Therefore, a armature oscillation period of 1.7 s corresponds to a motor RPM of 940.

[2]Max RPM 1740, Max Torque 12.75 lb-in

[3]Iron Horse Speed Reducer (Gear Box) WG-175-040-R

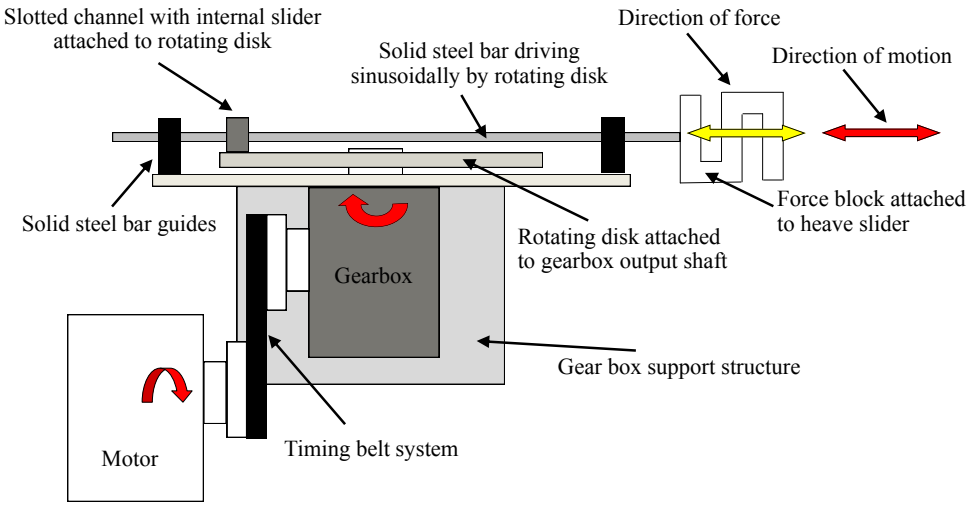

Figure 4.8: Schematic of dry-bench test.

The gear box is elevated on a structural platform constructed from square hollow steel tubes and plexiglass, Fig. 4.9 and 4.10 . The platform raises the output shaft of the gearbox approximately 7 inches above the floor. This allows a plastic disk, attached to the output shaft of the gear box, to rotate freely while accommodating the desired amplitude of motion. A cylindrical slider is fixed on the plastic disk, but is free to rotate. The upper diameter of the cylindrical slider matches, as close as possible without binding, the internal width of the slotted channel. This decouples the horizontal and vertical forces the cylindrical slider applies to the slotted channel while allowing for oscillating movement. The motion of the slotted channel is passed to the heave rod slider through a steel bar. A strain-gauge transducer acts as an intermediate link between the solid steel bar and heave slider, which can measure the horizontal force required to drive the armature. As described in Sec. 3.3.1, a string potentiometer is used to measure the position of the armature during the experiment, which is used to calculate the corresponding velocity and acceleration.

4.5.2 Bench Test Instrumentation

The RFS facility provides the following instrumentation for use by investigators with some identified in Fig. 4.11:

- Celesco SP1 String Potentiometer
- Custom strain gauge transducer and Interface signal conditioners[4]
- Measurement Computing USB-1208FS data acquisition units[5]

[4] http://www.interfaceforce.com/dma-din-rail-mount-signal-conditioner-p-96.html
[5] http://www.mccdaq.com/usb-data-acquisition/USB-1208FS.aspx

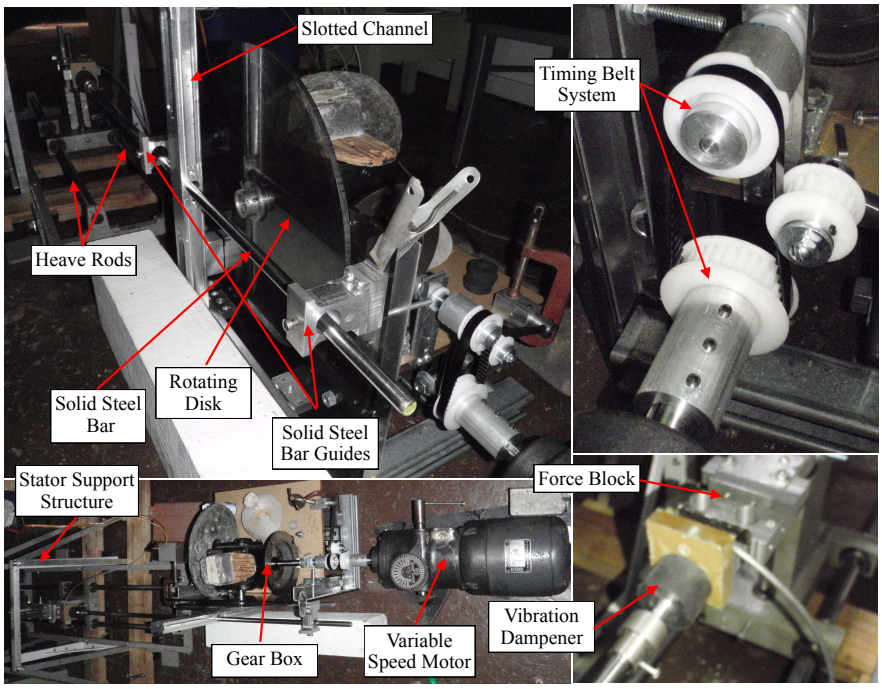

Figure 4.9: Bench Test photos with component identification.

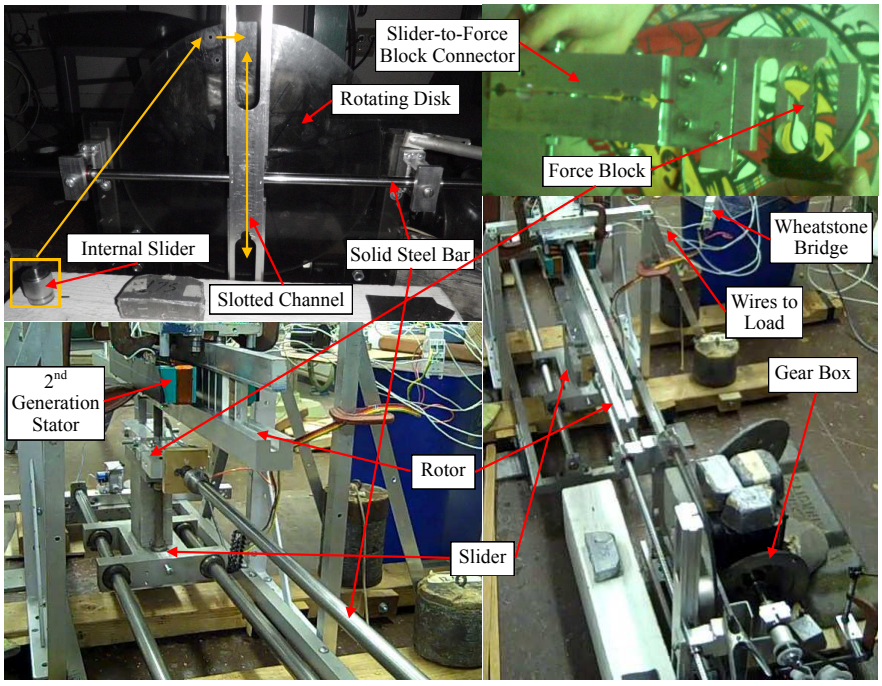

Figure 4.10: Bench Test photos with generator attached. Orange lines denote connection of internal slider and its movement inside of the slotted channel.

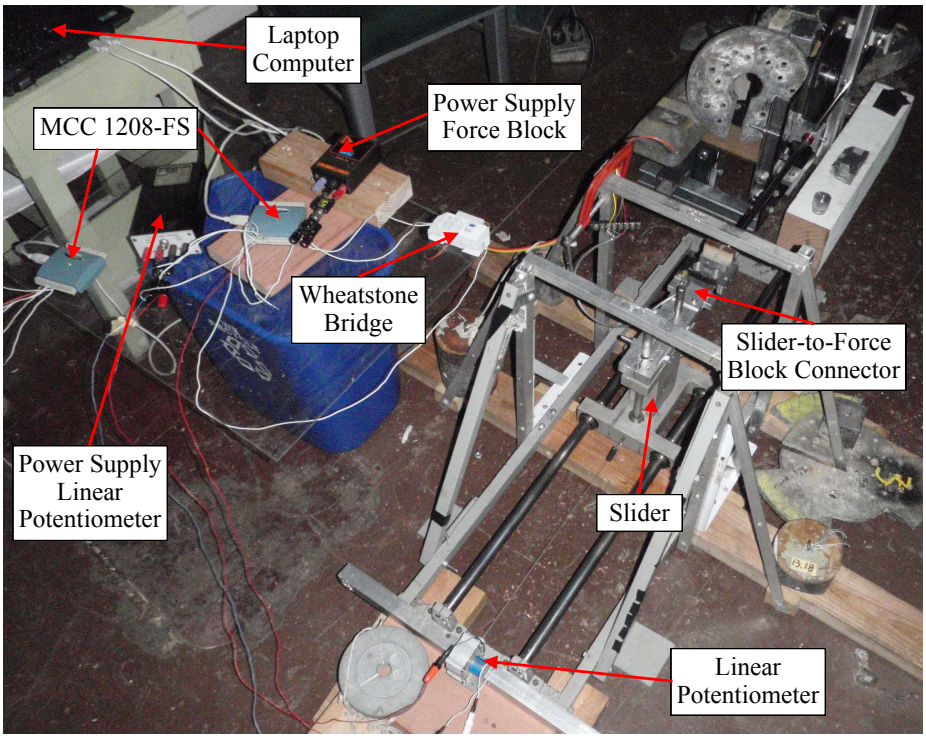

Figure 4.11: Bench Test photos with instrumentation identification.

- Power Potentiometers
- Low Current Power Supplies

The experiment monitors 8 electrical signals requiring the use of 2 USB-1208FS, given each can handle 4 separate analog inputs in differential mode. 3 channels on each USB-1208FS measure the voltage drop across the electrical loads of each phase, Fig. 4.12. The remaining channel on each measurement device records either the voltage time history of position or driving force.

4.5.3 Electro-Magnetic Signal Analysis

In order to measure generator performance under varying resistive load, R, a power potentiometer is placed across each phase on either stator side. This results in 6 measured voltage time histories as the output signal is not rectified. This work does not address the signal conditioning required for connection to the grid. The three phase loads were kept balanced though some drift in resistive load was observed. A sample time history of the voltage drop across each load can be seen in Fig. 4.13, which corresponds to the same frequency of motion as modeled in Fig. 4.7a. As expected the voltage signals per stator side are 120 degrees out of phase and with a varying oscillation frequency and magnitude. The induced voltage magnitude and frequency are proportional to the armature velocity; however, the voltage

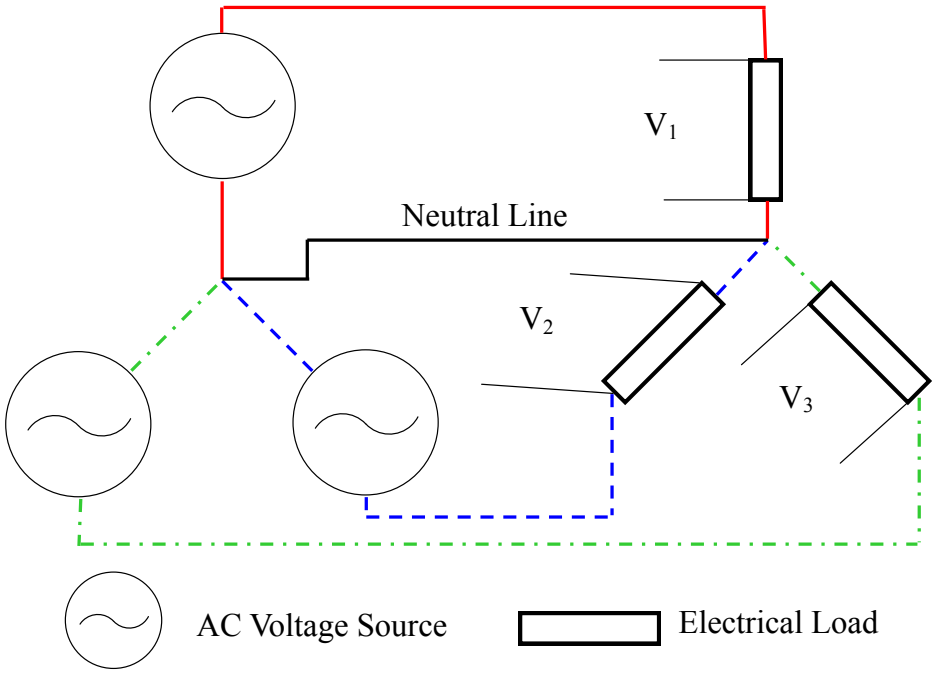

Figure 4.12: Diagram of 3 phase wye wiring of a single stator side where V_i, $i = 1, 2, 3$ denotes the location of the measured voltage drop.

frequency is greater than of the armature motion.

A power spectral density analysis of the voltage time series can identify the dominant frequencies in the signal and can be found in Fig. 4.13. The spectral density magnitude lies between 8 - 12 Hz with the dominant frequency at 10.9 Hz, which is approximately 20 times the armature oscillation matching very well against Fig. 4.7b.

The power consumed by the potentiometers is calculated by Ohm's law:

$$V(t) = i(t)R \quad , \tag{4.48}$$

$$P_{load}(t) = i(t)V(t) = \frac{V(t)^2}{R} \quad . \tag{4.49}$$

The potentiometers are not the only resistive source that consumes power. The stator coil resistance, r, will also dissipate energy and is calculated from the following:

$$i(t) = \frac{V(t)}{R} \quad , \tag{4.50}$$

$$P_{coil}(t) = i(t)^2 r = \left(\frac{V(t)}{R}\right)^2 r = P_{load}(t)\frac{r}{R} \quad , \tag{4.51}$$

which assumes the same current flows in both coil and load. The time-averaged power, over one period of oscillation, is calculated by:

$$\overline{P}_{load} = \frac{1}{T}\int_t^{t+T} \frac{V(t')^2}{R} dt' = \frac{1}{T}\int_t^{t+T} P_{load}(t')dt' \quad , \tag{4.52}$$

$$P_{el} = \sum_{n=1}^{6} \overline{P}_{load:n} \quad . \tag{4.53}$$

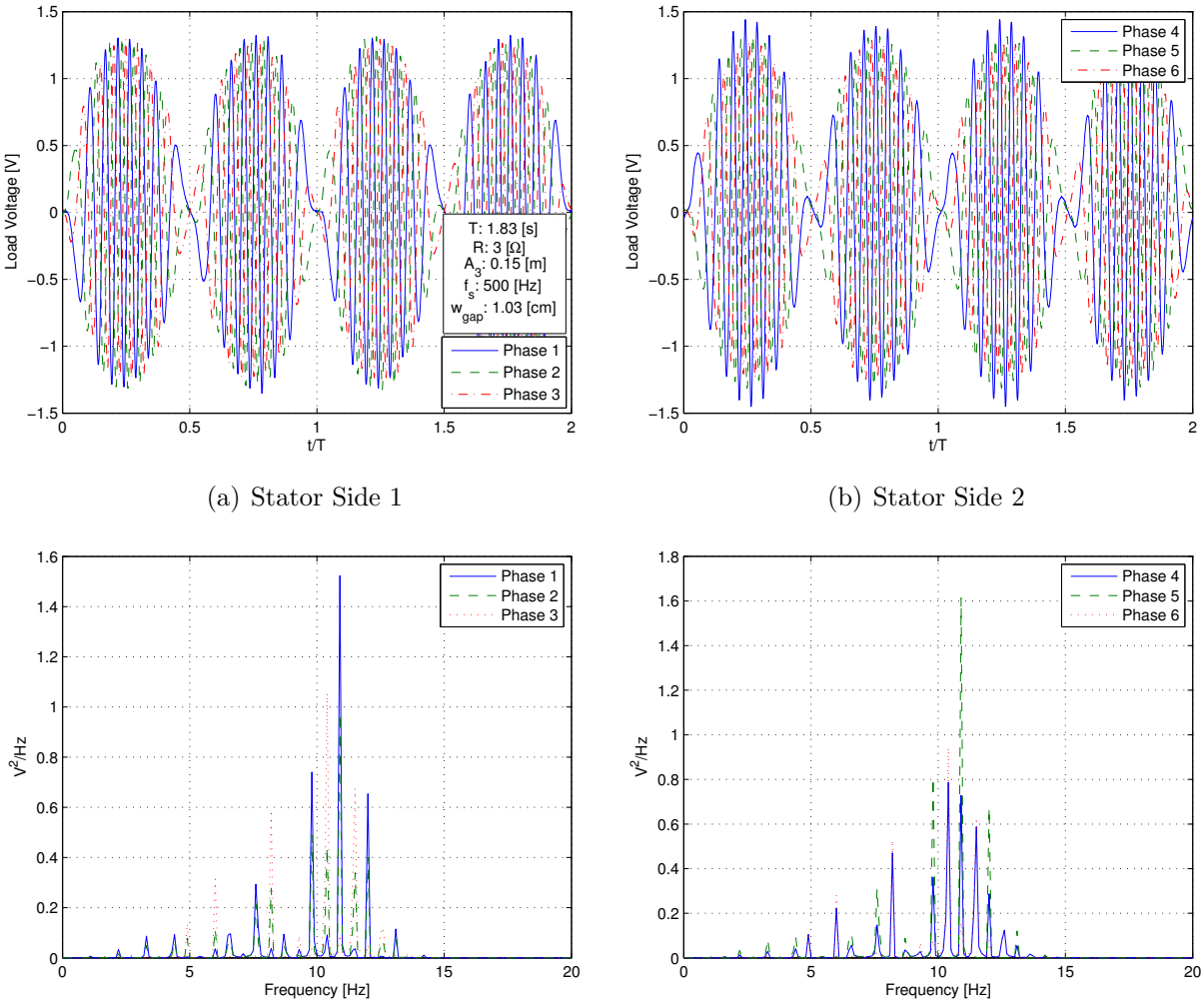

(a) Stator Side 1

(b) Stator Side 2

(c) Stator Side 1

(d) Stator Side 2

Figure 4.13: Time history and power spectral density of voltage drop across each resistive load, R.

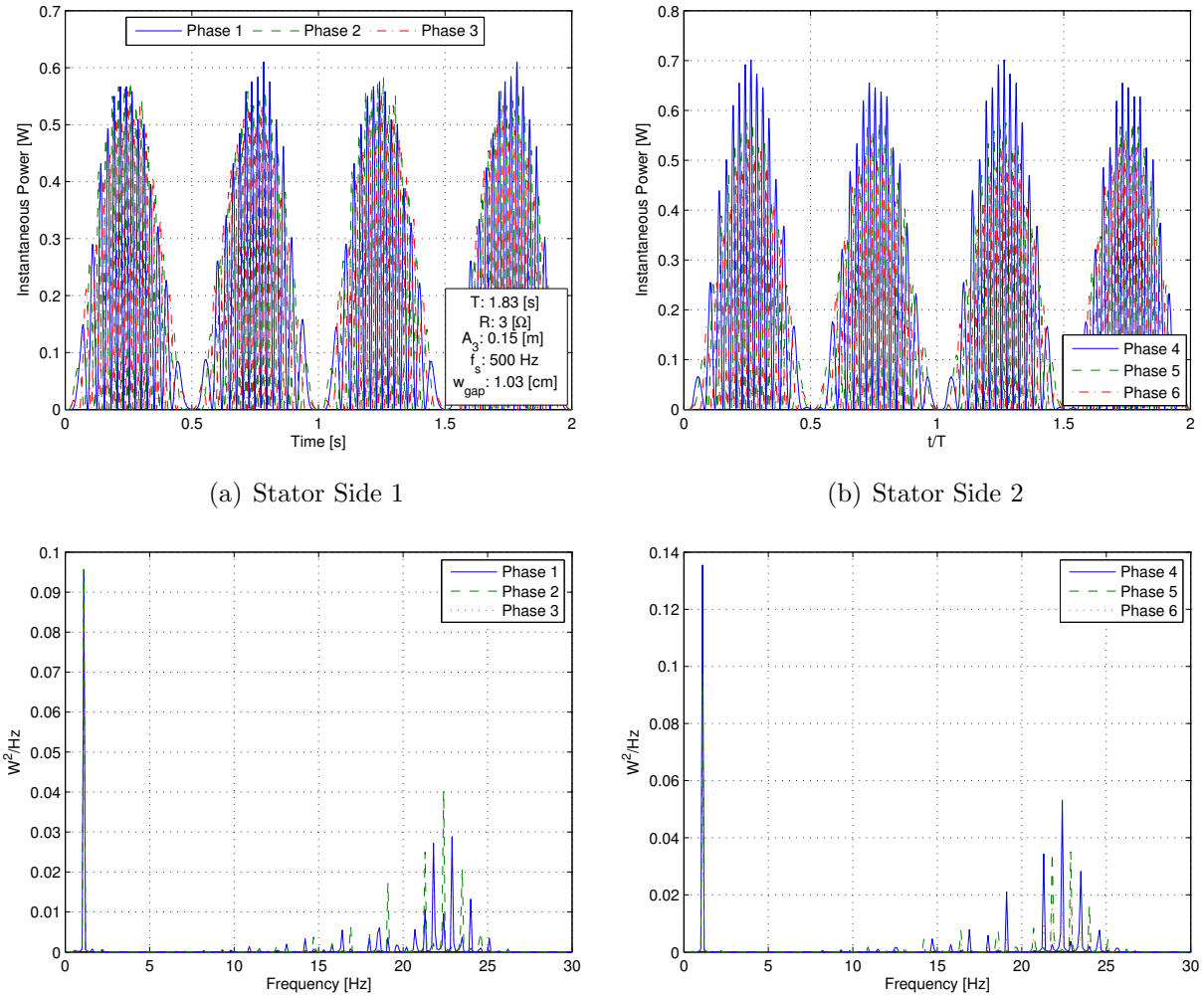

(a) Stator Side 1

(b) Stator Side 2

(c) Stator Side 1

(d) Stator Side 2

Figure 4.14: Time history and power spectral density of P_{load} for each phase.

The time histories of P_{load} for each individual phase can be seen in Fig. 4.14 where the summation of power for each stator side is found in Fig. 4.15. The power from each phase has a form similar to that of the absolute value of the floater velocity with higher internal oscillations. A spectral analysis of the instantaneous power is shown in Fig. 4.14, though the DC component of the signal is not plotted. The plot contains a low frequency component, double the frequency of motion, and high frequency section that is approximately double the rate of the induced voltage. The summation of power for each stator side smooths the signal becoming proportional to the armature's velocity. In Fig. 4.15 there appears to be a slight phase lag between velocity and stator power. This may indicate that the inductance is non-negligible or the flux linkage with the solid steel back plate may be significant.

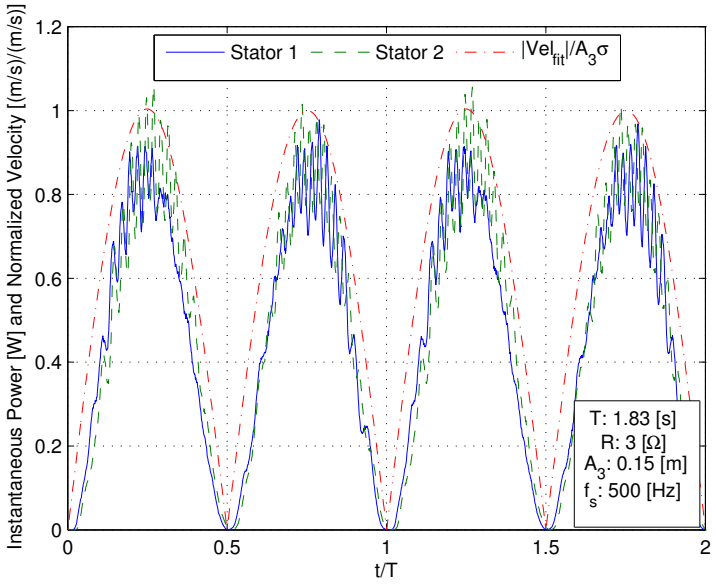

Figure 4.15: Time history of the summation of P_{load} per stator side with the armature velocity normalized by $\mathcal{A}_3\sigma$.

4.5.4 Position Signal Analysis

The armature position is obtained from the Celesco string potentiometer, which is an invasive measurement as it applies a constant tension force to the armature; however, this was found to be negligible. A sample time history of the armature position can be found in Fig. 4.16. Given the noise level of the raw signal, it will be difficult to obtain a numerically derived velocity or acceleration that is smooth, for example, using the 5 point stencil:

$$\dot{\zeta}_3(t) = \frac{1}{12\Delta t}\left[\zeta_3(t-2\Delta t) - 8\zeta_3(t-\Delta t) + 8\zeta_3(t+\Delta t) - \zeta_3(t+2\Delta t)\right] \quad , \tag{4.54}$$

$$\ddot{\zeta}_3(t) = \frac{1}{12\Delta t^2}\left[-\zeta_3(t-2\Delta t) + 16\zeta_3(t-\Delta t) - 30\zeta_3(t) + 8\zeta_3(t+\Delta t) - \zeta_3(t+2\Delta t)\right] \quad . \tag{4.55}$$

In order to resolve this issue three methods were used to clean up the position signal and are shown in Fig. 4.16.

1. A second order Fourier series representation was best fit to the data,

$$\zeta_3(t) = a_1\cos(\sigma t) + b_1\sin(\sigma t) + a_2\cos(2\sigma t) + b_2\sin(2\sigma t) \quad . \tag{4.56}$$

   This fit allows for time derivatives to be taken for $\dot{\zeta}_3$ and $\ddot{\zeta}_3$; however, for non-sinusoidal motions a higher order will be necessary to properly reconstruct the signal.

2. A Savitzky-Golay filter (SGF) is applied to smooth the raw signal using the Matlab function, **smooth**, with a span of 2000 and order 30. This method still requires numerical derivatives for $\dot{\zeta}_3$ and $\ddot{\zeta}_3$, but can handle non-sinusoidal motion.

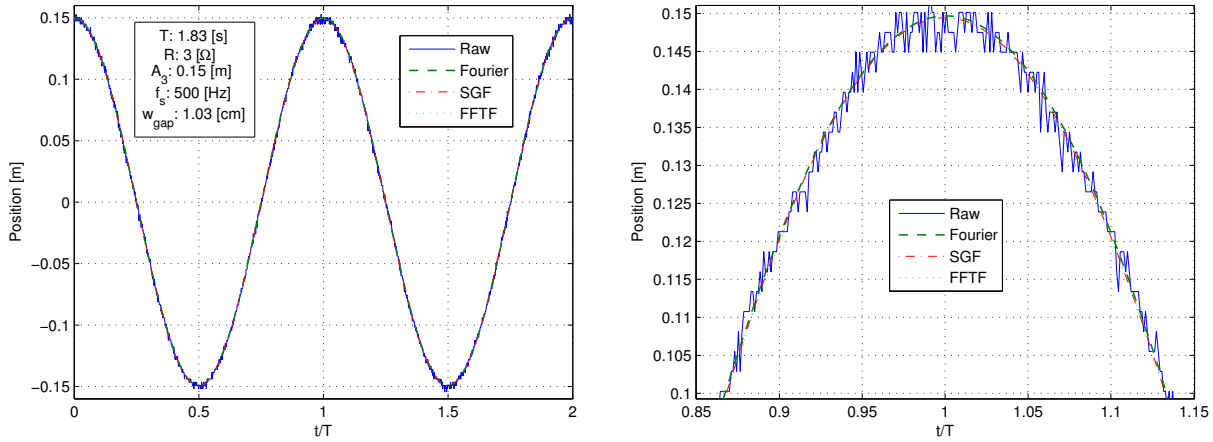

(a) Two periods of oscillation.

(b) Zoomed view of max amplitude of position.

Figure 4.16: Time history of armature position.

3. A power spectral density (PSD) is applied to the position signal and the dominant frequencies are noted. The results from Fast Fourier Transform provide the Fourier modes and frequencies where the modes of interest are kept while the remaining are zeroed. The corrected Fourier modes are then passed through an Inverse Fast Fourier Transform reconstructing the filtered signal. This is a very simplistic approach to FFT filtering (FFTF) with much more advanced methods found in digital signal processing. As with the SGF, numerical differentiation is required to obtain $\dot{\zeta}_3$ and $\ddot{\zeta}_3$.

It should be noted that decreasing the sample rate will reduce some of the localized noise and will be better for control applications. After obtaining a smoothed position signal three methods were compared for calculating $\dot{\zeta}_3$ and $\ddot{\zeta}_3$. All methods match well with the greatest discrepancies appearing in the $\ddot{\zeta}_3$ calculation. The armature velocity will be used to calculate the input power required to the drive the generator at a given speed.

1. The first and second order time derivatives of Eqn. (4.56) were taken.

2. A spline was fit to the SGF position signal and the third order polynomials were differentiated for $\dot{\zeta}_3$. The same procedure was completed to calculate $\ddot{\zeta}_3$ from $\dot{\zeta}_3$.

3. The 5 point stencil from Eqn. (4.54) & (4.55) were applied to the SGF and FFTF signals.

4.5.5 Force Signal Analysis

A sample time history of the force measurements recorded during the bench test can be found in Fig. 4.17. From the sample time history it can be observed that the force signature contains several harmonics. A Fourier analysis was performed to identify the dominant frequencies and if some contributions were due to external sources. The power spectral density

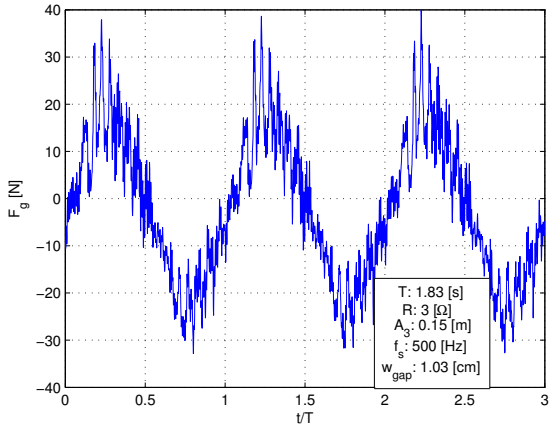

(a) Time history of F_g as measured from force block.

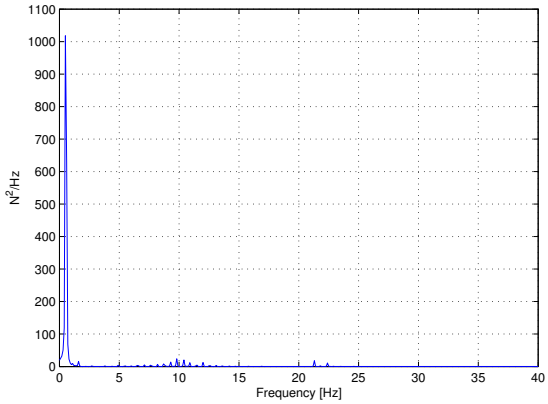

(b) Spectral density with largest magnitude captured.

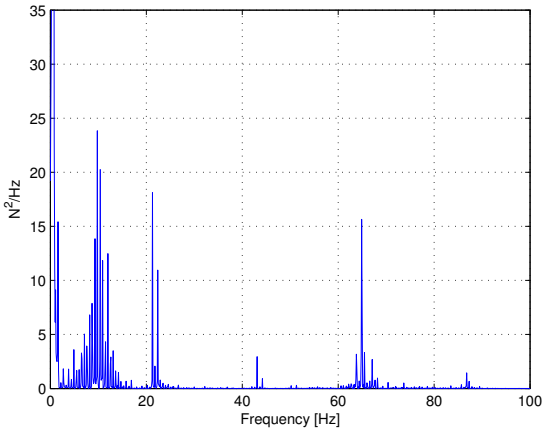

(c) Zoomed view of lower magnitude modes.

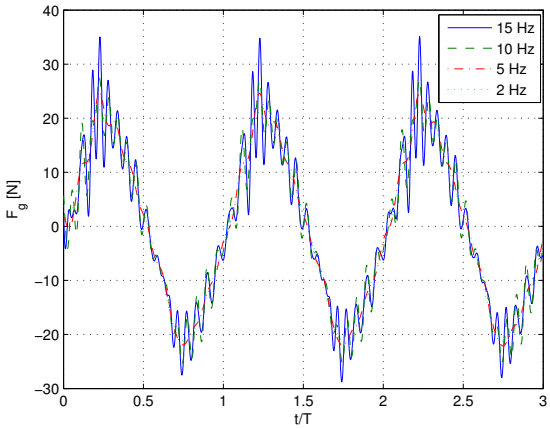

(d) FFTF of time history of F_g measured from force block.

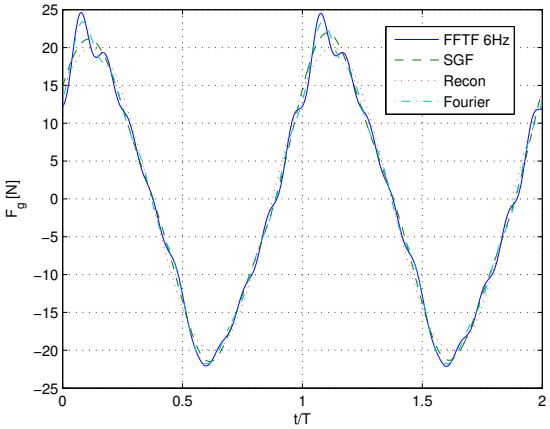

(e) Low frequency representations of F_g .

Figure 4.17: Time history and spectral power density of F_g.

of the force time history is provided in Fig. 4.17. The dominant mode is found at 0.5464 Hz corresponding to the period of oscillation; however, after zooming to the magnitude of the next significant mode higher harmonics can be seen. One frequency range that can be accredited as an exterior excitation is at approximately 22 Hz. This corresponds to the rotation speed of the input shaft to the gearbox. The timing belt system was constructed to minimize misalignment in the system, which can lead to unwanted vibrations; however, it appears that vibrations at this rotational speed were not adequately damped. The higher Fourier modes appear at integer multiples of the input shaft speed, which may be a result of vibrations of the supporting structure.

The remaining lower frequency modes center around 10 Hz, though at the moment it is unclear what is the cause of this excitation. Two postulations are provided for the moment: 1) The vibrational dampener used was subjected to forces exceeding its axial stiffness resulting in springing. This may be the cause of the springing effect seen in Fig. 4.17 which occurs at a change in direction of armature motion corresponding to the highest acceleration or 2) Inconsistencies with the machining of the slotted channel and cylindrical slider lead to situations where contact between the two were lost which also would lead to additional oscillations in the recorded force.

Before attempting to obtain the generator coefficients from the force signature several signal processing procedures were applied.

1. A eighth order Fourier series representation was best fit to the raw force signal:

$$\begin{aligned} F_g(t) = a_{11}\cos(\sigma t) &+ b_{11}\sin(\sigma t) + a_{22}\cos(2\sigma t) + b_{22}\sin(2\sigma t) + \cdots \\ &+ a_{88}\cos(8\sigma t) + b_{88}\sin(8\sigma t) + c \quad . \end{aligned} \tag{4.57}$$

2. The Savitzky-Golay filter (SGF), described in Sec. 4.5.4, was applied to the raw force signal.

3. The Fast Fourier Transform Filtering (FFTF), described in Sec. 4.5.4, was applied to the raw force signal. Different cut-off frequencies were used to investigate how the modes observed in Fig. 4.17 affected the force signal.

Figure 4.17d plots the FFTF force signal for different cut-off frequencies. The low pass 15 Hz signal significantly cleans up the raw signal, though a springing oscillation is still present and increases in magnitude at the force peaks. In Fig. 4.17e the various signal processing procedures applied to F_g are compared. The reconstructed force signal, *Recon*, is calculated from the first order generator coefficients that will described in greater detail in the following section. All procedures converge to the same form indicating that the input power to the generator should not vary on the smoothing procedure.

Estimation of K_g, B_g, and μ_g

The sinusoidal motion of the armature allows the generator force to be represented in the following form:

$$F_g(t) = -\left(K_g(\sigma,R) - \mu_g(\sigma,R)\sigma^2\right)\zeta_3(t) - B_g(\sigma,R)\dot{\zeta}_3(t) \quad . \tag{4.58}$$

Keeping the dominant term of the Fourier series representation for ζ_3 and F_g provides:

$$\zeta_3(t) = a_1\cos(\sigma t) + b_1\sin(\sigma t) \quad , \tag{4.59}$$

$$F_g(t) = a_{11}\cos(\sigma t) + b_{11}\sin(\sigma t) \quad . \tag{4.60}$$

After inserting Eqn. (4.59) into Eqn. (4.58) and equating like terms with Eqn. (4.60) leads to:

$$a_{11} = -\left(K_g(\sigma,R) - \mu_g(\sigma,R)\sigma^2\right)b_1 + B_g(\sigma,R)\sigma a_1 \quad , \tag{4.61}$$

$$b_{11} = -\left(K_g(\sigma,R) - \mu_g(\sigma,R)\sigma^2\right)a_1 - B_g(\sigma,R)\sigma b_1 \quad . \tag{4.62}$$

The system of equations can be solved for $(K_g(\sigma,R) - \mu_g(\sigma,R)\sigma^2)$ and $B_g(\sigma,R)$ which is given by:

$$\left(K_g(\sigma,R) - \mu_g(\sigma,R)\sigma^2\right) = -\frac{a_1a_{11} + b_1b_{11}}{a_1^2 + b_1^2} \quad , \tag{4.63}$$

$$B_g(\sigma,R) = \frac{a_1b_{11} - b_1a_{11}}{\sigma\left(a_1^2 + b_1^2\right)} \quad . \tag{4.64}$$

In order to separate $(K_g(\sigma,R) - \mu_g(\sigma,R)\sigma^2)$ into its spring and inertia components the calculated values are plotted against the angular frequency squared. If the plot follows a linear trend it will be assumed that both K_g and μ_g are not frequency dependent. A simple linear fit, $-c\sigma^2 + b$ can be applied and the coefficients can be equated as follows $c = \mu_g$ and $b = K_g$.

The generator coefficients calculated under several resistive loads can be found in Fig. 4.18. An average of generator coefficients obtained from linear fits applied to Fig. 4.18b, per R, provided $\mu_g = 8.80$ kg and $K_g = 4.4$ N/m. The value of K_g is less than 1% of the floater's spring constant and thus is considered negligible or merely a result of the numerical force fit. The generator inertia needs to be corrected for the moving mass during the bench test, which is listed in Table 4.2, which indicates that there is essentially no added inertia due to the presence of the generator. Since the contributions from K_g and μ_g are small compared to the spring constant and mass of the floater, the reaction force from the generator will be approximated as follows:

$$F_g(t) = -\left(K_g(\sigma) - \mu_g(\sigma)\sigma^2\right)\zeta_3(t) - B_g(\sigma)\dot{\zeta}_3(t) \quad , \tag{4.65}$$

$$\approx -B_g(\sigma)\dot{\zeta}_3(t) \quad . \tag{4.66}$$

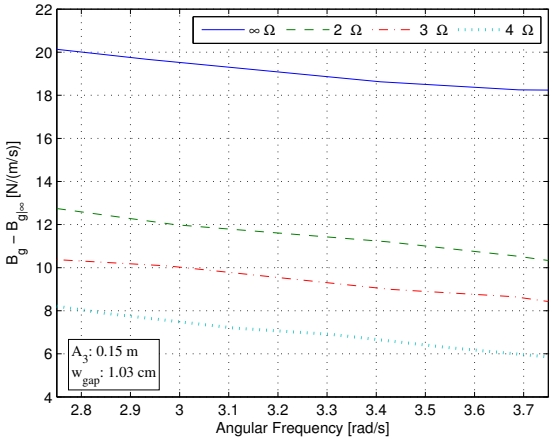

(a) B_g as a function of σ. The damping generated with an open circuit, $B_{g|\infty}$, has been subtracted off leaving only the EM contribution.

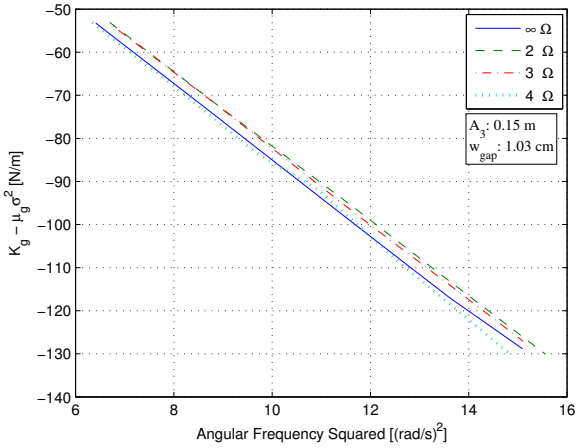

(b) $K_g - \mu_g\sigma^2$ as a function of σ^2.

Figure 4.18: Generator Coefficients as a function of armature speed and R. A resistive load of ∞ was tested by disconnecting the wires across each phase creating an open circuit thereby preventing power generation.

Table 4.2: Mass, m_b, of moving components used in bench test.

Armature Magnet Array	4.00	kg
Slider-Force Block Connector	0.57	kg
Heave Slider	4.24	kg
Total	8.86	kg

Furthermore, it is observed from Fig. 4.18a that the generator damping is influenced by the maximum armature speed decreasing by as much as 20% over the tested range. This inverse relationship between generator damping and armature speed is also captured in [9]. In addition, it should be noted that B_g at $R = \infty\ \Omega$ produces 70% of the damping at $R = 3\ \Omega$, which has the highest power output. Since $R = \infty\ \Omega$ prohibits power generation it signifies a substantial initial power loss.

4.5.6 Generator Input Power

With the armature velocity known it is possible to estimate the time averaged power input to the generator and the corresponding efficiency:

$$\overline{\dot{W}} = P_{me} = \frac{1}{T}\int_t^{t+T} F_g(t')\dot{\zeta}_3(t')dt' = \frac{1}{T}\int_t^{t+T} B_g\dot{\zeta}_3^2(t')dt' \quad , \tag{4.67}$$

$$\eta_{el} = \frac{P_{el}}{\overline{\dot{W}}} = \frac{P_{el}}{P_{me}} \quad . \tag{4.68}$$

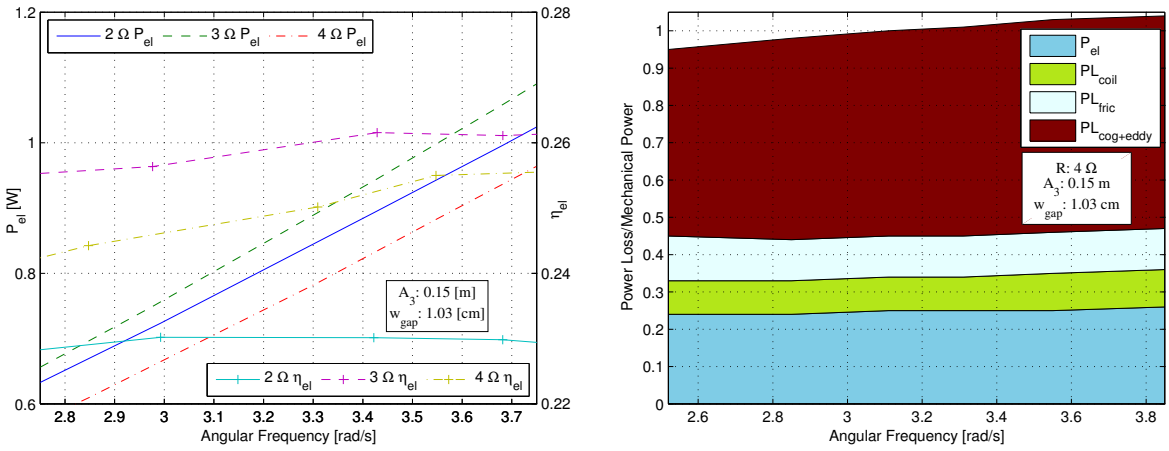

(a) P_{el} and η_{el} as a function of σ.

(b) Power-loss breakdown for 1st generation stator.

Figure 4.19: P_{el}, η_{el}, and power-loss breakdown for 1st generation stator as a function of σ.

The resulting power output and electrical efficiency is plotted for several applied loads in Fig. 4.19a. The maximum η_{el} and P_{el} occurs at 3 Ω with both efficiency and power output decreasing with an increase in applied load. The power output increases linearly with armature speed while the efficiency of the generator increases slightly, at most 1%, with the applied load having a stronger influence.

The largest P_{me} occurs at 2 Ω decreasing with larger resistive load. This is consistent with Eqn. (4.46), where the voltage drop across the open terminals is replaced by the voltage drop across R:

$$i = \frac{V_e}{r+R} \quad , \tag{4.69}$$

$$P_{load} = V_e^2 \frac{R}{(r+R)^2} = V_e^2 \frac{1}{R} \frac{1}{\left(\frac{r}{R}\right)^2 + 2\frac{r}{R} + 1} \quad . \tag{4.70}$$

As the load is increased the current and consequently the opposing force generated by the back emf, as described in Eqn. (4.29), are both reduced. The power across the applied load, under the assumptions made, should maximize when $r = R$ and then begin to decrease at a rate similar to the current for sufficiently large R.

4.5.7 Generator Power Losses

The maximum efficiency reached just over 26% producing a modest increase of 8% over results from [24] which indicates the cogging effects were not the dominant power loss as previously thought. The remaining power losses were explored as follows:

1. In order to determine power lost through friction in the experimental set-up the bench test was run to measure the force, $F|_f(t)$, with all components except the stator. The

power loss due to friction was then calculated by:

$$PL_{fric} = \frac{1}{T}\int_{t}^{t+T} \dot{\zeta}_3\left(t'\right) F|_f\left(t'\right) dt' \quad . \tag{4.71}$$

2. As stated in Sec. 4.5.3, the coil windings add resistive losses and its magnitude was calculated by:

$$PL_{coil} = \frac{r}{T}\int_{t}^{t+T} \left(V(t')/R\right)^2 dt' = \frac{r}{R} P_{load} \quad . \tag{4.72}$$

3. As discussed in Sec. 4.5.6, there was a significant power loss in the generator before extracting power. It was suspected that iron losses from eddy currents and hysteresis were now the dominating power losses as these are strongly linked to stator material and present with or without power generation. In order to obtain an estimate on this loss the generator was driven with an infinite electrical load, while measuring the force $F_g|_\infty$, and removing the frictional component:

$$PL_{cog+eddy} = \frac{1}{T}\int_{t}^{t+T} \dot{\zeta}_3 F_g|_\infty\left(t'\right) dt' - PL_{fric} \quad . \tag{4.73}$$

The results of the above analysis can be found in Fig. 4.19b which confirms that over 50% of the power losses were occurring even before power generation.

Eddy Currents

As seen from Fig. 4.19b the first generation stator suffered from eddy-current losses due to its construction from a single piece of steel. This provided little resistance to internal current loops generated in the steel material. A well-known, first order expression, provided by [71] for the eddy-current losses per unit volume of iron laminations, is written as:

$$PL_e = \frac{\sigma^2 B_m^2 b_{Fe}^2}{12\rho_{Fe}} \tag{4.74}$$

where b_{Fe} is the width of the lamination and ρ_{Fe} is the resistivity of the used material. From Eqn. (4.74), power losses can be substantially reduced by replacing the single iron stator with multiple electrically insulated layers.

Magnetic Hysteresis

When a ferromagnetic material is magnetized in one direction it will not relax back to zero after the magnetic field is removed. The magnetization must be driven back to zero with an applied magnetic field in the opposite direction. If an alternating magnetic field is applied to a given material, the resulting magnetization will trace out what is called the hysteresis

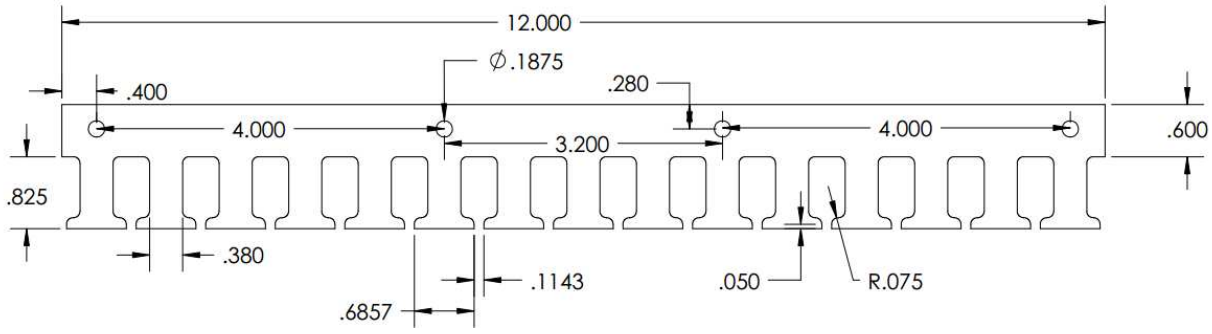

Figure 4.20: CAD model of top-down cross section of each lamination. All dimensions have the units of inches.

loop. This loop is caused in part by the magnetic domains of the material. These domains orient themselves in the direction of the magnetic field, thus as the direction is changed the domains will follow. The reorientation of the domains results in energy dissipation due to friction at the microscopic level. An estimate on the power loss from hysteresis due to pulsating fields [76] is given by:

$$PL_h = k_h \sigma B_m^{\alpha} \quad , \tag{4.75}$$

where the constant k_h and the power α are experimentally derived constants. Losses can be minimized when the stator material has a narrow hysteresis loop implying a smaller amount of energy is dissipated when repeatedly reversing the magnetization direction. However, a large hysteresis loop is desired for the permanent magnets as it prevents demagnetization.

4.6 Second Generation Stator

4.6.1 Construction

A new laminated steel stator (LSS) was designed and constructed. The solid steel stator (SSS) used earlier was broken into 90 laminated sheets to reduce the area, perpendicular to the direction of motion, available for eddy current generation. These laminations were manufactured[6] from M-15 non-grain oriented silicon iron steel with a thickness of 0.014 in (0.356 mm) (Gauge number 29) leading to a stack thickness of 1.26 in (3.2 cm). An inorganic-based surface insulation, equivalent to ASTM Type C-5, was chosen to electrically isolate the laminations. The stator maintained 15 teeth with the dimensions described in Table 4.1 and geometry shown in Fig. 4.20. As shown in the top photo in Fig. 4.21, the laminations after being cut were loosely bound and shipped. In order to facilitate the coating of the stator with epoxy it was decided to laser weld[7] the laminations. Once laser welded the stator was

[6]Proto Laminations, http://www.protolam.com/

[7]Laser Technologies, http://www.laswertechnologiesinc.com/

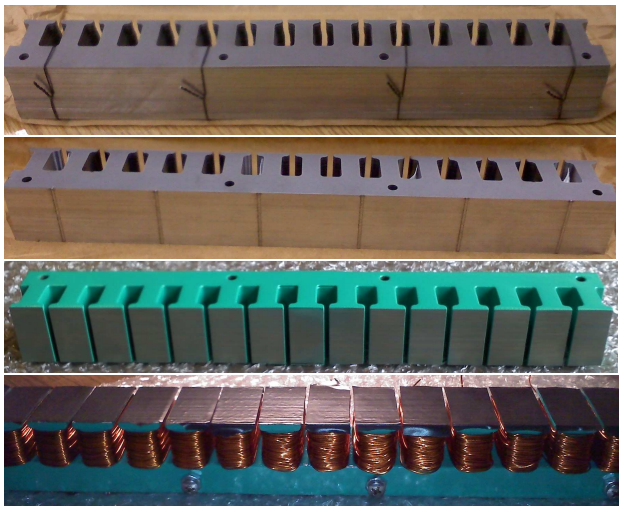

Figure 4.21: Photos depicting the construction process of the laminated steel stator.

covered with a class H epoxy[8] powder to insulate the copper wires from the laminations. Each tooth was then wound approximately 70 times, by hand, with 22 gauge magnet wire, giving an approximate resistance of 0.36 ohms per coil and 2 ohms per phase. The individual teeth windings followed the same pattern shown in Fig. 4.1, and the phases were connected in a wye-winding for greatest efficiency. The stator is connected to the back support plate through 4 stainless steel rods, Fig. 4.22, that are linked to the stator by screws that lay in the through holes of the stator, Fig. 4.20. Therefore, a cantilever structure continues to oppose the normal force between stator and armature while maintaining the desired magnet coil gap width. It is suggested that for any future development a revised structure be made to reduce the moment created by the cantilever structure.

4.6.2 Generator Force Coefficients

The bench test was repeated with the new laminated steel stator to obtain the generator coefficients which can be found in Fig. 4.23. The results of the bench test provided $\mu_g = 9.00$ kg and $K_g = 0.53$ N/m. The value of K_g is again negligible compared to the floater's spring constant and though there appears to be a small added inertia, it comprises less than 2% of the moving mass. The most significant change comes from the reduction in $B_{g|\infty}$ which is now only 20% of the solid steel stator. Furthermore, after subtracting off $B_{g|\infty}$, the generator damping in Fig. 4.23a remains nearly constant unlike Fig. 4.18a. Furthermore, the damping due to power generation is substantially greater than at infinite load indicating that a greater amount of the input energy is being put towards the conversion process.

[8]Electro Star Industrial Coating, Inc., http://www.electrostar.net/index.html

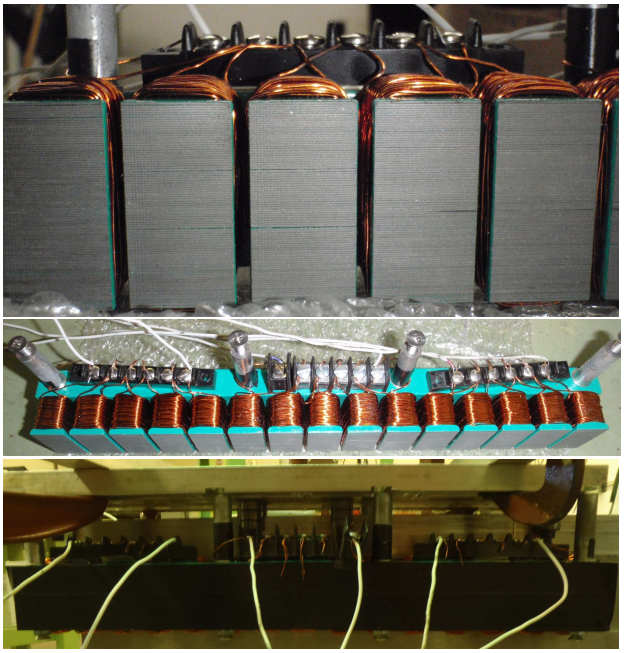

Figure 4.22: Photos depicting the fully constructed laminated steel stator and its attachment to the back support plate.

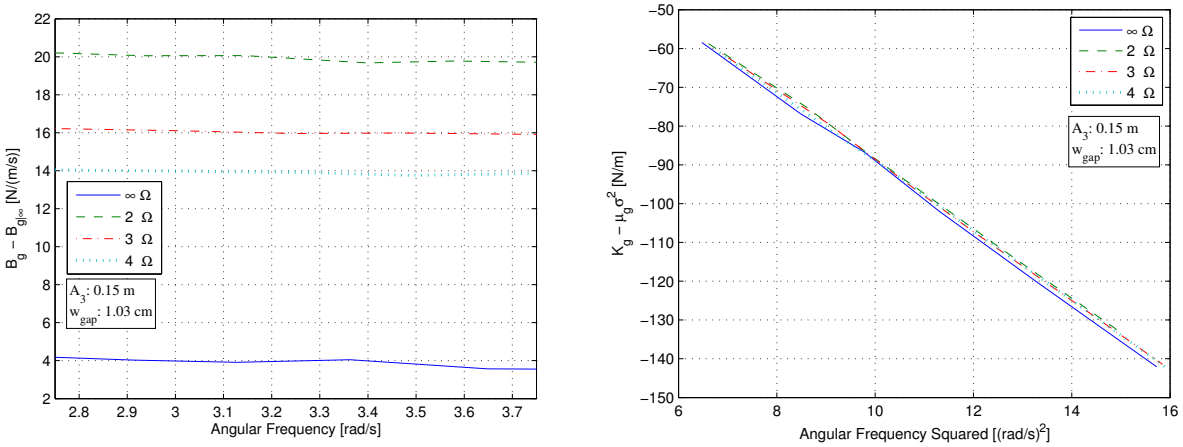

(a) B_g as a function of σ. The damping generated with an open circuit, $B_{g|\infty}$, has been subtracted off leaving only the EM contribution.

(b) $K_g - \mu_g\sigma^2$ as a function of σ^2.

Figure 4.23: Generator Coefficients as a function of armature speed and R for second generation stator.

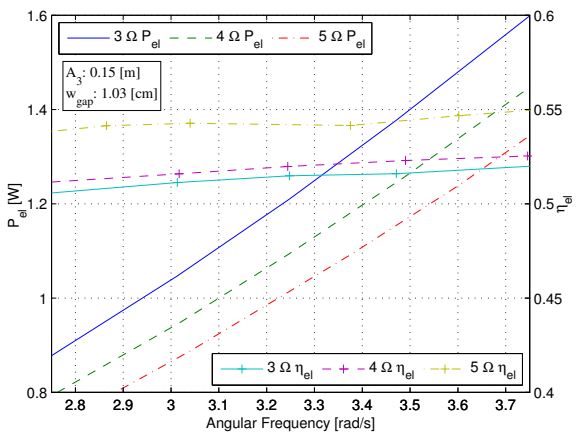

(a) P_{el} and η_{el} as a function of σ for 2nd generation stator.

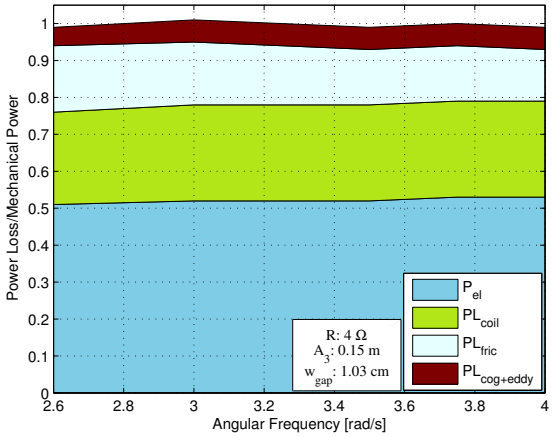

(b) Power-loss breakdown as a function of σ.

Figure 4.24: Power output, efficiency, and power-loss breakdown for second generation stator.

4.6.3 Generator Power Output and Losses

The resulting power output and electrical efficiency is plotted for several applied loads in Fig. 4.24a. The power output peaks between $2-3\Omega$ then decreases with increasing applied load while it is at minimum 40% greater than the solid steel stator. However, the electrical efficiency increases with electrical load, but saturates at approximately 56% after 6 Ω, which is approximately double that of the solid steel stator under most testing conditions. The increase in efficiency with load is consistent as coil power losses will decrease due to the lower current and a greater proportion of the input power will be consumed by the larger load. The power-loss breakdown described in the previous chapter, can be found in Fig. 4.24b. It can be seen that hysteresis and eddy currents now comprise approximately 6% of the total power input, a factor of 8 reduction. The electrical losses due to the resistance, r, of the coils, was roughly calculated to be 25% for the LSS and now becomes the generator's largest power sink. However, this is a consequence of working at the model scale and when scaling up the coil losses are expected to decrease as the wire diameter will increase thereby reducing its resistivity.

4.6.4 Effect of Magnet Coil Gap Width (MCGW)

As will be discussed in Sec. 5, it is important to select the appropriate generator, B_g, that maximizes the time-averaged power. For a given MCGW, varying the PTO resistor may not achieve the desired $B_g = \lambda_T$ when at resonance, therefore it may be necessary to adjust the MCGW to match the damping impedance. An increase of the MCGW by 37% decreases the the generator damping by 54% and P_{el} by as much as 50%, see Fig. 4.25. Lower efficiencies at larger MCGWs is consistent with the magnetic leakage becoming more prevalent. In addition, it has become apparent that very small changes in the MCGW can have dramatic effects on the generator's performance. This is important if investigation into dynamic

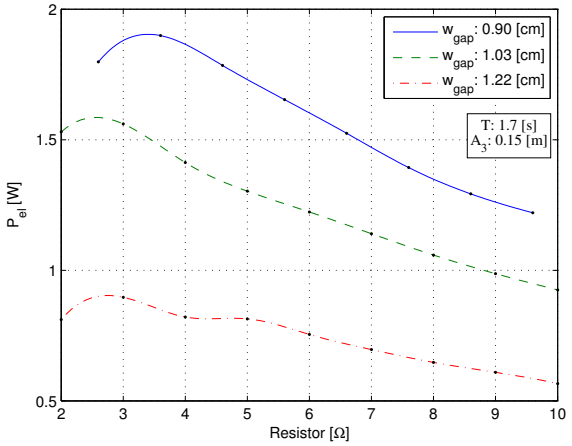

(a) P_{el}.

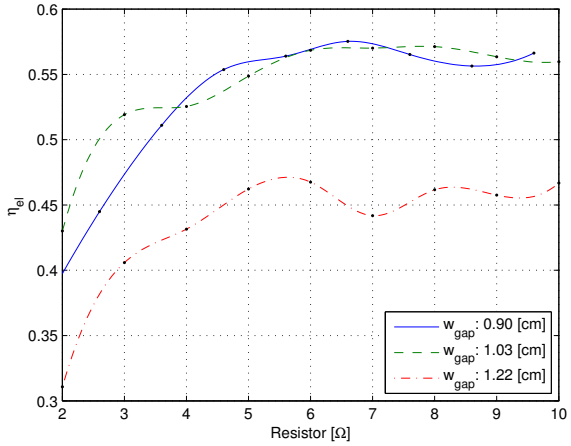

(b) η_{el}.

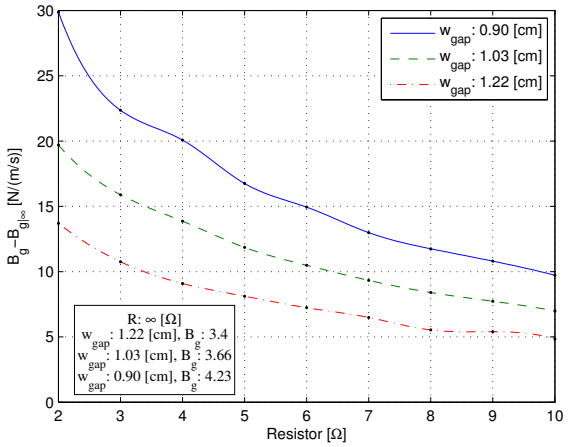

(c) B_g.

Figure 4.25: Effect of MCGW on P_{el}, η_{el}, and B_g for varying load resistance R.

control of the MCGW is pursued in an attempt to control the motion of the floater. However, given the high attractive force between the armature and stator, as discussed in Sec. 4.3.1, it is in the mind of the author that this actuation cannot be completed efficiently unless used in a stochastic rather than real-time application.

Chapter 5

Coupled Floater-Generator System Modeling

5.1 Coupled System Heave Response Amplitude Operator

In order to extract power from the incident wave train, it is necessary that a proper power-take-off (PTO) device is chosen. There are various designs on the market and underdevelopment, but the Computational Marine Mechanics Laboratory has chosen to focus on the design and testing of a direct drive permanent magnet linear generator, which was expanded upon in Chapter 4. For the time being, the force produced by the PTO unit will be modeled by Eqn. (4.47). If time harmonic floater motion, Eqn. (3.2), is assumed then Eqn. (4.47) can be rearranged as:

$$F_g(t) = -\left(K_g - \mu_g \sigma^2\right)\zeta_3(t) - B_g\dot{\zeta}_3(t)\,. \tag{5.1}$$

The PTO force contributions can be added to the left hand side of Eqn. (3.3) leading to:

$$\left\{\left[K + K_g - \sigma^2\left(m + \mu_{33}(\sigma) + \mu_g(\sigma)\right)\right] - i\sigma\left(\lambda_{vis}(\sigma) + \lambda_{33}(\sigma) + B_g(\sigma)\right)\right\}\mathcal{A}_3 = AX_3(\sigma) \tag{5.2}$$

which allows one to construct the coupled response amplitude operator. The RAO of the coupled cylindrical floater and PMLG system, in non-dimensional form, is then given by:

$$\left|\frac{\mathcal{A}_3}{A}\right|^2 = \frac{\overline{K}^2|\overline{X}_3|^2}{[\overline{K} - \overline{\sigma}^2(\overline{d} + \overline{\mu}_T)]^2 + [\overline{\sigma}^2\overline{\lambda}_T(1+\tilde{f})]^2}\quad , \tag{5.3}$$

where additional non-dimensional variables are defined by:

$$\overline{\lambda}_T = \overline{\lambda}_{33} + \overline{\lambda}_{vis}\quad ,\quad \overline{K} = 1 + \frac{K_g + K_{sp}}{K}\quad ,\quad \overline{\mu}_T = \overline{\mu}_{33} + \overline{\mu}_g\quad ,\quad \tilde{f} = \frac{B_g}{\lambda_T}\quad , \tag{5.4}$$

where K_{sp} is any external spring constant which could be used to shift the resonance frequency of the coupled system.
The time-averaged mechanical power input into the generator is given by:

$$\overline{\dot{W}} = \frac{1}{T}\int_0^T B_g\dot{\zeta}_3(t)^2 dt = \frac{\pi}{2}\rho(ga)^{\frac{3}{2}}|\mathcal{A}_3|^2\overline{\sigma}^3\tilde{f}\ \overline{\lambda}_T\quad . \tag{5.5}$$

By dividing both sides of Eqn. (5.5) by A^2 allows one to insert Eqn. (5.3) leading to:

$$\begin{aligned}\frac{\overline{\dot{W}}}{A^2} &= \frac{\pi}{2}\rho(ga)^{\frac{3}{2}}\left|\frac{\mathcal{A}_3}{A}\right|^2\overline{\sigma}^3\tilde{f}\ \overline{\lambda}_T\quad ,\\ &= \frac{\frac{\pi}{2}\rho(ga)^{\frac{3}{2}}\ \overline{\lambda}_T\overline{K}^2|\overline{X}_3|^2\ \overline{\sigma}^3\ \tilde{f}}{[\overline{K} - \overline{\sigma}^2(\overline{d} + \overline{\mu}_T)]^2 + [\overline{\sigma}^2\overline{\lambda}_T(1+\tilde{f})]^2}\quad .\end{aligned} \tag{5.6}$$

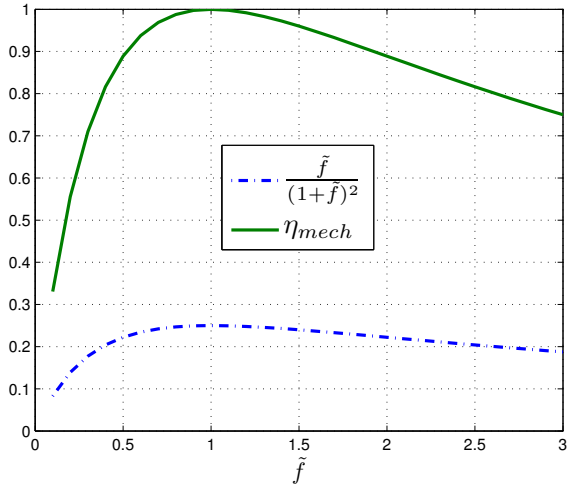

(a) Variation of η_{mech} and $\tilde{f}/(1+\tilde{f})^2$ against $\tilde{f}$.

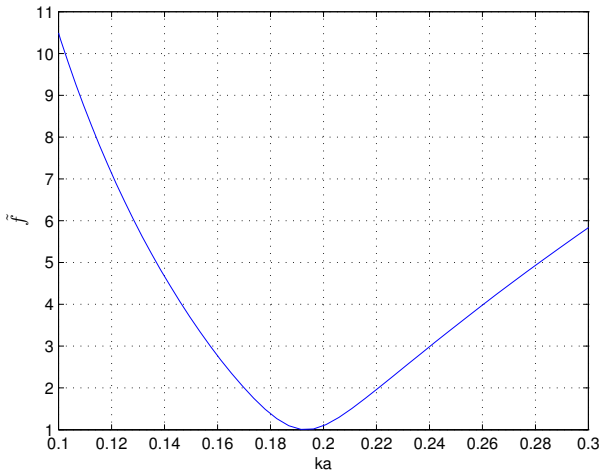

(b) $\tilde{f}$ as calculated by Eqn. (5.11).

Figure 5.1: Optimization of $\tilde{f}$ under varying operating conditions.

It is known from the Chapter 3 that the maximum motion occurs under resonance, which reduces Eqn. (5.6) to:

$$\frac{\overline{\dot{W}}}{A^2} = \frac{\pi}{2}\rho(ga)^{\frac{3}{2}}\frac{\overline{K}^2|\overline{X}_3|^2}{\overline{\sigma}\overline{\lambda}_T}\frac{\tilde{f}}{(1+\tilde{f})^2} \quad . \tag{5.7}$$

The above equation is maximized when $\tilde{f}=1$, visualized in Fig. 5.1, resulting in:

$$\frac{\overline{\dot{W}}}{A^2}|_{max} = \frac{1}{8}\frac{\overline{K}^2|X_3|^2}{\lambda_T} \quad . \tag{5.8}$$

If the floater is not excited by waves at the resonant frequency then the condition of $\tilde{f}=1$ will not lead to optimum extraction. The optimum generator damping at each frequency can be obtained from calculus by setting the partial derivative of Eqn. (5.6) equal to 0 and solving for $\tilde{f}$.

$$\begin{aligned}\frac{\partial}{\partial\tilde{f}}\frac{\overline{W}}{A^2} &= \frac{\frac{\pi}{2}\rho\,(ga)^{3/2}\,\overline{\sigma}^3\overline{\lambda}_T\overline{K}^2|\overline{X}_3|^2}{\left[[\overline{K}-\overline{\sigma}^2(\overline{d}+\overline{\mu}_T)]^2+[\overline{\sigma}^2\overline{\lambda}_T(1+\tilde{f})]^2\right]^2} \\ &\times \left[[\overline{K}-\overline{\sigma}^2(\overline{d}+\overline{\mu}_T)]^2+[\overline{\sigma}^2\overline{\lambda}_T(1+\tilde{f})]^2-2\tilde{f}(1+\tilde{f})\overline{\sigma}^4\overline{\lambda}_T^2\right]=0 \quad .\end{aligned} \tag{5.9}$$

After dropping the constants in Eqn. (5.9):

$$\underbrace{\left(\frac{\overline{K}-\overline{\sigma}^2(\overline{d}+\overline{\mu}_T)}{\overline{\sigma}^2\overline{\lambda}_T}\right)^2}_{K^*}+(1+\tilde{f})^2-2\tilde{f}(1+\tilde{f})=0 \quad , \tag{5.10}$$

$$\tilde{f}=\sqrt{1+K^*}=\sqrt{1+\left(\frac{\overline{K}-\overline{\sigma}^2(\overline{d}+\overline{\mu}_T)}{\overline{\sigma}^2\overline{\lambda}_T}\right)^2} \quad . \tag{5.11}$$

It is easy to see that $K^* \geq 0$ and $\tilde{f} \geq 1$ indicating that the optimal constant-continuous generator damping will increase as the wave frequency moves away from resonance, Fig. 5.1b.

5.2 Extraction Efficiency and Capture Width

The power contained in ocean waves per unit wave front is known to be proportional to the wave amplitude A squared and its period T [47]:

$$P_w = \frac{1}{2}\rho g A^2 V_g \quad , \tag{5.12}$$

$$V_g = \frac{1}{2}V_p\left[1+\frac{2kh}{\sinh(2kh)}\right] \quad , \tag{5.13}$$

$$V_p = \frac{\sigma}{k} = \sqrt{\frac{g}{k}\tanh(kh)} \quad , \tag{5.14}$$

where P_w, V_g, and V_p are the power, group velocity, and phase velocity of the propagating wave the later two can derived from the dispersion relation, Eqn. (2.28). Under the deep-water condition, $h \to \infty$, P_w can be simplified to:

$$P_w = \frac{1}{8\pi}\rho g^2 A^2 T \quad . \tag{5.15}$$

A measure of the extraction efficiency is the time-averaged mechanical power extracted, $\overline{\dot{W}}$, divided by the average power available from the waves per unit wave front:

$$C_w = \frac{\frac{1}{2}\frac{\overline{K}^2|X_3|^2}{\lambda_T}\frac{\tilde{f}}{(1+\tilde{f})^2}}{\frac{1}{8\pi}\rho g^2 A^2 T} \tag{5.16}$$

$$= 4\frac{\tilde{f}}{(1+\tilde{f})^2}\frac{\sigma\overline{K}^2|X_3|^2}{2\rho g^2\lambda_T} \tag{5.17}$$

$$= \eta_{mech}\frac{\sigma\overline{K}^2|X_3|^2}{2\rho g^2\lambda_T} \tag{5.18}$$

$$C_{w|max} = \frac{\sigma\overline{K}^2|X_3|^2}{2\rho g^2\lambda_T} \quad , \ \tilde{f}=1 \ \& \ \eta_{mech}=1 \quad . \tag{5.19}$$

Eqn. (5.16) can be normalized by $\lambda/2\pi$, the maximum inviscid-fluid result, which leads to:

$$kC_{w|max} = \frac{\sigma^3\overline{K}^2|X_3|^2}{2\rho g^3\lambda_T} \quad . \tag{5.20}$$

In Eqn. (5.20), the wave-exciting force is considered to be independent of the wave damping. The Haskind relation [54] provides the following relationship between wave-exciting force

and radiation damping:

$$\frac{\sigma^3|X_3|^2}{2\rho g^3 \lambda_{33}} = 1 \quad . \tag{5.21}$$

If Eqn. (5.21) is used in Eqn. (5.20) and $\overline{K} = 1$ then $kC_{w|max} = 1$, which follows the well-known result of [7, 77]. Though, Eqn. (5.16) is a more general form and does not include any relation between wave damping and wave-exciting force. As a reminder, Eqn. (5.16) is a measure of time-averaged power absorbed by the generator, thus the useful output power will depend on the PTO conversion efficiency, η_{PTO}:

$$C_{w|out} = \eta_{PTO}\eta_{mech}\frac{\sigma\overline{K}^2|X_3|^2}{2\rho g^2 \lambda_T} \quad , \tag{5.22}$$

which acts as an upper limit for a coupled floater-PTO system [25]. Although maximum extraction occurs when $\tilde{f} = 1$, η_{mech} can be sustained at 89% or larger for $\tilde{f}$ between 0.5 and 2. The slow rate of change around $\tilde{f} = 1$ indicates that energy extraction will not drastically change as one moves away from the optimum operating point.

5.3 Coupled Floater-Generator Wave Tank Testing

The performance of the modified floater shape and PMLG were independently validated to verify the conclusions made at the end of Section 5.2. Experiments on the coupled system were performed at the UC Berkeley Richmond Field Station Model-Testing Facility, under sinusoidal wave excitation of varying amplitude and frequency. In this section the experimentally measured capture width, C_w, will be normalized by the diameter of the floater:

$$C_w = \frac{P_{el}}{P_w} \quad , \tag{5.23}$$

$$\overline{C}_w = \frac{C_w}{D} \quad , \tag{5.24}$$

and due to the wave tank dimensions P_w will be given by Eqn. (5.12).

5.3.1 Experimental Set-Up

The wave tank experimental set-up combined the free motion test with the bench test electronics. The only addition to the free motion set-up was the stator which remains attached to the back support plate, which is then held to the stator support structure by C-clamps. The armature was used in the free-motion tests to provide the weight necessary to achieve the desired draft. During testing there were 8 channels available on the two MCC USB-1208FS data acquisition devices. Theses channels recorded the floater's heave position, the incoming

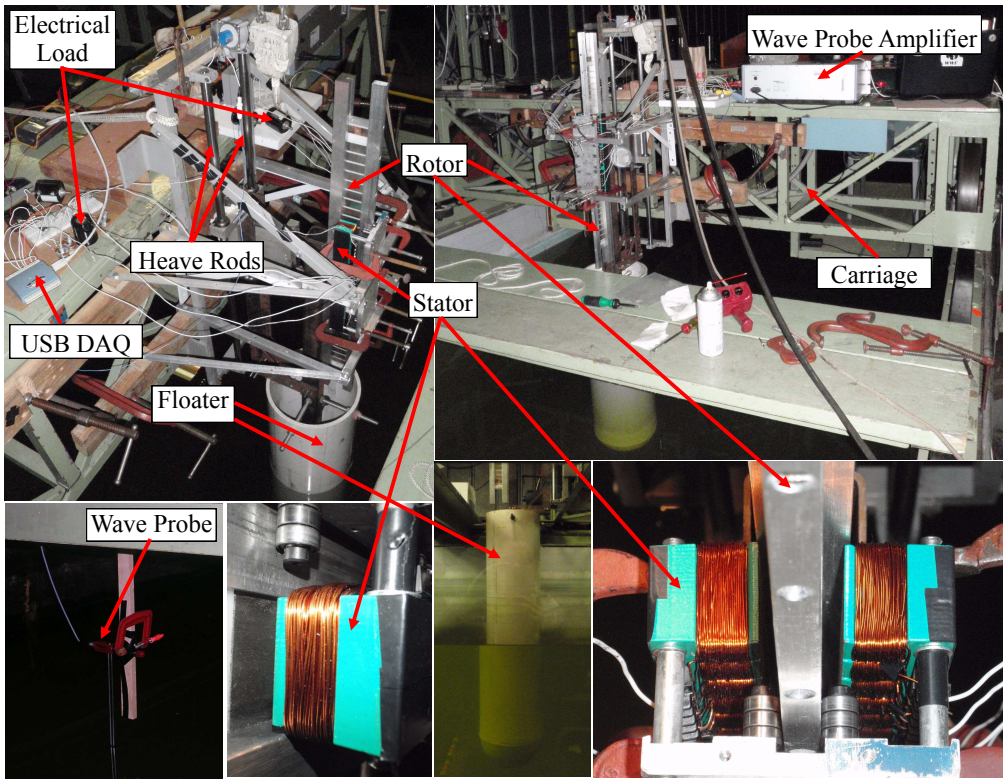

Figure 5.2: Photos showing the coupled system during wave-tank tests.

wave amplitude, and the voltage drop across the electronic load placed across the 3 phases of each stator. A MCGW of 1.03 cm was selected so the results from the bench test could be used to estimate $\tilde{f}$ and verify the measured power output. In order to estimate the value of $\tilde{f}$, the RAO obtained from the wave tank tests was used, as described in Sec. 3.4.1, to estimate the total damping in the system. Results from the bench test provided the damping contribution from the generator which, after its removal from the total damping, provided an estimate of λ_T. It is not expected that the value of λ_T would be same as in the free motion test given the difference in the amplitude of motion or the free decay tests as the amplitude of motion is not sinusoidal. The results presented in this chapter are focused on the performance near resonance where the impedance matching is of greater importance. Strategies to control the damping values from the generator when moving away from resonance are discussed in the following chapters.

5.3.2 Experimental Results

The tests combining the RB floater with the LSS reported significant gains in both $\overline{C}_w$ and P_{el}, Fig. 5.3. The wave amplitude used for these tests was approximately 40% less than for the RB - SSS producing 35% more power. The $\overline{C}_w$ also increased significantly obtaining a maximum wave-to-wire efficiency of 35%; however, it must be noted that during the RB -

LSS tests the floater's motion was restricted to ensure the stator was fully covered by the armature. The consequence of not restraining the floater amplitude is shown in Fig. 5.4. As the floater amplitude of motion increases with wave height it eventually will exceed the magnet overlap of 0.181 m, Fig. 5.4b. When this situation occurs, the outer portions of the stator will see a reduction in the magnetic flux thereby saturating the time averaged power and reducing the capture width. Thus, the non-dimensional capture width values presented in Fig. 5.3 for the solid steel stator may be 26% lower than the realizable maximum.

Overall, doubling the efficiency with a 50% increase in power output of the LSS over the SSS lead to a factor of 3.5 gain in the normalized capture width. The RB-LSS results when compared to [24] show a factor of 2.6 increase in P_{el}, a factor of 10 in $\overline{C}_w$, with a one-half reduction in wave amplitude. Furthermore, with no restrictions on the floater motion, a wave amplitude of 7.59 cm (3 in) provided a maximum P_{el} of 3.79 W, a 430% increase over [24], with a 33% decrease in wave amplitude.

As expected the greatest performance was achieved when the floater was excited at the resonance frequency. Furthermore, at resonance the time averaged power increased as $\tilde{f} \rightarrow 1$; however, the increase in magnitude is not constant becoming weaker the closer one gets to matching [25]. As shown in Eqn. (5.11), as the wave frequency moves away from resonance the optimum value of $\tilde{f}$ rapidly increases, thus it is necessary to investigate methods to vary the generator damping to extract the greatest amount of power under any environmental condition.

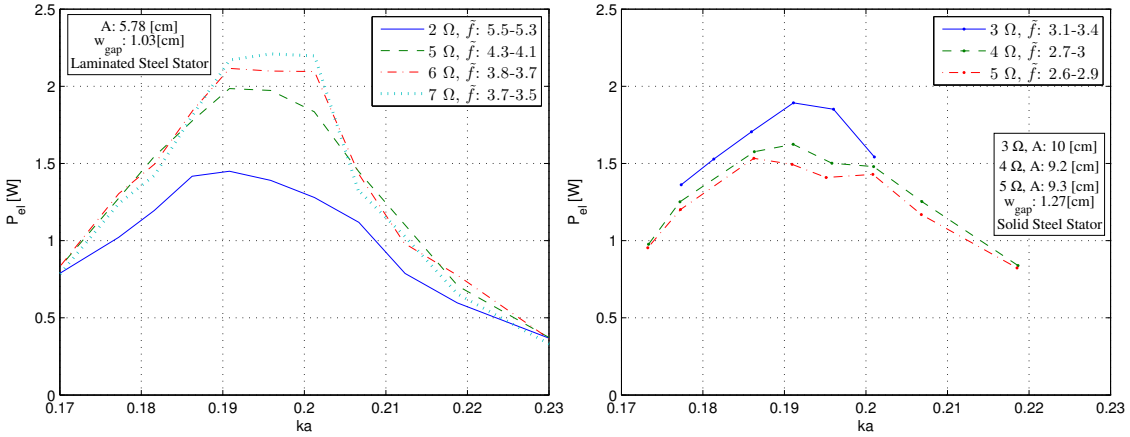

(a) Time Averaged Power (TAP).

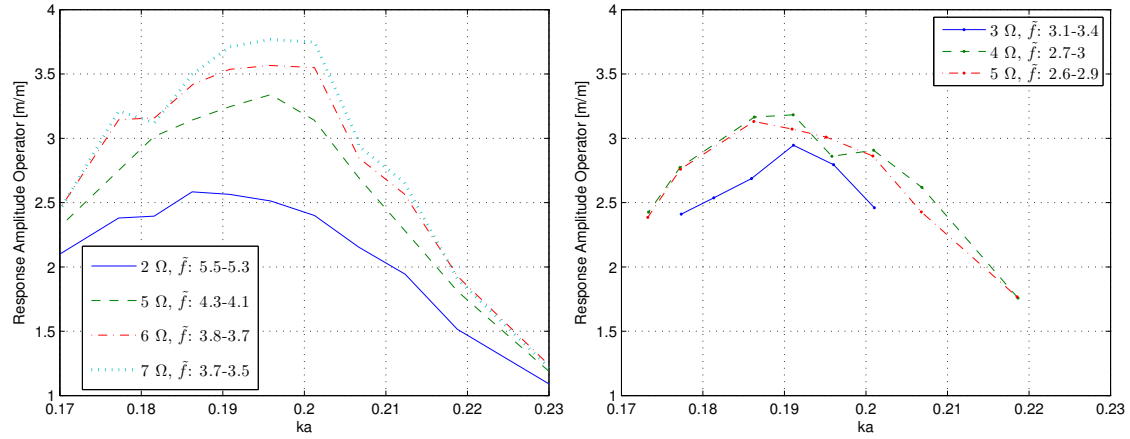

(b) Response Amplitude Operator (RAO) ζ_3/A.

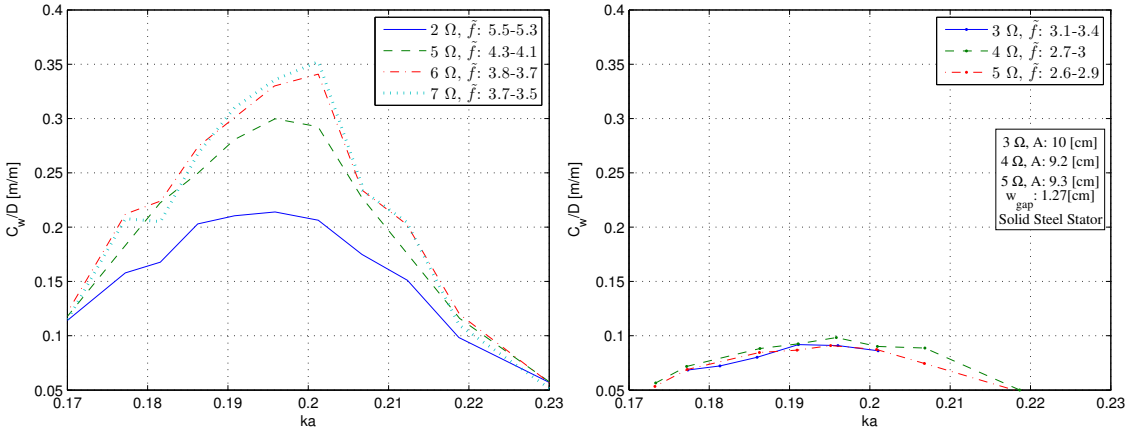

(c) Non-dimensional capture width C_w/D.

Figure 5.3: Frequency domain performance metrics with rounded bottom floater.

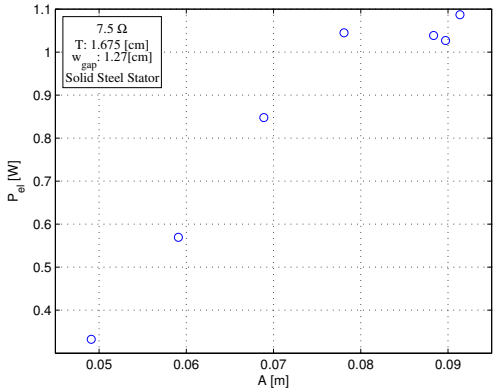

(a) Time Averaged Power.

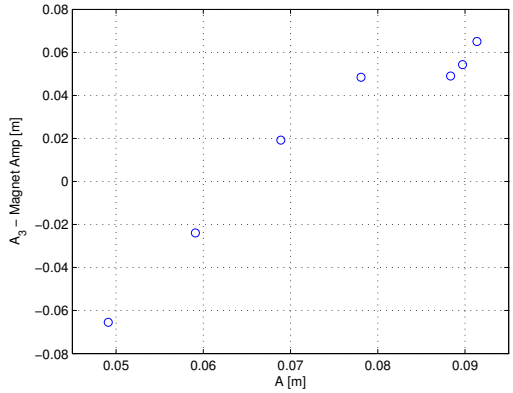

(b) Floater amplitude of motion minus permanent magnet amplitude.

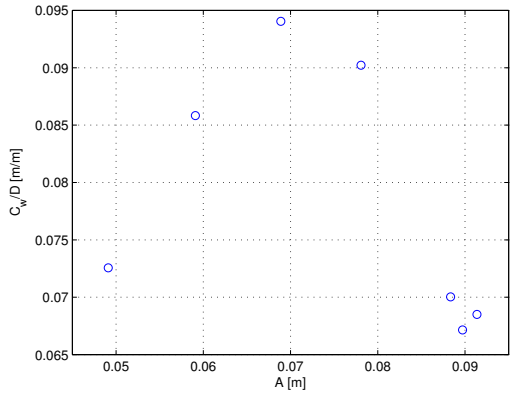

(c) Non-dimensional capture width.

Figure 5.4: Sensitivity of frequency domain performance metrics to incident wave amplitude.

Chapter 6

Wave-Energy Converter Control

6.1 Overview of WEC Control

The control of point absorbers and other ocean energy harvesting devices has been a topic of great interest in the ocean engineering community in recent years [14, 42, 79, 80, 81, 82, 83, 84, 85, 86, 87, 88, 89]. Some of these strategies investigated include reactive control, adaptive tuning, inertia adjustment, latching, and Linear Quadratic Gaussian (LQG) design. One of the main difficulties that remains to be solved is the amount of past and future information required to properly model the future behavior of the absorber.

This work will focus on the application of model predictive control (MPC) to optimize the power absorbed from a model-scale WEC [24, 25]. Previous investigations utilized MPC to solve for an optimum reaction force from the PTO unit that lead to the greatest energy absorption. This approach allows solutions to be obtained from quadratic programming [90] with relaxed constraints. The work presented in this document closely follows the published material in [39], but will be expanded and include considerations for experimental implementation as well as the combination with a latching force. The emphasis of this section will be placed on solving for the time-varying PTO damping that maximizes the absorbed energy from a WEC. Therefore, the PTO reaction force is now a function of the instantaneous floater velocity and PTO damping. This direction was chosen as the previous works of [24, 25] were completed with the aim to achieve damping control on the model scale. A WEC device using any control scheme should theoretically have significant advantages over passive systems, as they will have additional degrees of freedom to amplify the point absorber's motion, whereas passive systems do not, relying mainly upon the resonance of the floating body for efficient energy harvesting. However, passive systems benefit from the lack of additional losses induced by configuring the PTO unit to generate the desired reaction force and no controller design is required.

6.2 Model Predictive Control

6.2.1 Basic Strategy

Model Predictive Control (MPC), also known as a Receding Horizon Controller, is a time-domain based strategy with the following general procedure:

- At each sampling time a constrained finite time optimal control problem (CFTOC) is solved,

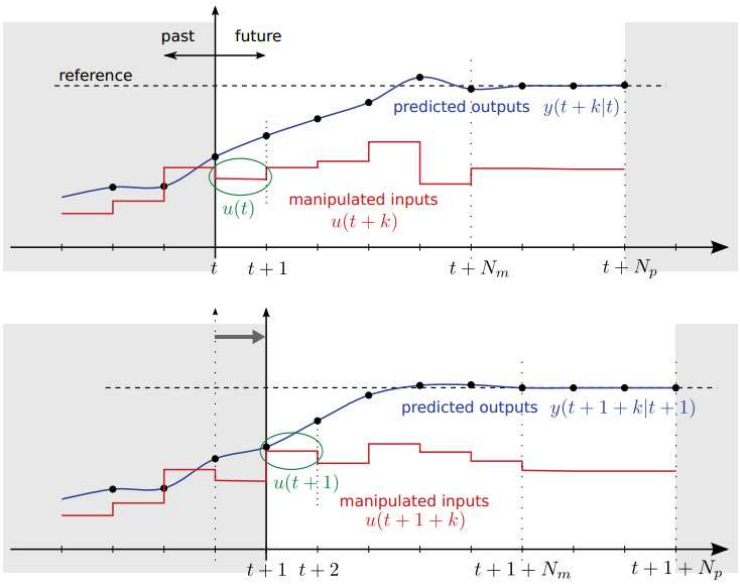

Figure 6.1: Diagram of Model Predictive Control Scheme from [91].

- The optimal control input is applied only during the $[t, t+1]$ time interval,
- At time $t+1$, new state measurements are taken and a CFTOC is solved with a shifted horizon,

which is graphically depicted in Fig. 6.1. The horizon includes the number of discrete steps, or time, that the system dynamics will be predicted in an attempt to meet the goals set by the designer. Historically, proportional-integral-derivative (PID) control has been chosen over MPC because of the rather high computational time required which creates problems in implementation with short time-scales. However, with significant gains in computational power and the relatively large time-scales associated with ocean waves it is believed that MPC has the ability to make an impact on increasing the amount of absorbed power by wave energy converters. It is also desirable to chose MPC because of its ability to set state, input, or output constraints that may appear in the final design specifications, which is much more difficult with PID.

6.2.2 General Constrained Finite Time Optimal Control

A continuous non-linear optimization problem has the following general form:

$$\begin{aligned} \min_{x \in \mathbb{R}^n} \quad & J(x) \\ \text{subject to} \quad & g(x) \leq 0 \\ & h(x) = 0 \\ & x_L \leq x \leq x_U \end{aligned} \tag{6.1}$$

where $J(x)$ is the objective function, the vectors g and h denote the inequality and equality constraints respectively, and the vectors x_L and x_U are the bounds on the variable x. The functions $J(x)$, $g(x)$, $h(x)$ can be non-linear and non-convex, but should be twice continuously differentiable.

- In general, no analytical solution exists where a feasible solution and global optimality are not guaranteed.
- Solutions for x are usually computed by recursive algorithms which start from an initial guess of x_o and at step k, generate a point x_k such that $\{J(x_k)\}_{k=0,1,2,\ldots}$ converges to J^*, the minimum value of the objective function.
- These recursive algorithms use and/or solve analytical conditions for optimality.
- A variety of packages are available to try and solve these types of problems, fmincon in Matlab, NPSOL, and IPOPT to name a few.

6.2.3 Optimality Conditions

In order for a solver to determine if a solution, x^*, provides the minimum value of the objective function, a set of optimality conditions must be met. The basics of optimization theory will now be discussed which strongly parallels the notes of [91].

Lagrange Dual Problem

The Lagrange function is given by:

$$\begin{aligned} \mathcal{L}(x,u,v) &= J(x) + u_1 g_1(x) + \ldots + u_m g_m(z) + v_1 h_1(x) + \ldots + v_p h_p(x) \quad , \quad (6.2) \\ \text{or } \mathcal{L}(x,u,v) &= J(x) + u^T g(z) + v^T h(z) \quad , \quad (6.3) \end{aligned}$$

where u_i and v_i are called Lagrange multipliers or dual variables. Thus, if x is in the feasible set, then the arbitrary vectors $u \geq 0$ and v provide:

$$\mathcal{L}(x,u,v) \leq J(x) \quad . \quad (6.4)$$

Thus, the best lower bound on J is the least upper bound, or supremum, for the Lagrange function. The Lagrangian dual problem now becomes:

$$\Theta(u,v) \equiv \min_{x \in \mathbb{R}^n} \mathcal{L}(x,u,v) \quad \in [-\infty, \infty] \quad , \quad (6.5)$$

$$\sup_{(u,v),\ u \geq 0} \Theta(u,v) \quad . \quad (6.6)$$

The dual problem is now an unconstrained optimization problem and $\Theta(u,v)$ is always concave and easier to solve that the original (primal) problem.

Duality Gap

From the following definitions:

$$d^* = \max_{(u,v),\ u\geq 0} \Theta\left(u,v\right) \quad , \tag{6.7}$$

$$J^* = \min_{x\in\mathbb{R}^n,\ g(x)\leq 0, h(x)=0} J\left(x\right) \quad , \tag{6.8}$$

then $d^* - J^*$ is called the optimal duality gap. Strong duality occurs if $d^* = J^*$ in which case u^* and v^* serve as certificate of optimality.

Complementary Slackness

If we suppose that x^*, u^*, and v^* are primal and dual, provide feasible solutions, and have zero duality gap:

$$\begin{aligned} J\left(x^*\right) &= \Theta\left(u^*,v^*\right) && (6.9)\\ &= \inf_x \left(J\left(x\right) + u^{*T} g\left(x\right) + v^{*T} h\left(x\right)\right) && (6.10)\\ &\leq J\left(x^*\right) + u^{*T} g\left(x^*\right) + v^{*T} h\left(x^*\right) \quad , && (6.11) \end{aligned}$$

which requires

$$\sum_{i=1}^m u_i^* g_i\left(x^*\right) = 0 \quad , \tag{6.12}$$

$$u_i^* g_i\left(x^*\right) = 0 \quad , \ \mathrm{i} = 1,\ldots,m \quad , \tag{6.13}$$

which is called the complementary slackness condition.

Karush-Kuhn-Tucker (KKT) Conditions

If J, g, and h are differentiable and x^*, u^*, and v^* are primal and dual optimal with zero duality gap, then by complementary slackness:

$$J\left(x^*\right) + \sum_{i=1}^m u_i^* g_i\left(x^*\right) + \sum_{j=1}^p v_j^* h_j\left(x^*\right) = \min_x \left(J\left(x\right) + \sum_i u_i^* g_i\left(x\right) + \sum_j v_j^* h_j\left(x\right)\right) \tag{6.14}$$

$$\therefore \nabla J\left(x^*\right) + \sum_i u_i^* \nabla g_i\left(x^*\right) + \sum_j v_j^* \nabla h_j\left(x^*\right) = 0 \quad . \tag{6.15}$$

The values of x^*, (u^*, v^*) for an optimization problem, with differentiable cost and constraints as well as zero duality gap, must satisfy the following conditions:

$$\begin{aligned} \nabla J\left(x^*\right) + \sum_i u_i^* \nabla g_i\left(x^*\right) + \sum_j v_j^* \nabla h_j\left(x^*\right) &= 0 \quad , && (6.16)\\ u_i^* g_i\left(x^*\right) &= 0 \quad , && (6.17)\\ u_i^* &\geq 0 \quad , && (6.18)\\ g_i\left(x^*\right) &\leq 0 \quad , && (6.19)\\ h_j\left(x^*\right) &= 0 \quad , && (6.20) \end{aligned}$$

which are called the Karush-Kuhn-Tucker (KKT) conditions.

6.3 MPC Design for Model Scale WEC

6.3.1 Modified Equation of Motion

The equation of motion, first introduced in Sec. 3.4.5, must now include the effect of the PTO:

$$[m+\mu_{33}(\infty)]\ddot{\zeta}_3(t)+[\lambda_{33}(\infty)+\lambda_{vis}]\dot{\zeta}_3(t)+\rho g A_{wp}\zeta_3(t) \quad + \quad \int_{-\infty}^{t} K_r(t-\tau)\dot{\zeta}_3(\tau)d\tau = f_e(t)+f_{gen}(t)\ . \quad (6.21)$$

The time-invariant state-space matrices now include the input gain for f_{gen} and are rewritten here as a reminder:

$$A_{sys}=\underbrace{\begin{bmatrix} A_r & 0 & B_r \\ 0 & 0 & 1 \\ \frac{-C_r}{m+\mu_{33}(\infty)} & \frac{-\rho g A_{wp}}{m+\mu_{33}(\infty)} & \frac{-(D_r+\lambda_{33}(\infty)+\lambda_{vis})}{m+\mu_{33}(\infty)} \end{bmatrix}}_{\in\ \mathbb{R}^{(n+2)\times(n+2)}} \quad (6.22)$$

$$X_{sys}=\underbrace{\begin{bmatrix} x_{r|1} \\ \vdots \\ x_{r|n} \\ \zeta_3 \\ \dot{\zeta}_3 \end{bmatrix}}_{\in\ \mathbb{R}^{(n+2)\times 1}} \quad B=\underbrace{\begin{bmatrix} 0 \\ 0 \\ \vdots \\ \frac{1}{m+\mu_{33}(\infty)} \end{bmatrix}}_{\in\ \mathbb{R}^{(n+2)\times 1}} \quad S_w=\underbrace{\begin{bmatrix} 0 \\ 0 \\ \vdots \\ \frac{A|X_3(\sigma)|\Re(e^{i\varphi})}{m+\mu_{33}(\infty)} \end{bmatrix}}_{\in\ \mathbb{R}^{(n+2)\times 1}} \quad (6.23)$$

where A, X_3, φ, and $\Re$ are the wave amplitude, complex wave-exciting force, phase of X_3, and the real component respectively. The complex wave-exciting force is defined as $X_3=|X_3|e^{i\varphi}$. The heave equation of motion in state-space vector form, with ζ_o as the wave elevation at the floater origin, i.e. $\zeta(0,t)$, can now be written as:

$$\dot{X}_{sys}(t)=A_{sys}X_{sys}(t)+Bf_{gen}(t)+S_w\zeta_o(t)\ . \quad (6.24)$$

6.3.2 Description of Controllable Input

Previous investigations [33, 34, 35, 36] used a linearized f_{gen} with little information provided on how such a force would be generated. Though it is expected to be a combination of external springs and or dampers, in order to perform any work a variable PTO damper is the most likely candidate. Previous attempts have worked with the optimum reaction force

generated by the PTO as a convex problem can be constructed ensuring the solution, if feasible, is a global minimum. The use of non-linear solvers generally requires an iterative solution and can be susceptible to local minimums [90]. However, difficulties can arise when attempting to set the limits on the ability of the PTO to produce a desired force.

If the dominant force from the PTO unit is approximated by a linear damping coefficient [25], then f_{gen} can be modeled in the following form:

$$f_{gen}(t) = -B_g(t)\dot{\zeta}_3(t) \ . \tag{6.25}$$

In principle, from a calculated optimum generator force, $f_{gen|opt}$, and floater velocity the required PTO damping over the time step, Δt, could be estimated as follows:

$$B_{g|opt}(t) = -\frac{f_{gen|opt}(t)}{\dot{\zeta}_3(t)} \quad . \tag{6.26}$$

This may lead to problems if the velocity of the floater is significantly reduced or halted by $f_{gen|opt}$, which will require a damping value approaching infinity. Thus, implementing such a strategy experimentally would be sub-optimal as the modeled dynamics would not be easily achievable. This is a limitation when using damping as the only control input to influence the system dynamics, as the reaction force is dependent on the instantaneous floater velocity.

This work will now focus on applying non-linear model predictive control to a variable PTO damper. If the PTO unit is modeled as a permanent magnet linear generator (PMLG) the magnitude of B_g can be manipulated either by altering the magnet coil gap width or the applied electrical load or both [24, 25]. The instantaneous power, P, absorbed by the PTO unit will be calculated by:

$$P(t) = B_g(t)\dot{\zeta}_3^2(t) \ . \tag{6.27}$$

The final equation of motion can then be written as:

$$[m + \mu_{33}(\infty)]\ddot{\zeta}_3(t) + [\lambda_{33}(\infty) + \lambda_{vis} + B_g(t)]\dot{\zeta}_3(t) + \rho g A_{wp}\zeta_3(t) \quad + \quad \int_{-\infty}^{t} K_r(t-\tau)\dot{\zeta}_3(\tau)d\tau = f_e(t) \quad . \tag{6.28}$$

The state space matrices now must take into account the time-varying generator damping as follows:

$$A_{sys}(t) = \begin{bmatrix} A_r & 0 & B_r \\ 0 & 0 & 1 \\ \frac{-C_r}{m+\mu_{33}(\infty)} & \frac{-\rho g A_{wp}}{m+\mu_{33}(\infty)} & \frac{-(D_r+\lambda_{33}(\infty)+\lambda_{vis}+B_g(t))}{m+\mu_{33}(\infty)} \end{bmatrix} \tag{6.29}$$

and the heave equation of motion is now be expressed by:

$$\dot{X}_{sys}(t) = A_{sys}(t)X_{sys}(t) + S_w\zeta_o(t) \ . \tag{6.30}$$

6.3.3 NMPC Objective Function and Constraints

The NMPC strategy will determine the sequence of control inputs, $B_g(t)$, that maximizes the absorbed energy of the WEC over a given time horizon. In this implementation, the solver will attempt to maximize the absorbed energy over a finite time horizon, T_h, by calculating the optimum B_g at each time step. The first control input in the optimized series will be applied and the system dynamics will move forward one time step, Δt, and the optimization will be repeated.

A benefit of MPC is the ability to set state, input, or output constraints that may surface in the final design specifications. For this investigation no restrictions were placed on the floater's velocity; however, to prevent the floater from becoming submerged or leaving the water surface ζ_3 was constrained to +/- the initial draft. These constraints were chosen as the floater and PTO under consideration are at model scale, thus the power capacity of the PTO is not currently a concern. A ceiling was placed on the absolute value of B_g allowing the output capabilities of the PTO system to be reasonably similar to experimental results [25].

The objective function, J, will represent the energy absorbed by the PTO, which is the integration of Eqn. (6.27) over the time horizon:

$$\min_{B_g} \quad -\int_0^{T_h} B_g(t)\dot{\zeta}_3^2(t)dt \quad , \tag{6.31}$$

$$\text{s. t.} \quad -d \leq \zeta_3(t) \leq d \quad , \tag{6.32}$$

$$0 \leq B_g(t) \leq B_{g|max} \quad . \tag{6.33}$$

Traditionally, MPC is performed in the discrete rather than continuous time regime. Heun's method, the explicit trapezoidal rule, of second-order accuracy in Δt, was used for discretizing the state dynamics with a fixed time step. The explicit trapezoidal rule is computed as follows:

$$\frac{dy(t)}{dt} = f(t, y(t)), \quad y(t_0) = y_0 \quad , \tag{6.34}$$

$$\tilde{y}_{i+1} = y_i + \Delta t f(t_i, y_i) \quad , \tag{6.35}$$

$$y_{i+1} = y_i + \frac{\Delta t}{2}(f(t_i, y_i) + f(t_{i+1}, \tilde{y}_{i+1}) \quad . \tag{6.36}$$

Thus, the final discrete objective function and state constraints are as follows:

$$\min_{B_g} \quad -\sum_{\mathrm{k}=1}^{H_p} B_g(\mathrm{k})\dot{\zeta}_3^2(\mathrm{k})\Delta t \quad , \tag{6.37}$$

$$s.\ t. \quad -d \leq \zeta_3(\mathrm{k}) \leq d \quad , \tag{6.38}$$

$$0 \leq B_g(\mathrm{k}) \leq B_{g|max} \quad , \tag{6.39}$$

$$H_p = T_h/\Delta t \quad , \tag{6.40}$$

where H_p is the number of time steps taken per T_h and Eqn. (6.30) was integrated in time by Eqn. (6.36). H_p acts as the maximum number of times $B_g(t)$ may change during T_h.

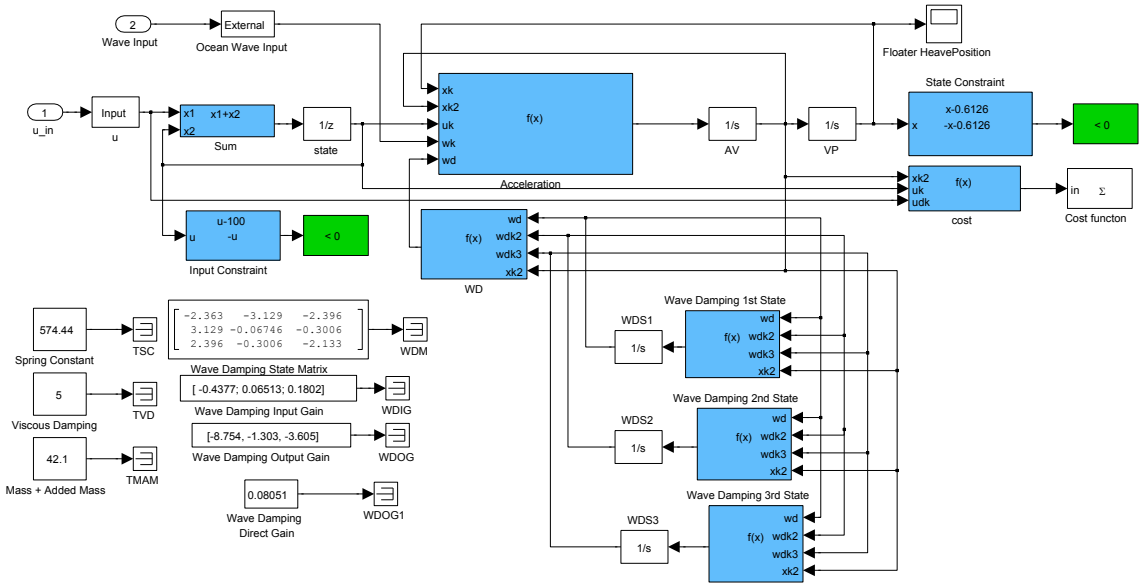

Figure 6.2: Screen Shot from Simulink using BLOM function blocks for the present problem.

Furthermore, in order to reduce highly oscillatory or a rapidly changing B_g a penalty term, Q_p, was included in the objective function so as to limit the change in generator damping per time step, ΔB_g. This penalty term provided better numerical stability and may be used to reflect losses associated with adjusting the generator configuration to achieve the desired $B_g(t)$. The final objective function can now be written as follows:

$$\min_{B_g} \quad \sum_{\mathrm{k}=1}^{H_p} [-B_g(\mathrm{k})\dot{\zeta}_3^2(\mathrm{k}) + Q_p \Delta B_g\,(\mathrm{k})^2]\Delta t \quad , \tag{6.41}$$

$$B_g(\mathrm{k}) = B_g(\mathrm{k}-1) + \Delta B_g(\mathrm{k}) \quad . \tag{6.42}$$

6.3.4 NMPC Solver

The non-linear solver used in this investigation was the Interior Point Optimizer (IPOPT) with HSL libraries [92, 93], an open source code software package for large-scale non-linear optimization. It is designed to find (local) solutions of mathematical non-linear optimization problems. In addition, the Berkeley Library for Optimization Modeling (BLOM) [94] was used for construction of the system model defined by Eqn. (6.30). The primary intended use of the BLOM library is for non-linear model predictive control (NMPC) problems. BLOM is a collection of block diagram components for the Simulink graphical modeling environment and Matlab functions to export system models to a variety of optimization solvers, in this case IPOPT. The visual block diagram representation of a system model in Simulink intuitively captures the signal flow, connectivity, and hierarchy of the problem. An example of a Simulink model utilizing BLOM is shown in Fig. 6.2.

6.4 NMPC Performance in Regular Waves

Modifications to the general design details and objective function were made to account for regular wave motion as follows:

$$H_p = \frac{T}{\Delta t} \quad , \tag{6.43}$$

$$\overline{P} = \frac{\Delta t}{T}\left[\frac{1}{2}B_g(\mathrm{k})\dot{\zeta}_3^2(\mathrm{k}) + \sum_{\mathrm{j}=1}^{H_p-1} B_g(\mathrm{k+j})\dot{\zeta}_3^2(\mathrm{k+j}) + \frac{1}{2}B_g(\mathrm{k}+H_p)\dot{\zeta}_3^2(\mathrm{k}+H_p)\right] \quad , \tag{6.44}$$

$$C_w = \frac{\overline{P}}{P_w} \quad , \tag{6.45}$$

$$P_w = \frac{1}{2}\rho g A^2 V_g \quad , \tag{6.46}$$

where T is the wave period, $\overline{P}$ the time averaged power absorbed by the PTO, C_w the capture width, and P_w the time averaged power per unit wave front. Simulations were initiated with the floater states set at $\zeta_3(0) = 0$ and $\dot{\zeta}_3(0) = 0$ and ramping A in Eqn. (3.1) to reach full elevation after 3 periods. The simulations were allowed to run until all transients died out and steady state was achieved. At this stage of the controller development the hydrodynamics were described by the impulse response function generated for the flat bottom floater, a viscous damping coefficient of equal to 5 kg/s, and a virtual mass of 42.1 kg, the later two values obtained were derived from experimental measurements.

6.4.1 Regular-Wave Results

The results collected from running the NMPC strategy in regular waves are presented in Fig. 6.3. There were significant performance differences depending on the allowable $B_{g|max}$. For the lower damping limit, $B_{g|max} = 50$ kg/s, the NMPC controller only outperformed the passive absorber in the range 0.14-0.18 while comparable at lower and higher ends of the tested periods. The most notable difference occurs at resonance where the controller under performed the passive absorber by nearly 60% when comparing the time averaged power. After doubling the damping limit, the controller outperformed the passive absorber over the entire tested range while remaining comparable near resonance. However, the increases in performance continued to decreases near the ends of the tested wave period. This effect is due to the significant drop in floater velocity evident from Fig. 6.3b. At the lower frequencies, the resultant f_{gen} is not large enough to shift the floater's velocity to be in phase with the wave-exciting force. The effect of Q_p was felt strongest at frequencies near resonance; whereas moving away from resonance a value of 10^{-7} was able to capture most of the benefits of the time-varying control.

6.4.2 Sensitivity to Δt

It was thought that gains in performance could be achieved by decreasing Δt as this was found to have a significant effect on controller performance in other investigations. The decreased time step was expected to provide better resolution in the system dynamics and

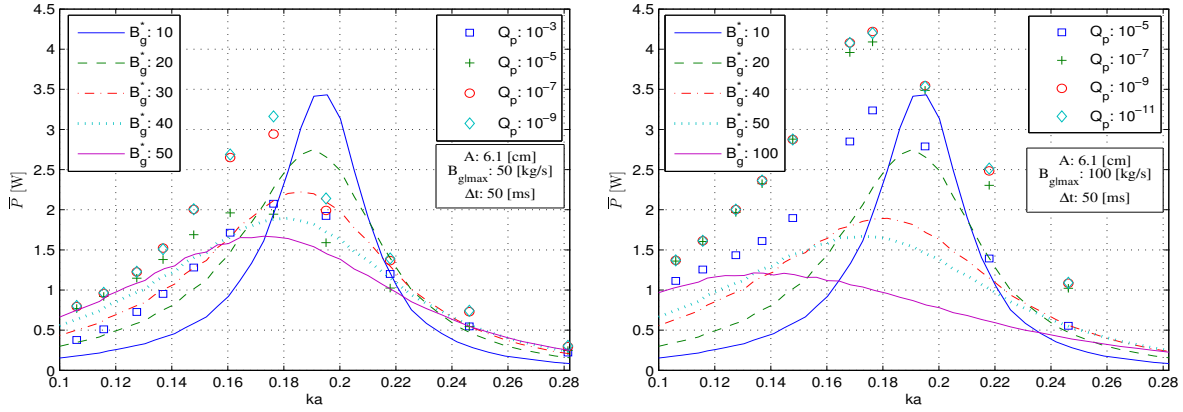

(a) Time averaged power.

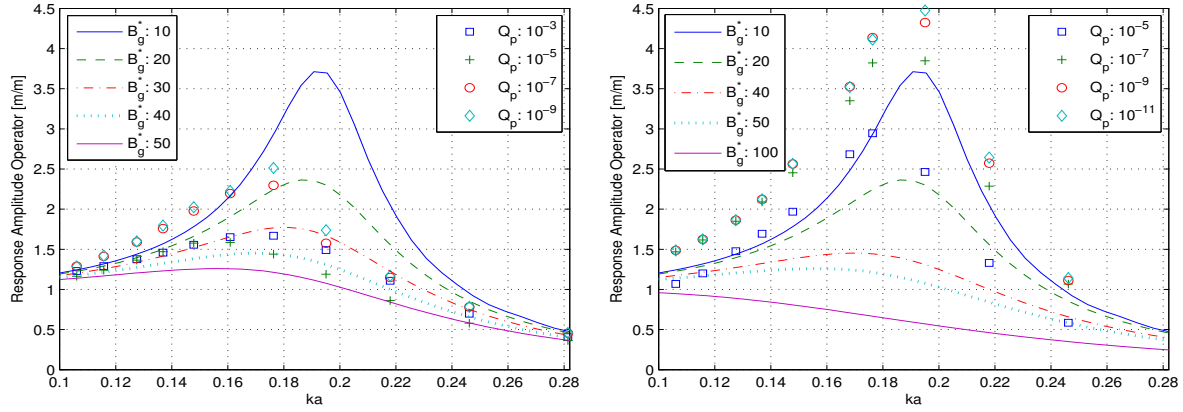

(b) Response Amplitude Operator (RAO) where $RAO_{max} = 10$.

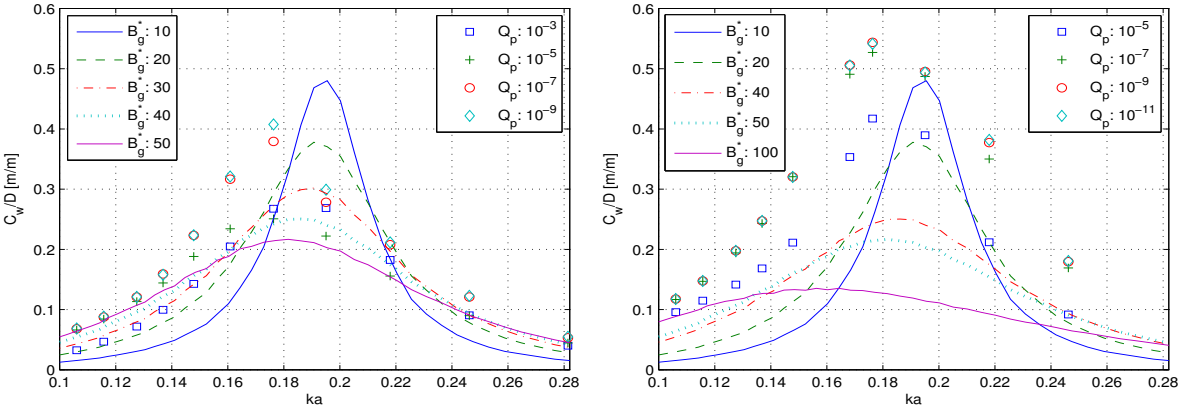

(c) Normalized capture width C_w/D.

Figure 6.3: Performance metrics vs ka. B_g^* represents linear damping coefficient used with passive absorber.

allow faster control actions to be made. However, after halving the time step only modest gains were made, Fig. 6.4. The only significant increases in performance occurred near resonance with a maximum increase of 8% at resonance; however, the controller still did not recover the theoretical maximum. When comparing the time series, the generator was deactivated slightly earlier leading to greater amplitudes of motion. From these results it was concluded the time step was not the dominant cause of the controller's poor performance, near resonance, when considering the lower damping limit.

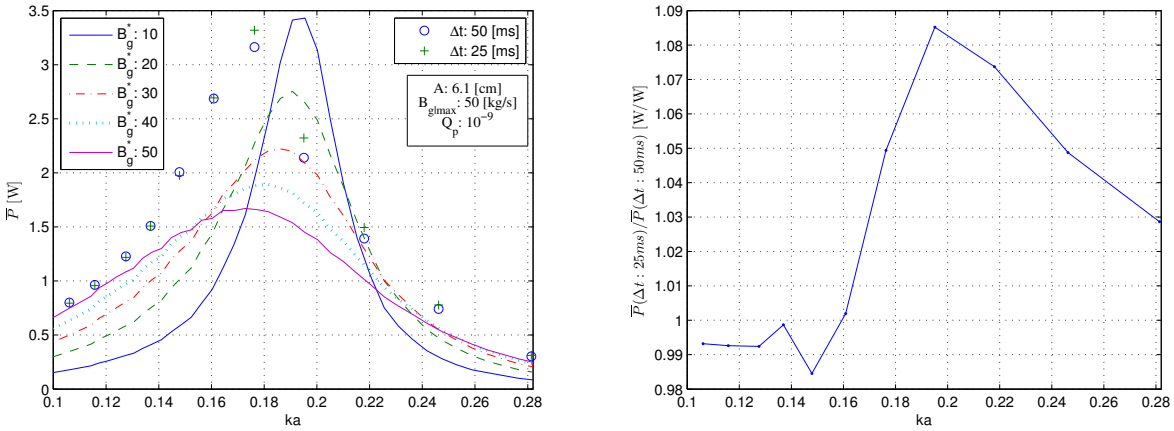

(a) Time averaged power.

(b) Ratio of time averaged power.

Figure 6.4: Performance metrics sensitivity to Δt.

6.4.3 Sensitivity to Prediction Horizon

The poor performance of the NMPC controller at the lower damping limit was unexpected especially given that it could not recapture the theoretical maximum time averaged power at resonance. It was hypothesized that the poor performance could be attributed to the transients due to the ramp up of the system dynamics. The lower limit on B_g causes the controller to have less influence on the system thereby making it more difficult to adjust or correct the floater motion. In this case, the controller needs to have a greater amount of information on the oncoming wave elevation for it to be effective. To address this concern simulations were run while increasing the prediction horizon up to two wave periods, $H_p = (2T)/\Delta t$, with results presented in Fig. 6.5. After extending the prediction horizon by 25% the time averaged power increased by 50% while increases to performance saturated at 60% starting at $H_p = 56$. Thus, it can be confirmed that in order for the controller to be effective after the ramp dynamics a longer prediction horizon is necessary. However, achieving 90% of the maximum gain in performance requires increasing the prediction horizon by only one quarter of the wave period. A final set of simulations were run with the prediction horizon set at two wave periods with results presented in Fig. 6.6. For $B_{g|max} = 50$ kg/s, this led to significant gains in performance for wave periods close to resonance with very little change

for $B_{g|max} = 100$ kg/s. These results confirms the hypothesis and it is expected that if the simulations were started with the floater dynamics already at steady state, then a prediction horizon of one period would be sufficient.

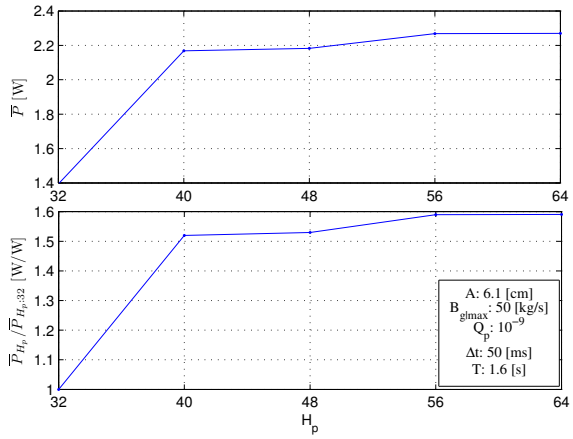

(a) Sensitivity of $\overline{P}$ to H_p.

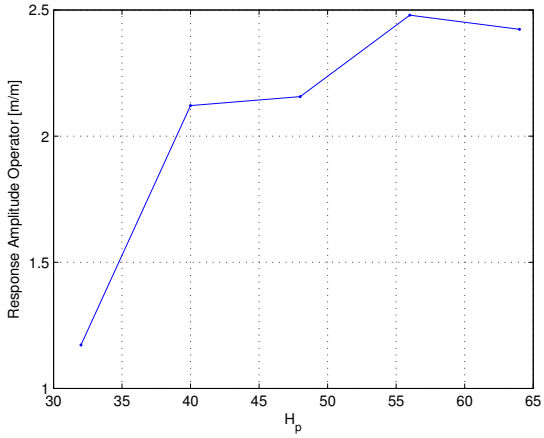

(b) Sensitivity of RAO to H_p.

Figure 6.5: Sensitivity of performance to H_p.

6.5 Time Series of Floater Motion and PTO Damping in Regular Waves

6.5.1 Effect of Q_p on Performance

The amplitude of B_g was strongly driven by the magnitude of the penalty term Q_p. The larger the penalty the less dynamic the generator became which generally led to poor performance. With the lowest penalty values, B_g would reach its imposed limit for all frequencies, except at resonance; however, the generator would be continuously switched on and off, similar to a duty cycle, see Fig. 6.7d. These results suggest that B_g need not necessarily be strongly time variant, but rather have the ability to decouple the floater from the PTO unit.

6.5.2 Comparison with Passive Systems

The performance advantage of NMPC versus a passive system is evident in the ability to ramp up/down B_g. For certain wave periods, the time-varying damping produced values of f_{gen} that were equal to or greater than the peak wave-exciting force working to shift the floater velocity in phase with the wave-exciting force, Fig. 6.8b. Though the time averaged power is higher for NMPC, the instantaneous power comes in sharper discrete pulses which may not be suitable for power transmission due to the power lull and the required increase

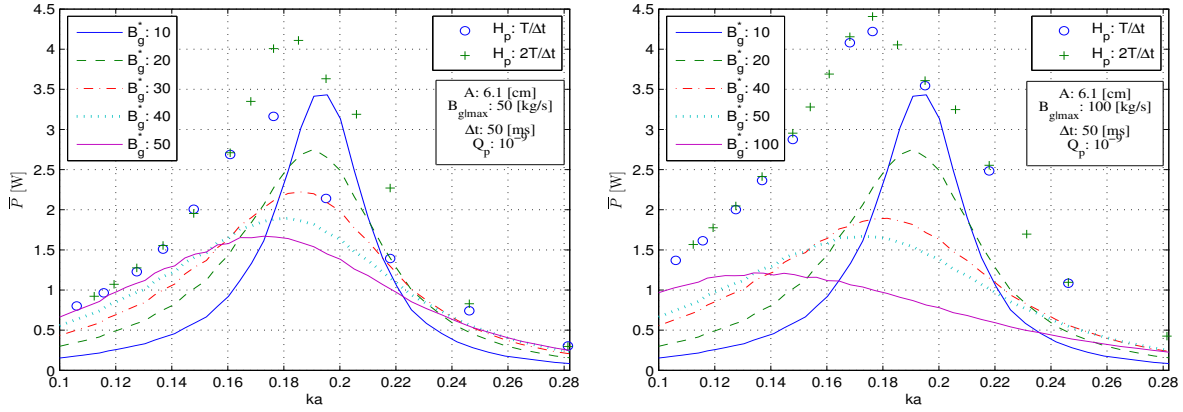

(a) Time averaged power.

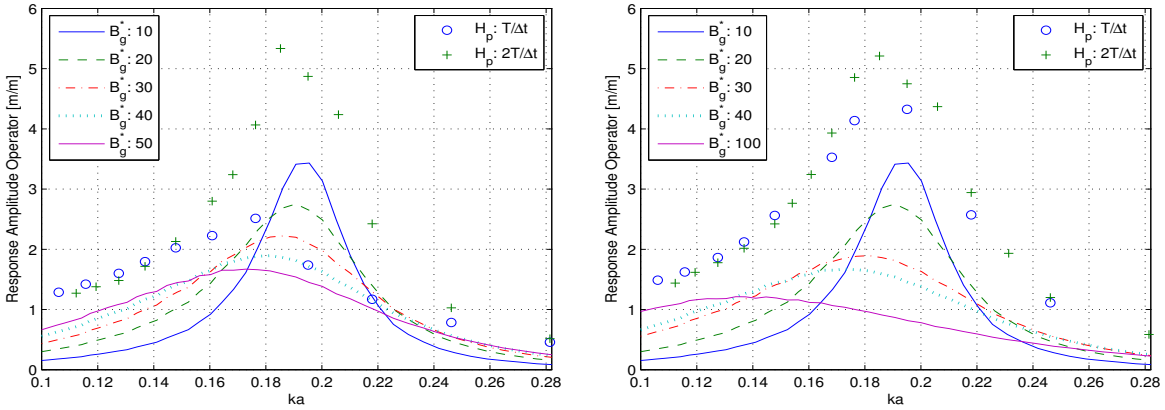

(b) Response Amplitude Operator (RAO) where $RAO_{max} = 10$.

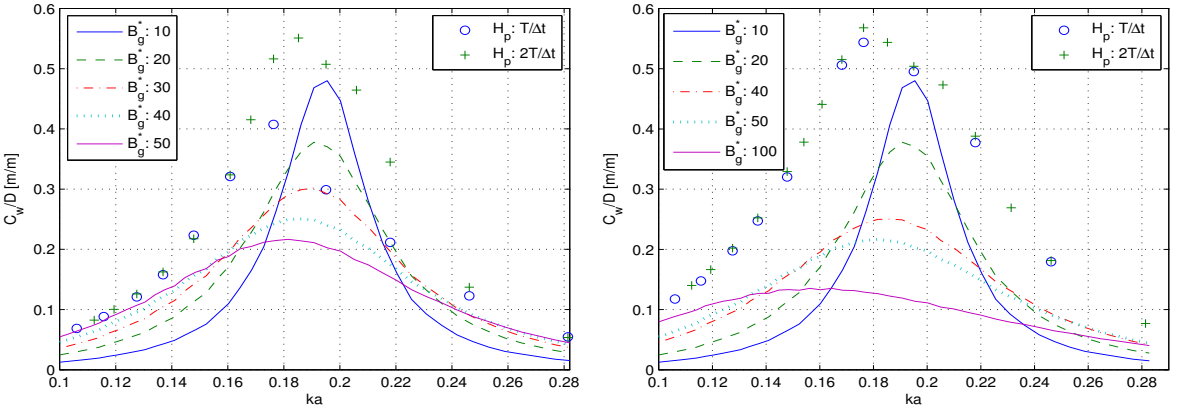

(c) Normalized capture width C_w/D.

Figure 6.6: Performance metrics sensitivity to H_p. B_g^* represents linear damping coefficient used with passive absorber.

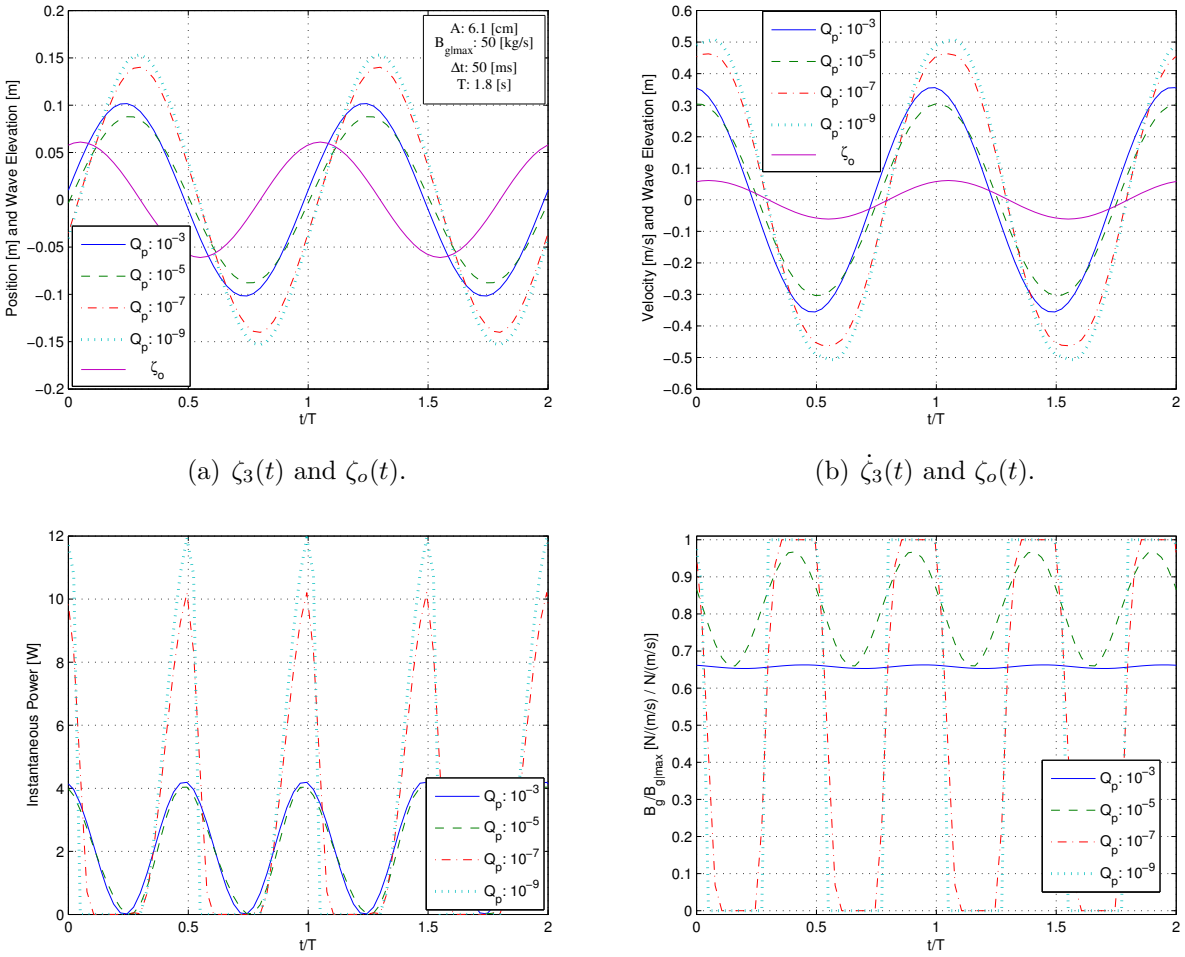

(a) $\zeta_3(t)$ and $\zeta_o(t)$.

(b) $\dot{\zeta}_3(t)$ and $\zeta_o(t)$.

(c) $P(t)$.

(d) $B_g(t)$.

Figure 6.7: Effect of Q_p of time history of floater and PTO system.

in power capacity of the transmission line. For example, at a wave period of 1.8 s, $\overline{P}$ is approximately 75% and P is 500% larger for NMPC, and the generator is active only during 39% of the wave the period, Fig. 6.9. As the wave frequency moves away from resonance the active generator duration increases to 47% and 75% of the wave period at 1.5 and 2.4 s respectively, which follows the growth in the optimum damping presented in Sec. 5.1. However, at 2.4 s the wave-exciting force is to too large to be overcome by f_{gen} due to the reduced floater motion. Therefore, the NMPC formulation in its current form allows for the greatest amount of absorbed energy, but may create issues with PTO power capacity and signal conditioning.

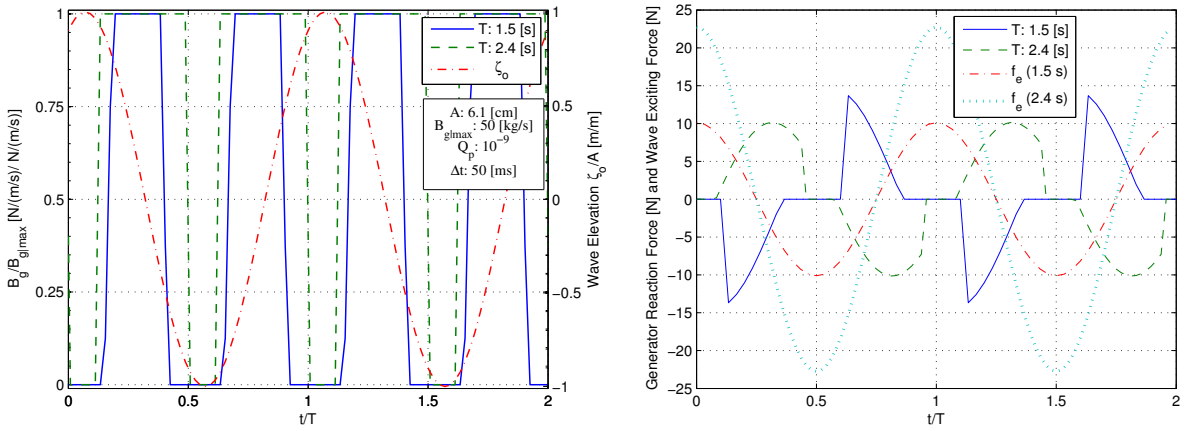

(a) $B_g(t)$ and $\zeta_o(t)$.

(b) $f_{gen}(t)$ and $f_e(t)$.

Figure 6.8: Comparison of time histories between NMPC between different wave periods.

6.5.3 Effect of λ_{vis}

The linear viscous damping coefficient was chosen based on measurements taken from logarithmic decrement and free motion tests at resonance; however, these estimates are only for a few choice cases. It is then of interest to assess how the controller will perform as λ_{vis} is varied. From Eqn. (5.22) in Sec. 5.2, the maximum power output will be reduced as the viscous damping is increased; however, it is unclear if the time-history of the PTO damping will be invariant to changes in λ_{vis}. After running the NMPC controller while increasing λ_{vis} by a factor of 2, 3, and 4 led to a reduction in time averaged power of 32.5%, 50.5%, and 61.4% respectively which is the result of lower amplitudes of motion, Fig. 6.10a. In order to accommodate for lower amplitudes of motion the duration the generator was active increased by 20%, Fig. 6.10b. However, for simulations with the highest viscous damping the PTO time series has a greater number of intermediate damping values moving away from an on/off sequencing.

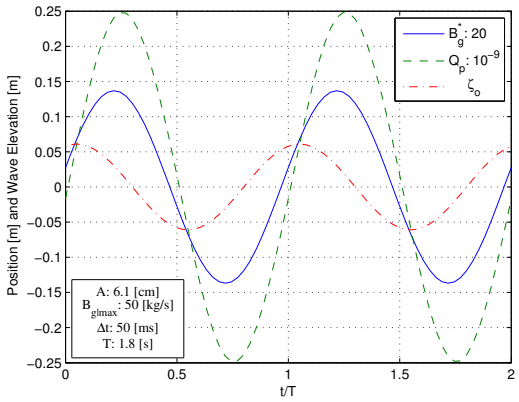

(a) $\zeta_3(t)$ and $\zeta_o(t)$.

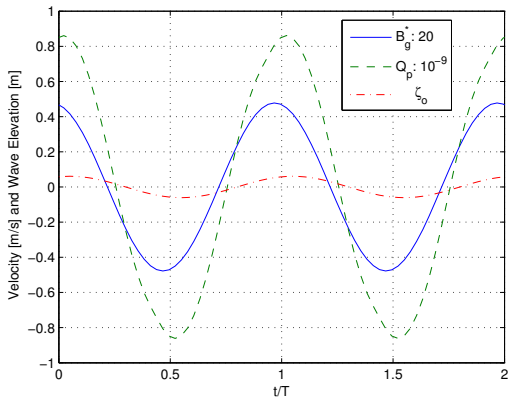

(b) $\dot{\zeta}_3(t)$ and $\zeta_o(t)$.

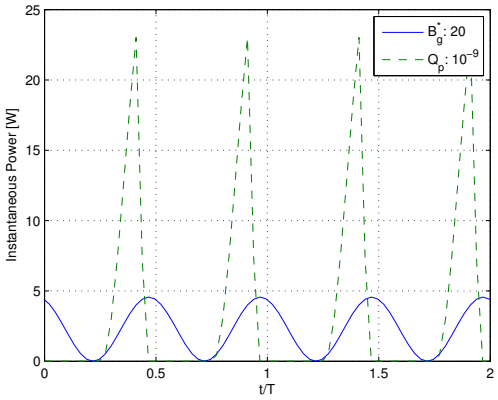

(c) $P(t)$.

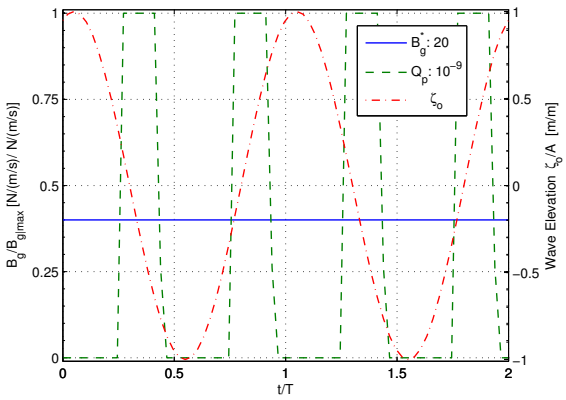

(d) $B_g(t)$ and $\zeta_o(t)$.

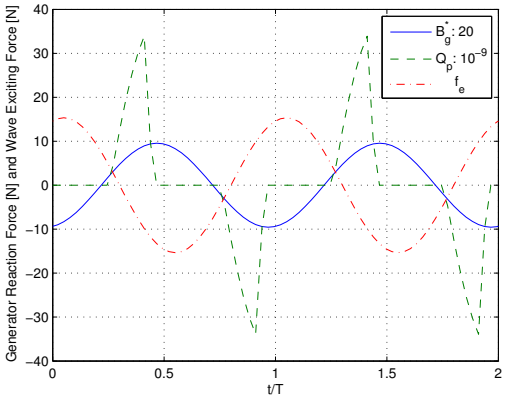

(e) $f_{gen}(t)$ and $f_e(t)$.

Figure 6.9: Comparison of time histories between NMPC and passive absorber. The value of B_g^* was chosen as it produced the greatest time averaged power at the given wave period. Results presented for NMPC are for a prediction horizon covering two wave periods.

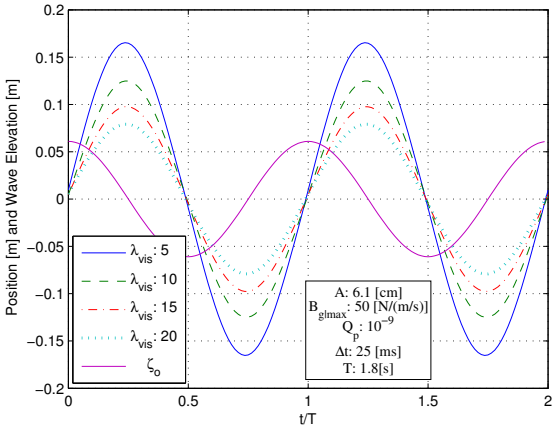

(a) $\zeta_3(t)$ and $\zeta_o(t)$.

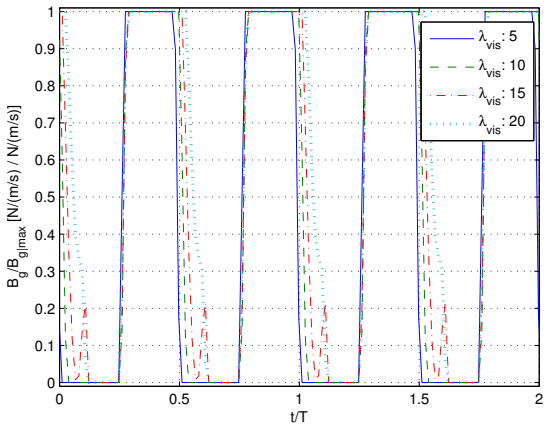

(b) $B_g(t)$.

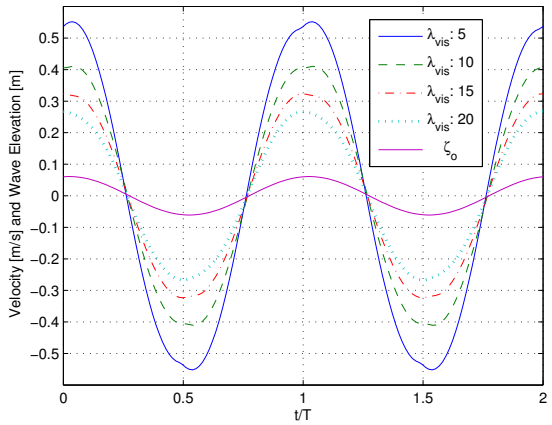

(c) $\dot{\zeta}_3(t)$.

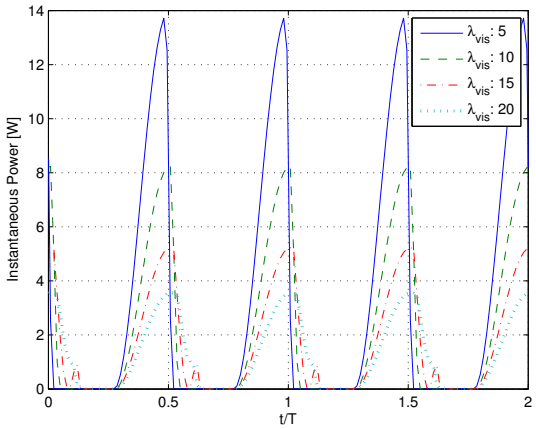

(d) $P(t)$.

Figure 6.10: Comparison of time histories with varying linear viscous damping coefficient.

6.5.4 Effect of $B_{g|max}$

The initial limit on $B_{g|max}$ is 40% greater than from the maximum measurements taken from the bench test [25]; however, it is believed that if the MCGW was reduced the limit could be reached. Similar to the previous section, it is important to understand how the controller will perform as $B_{g|max}$ is varied. The NMPC controller was run with $B_{g|max}$ set at 30, 40, 50, and 100 kg/s, which saw increases in time-averaged power of 9.3%, 15.0%, 26.4% over the lowest limit. The increase in time-averaged power is not proportional to $B_{g|max}$, as seen in Fig. 6.11c, as the magnitude of the instantaneous power increases the generator is active over a smaller time window. However, for 30-50 limit range the differences in activation vary by only 2-4 time steps which, given other uncertainties in the system modeling, can be argued that the PTO activation sequence has quasi-invariant performance. Furthermore, though the maximum time averaged power is achieved with the largest damping the required power capacity increases by 140% and increase in the lull period causes this to be a rather a poor development choice. After taking the ratio of the increase in time averaged power over the increase in the damping limit, a value of 40 kg/s appears to be optimal for experimental realization.

6.6 Irregular Sea Environmental Conditions

Performance of the model predictive control strategy was tested in irregular sea states described by an ISSC spectrum. An ISSC spectrum, a modified Pierson-Moskowitz spectrum [95], for fully developed seas was used to construct the irregular wave elevation profile.

$$S_p(\sigma) = H_{1/3}^2 T_1 \tfrac{0.11}{2\pi} \left(\tfrac{\sigma T_1}{2\pi}\right)^{-5} \exp\left[-0.44\left(\tfrac{\sigma T_1}{2\pi}\right)^{-4}\right] \quad , \tag{6.47}$$

$$T_1 = 0.7713 T_p \quad , \tag{6.48}$$

$$A(\sigma_j) = \sqrt{2 S_p(\sigma_j) \triangle\sigma} \quad , \tag{6.49}$$

$$\zeta_o(t) = \textstyle\sum_{j=1}^{N} A(\sigma_j) \sin(\sigma_j t + \varepsilon_j) \quad , \tag{6.50}$$

$$f_e(t) = \textstyle\sum_{j=1}^{N} |X_3(\sigma_j)| A(\sigma_j) \sin(\sigma_j t + \varphi_j + \varepsilon_j) \ , \tag{6.51}$$

where $H_{1/3}$, T_p, A_j, and ε are the significant wave height, peak period, wave amplitude, and random phase angle of the jth-component respectively. The random phase angles are uniformly distributed between 0 and 2π and constant with time. The range of angular frequencies used in the construction of Eqn. (6.51) was between 1.88-10.9 spaced at 0.05 rad/s. Simulations were run for 5 minutes (300 s), a Δt of 50 ms, with varying significant wave heights and peak periods. This investigation assumes full knowledge of the incoming wave train. Future wave prediction is a significant research topic and the author acknowledges such advances are necessary to take advantage of the proposed control strategies.

In the irregular sea simulations it is necessary to alter the structure of S_w as the wave

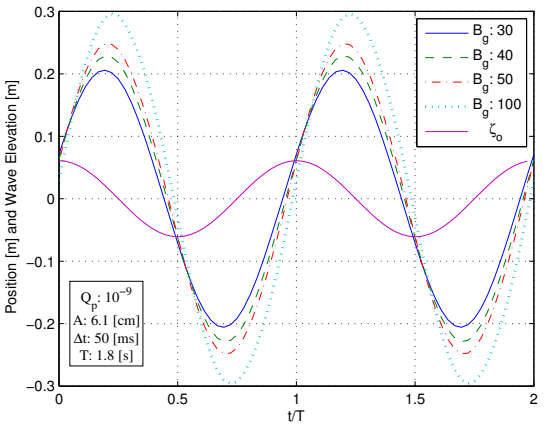

(a) $\zeta_3(t)$ and $\zeta_o(t)$.

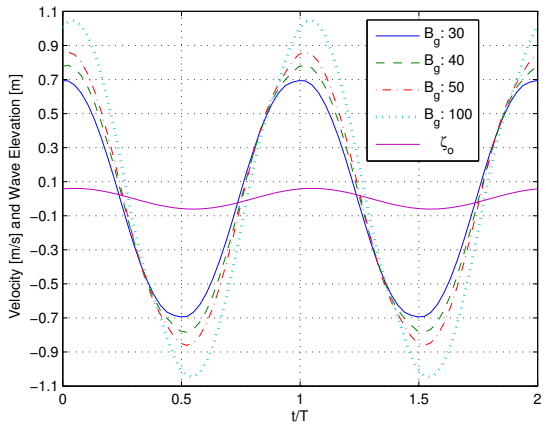

(b) $\dot{\zeta}_3(t)$ and $\zeta_o(t)$.

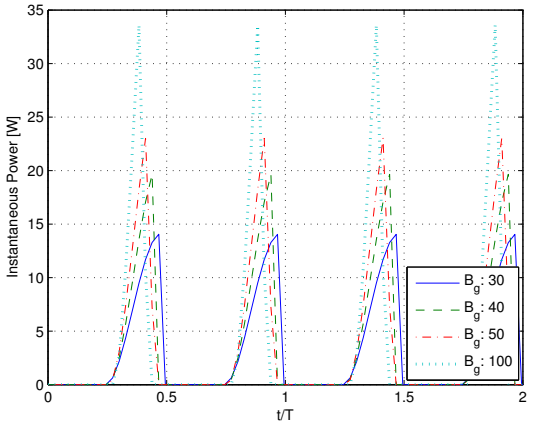

(c) $P(t)$.

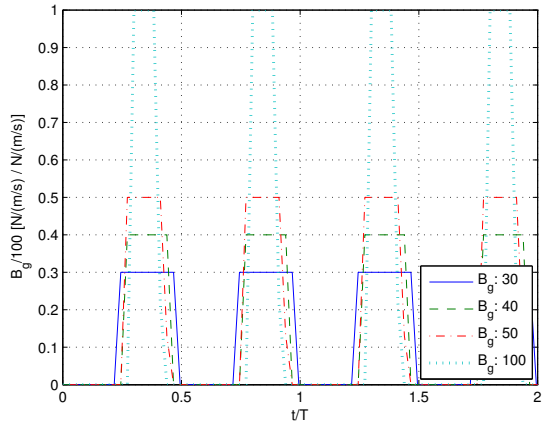

(d) $B_g(t)$.

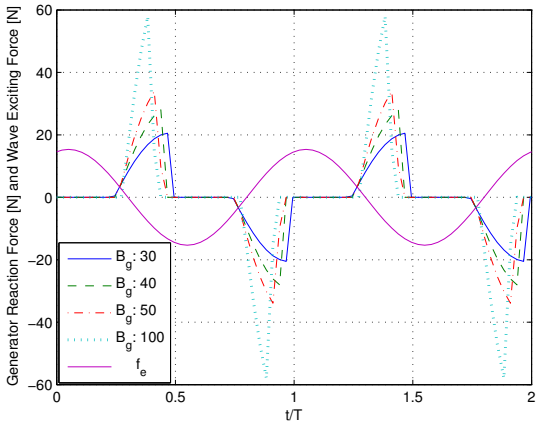

(e) $f_{gen}(t)$ and $f_e(t)$.

Figure 6.11: Comparison of time histories with varying $B_{g|max}$.

exciting force rather than wave elevation was used as the environmental input to the system:

$$S_w = [\ 0,\ 0,\ \cdots\ ,\ \frac{1}{m + \mu_{33}(\infty)}]^T \quad . \tag{6.52}$$

The metric that will be used to evaluate the performance in irregular sea states will be the cumulative absorbed energy (CAE) which is calculated as follows:

$$H_p = \frac{T_h}{\Delta t} \quad , \tag{6.53}$$

$$Ss = \frac{t}{\Delta t} \quad , \tag{6.54}$$

$$\sum E(t) = \sum_{\mathrm{k}=1}^{Ss} B_g(\mathrm{k})\dot{\zeta}_3^2(\mathrm{k})\Delta t \quad . \tag{6.55}$$

6.6.1 Irregular-Wave Results

It is important to assess the performance between the proposed NMPC strategy to a passive resonant absorber in irregular rather than regular seas as this will represent true operating conditions. Specifically, how much additional energy can be harvested to warrant the additional cost of including and designing the control system. The passive absorber results were obtained by running simulations while varying the constant-and-continuous PTO damping, B_g^*, and choosing the optimum value that produced the greatest cumulative absorbed energy per sea state.

As seen from Table 6.1, the NMPC strategy had, at minimum, a 23% increase in cumulative absorbed energy over the passive absorber for the simulated environmental conditions. For the largest $H_{1/3}$, the performance increase varied by only 5% over the set of T_p; however, when dropping the significant wave height by 25% the variation in performance was 11%. As seen in the regular wave results, at a wave period of 2.5 s and a $B_{g|max}$ of 50 kg/s, the NMPC performed just above the passive strategy so it should be expected that advantages with the time-varying control to decrease with increasing T_p. Furthermore, the average drop in performance with a reduced significant wave height is largely due to the decrease in floater velocity. These sea states have lower motion amplitudes limiting the achievable f_{gen}, thereby decreasing the effectiveness of the NMPC to force the optimum floater path.

A comparison of the time histories between the NMPC and passive absorber can be found in Fig. 6.12. The greater amplitudes of motion achieved using NMPC is consistent with the rapid on/off pattern of the PTO damping. It is interesting to see that the PTO damping continues its on-to-off sequencing with very few instances of intermediate values. This is not unexpected since the maximum damping will allow for the greatest f_{gen} to be achieved quickest, Fig. 6.12f. The time-varying damping lead to greater floater dynamics, PTO reaction forces, and instantaneous power; however, it did not lead to any phase shifts between the controller and the passive absorber. This is a consequence of using damping, rather than a conventional force, as the control input. This NMPC strategy may have a lower increase in

Table 6.1: Tabulated values correspond to the ratio of the cumulative absorbed energy (CAE) of NMPC over the passive absorber with $H_p = 34$. Last line indicates the constant-continuous generator damping that produced the greatest CAE for the passive absorber.

$H_{1/3}$: 10.16 cm	T_p: 1.7 s	T_p: 2.0 s	T_p: 2.5 s
$B_{g\|max}$: 50	1.31	1.33	1.26
$B_{g\|max}$: 100	1.71	1.77	1.69
B_g^*	20	30	70
$H_{1/3}$: 7.62 cm	T_p: 1.7 s	T_p: 2.0 s	T_p: 2.5 s
$B_{g\|max}$: 50	1.23	1.34	1.23
$B_{g\|max}$: 100	1.66	1.76	1.66
B_g^*	20	35	70

absorbed energy over other strategies, but the benefit is the on/off sequencing that is more likely to be achieved.

6.6.2 Performance Sensitivity of H_p in Irregular Waves

The performance of NMPC is strongly influenced by the amount of future knowledge on the approaching disturbances. For wave energy, a minimum amount of information on the future wave elevation is necessary to achieve improved performance over a passive absorber. The effect of H_p on the time-history can be seen in Fig. 6.13. As expected, motion amplitudes increased with the prediction horizon, which coincided with longer instances of generator inactivity. Though the PTO is generally activated at the same time, regardless of H_p, but the active duration is smaller as greater information is provided to the optimizer.

Performance statistics for three sea states with varying T_p and H_p can be found in Fig. 6.14. For most sea states, NMPC has significant performance advantages beginning at $H_p = 34$ corresponding to $T_h = 1.7$ s. The NMPC performance decreases with time horizon, even leading to cases where the absorbed cumulative energy is worse than the passive absorber; however, it should be noted that performance saturation begins to appear after $T_h = 2$ s. Heave motion as well as the time required for the optimizer to obtain a solution, T_{opt}[1], both increased with H_p. Over the tested range, the prediction horizon increased by 135%, but T_{opt} increased only by 72%. However, the computation time with the given hardware is still far from sufficient to meet the real-time requirements. Though the time

[1]The majority of the computations were completed on the first author's personal computer, a 1.90 GHz Dual-Core Processor, with 2.00 GB of RAM, running MATLAB (R2009a). The computer is 5 and 1/2 years old to date and optimization times are expected to be significantly reduced after a hardware update

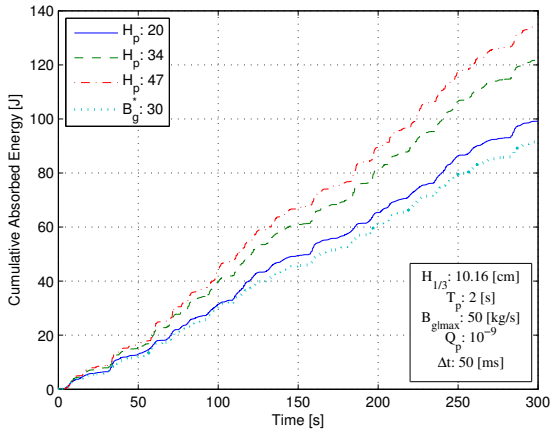

(a) $\Sigma E(t)$.

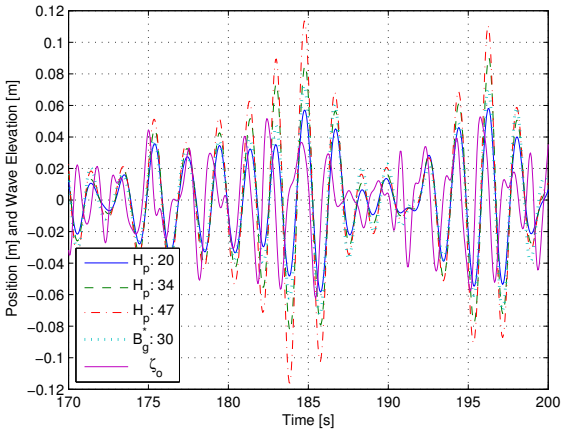

(b) $\zeta_3(t)$ and $\zeta_o(t)$.

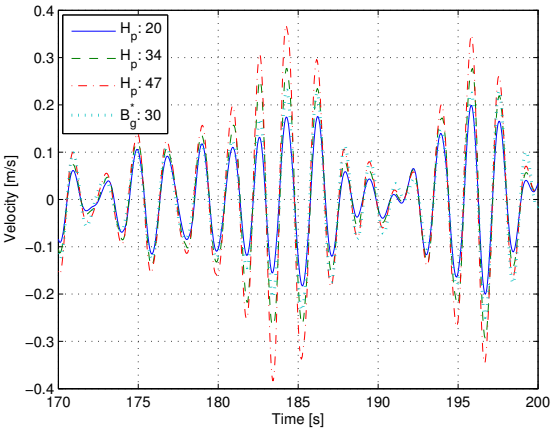

(c) $\dot{\zeta}_3(t)$.

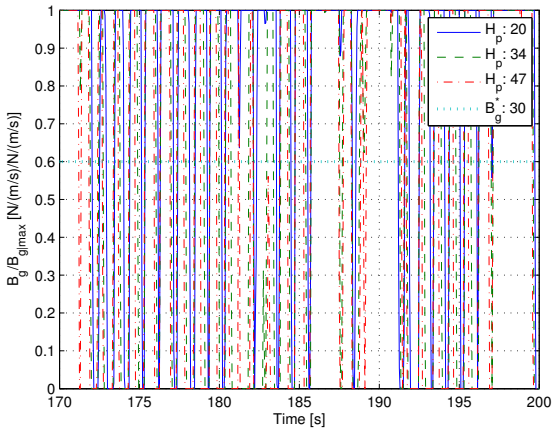

(d) $B_g(t)$.

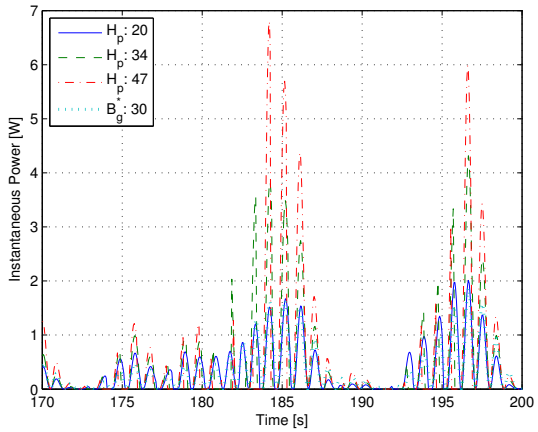

(e) $P(t)$.

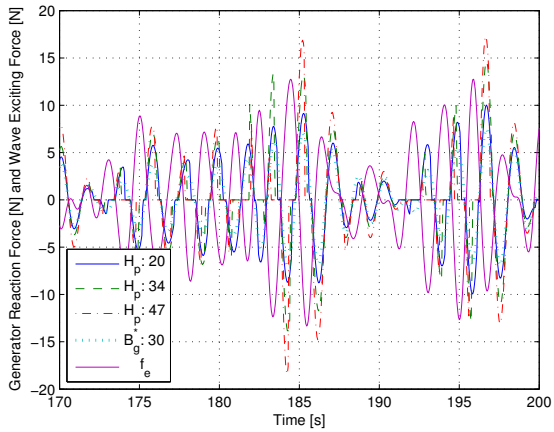

(f) $f_{gen}(t)$ and $f_e(t)$.

Figure 6.12: Comparison of random wave time series between NMPC and passive absorber.

constraint is significant at model scale, it will be relaxed with the square root of the scale factor.

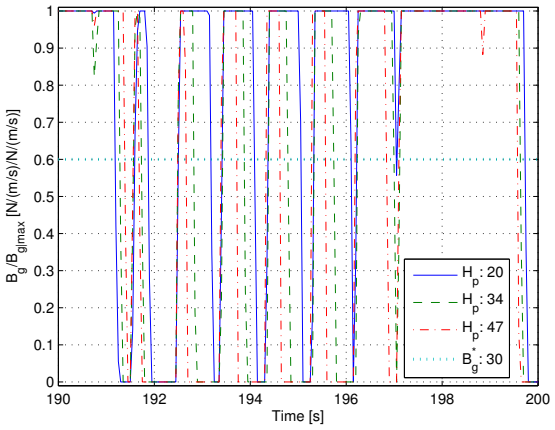

(a) $B_g(t)$.

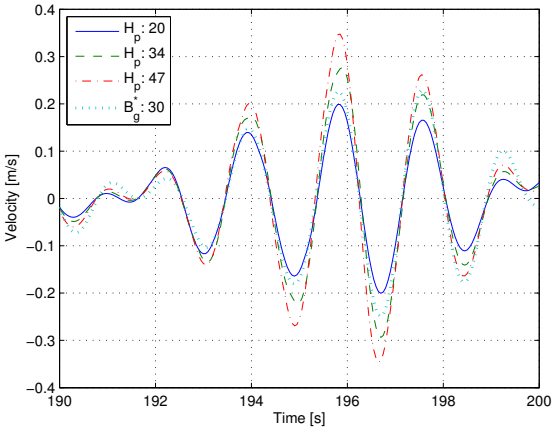

(b) $\dot{\zeta}_3(t)$.

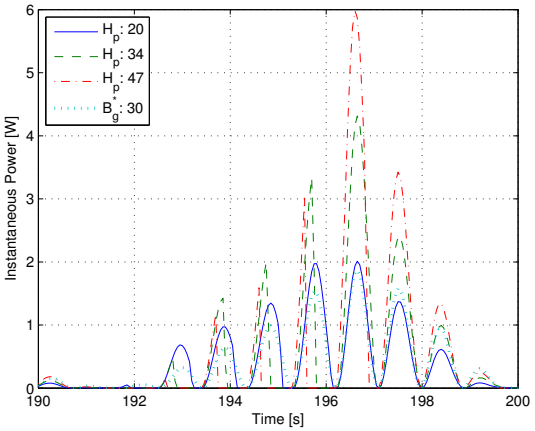

(c) $P(t)$.

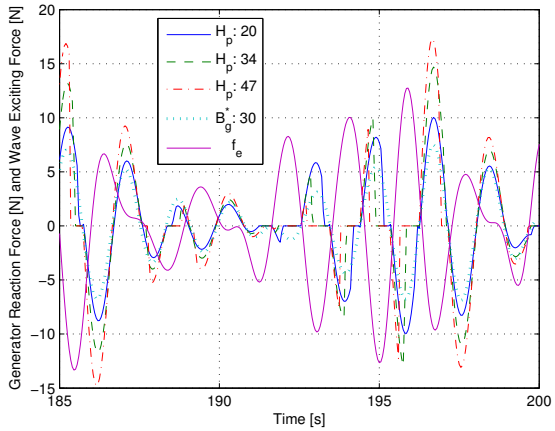

(d) $f_{gen}(t)$ and $f_e(t)$.

Figure 6.13: Comparison of random wave time series between NMPC and passive absorber with narrower time window.

6.7 Preliminary NMPC Conclusions

A nonlinear model predictive control (NMPC) strategy was successfully utilized to determine the optimum power-take-off damping for a generic point absorber of model scale. The strategy showed significant gains over a passive absorber with a relatively simple control requirement. The trapezoidal discretization appears to be sufficient in describing the system dynamics with proper time step selection. In the frequency domain, the NMPC strategy

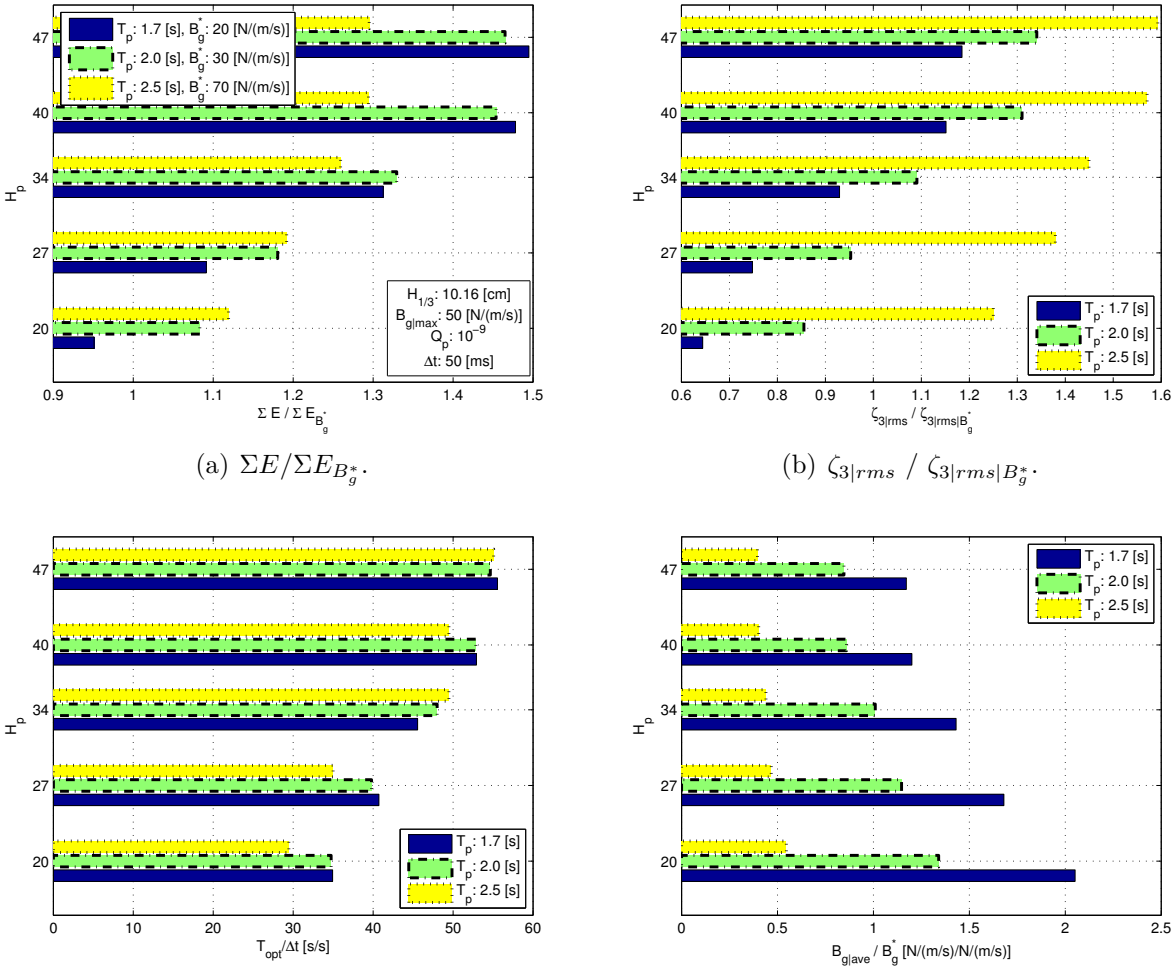

(a) $\Sigma E / \Sigma E_{B_g^*}$.

(b) $\zeta_{3|rms}$ / $\zeta_{3|rms|B_g^*}$.

(c) $T_{opt}/\Delta t$.

(d) $B_{g|ave}/B_g^*$.

Figure 6.14: Random wave statistics between NMPC and passive absorber with varying H_p. T_{opt} is defined as the average length of time the solver required to determine the optimum damping series.

performed substantially better when near the resonance frequency while comparable at higher and lower frequencies. The upper bound placed on the generator damping, B_g, led to a performance peak that is reminiscent of the resonance peak. It was found that the coupling between B_g and $\dot{\zeta}_3$ led to a damping time history that followed a strongly on/off periodic sequence. The time-averaged power was greater for NMPC, but the instantaneous power came in larger impulses and over smaller time windows.

The use of NMPC in irregular waves outperformed the passive strategy by approximately 25-50% over the simulated environments using the experimentally realizable $B_{g|max} = 50$ kg/s. The time histories of the floater's motion between the two strategies were primarily in phase, but with larger amplitudes occurring for the NMPC. The on/off activation of the PTO damping continued in irregular waves which should provide easier experimental implementation as a simple relay switch may be used to decouple the influence of the direct drive PMLG on the floater's motion.

The results presented in this section are considered to be the upper limit on the NMPC performance as the future wave train is considered to be fully known. It is recognized that a wave height prediction module [96, 97] was not used in this analysis but is a necessary component for a successful realization of the NMPC stategy and will most certainly lead to reductions in performance. The novel concept arising from this work has been the strong on/off activation of the PTO unit which requires significantly less control actuation. The following chapter will discuss how validation of the on/off control of the PTO will be pursued.

6.8 Time Varying PTO Damper and Latching Damper

The control of a variable PTO damper and active control force was also investigated in [38] using a projected gradient method and IPOPT with the following objective function:

$$\min_{B_g, f_{gen}} \int_0^{T_h} [-B_g(t)\dot{\zeta}_3^2(t) + f_{gen}(t)\dot{\zeta}_3(t)]dt \quad . \tag{6.56}$$

In Eqn. 6.56 when the first term in the integral, corresponding to a variable PTO damper, is removed the analysis falls back to the reactive control investigated by [33, 34, 35, 36]. When the second term, corresponding to the active control force, is dropped the analysis falls onto declutching investigated in [98] using the Pontryagin's Maximum Principle and [39]. However, [38] only presents results for the coupled objective function which still requires an external control force to be generated which is included in the calculation of the absorbed energy. It is in the mind of this author that focus should remain on sub-optimal control strategies that limit the flow of energy into the system. The bi-directional inefficiencies lead to additional complexities in control actuation which may increase the possibility of system failures prohibiting the device from producing power. In order to add a new component to the optimization of WEC control the investigation into an active variable PTO and latching damper, B_L, will be pursued through the use of non-linear optimization. The latching damper will provided a very large and finite value in an attempt to represent the stalling force

necessary to halt the floater motion, but will not be included for energy capture. However, unless a damping value approaching infinity is used, floater motion will not completely stall but rather dramatically slowed.

In this investigation, nonlinear model predictive control will attempt to maximize the absorbed energy over a finite time horizon by calculating the optimum B_g and B_L at each time step. The performance objective and state constraints now become:

$$\min_{B_g,B_L} \; -\int_0^{T_h} \left[B_g(t)\dot{\zeta}_3^2(t) + Q_p \Delta B_g\,(t)^2 \right] dt \tag{6.57}$$

$$\text{s. t.} \quad -d \leq \zeta_3(t) \leq d \quad , \tag{6.58}$$

$$0 \leq B_g(t) \leq B_{g|max} \quad , \tag{6.59}$$

$$0 \leq B_L(t) \leq B_{L|max} \quad , \tag{6.60}$$

with the system dynamics discretized by Eqn. 6.36 and satisfying:

$$\begin{aligned} [m+\mu_{33}(\infty)]\ddot{\zeta}_3(t) \;&+\; [\lambda_{33}(\infty)+\lambda_{vis}+B_g(t)+B_L(t)]\dot{\zeta}_3(t) + \rho g A_{wp}\zeta_3(t) \\ &+\; \int_{-\infty}^{t} K_r(t-\tau)\dot{\zeta}_3(\tau)d\tau = f_e(t) \quad . \end{aligned} \tag{6.61}$$

6.8.1 Regular-Wave Results

The results from the NMPC strategy with a variable PTO and latching damper in regular waves are presented in Fig. 6.15. For comparison the NMPC was also run with a fixed B_g^* and variable B_L to test whether the active PTO or the latching damper had a greater influence on the absorbed power. The active PTO and latching dampers were given upper limits of 50 and 5000 kg/s respectively with a penalty weight of 10^{-5}. Furthermore, the time step was reduced to 20 ms in order to obtain consistent and stable solutions from the solver while using a prediction horizon 50% greater than the wave period.

As seen from Fig. 6.15a the active PTO and latching damper achieved the greatest time averaged absorbed power over the simulated frequency range. The results from using a fixed PTO and latching damper were comparable to the single variable PTO at frequencies greater than resonance, but outperforming at the lower frequencies. The latching damper at frequencies greater than resonance act as a restrictive impulse force. This is expected to cause difficulties in physical implementation and the results from using the latching damper to converge to that of the single variable PTO damper in the high frequency regime. Near resonance, results from the variable PTO and latching damper, which will be denoted as $B_{g|L}$, are comparable with the use of only a variable PTO, B_g. However, as the wave period increases the performance drops quickly for B_g while $B_{g|L}$ has significant gains. In this regime, the latching damper plays a more significant role as it provides a greater control force to guide the motion of the floater [99]. The increase in absorbed power is accompanied by larger amplitudes of motion that may cause issues as the wave height increases or stricter motion constraints are in place.

As previously discussed in Sec. 6.3.2 most non-linear solvers use iterative methods based on an initial guess. When investigating a single control input the solutions would generally converge to the same values despite the initial guess being more dependent on the prediction horizon and penalty strength. The initial guess proved to be a greater issue when the optimizing two control variables. Since the problem is non-linear the solution is not guaranteed to be a global minimum and can be susceptible to local minimums that the solver is placed near due to the initial guess. In the end it was found that using an initial guess that was 90% of the solution at the previous time step provided the most consistent results. It must also be pointed out that due to the decreased time step required for feasible solutions the optimization time drastically increased likely due to the very large changes in acceleration when the latching damper was activated. For future investigations it is suggested that a Runga-Kutta discretization of the system dynamics be attempted as it should increase the allowable time step reducing the optimization time despite the increased number of equality constraints necessary to satisfy the equation of motion.

6.8.2 Time Series in Regular Waves

A comparison of the time histories resulting from NMPC between B_g and $B_{g|L}$ is presented in Fig. 6.16. The typical stalling of the floater motion is apparent in Fig. 6.16a and 6.16b which, though brief, is able to guide the floater velocity in phase with the wave exciting force. Since the latching mechanism is a damper it cannot completely eliminate motion leading to sub-optimal conditions with performance decreasing as the magnitude of the latching damper is decreased, which was also seen in [42, 85]. Furthermore, the non-linear transition of the floater motion can be seen in Fig. 6.16b as the velocity speeds up after the variable PTO is turned off. Furthermore, the control application still follows a strongly on/off pattern for both the variable PTO and latching dampers. An interesting result from the NMPC was the simultaneous activation of the PTO and latching damper, Fig. 6.16e, though very little energy is absorbed by the PTO the optimizer is attempting to slow the floater as much as possible in order to increase the amplitudes of motion.

6.8.3 Performance Sensitivity of T_h in Irregular Waves

The ISSC spectrum, described in Sec. 6.6, was used as the environmental input for the NMPC with variable PTO and latching damper. Due to the increase in optimization time the simulations were run for 2 minutes with a 20 ms time step and the results using varying prediction horizons can be found in Table 6.2 and Fig. 6.17. The greatest gain in CAE occurs between the time horizon of 1.4-1.7 s with diminishing gains as T_h increases. As the prediction horizon increases the activation of the variable PTO damper is reduced with the reverse for the latching damper. The variable PTO damper follows the same trend as shown in Fig. 6.14 while the activity of the latching damper is consistent with the frequency domain results. The latching damper was not active for more than a few periodic impulses until the wave period was greater than resonance. Thus as the prediction horizon increases to match the resonance period the largest gains in CAE are achieved and the latching damper

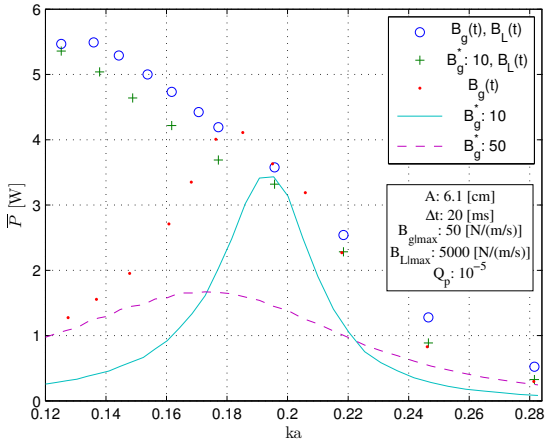

(a) $\overline{P}$.

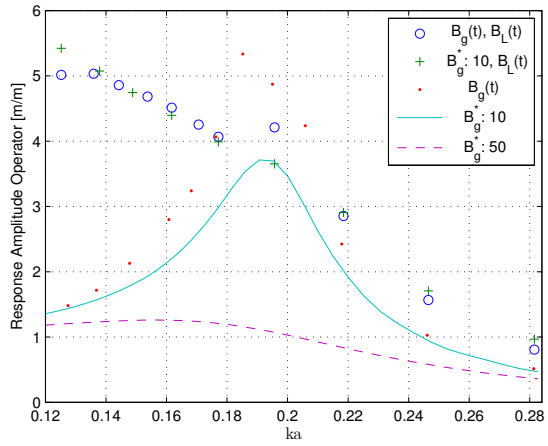

(b) RAO.

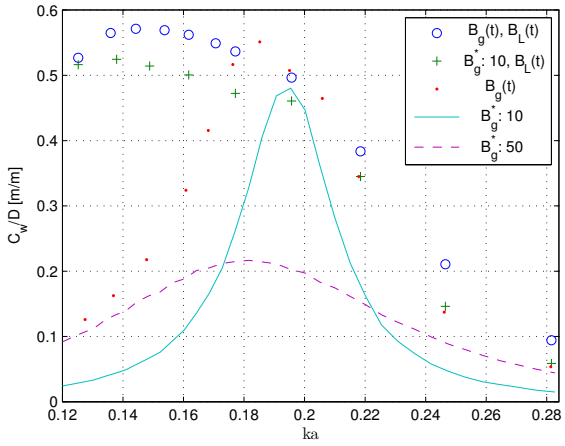

(c) C_w/D

Figure 6.15: Frequency domain performance of B_g and B_L simulations.

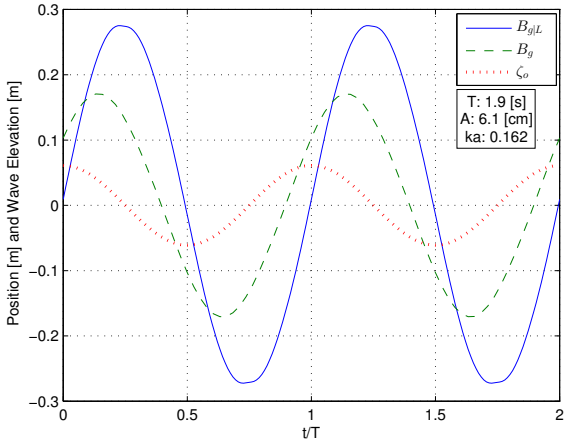

(a) $\zeta_3(t)$ and $\zeta_o(t)$.

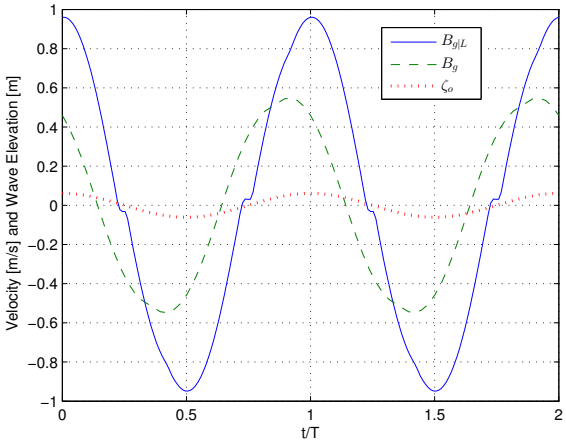

(b) $\dot{\zeta}_3(t)$ and $\zeta_o(t)$.

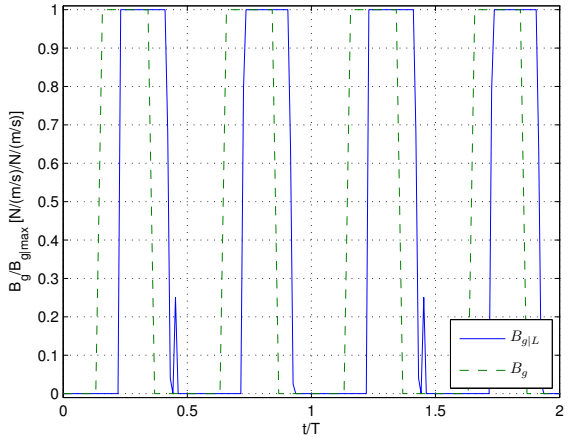

(c) $B_g(t)$

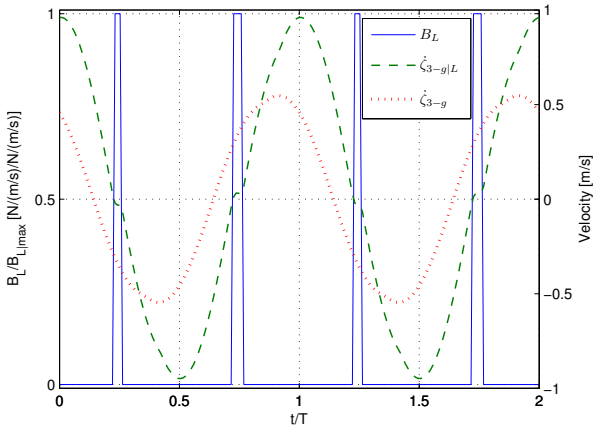

(d) $B_L(t)$ and $\dot{\zeta}_3(t)$.

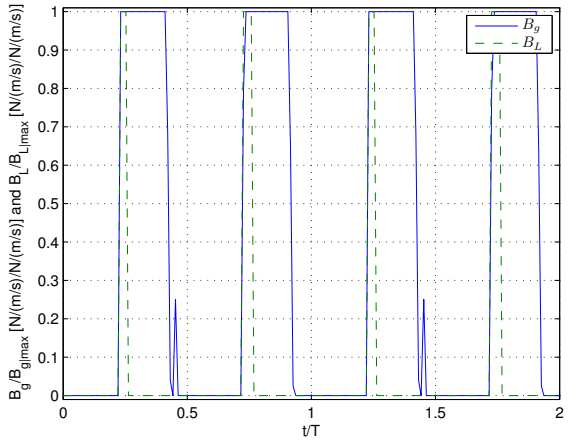

(e) $B_g(t)$ and $B_L(t)$ from $B_{g|L}$.

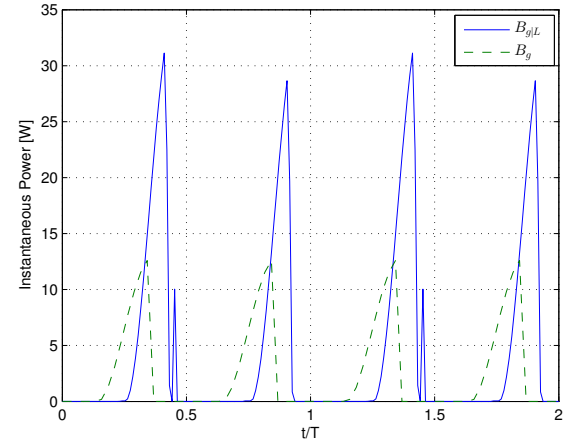

(f) $P(t)$.

Figure 6.16: Comparison of time histories between $B_{g|L}(t)$ and $B_g(t)$ simulations.

is increasingly active. Furthermore, the on/off characteristic for both control inputs remains prevalent though much stronger for the latching damper. The latching damper provides a greater control force yet the velocity time histories tend to remain in phase despite prediction horizon, Fig. 6.17c, though increased amplitudes of motion are achieved.
A comparison against the single variable PTO, $B_g(t)$, and the passive absorber, B_g^*, can be found in Fig. 6.18. The inclusion of the latching damper leads to a 30% increase in CAE, Table 6.3, when compared to the single variable PTO. Furthermore, a distinct phase shift can be found in Fig. 6.18c that is the result of the active latching damper. The additional control force is able to guide the floater velocity in phase with the wave exciting force, which the passive and single variable PTO fail to achieve.

Table 6.2: Tabulated values correspond to the ratio of the cumulative absorbed energy (CAE) of NMPC with $B_{g|L}$ over a passive absorber. Last line indicates the constant-and-continuous generator damping that produced the greatest CAE for the passive absorber.

$H_{1/3}$: 10.16 cm	T_p: 1.7 s	T_p: 2.0 s	T_p: 2.5 s
T_h: 1.0 s	1.14	1.57	2.18
T_h: 1.4 s	1.38	1.79	2.39
T_h: 1.7 s	1.73	2.08	2.65
T_h: 2.0 s	1.93	2.46	2.87
B_g^*	20	30	70

Table 6.3: Tabulated values correspond to the ratio of the cumulative absorbed energy (CAE) of NMPC with $B_{g|L}$ and B_g over a passive absorber with a T_h of 2.0 s. Last line indicates the constant-and-continuous generator damping that produced the greatest CAE for the passive absorber.

$H_{1/3}$: 10.16 cm	T_p: 1.7 s	T_p: 2.0 s	T_p: 2.5 s
$B_g(t)$	1.47	1.46	1.28
$B_{g\|L}(t)$	1.93	2.46	2.87
B_g^*	20	30	70

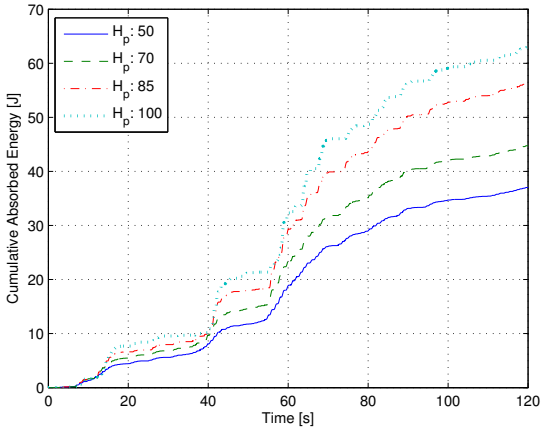

(a) $\Sigma E(t)$.

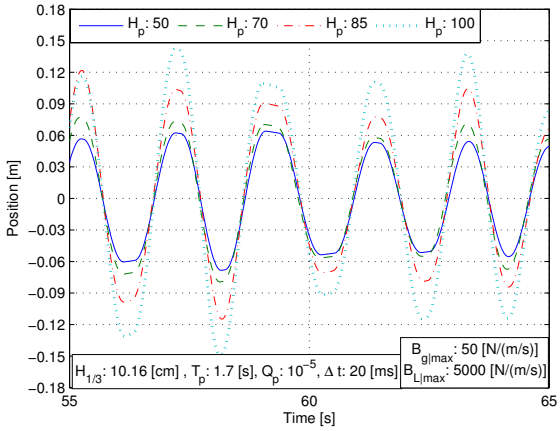

(b) $\zeta_3(t)$.

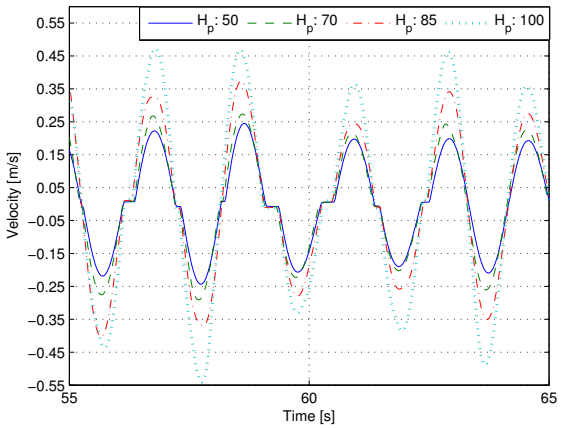

(c) $\dot{\zeta}_3(t)$.

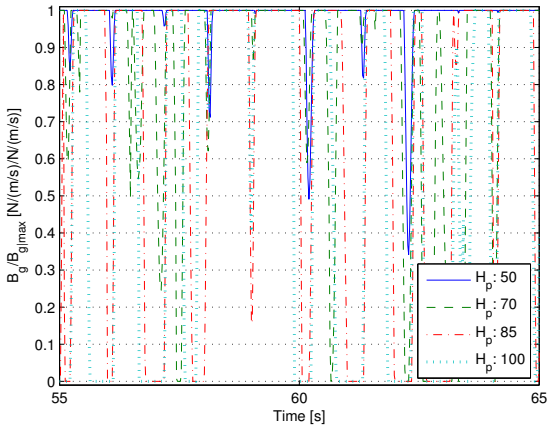

(d) $B_g(t)$.

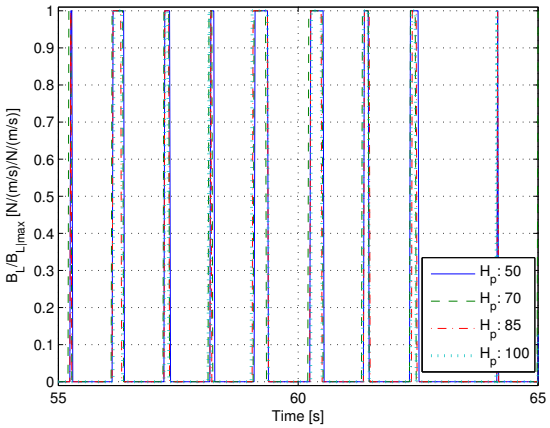

(e) $B_L(t)$.

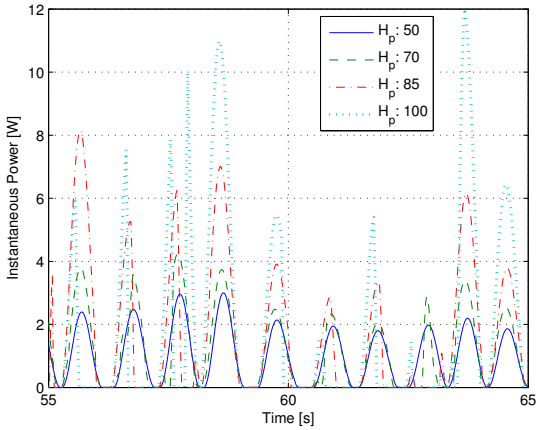

(f) $P(t)$.

Figure 6.17: Comparison of random wave time series of $B_{g|L}$ for varying T_h.

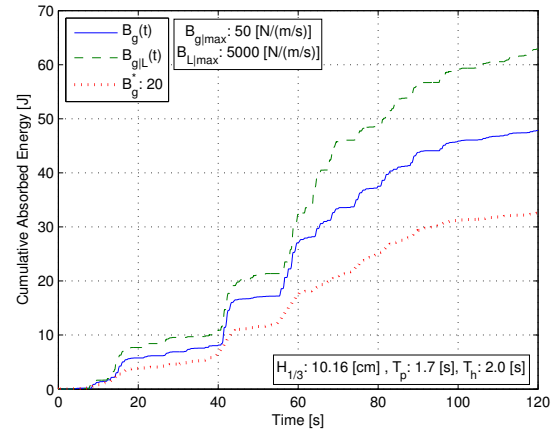

(a) $\Sigma E(t)$.

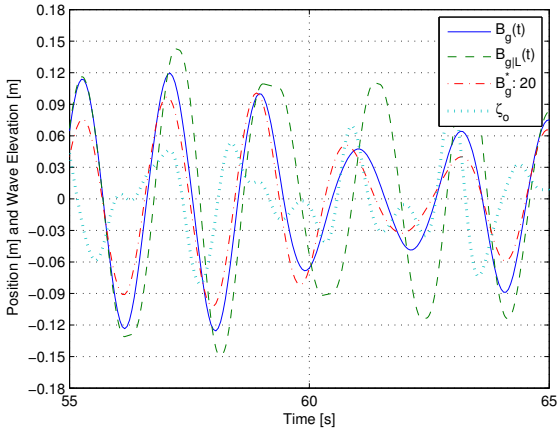

(b) $\zeta_3(t)$ and $\zeta_o(t)$.

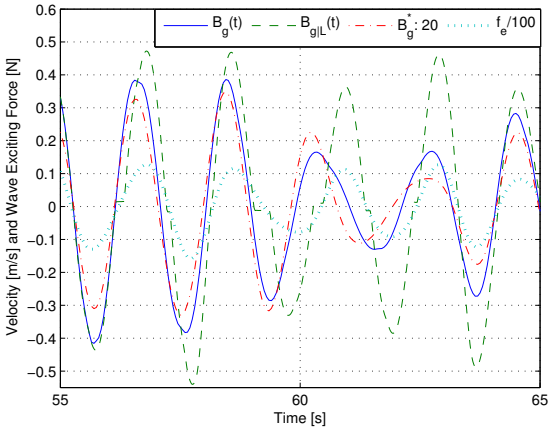

(c) $\dot{\zeta}_3(t)$.

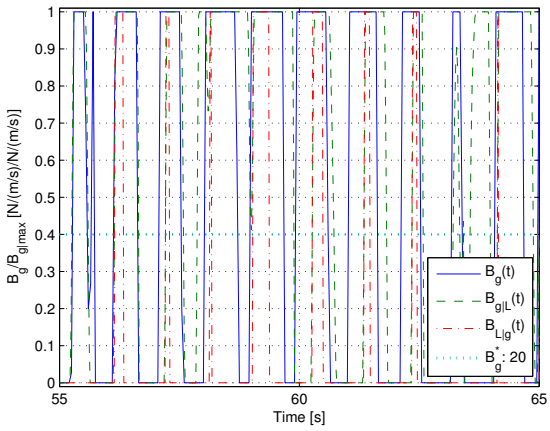

(d) $B_g(t)$.

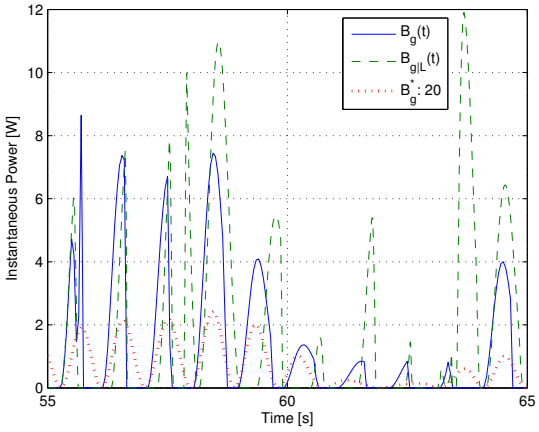

(e) $P(t)$.

Figure 6.18: Comparison of random wave time series between $B_{g|L}$, B_g, and passive absorber with a T_h of 2.0 s.

Chapter 7

Experimental Validation of WEC Control

The UC Berkeley PMLG is a strong candidate for a PTO unit to handle on/off sequencing as it is a direct drive system. The direct drive system does not require any additional gearing as the power is converted from the alternating magnetic field to a coil current. Therefore, if power generation of the PMLG is eliminated it will have a minimum effect on the floater dynamics. This can be achieved either by applying an infinite resistive load or breaking the wye circuit. However, there will still be a residual damping component because of the generation of eddy currents, hysteresis, as well as friction created by the interaction between the armature and roller bearings. For the time being, experimental validation will focus on controlling the variable PTO and leave the combination with a latching damper for future investigation.

The validation procedure will consist of a two-step process. First, a modified bench test will be repeated to validate the operation of the hardware constructed to handle activation and deactivation of the PMLG. In addition, modifications will be made to the PMLG geometry to increase the electromagnetic damping. Second, after a successful bench test has been completed, the validated hardware will be transferred to the wave tank. The wet test will be conducted to validate that use of the NMPC strategy does lead to greater absorbed power. The NMPC algorithm will not be run in real-time and will require pre-recorded wave elevation time series to be used as the environmental input. A schematic of the necessary instrumentation, signal flow, and measurement variables can be found in Fig. 7.1. The operation and interaction of the schematic components will be elaborated in the following sections.

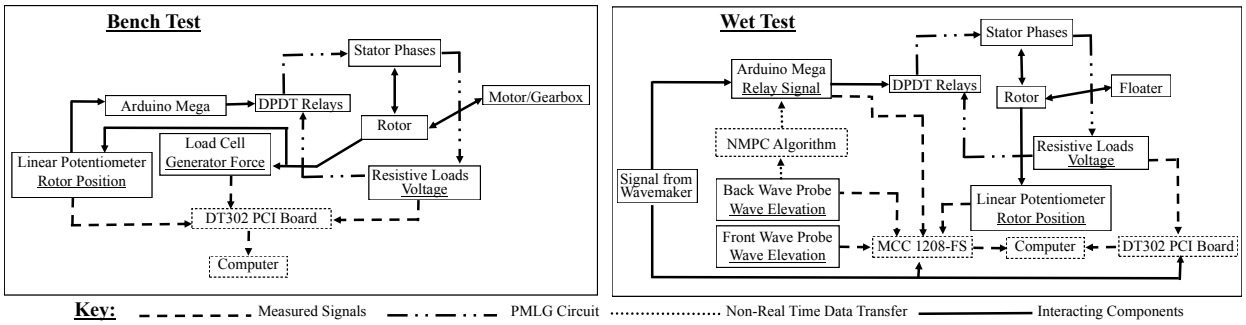

Figure 7.1: WEC control schematic for the modified bench and wet test.

7.1 Controller Hardware

Given the simplicity of the on/off controller design it was decided to use mechanical relays with a microcontroller board to disconnect the resistive loads across each of the electrical phases. The Arduino Mega 2560[1] was the chosen microcontroller as it contains 54 digital input/output pins and 16 analog inputs. In addition, a Sparkfun[2] MegaShield Kit for Arduino was ordered to act as a protective shield for the Arduino Mega as well as expand the available prototyping surface. The mechanical double pole double throw (DPDT) Telecom Relay[3] was chosen as the required activation current and voltage for each relay was 10 mA and 5 V which lie within the output range of the Arduino Mega. The Telecom relays were soldered to the Megashield with additional vertical connectors to feed in each phase. Photos of the described components can be found in Fig. 7.2.

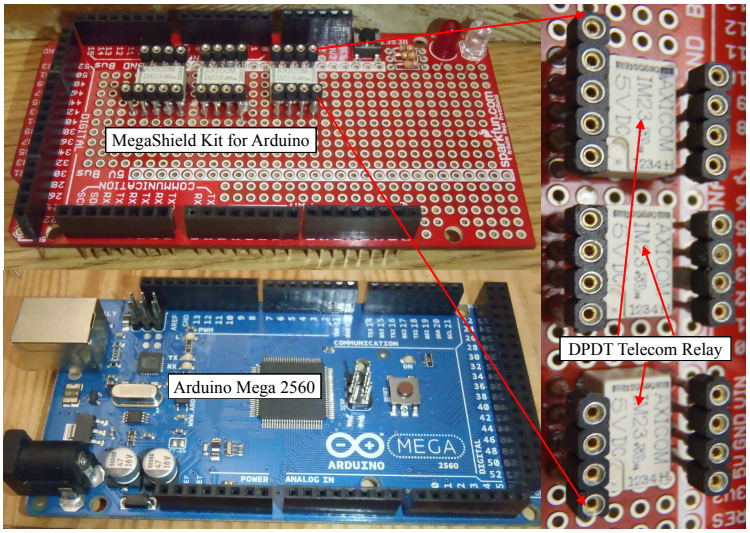

Figure 7.2: Photos of Arduino Mega 2560, Megashield Kit, and Telecom DPDT Relays.

7.2 Controller Software

The Arduino Mega comes with its own compiler allowing custom programs to be constructed. Rather than constructing the code from scratch, Matlab supports an interface package called the Arduino Support for Simulink[4]. This package allows Simulink models to be converted into the format required for upload to the Arudino Mega. This is highly desirable as a large number of Matlab functions are readily available, allowing modifications to the controller

[1]Based on the ATmega2560 chip, http://arduino.cc/en/Main/arduinoBoardMega2560
[2]https://www.sparkfun.com/products/9346
[3]http://www.digikey.com/product-detail/en/IM23GR/PB1165CT-ND/1828459
[4]http://www.mathworks.com/hardware-support/arduino-simulink.html

program to be made quickly.

7.3 Revised Instrumentation for Updated Bench Tests & Testing Procedure

The following is a list of the additional instrumentation required for on/off control of the PMLG during the bench test:

- Arduino Mega 2560,
- Megashield kit with soldered Telecom DPDT relays,
- Texas Instrument TL082 Dual BiFet OP Amp,
- Microchip TC962 High Current Charge Pump DC-to-DC Converter[5],
- Data Translation DT302 PCI board and STP300 shielded screw terminal panel .

Owing to transient electronic signals that result from the on/off sequencing of the PMLG, the MCC USB-1208FS DAQs could not be used. Therefore a Data Translation DT302 PCI data acquisition board was used with a desktop computer to gather test data. The DT302 board can handle up to 8 differential inputs or 16 single-ended inputs which monitored the armature position, force, and phase voltages. The output of the linear potentiometer was fed into the analog input of the Ardunino Mega as well as the DT302 screw terminal after passing through an op-amp wired as a voltage follower. The DC-to-DC range converter takes a regulated +5 V output from the Arduino Mega and inverts it to -5 V to provide the amplification rails necessary for the op-amp [57]. A photo of the bench-test experimental set-up is provided in Fig. 7.4 while a wiring schematic can be found in Fig. 7.5.

As each relay is double pole double throw, it can handle two phases and only 3 are required to handle the entire stator. The relays act as a switch between the end of one phase and the electronic load. Each mechanical relay will be activated by a separate 5 V DC digital signal from the Arduino Mega causing the armature to swing from closed to open, see Fig. 7.5. When all three relays are powered, the phases will be in an open circuit thereby prohibiting power generation and deactivating the PMLG, see Fig. 7.3. The individual relays are rated at 50 mW when active requiring a total of 150 mW to handle the stator. The bench-test will maintain a 0.152 m-stroke length and will be run at various frequencies and resistive loads though a smaller magnet coil gap width was set to achieve the greatest damping possible.

In order to test the performance of the PMLG with on/off sequencing during the bench test, it was decided to activate the relays for half the period of oscillation. This was achieved by programming the Arduino Mega to activate the relays for all time instances

[5]http://www.digikey.com/product-detail/en/TC962CPA/TC962CPA-ND/115289?cur=USD

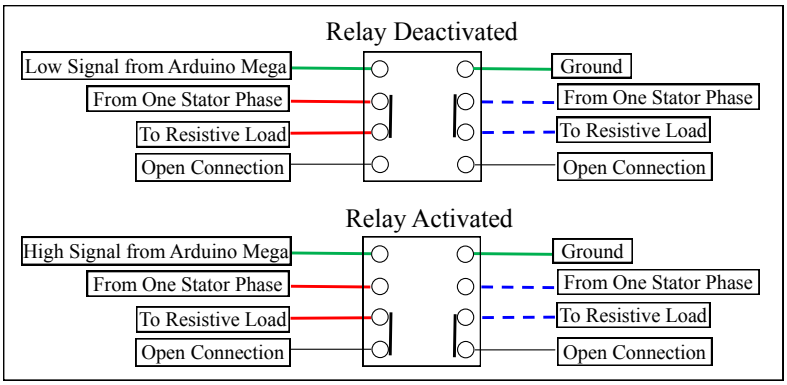

Figure 7.3: Wiring schematic of the Telecom relays.

when the position variable $\zeta_3 > 0$. By deactivating the generator in this manner, the time-averaged damping coefficient, Eqn. 4.64, for trials with and without on/off sequencing can be compared. The calculation of the generator coefficients, as described in Chapter 4.5.5, assumes the PMLG is continuously active. Therefore, if the relays work correctly, the time-averaged damping coefficient calculated during on/off sequencing should be 1/2 of the value corresponding to the continuously active PMLG.

7.3.1 Time Series from Bench Test with On/Off Sequencing

A sample of the recorded time series from the bench test can be found in Fig. 7.6, where the left column depicts a trial with on/off sequencing and the right without. It is evident from Fig. 7.6c, that the relay and Arduino Mega combination is successful at eliminating power generation for instances when the position variable $\zeta_3 > 0$. When examining the raw force signature without on/off sequencing the signal has a dominant low frequency periodic oscillation with a high-frequency component superposed as previously discussed. The force signature with the on/off sequencing still has a dominant low-frequency component, but is not symmetric. During time instances when the generator is active, the force is similar in shape and magnitude as when there is no on/off sequencing. However, when the generator is deactivated the force signature becomes highly erratic ranging from -20 to 50 N. This is indicative of the elimination of the damping contribution as the force felt is now predominantly due to inertial and cogging forces.

7.3.2 Time Series Analysis with On/Off Sequencing

In order to better illustrate the effect of the on/off sequencing, the signal analysis described in Sec. 4.5.5 was repeated with results presented in Fig. 7.7. In all plots the high-frequency components have been filtered out as they will have little effect on the floater dynamics. The low frequency component of the force signature with on/off sequencing is not symmetric about $F_g = 0$, having a smaller mean amplitude when the generator is deactivated. The contribution to $F_g(t)$, from the electromagnetic damping, can be obtained by subtracting off

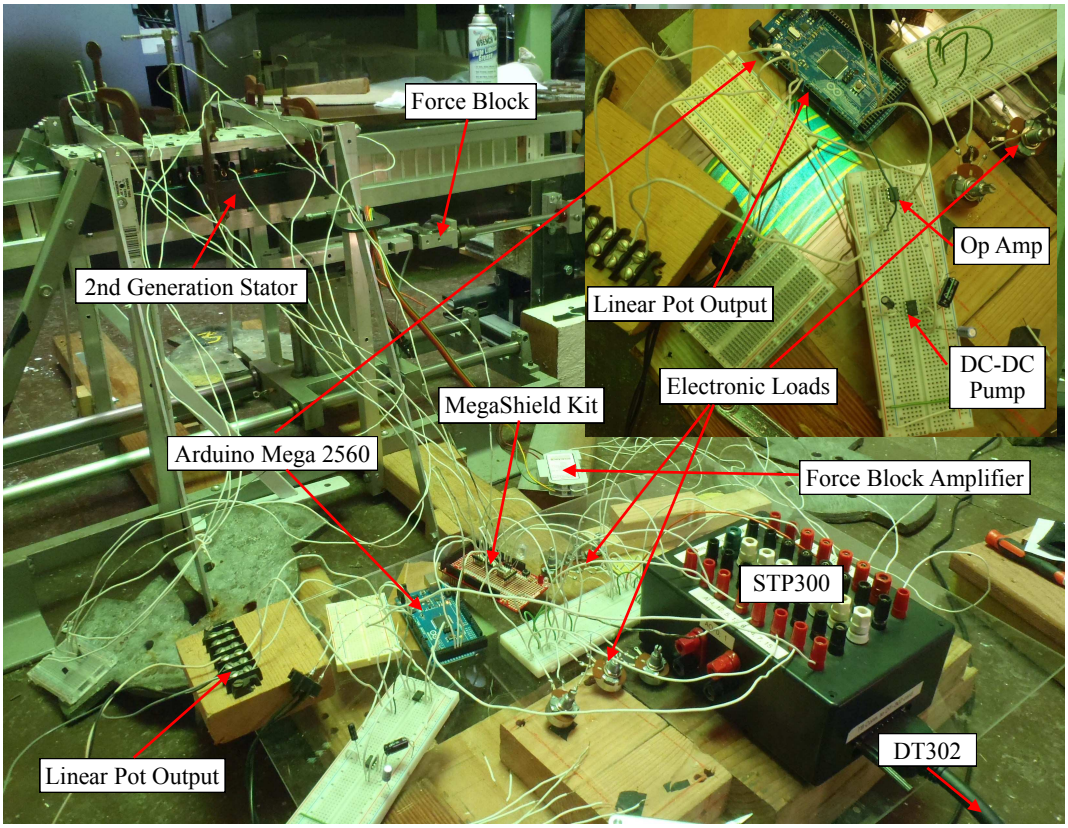

Figure 7.4: Photo of the bench test with on/off controller and supplementary electronics.

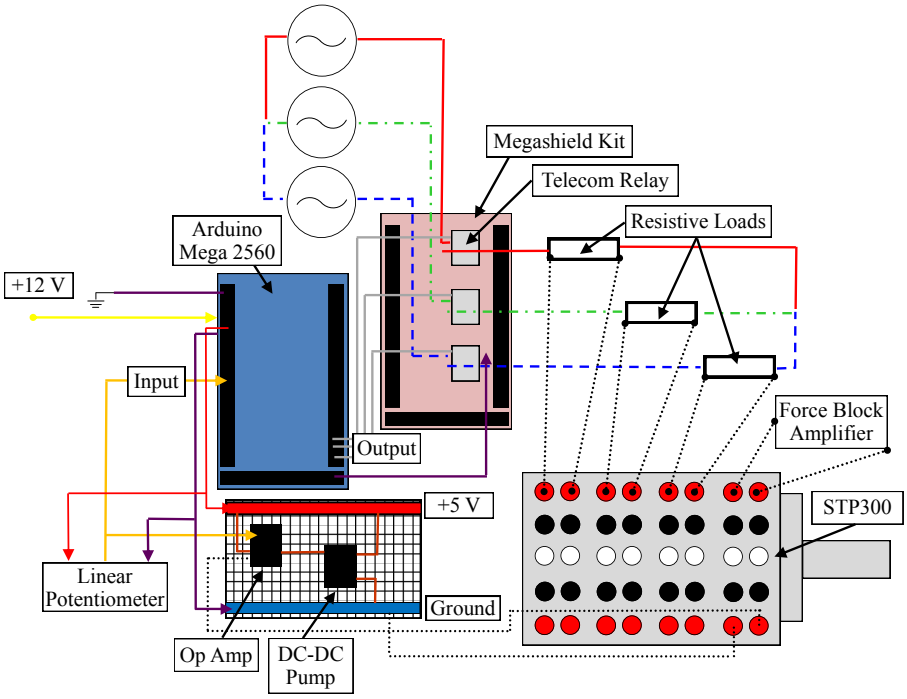

Figure 7.5: Wiring and electronics schematic for the bench test with on/off controller. Dotted black lines denote measured signals as differential input.

the inertial component from the filtered force signal, Fig. 7.7b. After removing the inertial contribution, the force signal is predominantly in phase with the velocity agreeing with the earlier claim that the damping is the only significant reaction force from the generator since the moving mass of the armature is used to ballast the floater. For the on/off sequencing trial the reconstructed force signal, *Recon* described in Chapter 4.5.5, reaches approximately half the maximum amplitude of the generator reaction force. This should be expected as calculation of the generator coefficients assumes a continuously activate PMLG. However, for the FFTF and Fourier signals the active generator has the same force magnitude when compared to the continuous run. When the generator is deactivated the force signal drops dramatically though it is not fully eliminated due to friction and electromagnetic losses in the generator material. These effects will be combined and modeled as a residual linear damping coefficient, $B_{g|\infty}$, for the open circuit condition. In Fig. 7.7b, it appears for the on/off sequencing that the reaction force ramps up before reaching its maximum amplitude; however, this is a consequence of the filtering process. At the moment the phase circuits are broken the damping due to power generation should be eliminated nearly instantaneously; however, to capture this type of behavior requires a greater number of Fourier modes. This effect can be seen in Fig. 7.7c, when the FFTF frequency limit is increased the resulting signal is closer to an instantaneous activation and deactivation, but consequently higher harmonics appear. Furthermore, the product of damping and velocity, calculated from the measured time series, was compared to the force signal after the inertial component had been removed. Without on/off sequencing there was good agreement between the two signals as

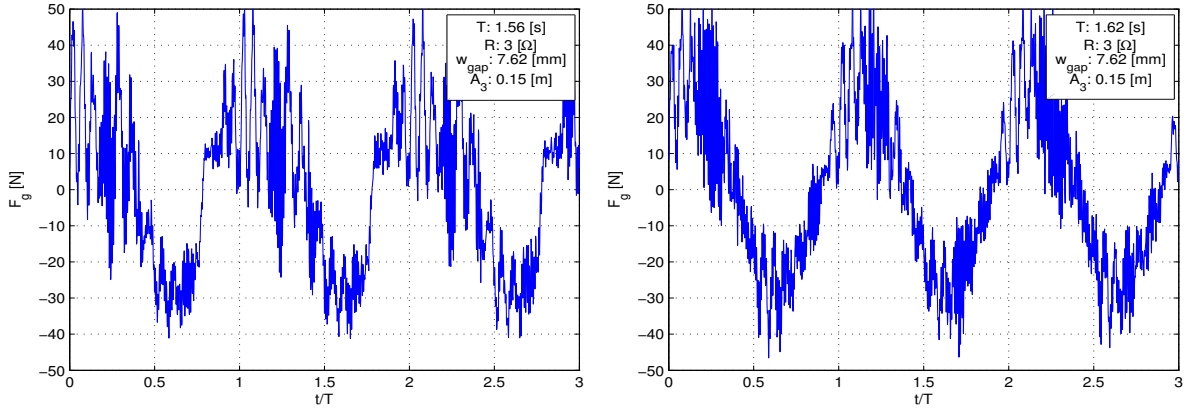

(a) $F_g(t)$.

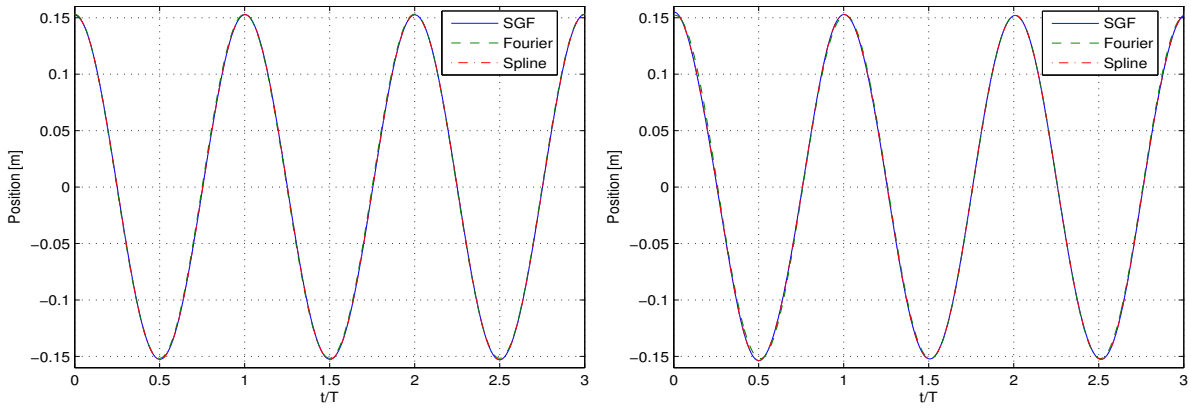

(b) $\zeta_3(t)$.

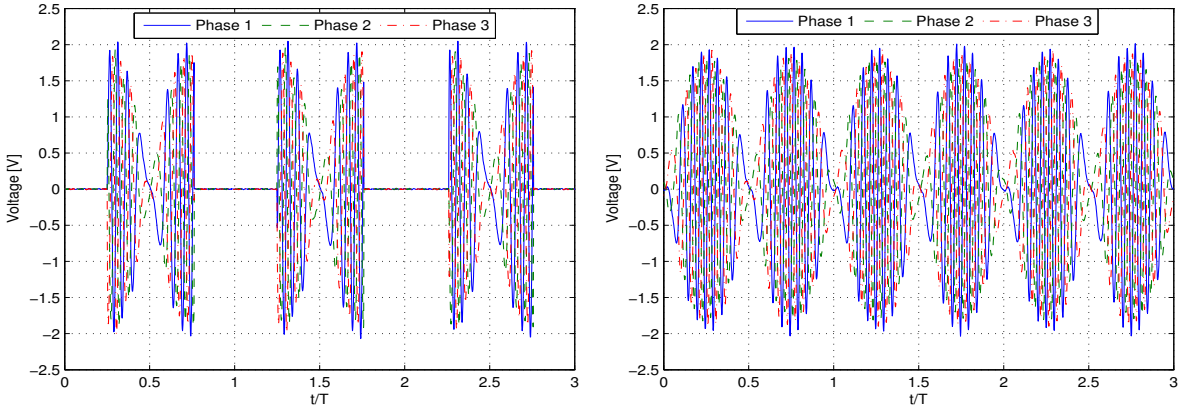

(c) $V(t)$.

Figure 7.6: Measured time histories of generator force, armature position, and stator phase voltage from the dry bench test with on/off sequencing (left) and without (right).

well as the on/off sequencing after the calculated damping coefficient was doubled and $B_{g|\infty}$ was subtracted off. The subtraction was required as only the electromagnetic damping should be doubled when the generator is active.

7.3.3 Frequency Domain Analysis

A frequency spectrum was obtained for each of the two force signals presented in Fig. 7.6 to determine if any additional harmonics were added to the system. As seen from Fig. 7.8, the dominant frequency remains at the period of oscillation for both force signals. For on/off sequencing the next highest mode appears at twice the period of oscillation which occurs due to the half period deactivation of the generator. In addition, the frequency band between 5-15 Hz has widened and strengthened as compared to the results with a continuously active generator whereas the contribution near 75 Hz has decreased roughly by a factor of 2. A discussion of the change in the high order harmonics will not be provided as they will have little effect on the floater dynamics.

Generator Force Coefficients and Power Output

The same frequency-domain generator force coefficients were calculated for cases with and without on/off sequencing. In both cases the experimentally derived values for μ_g and K_g, in Eqn. (4.63), were 9.06 kg and 7.71 N/m which remain negligible after taking into account the floater mass and spring constant. After setting $w_{gap} = 0.76$ cm the maximum electromagnetic damping was 40 kg/s at R = 2 Ω, see Fig. 7.9a. The average value of $B_{g|\infty}$ is 5 kg/s which is a minor increase over $w_{gap} = 0.89$ cm. In order to compare with data gathered from the on/off sequencing, an average damping value was calculated from the force time series assuming the generator was continuously active. The damping values, due to the power conversion process, calculated from runs without on/off sequencing were reduced by a factor of 2 and compared to the average damping values with on/off sequencing, as presented in Fig. 7.9c. The results show that the relays were prohibiting power generation and thereby significantly reducing the influence of the PMLG on the floater dynamics. Thus, the total generator damping is comprised of a possibly time-varying electromagnetic component, $B_{g|em}$, and a constant residual component, $B_{g|\infty}$:

$$B_g(R,t) = B_{g|em}(R,t) + B_{g|\infty} \quad . \tag{7.1}$$

When compared to $w_{gap} = 0.89$ cm, the MCGW has been reduced by 16%, the power output increased by 40%, and η_{el} has remained nearly constant.

7.4 PMLG On/Off Sequencing Conclusions

As discussed in Chapter 6, it is desirable to have the largest achievable damping in order for the greatest power absorption. The bench test has shown that the maximum electromagnetic

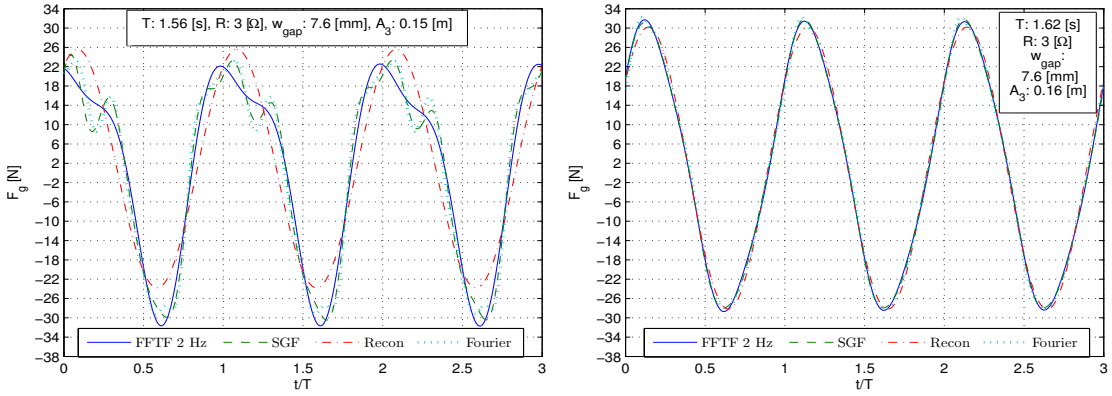

(a) Comparison between representations of $F_g(t)$.

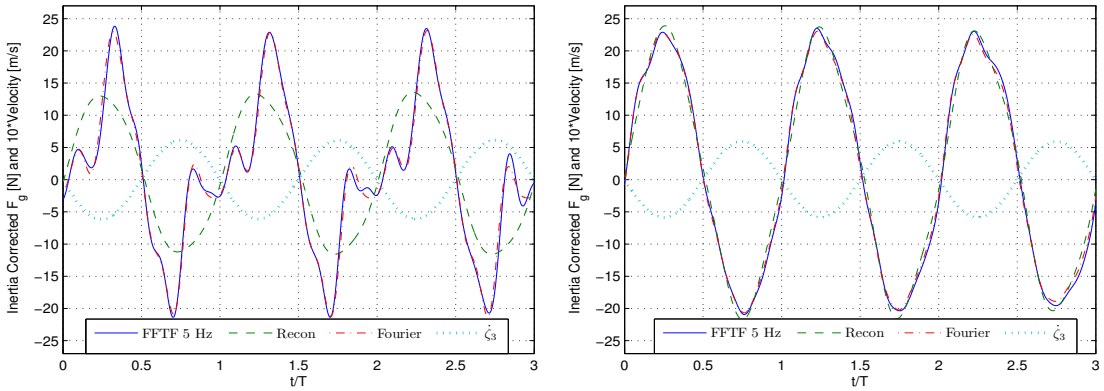

(b) $F_g(t) - m_b\ddot{\zeta}_3(t)$.

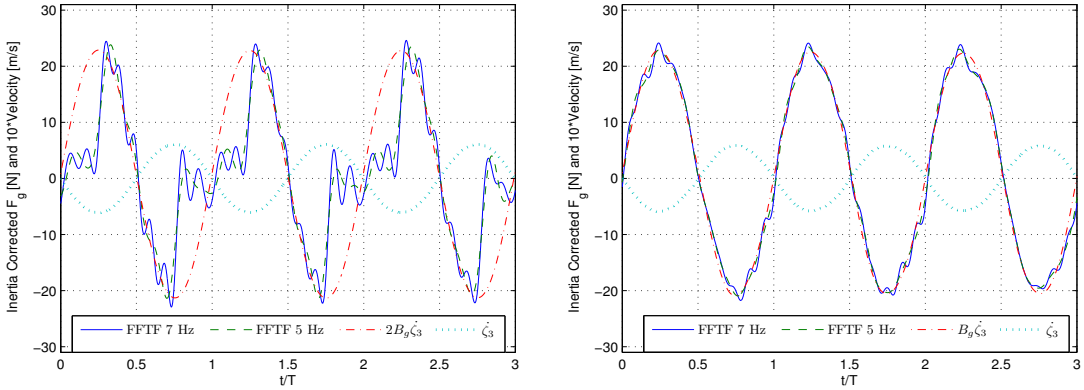

(c) Comparison between $2B_g\dot{\zeta}_3$, for left figure, $B_g\dot{\zeta}_3$, for right figure, and $F_g(t) - m_b\ddot{\zeta}_3(t)$.

Figure 7.7: Post processed time histories of F_g from the bench-test with on/off sequencing (left) and without (right). The relays were activated when the armature reached its maximum velocity and deactivated at the minimum velocity.

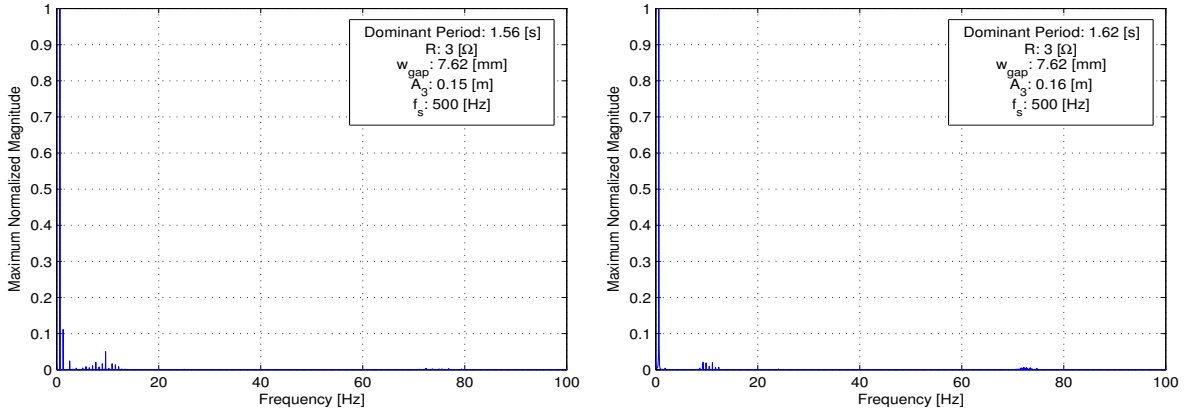

(a) FFT of F_g.

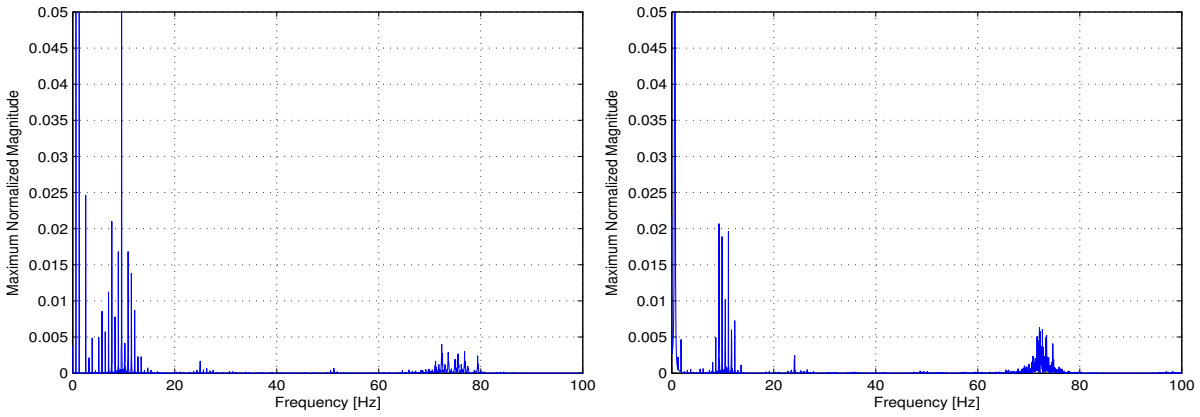

(b) FFT of F_g with zoom on higher order modes.

Figure 7.8: Comparison of the FFT spectrums obtained for F_g with on/off sequencing (left) and without (right).

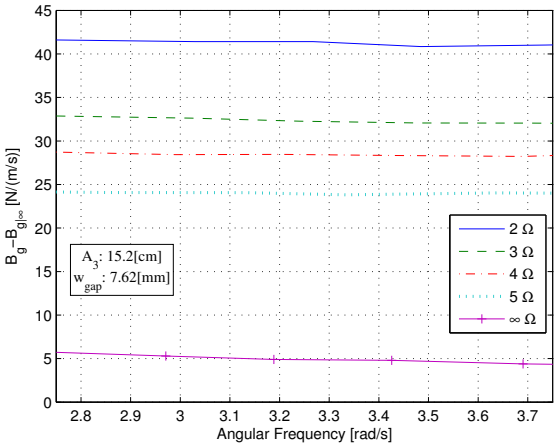

(a) B_g as a function of σ without on/off sequencing. $B_{g|\infty}$, has been subtracted off leaving only the EM contribution.

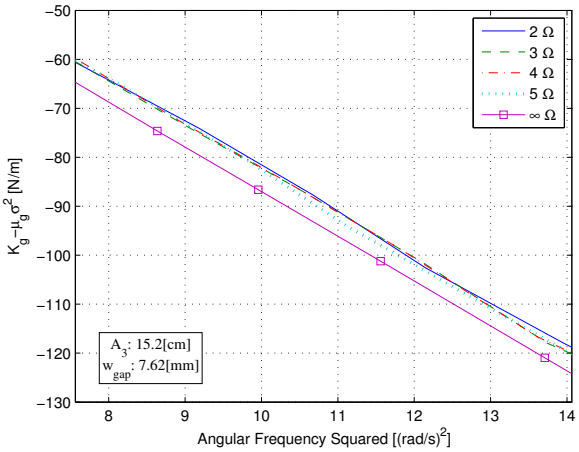

(b) $K_g - \mu_g \sigma^2$ as a function of σ^2.

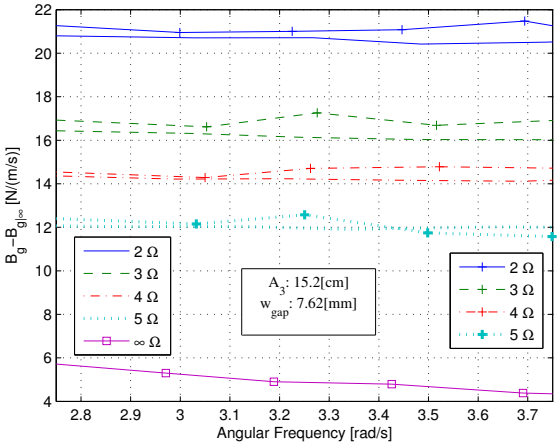

(c) B_g as a function of σ. The damping values presented in Fig. 7.9a have been reduced by a factor of 2 (left legend) for comparison with results from on/off sequencing.

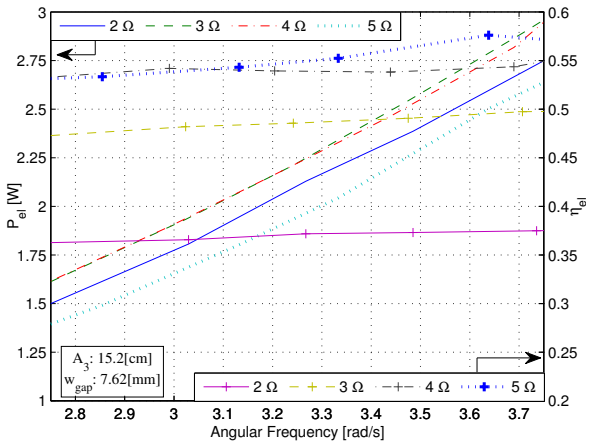

(d) P_{el} and η_{el} as a function of σ.

Figure 7.9: Generator coefficients and power output as a function of frequency and R with smallest achievable magnet coil gap width.

damping values are approximately 40 and 30 kg/s for $R = 2$ and 3 Ω respectively with a 7% difference in time-averaged electrical power output. For experimental validation the NMPC controller will be run for both cases given the benefits of the larger damping is felt when one moves away from resonance. In addition, the damping from the generator cannot be completely eliminated due to friction and eddy current generation. Thus, an additional constant linear damping coefficient representing $B_{g|\infty}$ will be included in the system dynamics.

7.5 Measurement of Wave Elevation Time Series

In order to have the most accurate environmental input for the NMPC algorithm, the full wave elevation time series, including ramp up, was recorded by running regular and irregular waves at the Richmond Field Station as shown in Fig. 7.10. The distance separating the wave probes was used to calculate T_{shift}, the time a plane progressive wave takes to travel between two points:

$$T_{shift} = \frac{L_s}{V_p} \quad , \tag{7.2}$$

where L_s is the separation distance. Once T_{shift} has been calculated the recorded elevation from the front wave probe can be time shifted to compare with the back wave probe, examples are provided in Fig. 7.11. Measurements show that the time shift calculated by Eqn. (7.2) pushes the front wave probe in phase with the back; however, during the ramp up of the wave elevation the amplitude is lower for the back wave probe. This is likely caused by viscous effects from walls, which will be more detrimental for smaller wave amplitudes as they have lower propagating energy [57]. Despite the differences in the transient wave dynamics the two signals are almost identical after steady state has been reached. The floater will be placed at the same location as the back wave probe and the recorded wave elevation time history will be used as the environmental disturbance in the NMPC. It should be noted that the NMPC algorithm was not run in real-time and model tests were completed to validate greater power absorption was achieved.

7.6 Wet-Test of PMLG Control

7.6.1 Updated Experimental Set-Up

The majority of the hardware set-up for controlling the PMLG, under wave excitation, was the same as that described in Sec. 5.3.1. The major difference being that the phase wires now pass through the relays before connecting to the remainder of the wye circuit. In addition, the DT302 PCI data acquisition board replaced *one* of the MCC 1208-FS modules so as to handle the measurement issues associated with the on/off sequencing. The two data

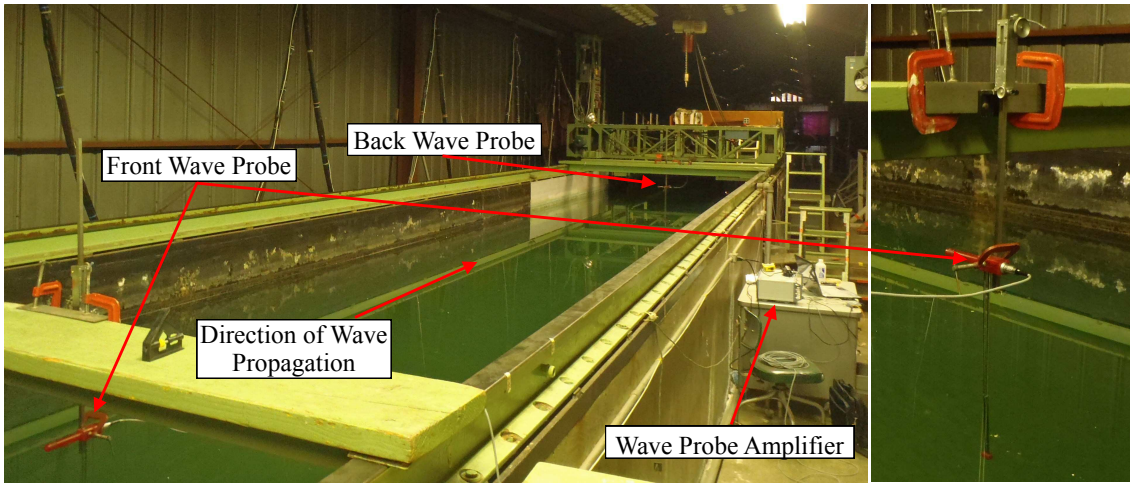

Figure 7.10: Wave probe placement for measurement of surface elevation time series.

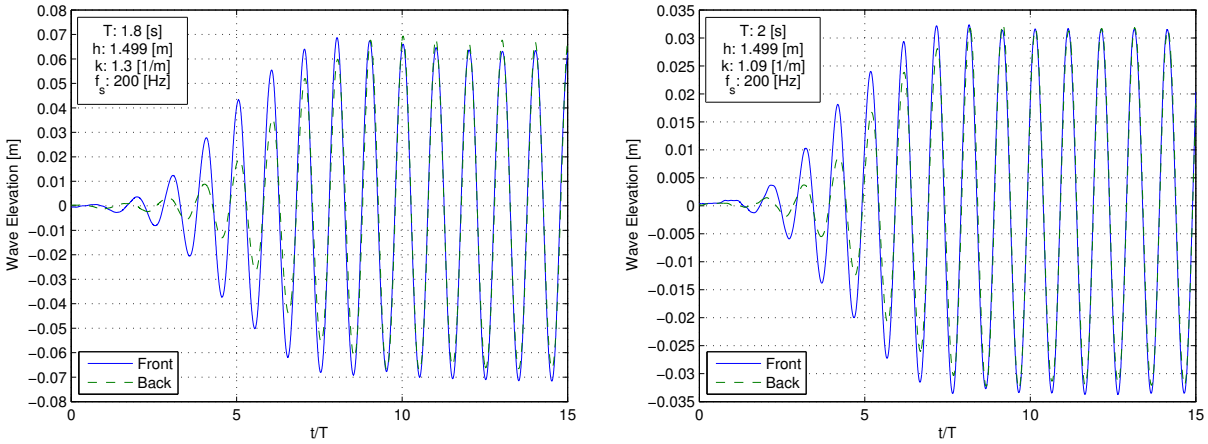

(a) Front probe shifted by 3.62 s with H of 0.134 m. (b) Front probe shifted by 3.38 s with H of 0.064 m

Figure 7.11: Measured wave elevation time series of varying wave height and period with a probe separation of 9.76 m.

acquisition boards recorded a total of 10 signals: heave position, wave elevation at the front and back wave probe, control signal from the Arduino Mega, and the voltage drop across each of the 6 resistive loads. An additional digital signal was sent from the wavemaker to trigger both the DT302 PCI and MCC 1208- FS data acquisition devices simultaneously. Furthermore, the back wave probe was moved toward the wavemaker by 4.88 m allowing installation of the floater. The front wave probe remained in its initial position set 4.88 m in front of the back wave probe and 9.76 m in front of the floater. Photos of the final experimental set-up can be found in Figs. 7.12, for the global set-up, and 7.13 for a focus on the electronics.

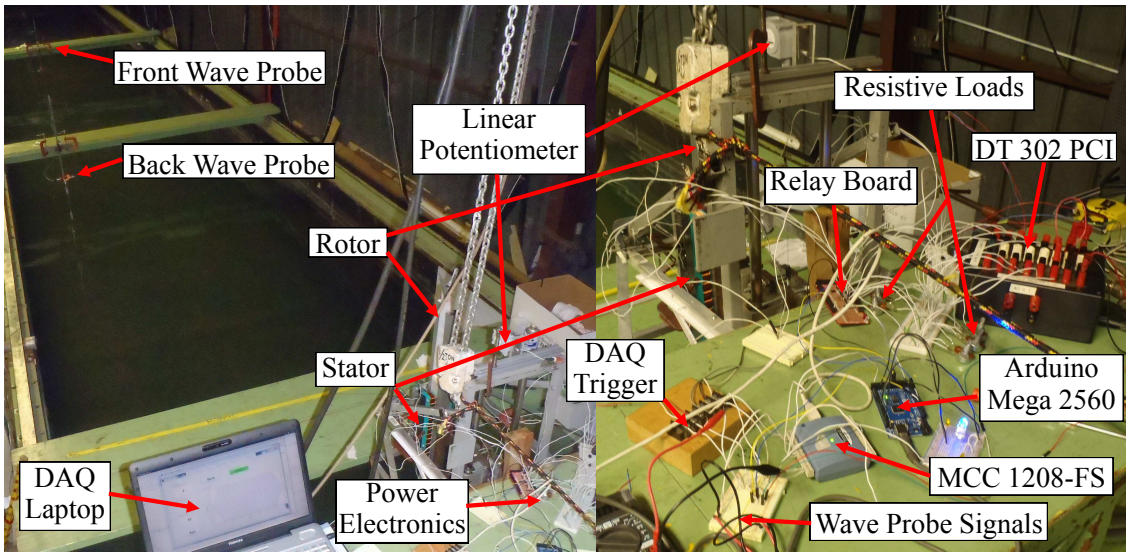

Figure 7.12: Experimental set-up for PMLG control.

7.6.2 Updated Controller Software

The recorded wave elevation taken from the back wave probe was convolved with the wave-exciting force kernel, given by Eqn. (2.4), and used as the environmental input to the NMPC algorithm. The resulting damping time series was used to determine the instances when the generator would be active and deactivated; however, no intermediate damping values were considered. The on/off time series was inserted as a lookup table in the Simulink model, see Fig. 7.14, which was loaded onto the Arduino Mega. The Arduino Mega was programmed to be triggered by the same signal that activated both data acquisition devices. Once triggered, the Arduino Mega would begin exporting the loaded time series as a high/low digital output signal to the DPDT relays. At the end of the control signal, the generator would remain active thereby preventing extreme motions while allowing for passive data to be collected. The default condition of the relays completed the wye circuit, thus when the control signal was high the generator was deactivated.

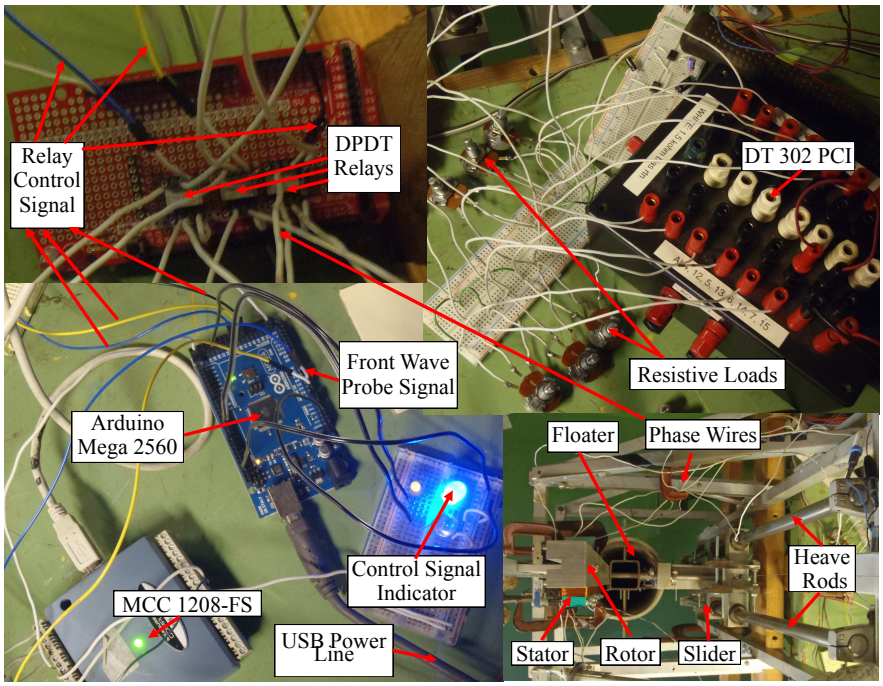

Figure 7.13: Electronics used during PMLG control experiments.

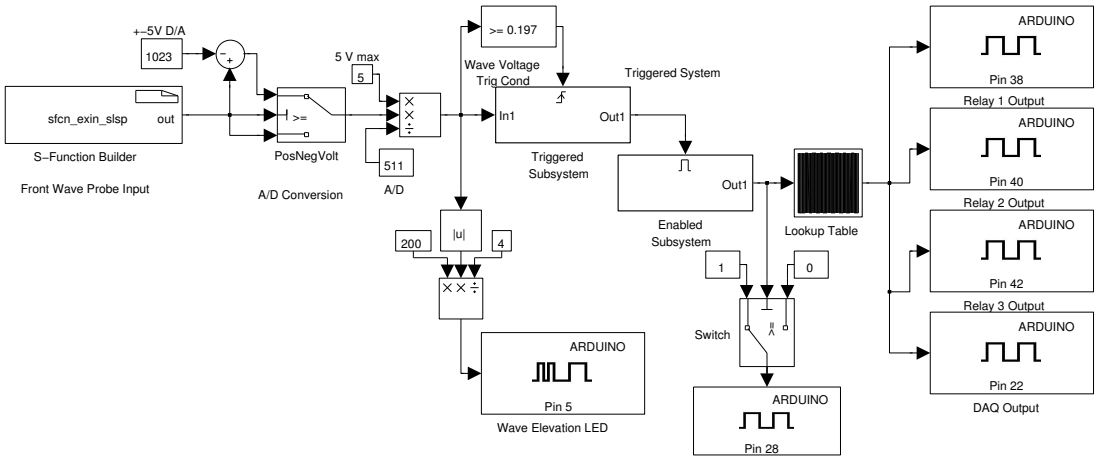

Figure 7.14: Simulink model uploaded to the Arduino Mega.

7.6.3 Time Series of PMLG Control Under Wave Excitation

A sample of the heave motion and instantaneous absorbed power from the controlled and passive absorber can be found in Fig. 7.15. Fig. 7.15a depicts the ramp up of the absorber dynamics as well as the transition of the absorber as it converges to passive motion after the control signal has ended. In this example the controlled RAO and normalized capture width is 2.23 and 1.71 times greater than the passive with a factor of 4 increase in peak power. Two plots, Figs. 7.15c and 7.15d, depict different representations on the instantaneous power. The absorbed power represents the input to the PMLG whereas the electrical power takes into account the conversion efficiency describing the electrical power output. The NMPC strategy at the moment and as described in Chapter 6 does not include efficiency considerations, therefore, both metrics will be used to evaluate the controller performance.

Comparison Between Controlled and Passive Trial

At a wave period of 1.8 s, control application with $R = 3\ \Omega$ had greater time-averaged electrical power output than the best tested passive absorber, see Fig. 7.16. The RAO, time-averaged electrical power output, and peak electrical power is 52%, 18%, and 70% greater. In Fig. 7.16b there is a distinct phase shift between the controlled and passive motion. The controlled motion is such that the floater velocity is closer in phase with the wave-exciting force.

Controller Timing

It should be noted that since the control action reduces the active duration of the PMLG, larger motions do not directly translate to greater absorbed power. If the timing of the control signal is incorrect, then the generator may be active when the floater is at lower velocities, Fig. 7.17. Based on the NMPC algorithm the generator should be switched off once the floater velocity reaches zero, as shown in Fig. 6.8; however, in Fig. 7.17b the second control signal causes the generator to remain active as the floater velocity changes direction. The overlap might appear small, but it comprises 13% of the time the generator is active. The resulting RAO from the delayed control signal is 20% greater, but the time-averaged absorbed power is the same.

7.6.4 Frequency Domain Results

A compilation of the results between the controlled and passive strategies for various wave periods and resistive loads can be found in Fig. 7.18. The control application was completed with load resistances of $R = 2$ and $3\ \Omega$ as they provided the greatest damping values. A resistive load of $5\ \Omega$ was used as a basis for the passive strategy as it provided the lowest damping value tested for the magnet coil gap width used during control experiments. As

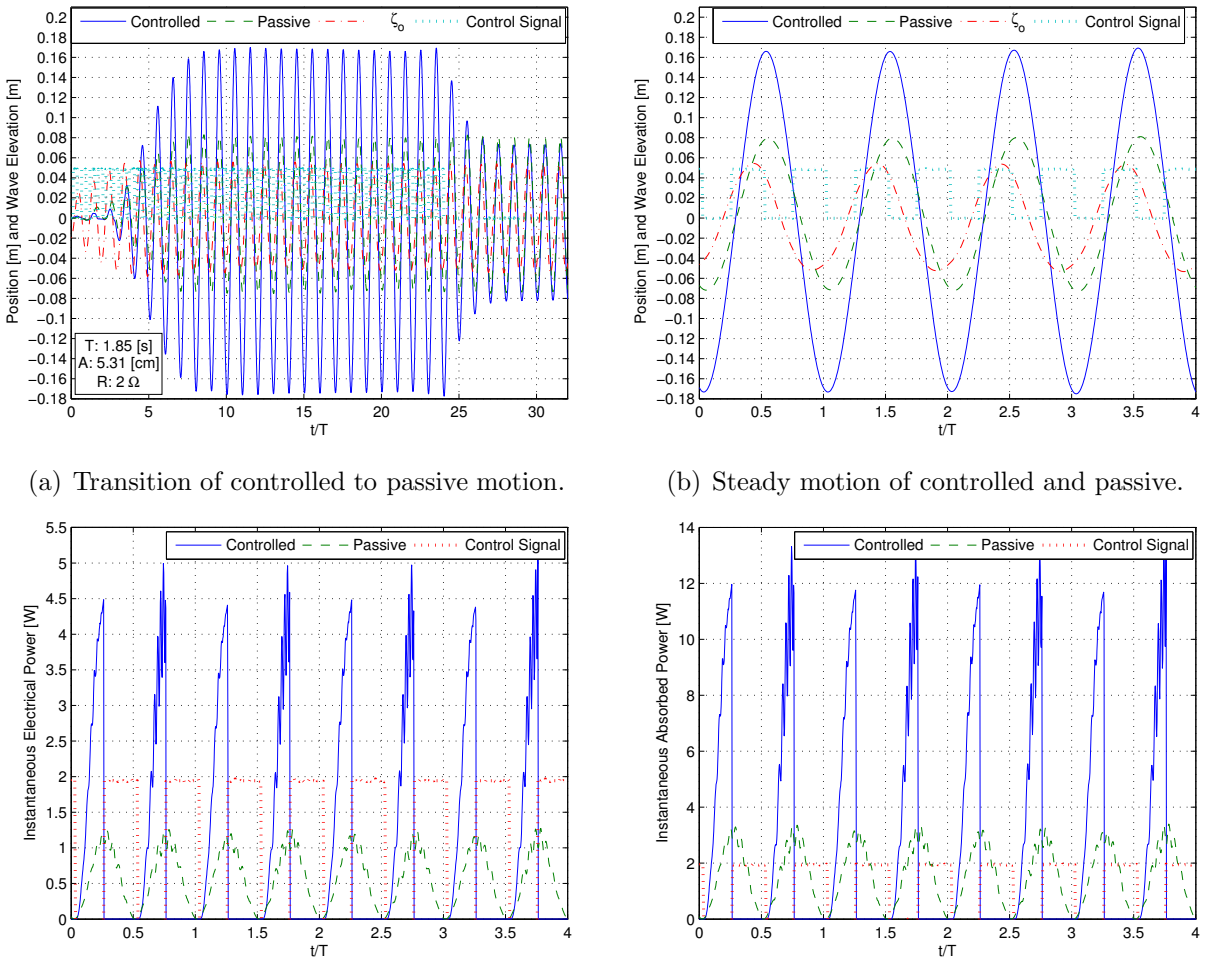

(a) Transition of controlled to passive motion.

(b) Steady motion of controlled and passive.

(c) Instantaneous electrical output power.

(d) Instantaneous absorbed power.

Figure 7.15: Comparison of the passive and controlled time histories of floater position and absorbed power. The control signal has no units and has been scaled to allow easier viewing per plot.

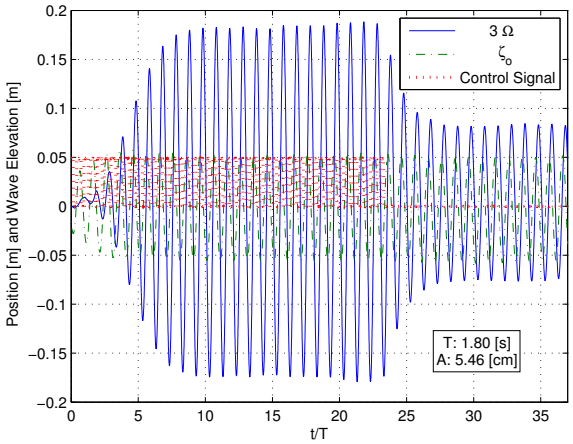

(a) Transition between controlled and passive motion.

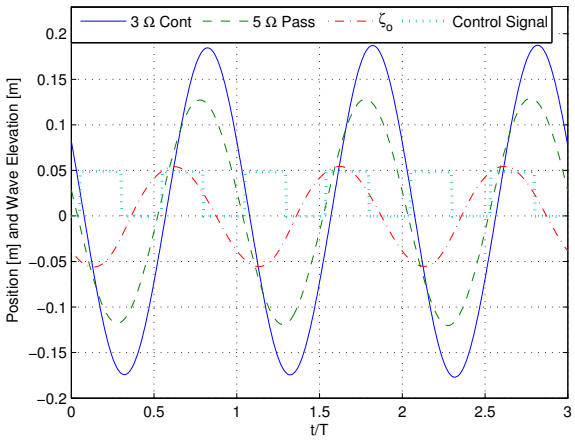

(b) Motion between controlled and passive strategies.

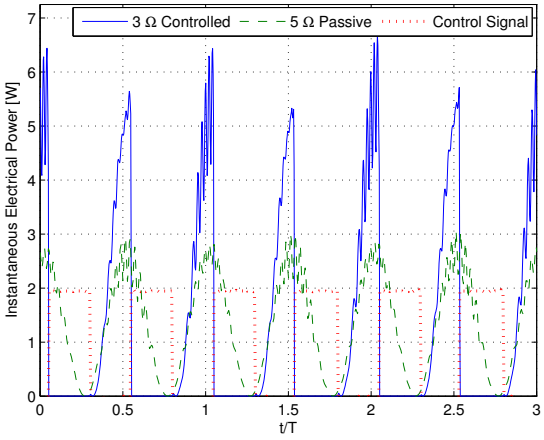

(c) Instantaneous electrical output power.

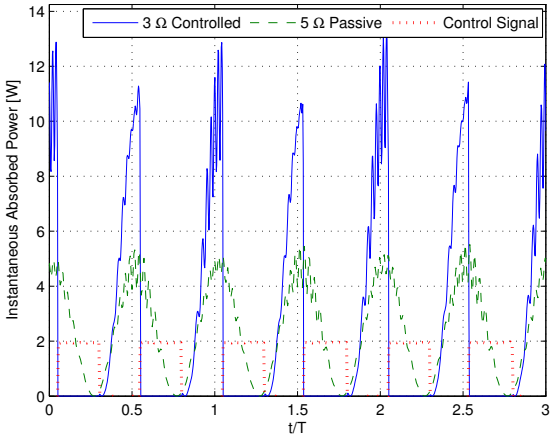

(d) Instantaneous absorbed power.

Figure 7.16: Comparison of time histories between 3 Ω controlled and 5 Ω passive absorber.

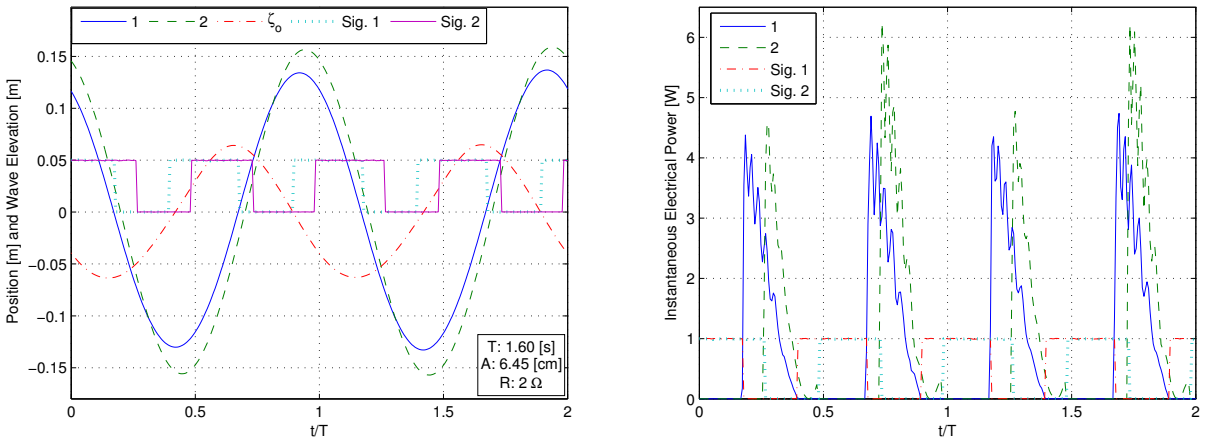

(a) Steady controlled motion.

(b) Steady instantaneous electrical power.

Figure 7.17: Comparison of time histories with time shifted control signals.

such the curve would be expected to increase near resonance, but decrease off resonance as $\tilde{f} \to 1$ as depicted in Eqn. (5.11). Furthermore, control tests were not undertaken between 1.70 - 1.75 s as the solution from NMPC no longer displayed a strongly on/off time history. In this range the damping profile has an increased number of intermediate occurrences leading to an average value approaching $\tilde{f} = 1$, which is consistent as the said range straddles the resonance period of the floater.

The left column of Fig. 7.18 plots the results for all completed trials in an effort to show that control implementation had good repeatability. Over the tested frequency range, the controlled RAO was greater than passive with the largest increases near resonance. This trend continues for the time-averaged absorbed power with the greatest values measured with a load resistance of $R = 2\ \Omega$ consistent with NMPC simulations. However, after including the efficiency of the PMLG the $R = 5\ \Omega$ passive absorber, under most testing conditions, has an electrical power output comparable to the controlled cases. This is not unsurprising as the difference in efficiency between $R = 2$ and $5\ \Omega$ is nearly 20%. Though for wave periods of 1.8 and 1.85 s the controlled cases lead to greater electrical output. Therefore, the success of the NMPC is confirmed by the absorbed power as it does not include the PMLG efficiency in the optimization. However, in order to maximize electrical power output from the PMLG an efficiency model must be included in the control algorithm.

7.6.5 Irregular Wave Trials

Experiments were completed in irregular sea statess, unfortunately difficulties with the wave-maker operation during experimentation limited the number of completed trials. As in the previous experiments, the wave elevation was recorded at the floater's point of installation and used as the environmental input to the NMPC. The NMPC was run with a two second time horizon as gains in cumulative absorbed energy saturated past this value, Fig. 6.14. The calculated damping time series was analyzed to determine when the generator would

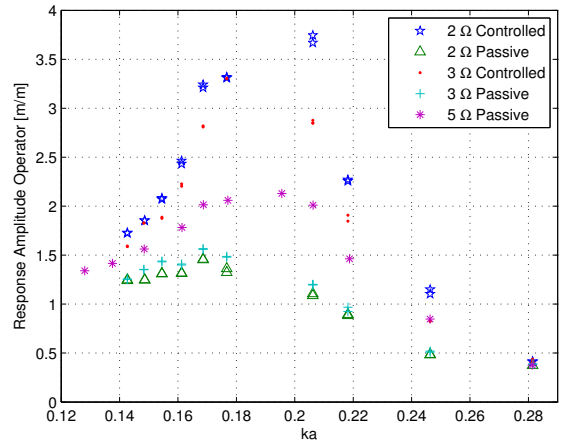

(a) RAO.

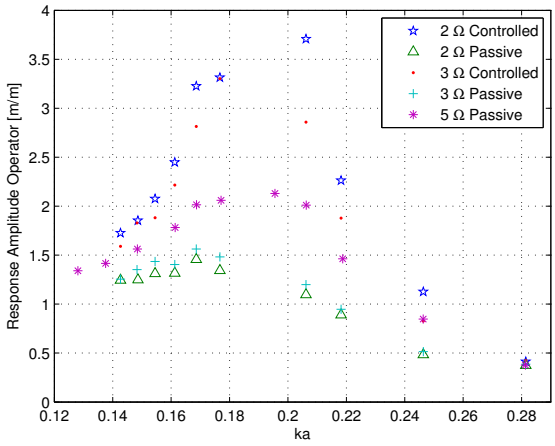

(b) RAO averaged per period.

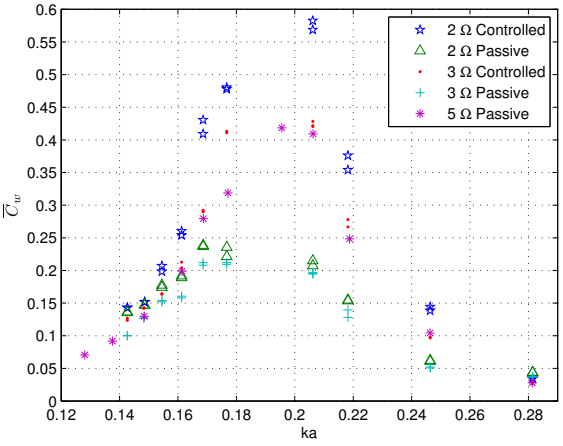

(c) Capture width based on absorbed power.

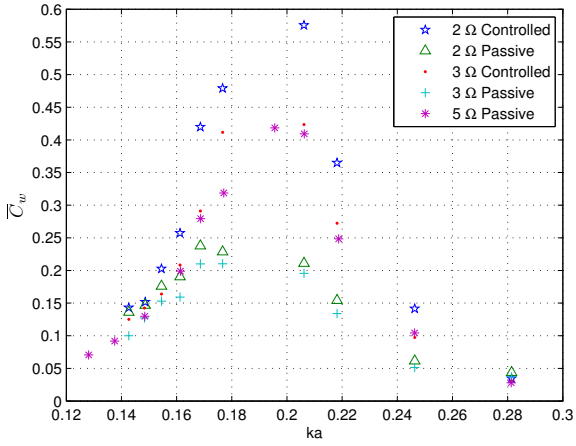

(d) Absorbed power averaged per period.

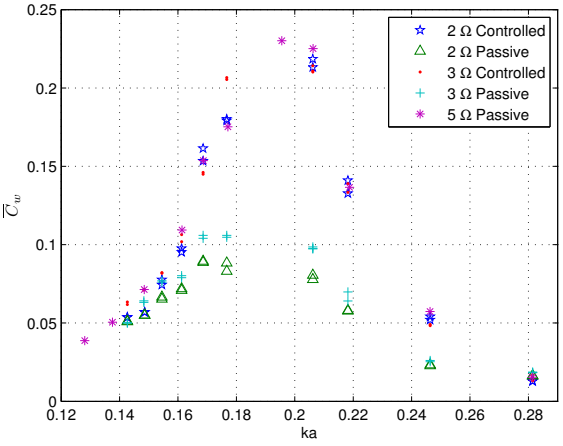

(e) Capture width based on electrical power output.

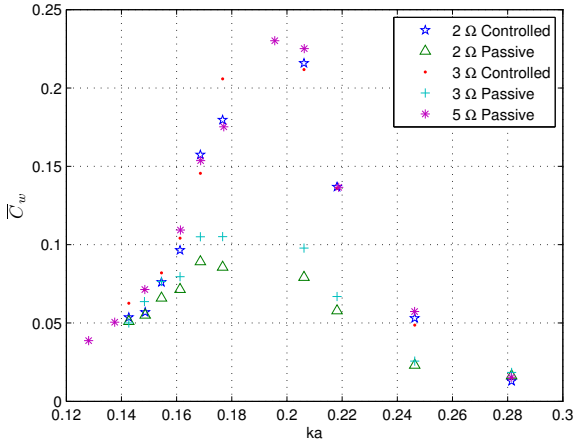

(f) Electrical power output averaged per period.

Figure 7.18: Frequency domain performance for controlled versus passive absorber.

be activated and deactivated without considering intermediate values. This was considered a valid approximation as there were very few instances of intermediate damping values as well as focusing on the use of relays as the only control actuation.

The recorded time histories for two sea states can be found in Fig. 7.19, given some variation in the recorded wave elevation, it was decided to scale the results using the measured significant wave height for comparison. In both sea states, the cumulative absorbed energy is maximized when control is applied with the largest damping exceeding the maximum passive run by 17%. Though after considering the PTO efficiency, the electrical output power is 20% lower than the maximum passive trial, which reinforces the need for an efficiency evaluation module for the PMLG. Furthermore, as expected from the on/off sequencing the controlled $R = 2$ and 3 Ω trials saw increases in motion between 7 - 15% over the best passive trial, Fig. 7.19b. This leads to a standard deviation in electrical output power that was 20% greater indicating that the control application was extracting greater power from each wave packet, but it was not enough to overcome the constant absorption of the passive absorber, Fig. 7.19c. This is exacerbated further if the ratio between the standard deviation and mean electrical output power is considered, which is 50% greater for $R = 2$ than 5 Ω. The consequences of a larger standard deviation in the output power signal must be considered in order to evaluate feasibility of the control structure.

The controlled runs generally had greater power absorption over the trial though the effects decreased as the generator damping limit was reduced. However, the on/off switching still must be coincident with the proper phasing of the incoming wave elevation. A trial with a 1.7 s peak period had a delay of 3.1 s between the wave elevation used in the control algorithm and during experimentation. In this case, the controlled runs achieved lower power absorption than their corresponding passive trials. This confirms that the gains in using the control scheme are not simply due to the increased floater motion resulting from deactivation of the PTO unit, but being more opportunistic when absorbing power. Results from irregular wave trials are positive and it is believed that the tests suffered from lower generator efficiency associated with lower armature speeds and exacerbated cogging forces which are not modeled in the system dynamics. Therefore, additional testing over a greater range of sea states needs to be completed before a final evaluation can be made.

7.7 Efficiency Considerations

As the PMLG electrical power output performance was not consistently maximized, it has become apparent that an efficiency module must be included in the optimization process. In an attempt to model the efficiency of the generator, a best fit curve can be constructed from the efficiency and damping values measured during the bench test. Two mathematical approximations, that may be fitted to experimental data, can be found in Eqns. (7.3) and (7.4). The variables, a, b, c, would be calculated based on best fit methods. The mathematical approximation can be placed as an additional block in the BLOM Simulink model connecting the damping input to the objective function. Thus, the full strength of the damping input

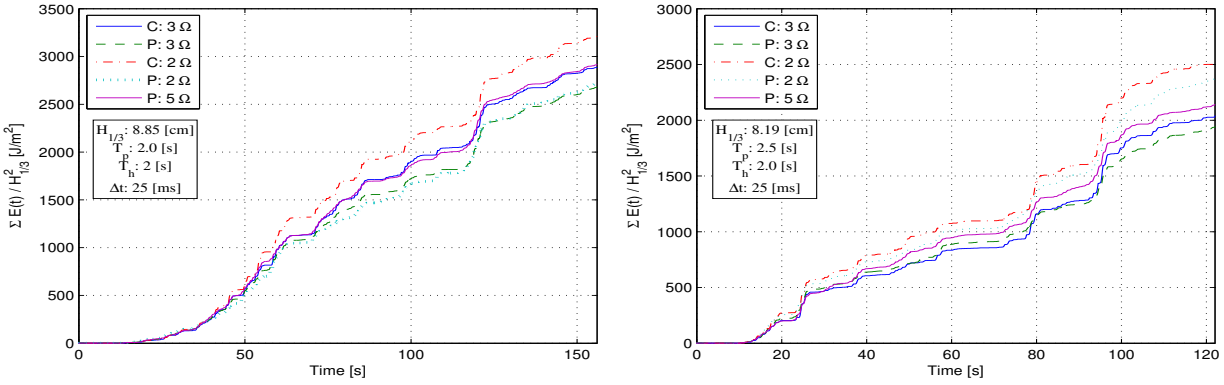

(a) Cumulative absorbed energy.

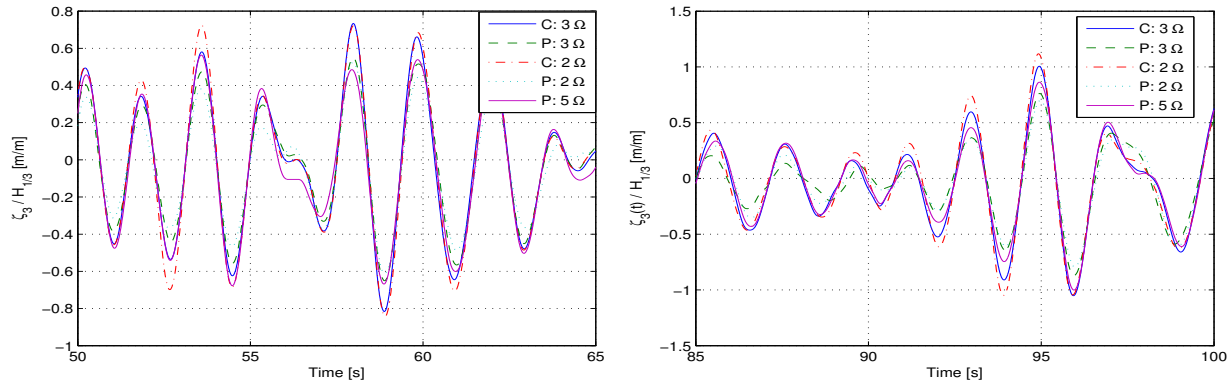

(b) Position.

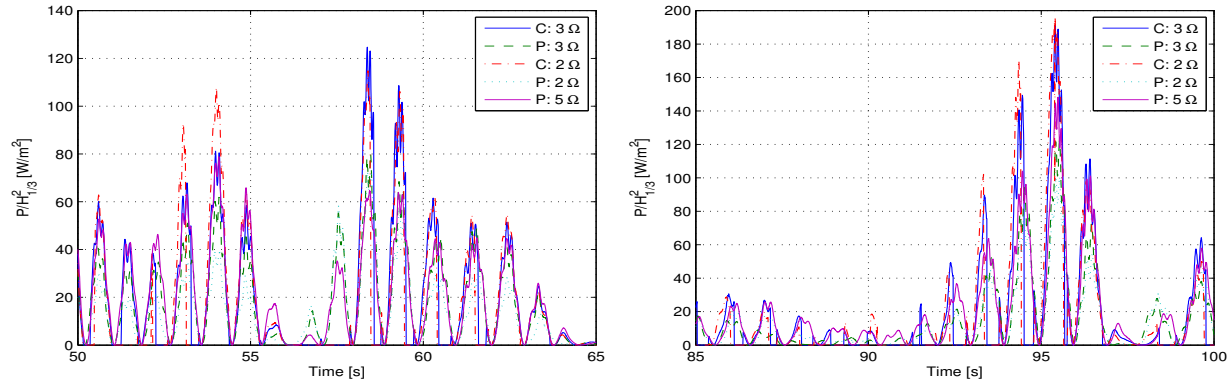

(c) Electrical output power.

Figure 7.19: Comparison of irregular wave time histories for cumulative absorbed power, position, and instantaneous electrical power. In these plots, C denotes when the control signal is applied and P denotes passive with no control application.

is felt by the system dynamics, but the resulting conversion efficiency is reflected in the objective function.

$$\eta_{el|fit} \approx a\left(1 + b((B_{g|max} - B_g)/B_{g|max})^{1/c}\right) \tag{7.3}$$

$$\eta_{el|lin} \approx a\left(1 + b(B_{g|max} - B_g)/B_{g|max}\right) \tag{7.4}$$

Eqn. (7.3) was fitted to the efficiency and damping values presented in Fig. 7.9 resulting in the following values: a = 0.375, b = 0.57, and c = 2.6. This representation of the measured PTO efficiency was included in the BLOM Simulink model to understand how the optimum time-varying damping would change. The inclusion of an efficiency model led to significant changes in the damping time history, Fig. 7.20b. For the presented simulations, the duration the generator was active increased by 30% of the wave period. The damping profile had greater time variability as it required a change at each time step, when the PMLG is active, rather than a discrete step when transitioning from on to off. In both simulations, the time-averaged absorbed power was 17% greater when the optimizer neglected the PTO efficiency, but had an electrical power output that was 17% lower. However, this damping profile will require the actuation of the resistive loads which adds complexities to the control structure. When moving away from resonance the damping profile moved closer to on/off sequencing as the reduction in motion required a larger damping force to guide the velocity of the floater thereby absorbing more power. Rather than proceed with resistive load actuation, a re-design of the PTO unit to increase efficiency at larger damping values may provide a better strategy for optimization of the electrical output power as the on/off characteristics would provide easier implementation.

The efficiency evaluation does not include the power consumption required to run the NMPC algorithm in real-time, the Arduino Mega, or the Telecom relays. The laptop used for computation required 60 Watts during operation. This is substantially larger than both the Arduino Mega and Telecom relays which together cost half a Watt. At 60 Watts the computational speed did not meet the 25-50 ms time step required to properly simulate the model dynamics. The required increase in processor speed will likely double the necessary power consumption. Fortunately, at the prototype scale the required time step will grow with the square root of the scale factor, Λ. The absorbed power of the WEC scales by $\Lambda^{7/2}$ and combined with a reduction in the computational power consumption is expected to provide a net gain in energy absorption.

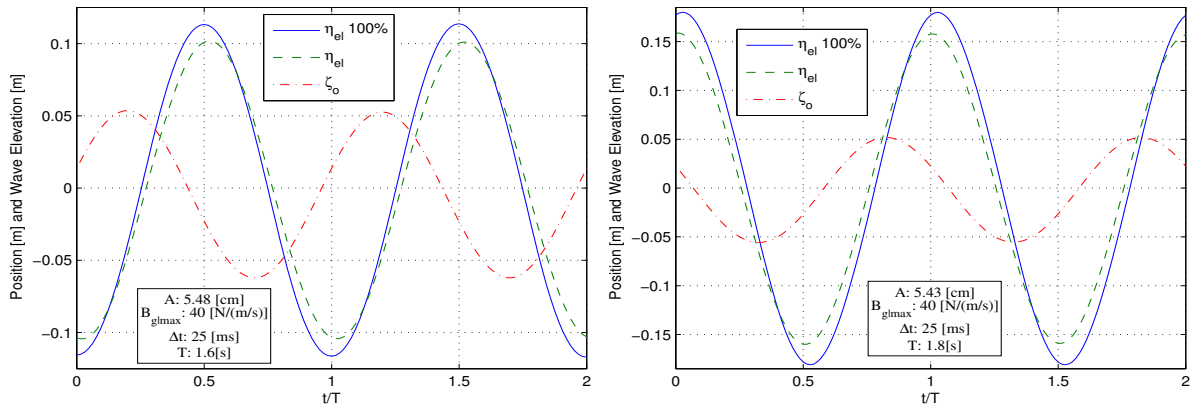

(a) $\zeta_3(t)$ and $\zeta_o(t)$.

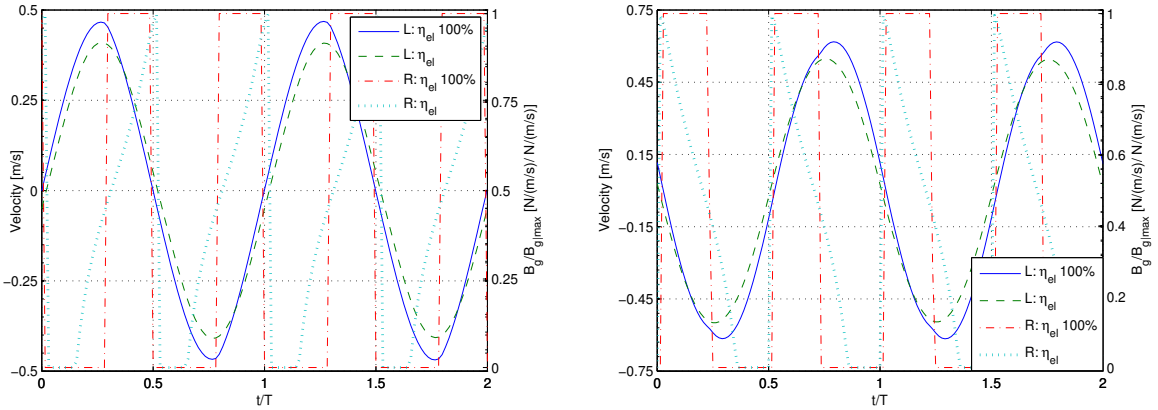

(b) $\dot{\zeta}_3(t)$ and $B_g(t)/B_{g|max}$, where L and R denote left and right axis.

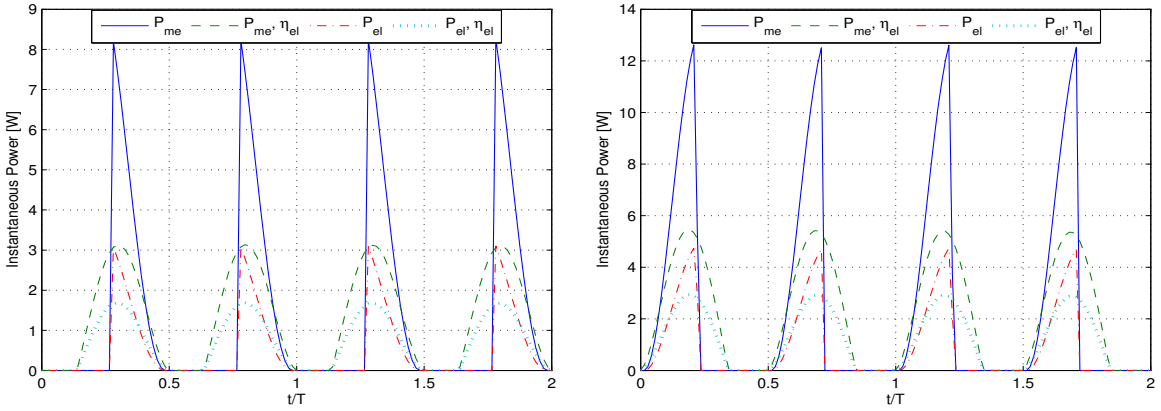

(c) $P(t)$ and $P_{el}(t)$.

Figure 7.20: Comparison of time histories with and without η_{el} considerations.

Chapter 8

Conclusions

This work has addressed several areas of concern in the development of wave energy converters. The research began with an investigation into the hydrodynamic effects of two floater shapes in an effort to increase motion and decrease viscous losses. A simple rounded bottom shape led to a factor of 2 increase in motion at resonance, significantly improving power extraction. A time-domain mathematical model was constructed using Cummin's [40] decomposition while the convolution kernel was approximated as a set of ordinary differential equations allowing for a state space representation. This mathematical model was compared against experiments and found to require the use of corrective terms. The most notable corrective term corresponds to the contribution of the viscous damping associated with the floater shape.

The extended development of a UC Berkeley permanent magnet linear generator has focused on increasing the mechanical-to-electrical efficiency and control of the generator damping. Modifications made to the armature length and permanent magnet spacing increased power output, but with only modest increases to the efficiency. The power losses in the first-generation stator were found to be associated with hysteresis and eddy currents rather than cogging losses. In order to combat these losses, a new stator was constructed from silicon iron steel laminations. The new design led to an increase in power output of 40%, which, when combined with a significant reduction in power losses, more than doubled the previous maximum efficiency of the first generation design. The largest power sink is now attributed to the resistive losses of the coils, this is a consequence of the model scale and expected to decrease when the laboratory model is scaled up.

The floater and PMLG were coupled only after verification of the hydrodynamic and electromagnetic performance of each respective component. The ability to alter the magnet coil gap width (MCGW) in conjunction with the electrical loads has the potential to achieve any desirable operating point of the PMLG. The experimental wet test results, though limited, indicate increases in capture width are indeed greatest at resonance as the fluid and PTO damping are matched. The current experimental set-up led to a maximum wave-to-wire efficiency of 35%, a factor of 7 improvement over [24]. As the wave frequency moves off resonance, the optimum generator damping, if assumed constant and continuous, must quickly increase in order to compensate for the reduction in floater motion. The time-domain control of the generator damping is expected to increase the effective capture width of the device since it allows for more opportunistic power absorption.

The time-domain mathematical model was successfully implemented in a nonlinear model predictive control (NMPC) strategy. The controller was focused on determining the optimum power-take-off damping for a generic point absorber of a model scale. A passive absorber, with optimum linear PTO damping, was used as the baseline for comparison. The IPOPT solver used for NMPC was run with a modified trapezoidal discretization to convert from

continuous to discrete time. In the frequency domain, the NMPC strategy performed substantially better when near the resonance frequency while comparable at higher and lower frequencies. It was found that the coupling between the generator damping and floater velocity led to a damping time history that followed a strongly on/off periodic sequence. The time-averaged power was greater for NMPC, but the instantaneous power came in larger pulses and over smaller time windows. The use of NMPC in irregular waves outperformed the passive strategy by approximately 25-50% over the simulated environments using the experimentally realizable $B_{g|max} = 50$ kg/s. The time histories of the floater's motion obtained by the two strategies were primarily in phase, but with the larger amplitudes occurring for the NMPC. The on/off activation of the damping provided evidence for easier experimental implementation as a simple relay switch could be used to decouple the PTO's influence on floater motion. The same behavior was seen when a latching damper was included as an additional control input. The latching damper was most effective for wave frequencies below resonance and greatly surpassing the performance of a single variable PTO. The author recognizes that a wave-height prediction module was not used in this analysis but is a necessary component for a successful realization of the NMPC strategy at any scale.

The experimental validation of the PMLG on/off control began with a revised bench test. The combination Arduino Mega 2560 micro-controller with mechanical relays provided a simple but effective means of controlling the period of activation for the PMLG. The control is almost completely electrical, thereby eliminating the need for additional hardware. In addition, the default condition of the hardware led to an active generator; therefore, if the controller were to malfunction, power could still be captured. The dry bench test results provided confidence that the wet-test experimental set up would achieve the desired performance. The PMLG control experiments verified the effectiveness of the NMPC controller in regular, and to a lesser extent, irregular waves showing an increase in absorbed power using the on/off sequencing. A few experiments did achieve better electrical output power, and it is expected that further updates of the mathematical model and inclusion of the PTO efficiency should increase performance. An approximation of the generator efficiency as a function of damping was inserted in the system model to maximize power output. As expected, the results move away from the strongly on/off sequencing while providing intermediate damping values with greater conversion efficiency. Therefore, it is suggested that additional modifications be made to the generator in an effort to increase the efficiency at greater damping values while retaining the simplicity of the on/off control.

This work has encompassed the theory, design, fabrication, testing, optimization, and control of a coupled permanent magnet linear generator and cylindrical floater system for wave-energy conversion. The nonlinear model predictive control strategy can be applied to any single or multiple degrees of freedom system. The on/off characterization of the PTO damping can also be used in conjunction with rotary generators as the operating principles are very similar. The hydrodynamic, electromagnetic, and control modules were individually tested to facilitate efficient final integration. This work has highlighted and addressed many areas of concern for the optimization of a wave energy converter, providing future avenues of research, and helping to make ocean energy a realizable power source for the future.

References

[1] Thorpe, J. W. A brief review of wave energy. ETSU-120 DTI, United Kingdom, 1999.

[2] Previsic, M., Bedard, R., and Hagerman, G., 2004, "Assessment offshore wave energy conversion devices," Report No: E2I EPRI. WP-004-US-Rev 1, June 16, 2004.

[3] Falnes, J., 1980, "Radiation impedance matrix and optimum power absorption for interacting oscillators in surface waves," *Appl. Ocean Res.*, **2** (2), pp. 75-80.

[4] Thorburn, K. and Leijon, M., 2007, "Farm size comparison with analytical model of linear generator wave energy converters," *Ocean Eng.*, **34**, pp. 908-916.

[5] Garnaud, X. and Mei, C., 2009, "Wave-power extraction by a compact array of buoys," *J. Fluid Mech.*, **635**, pp. 389-413.

[6] Falnes, J. and Lovseth, J., 1991, "Ocean wave energy," *Energy Policy*, **19** (8), pp. 768-775.

[7] Budal, K. and Falnes, J., 1975, "A resonant point absorber of ocean-wave power," *Nature*, **256**, pp. 478-479.

[8] Rhinefrank, K. et al, 2006, "Novel ocean energy permanent magnet linear generator buoy," *Renewable Energy*, **31**, pp. 1279-1298.

[9] Eriksson, M., Waters, R., Svensson, O., Isberg, J., and Leijon, M., 2007, "Wave power absorption: experiments in open sea and simulation," *J. Applied Physics*, **102**, 084910.

[10] Rhinefrank, K., Schacher, A., Prudell, J., Stillinger, C., Naviaux, D., Brekken, T., von Jouanne, A., Newborn, D., Yim, S., and Cox, D., 2010, "High Resolution Wave Tank Testing of Scaled Wave Energy Devices," *Proceedings of the 29th ASME International Conference on Offshore Mechanics and Arctic Engineering (OMAE-10)*, Shanghai, China, June 6 - 11.

[11] Grilli, A., Merrill, J., Grilli, S., Spaulding, M., and Cheung, J., 2007, "Experimental and numerical study of spar buoy-magnet/spring oscillators used as wave energy absorbers," *Proceedings of the 17th International Society of Offshore and Polar Engineers (ISOPE-07)*, Lisbon, Portugal, July 1-6, pp. 489-496.

[12] Vidal, E., Hansen, R. H., and Kramer, M., 2012, "Early performance assessment of the electrical output of Wavestar's prototype," in *Proceedings of the 4th International Conference on Ocean Engineering (ICOE-12)*, Dublin, Ireland, October 17.

[13] Wacher, A. and Neilsen, K., 2010, "Mathematical and numerical modeling of the AquaBuOY wave energy converter," *J. Mathematics-in-Industry Case Studies*, **2**, pp. 16-33.

[14] Nunes, G., and Valério, D., Beirão, P., and Sá da Dosta, J., 2011, "Modelling and control of a wave energy converter," *Renewable Energy*, **36**, pp. 1913-1921.

[15] Elwood, D., Yim, S., Prudell, J., Stillinger, C., von Jouanne, A., Brekken, T., Brown, A., and Paasch, R., 2010, "Design, construction, and ocean testing of a taut-moored dual-body wave energy converter with linear generator power take-off," *Renewable Energy*, **35** (2), pp. 348-354.

[16] Oprea, C., Martis, C., Biro, K., and Jurca, F., 2010, "Design and Testing of a Four-sided Permanent Magnet Linear Generator Prototype," *Proceedings of the 19th International Conference on Electrical Machines (ICEM-10)*, Rome, Italy, Sept. 6-8, pp. 1-6.

[17] Leijon, M., Bernhoff, H., Agren, O., Isberg, J., Berg, M., Karlsson, and K.E, Wolfbrandt, A, 2005, "Multiphysics simulation of wave energy to electric energy conversion by permanent magnet linear generator," *IEEE Transactions on Energy Conversion*, **20** (1), pp. 219 - 224.

[18] Vermaak, R. and Kamper, M., 2012, "Experimental evaluation and predictive control of an air-cored linear generator for direct-drive wave energy converters," *IEEE Transactions on Industry Applications*, **48** (6), pp. 1817 - 1826.

[19] Mueller, M.A., Polinder, H., and Baker, N., 2007, "Current and novel electrical generator technology for wave energy converters," *Proceedings of the IEEE International Conference on Electric Machines & Drives (IEMDC-07)*, **2**, Antalya, Turkey, May 3-5, pp. 1401-1406.

[20] Matlak, T. J., 2008, "Wave power: wave-energy extraction using a linear electromagnetic generator," Master's Report, University of California at Berkeley, Berkeley, CA.

[21] Peiffer, A., 2009, "Modeling and evaluation of a wave-energy device - a point absorber with linear generator," Master's Report, University of California at Berkeley, Berkeley, CA.

[22] Sinclair, M. E., 2011, "Design and Properties of a Horizontal Cylindrical Wave-Energy Extractor," Master's Thesis, University of California at Berkeley, Berkeley, CA.

[23] Madhi, F., 2012, "Design, Fabrication, and Testing of a Horizontal Cylindrical Wave-Energy Device of High Performance," Master's Thesis, University of California at Berkeley, Berkeley, CA.

[24] Yeung, R. W., Peffier, A., Tom, N., and Matlak, T. J., 2010, "Design, analysis, and evaluation of the UC-Berkeley wave-energy extractor," *J. Offshore Mech. Arct. Eng.*, **134** (2), 021902.

[25] Tom, N. and Yeung, R. W., 2012, "Performance enhancements and validations of the UC-Berkeley ocean-wave energy extractor," *J. Offshore Mech. Arct. Eng.*, **135** (4), 041101-1.

[26] Yeung, R. W. and Vaidhyanathan, M., 1994, "Highly separated flows near a free surface," *Proceedings of the International Conference on Hydrodynamics*, Wuxi, China, Oct. 30 - Nov. 3.

[27] Ananthakrishnan, P. and Chafin, J., 2008, "Inviscid and viscous flow analysis of multihull ships under forced oscillations in a free surface," *Proceedings of the 8th International Conference on Hydrodynamics*, Nantes, France, Sept. 30 - Oct. 3, pp. 229-237.

[28] Evans, D. V., 1981, "Maximum wave-power absorption under motion constraints," *Appl. Ocean Res.*, **4** (3), pp. 200-203.

[29] Stalberg, M., Waters, R., Danielsson, O., and Lejion, M, 2008, "Influence of generator damping on peak power and variance of power for a direct drive wave energy converter," *J. Offshore Mech. Arct. Eng.*, **130** (3), 031003.

[30] Falcão, A. F., 2007, "Modelling and control of oscillating-body wave energy converters with hydraulic power take-off and gas accumulator," *Ocean Eng.*, **34**, pp. 2021-2032.

[31] Eidsmoen, H., 1998, "Tight-moored amplitude-limited heaving-buoy wave-energy converter with phase control", *Appl. Ocean Res.*, **20** (3), pp. 157-161.

[32] Rossiter, J. A., 2003, *Model-Based Predictive Control: A Practical Approach*, CRC Press, New York.

[33] Brekken, T. K. A., 2011, "On model predictive control for a point absorber wave energy converter," *Proceedings of the 2011 Trondheim PowerTech Conference*, Trondheim, Norway, June 19-23, pp. 1-8.

[34] Hals, J., Falnes, J., and Moan, T., 2011, "Constrained optimal control of a heaving buoy wave-energy converter," *J. Offshore Mech. Arct. Eng.*, **133**, 011401-1.

[35] Cretel, J. A. M., Lightbody, G., and Thomas, G. P., 2010, "An application of model predictive control to a wave energy point absorber," *Proceedings of the IFAC Conference on Control Methodologies and Technology for Energy Efficiency*, Vilamoura, Portugal, March 29-31, pp. 1-8.

[36] Cretel, J. A. M., Lightbody, G., Thomas, G. P., and Lewis, A. W., 2011, "Maximisation of energy capture by a wave-energy point absorber using model predictive control," *Proceedings of the 18th IFAC World Congress*, Milano, Italy, Aug. 28 - Sept. 2, pp. 3714-3721.

[37] Richter, R., Magana, M., Sawodny, O., and Brekken, T., 2013, "Non-linear model predictive control of a point absorber wave energy converter," *IEEE Transactions Sustainable Energy*, **4** (1), pp. 118-126.

[38] Abraham, E. and Kerrigan, E. C., 2013, "Optimal active control and optimization of a wave energy converter," *IEEE Transactions on Sustainable Energy*, **4** (2), pp. 324-32.

[39] Tom, N. and Yeung, R. W., 2013, "Non-linear model predictive control applied to a generic ocean-wave energy extractor," *Proceedings of the 32nd International Conference on Ocean, Offshore and Arctic Engineering (OMAE-13)*, Nantes, France, June 9-14.

[40] Cummins, W. E., 1962, "The impulse response function and ship motions," *Schiffstechnik*, **9**, pp. 101-109.

[41] Falnes, J., 2002, *Ocean Waves and Oscillating Systems*, Cambridge University Press, New York.

[42] Babarit, A. and Clement, A. H., 2006, "Optimal latching control of a wave energy device in regular and irregular waves," *Appl. Ocean Res.*, **28**, pp. 77-91.

[43] Bedard, R., et al., 2005, "US Final Report", Report No: E2I EPRI Global, WP-009-US-Rev 2, September 22, 2005.

[44] U.S. Energy Information Administration, 2011, "U.S. Hydropower Output Varies Dramatically from Year to Year," `http://www.eia.gov/todayinenergy/detail.cfm?id=2650#`.

[45] Gunn, K. and Stock-Williams, C., 2012, "Quantifying the potential global market for wave power," *Proceedings of the 4th International Conference on Ocean Engineering (ICOE-12)*, Dublin, Ireland, October 17.

[46] U.S. Energy Information Administration, International Energy Statistics, 2013, `http://www.eia.gov/cfapps/ipdbproject/IEDIndex3.cfm?tid=2&pid=2&aid=2`.

[47] Wehausen, J. V., and Laitone, E. V., 1960, "Surface Waves", *Encyclopaedia of Physics*, Vol. **IX**, Springer Verlag, New York, pp. 446-778. (Online edition: http://coe.berkeley.edu/SurfaceWaves/)

[48] Baker, D. R., 2009, "Offshore resources go beyond oil wells", San Francisco Chronicle, `http://articles.sfgate.com/2009-04-15/news/17191875_1_offshore-energy-wave-energy-wind-farms`, April 15.

[49] Johnson, K., 2012, "Project Aims to Harness the Power of Waves", New York Times, `http://www.nytimes.com/2012/09/04/us/project-aims-to-harness-wave-energy-off-the-oregon-coast.html?_r=0`, September 3.

[50] Cornett, A. M., 2008, "A global wave energy resource assessment," *Proceedings of the 18th International Society of Offshore and Polar Engineers (ISOPE-08)*, Vancouver, Canada, July 6-11.

[51] Falnes, J., 1995, "On non-causal impulse response functions related to propagating water waves," *Appl. Ocean Res.*, **17**(6), pp. 379-389.

[52] Yeung, R. W., 2008, "Hydrodynamics of ships and ocean systems," Course ME 241A & B. Lecture notes, Department of Mechanical Engineering, University of California at Berkeley, Berkeley, CA.

[53] Lee, C. H., 1995, "WAMIT Theory Manual," MIT Report 95-2, Dept. of Ocean Eng., Massachusetts Institute of Technology.

[54] Yeung, R. W., 1981, "Added mass and damping of a vertical cylinder in finite-depth waters," *Appl. Ocean Res.*, **3** (3), pp. 119-133.

[55] Yeung, R. W. and Sphaier, S. H., 1989, "Wave-interference effects on a floating body in a towing tank," *Proccedings of the 4th International Symposium on Practical Design of Ships and Mobile Units (PRADS)*, Varna, Bulgaria, Oct. 23-28.

[56] Yeung, R. W. and Sphaier, S. H., 1989, "Wave-interference effects on a truncated cylinder in a channel," *J. Engineering Mathematics*, **23**, pp. 95-117.

[57] Tom, N., 2009, "Data-acquisition design for experimental methods at the Richmond-Field-Station Model-Testing Facility", Master's Report, University of California at Berkeley, Berkeley, CA.

[58] Kung, S. Y., 1978, "A new identification and model reduction algorithm via singular value decompositions," *Proceedings of the 12th IEEE Asilomar Conference on Circuits, Systems and Computers*, Pacific Grove, CA, USA, pp. 705-714.

[59] Taghipour, R., Perez, T., and Moan, T., 2008, "Hybrid frequency-time domain models for dynamic response analysis of marine structures," *Ocean Eng.*, **35** (7), pp. 685-705.

[60] Kristiansen, E., Hijulstad, A., and Egeland, O., 2005, "State-space representation of radiation forces in time-domain vessel models," *Ocean Eng.*, **32** (17-18), pp. 2195-2216.

[61] Yu, Z. and Falnes, J., 1996, "State-space modelling of a vertical cylinder in Heave," *Appl. Ocean Res.*, **17** (5), pp. 265-275.

[62] Yeung, R. W. and Jiang, Y. 2011, "Effects of shaping on viscous damping and motion of heave cylinder," *Proceedings of the 30th International Conference on Ocean, Offshore and Arctic Engineering (OMAE-11)*, Rotterdam, Netherlands, June 19-24.

[63] Jiang, Y. and Yeung, R. W., 2012, "Computational modeling of rolling cams for wave-energy capture in a viscous fluid," in *Proceedings of the 31st International Conference on Ocean, Offshore and Arctic Engineering*, Rio de Janerio, Brazil, July 1 - 6, Paper Number OMAE2012-84150.

[64] Seah, R. K. M. and Yeung, R. W., 2008, "Vortical-flow modeling for ship hulls in forward and lateral motion," *Proceedings of the 27th Symposium on Naval Hydrodynamics*, Seoul, Korea, Oct. 5-10.

[65] Lieu, D. K., 2009, "Design of basic electro-mechanical devices", Course ME 229. Lecture notes, Department of Mechanical Engineering, University of California at Berkeley, Berkeley, CA.

[66] Griffiths, D. J., 1999, *Introduction to Electrodynamics*, Prentice Hall, New Jersey.

[67] Ivanova, I. A., Agren, O., Bernhoff, H., and Leijon, M., 2005, "Simulation of a 100 kW permanent magnet octagonal linear generator for ocean wave conversion," *IEEE Journal of Oceanic Engineering*, **30** (3) pp. 619-629.

[68] Prudell, J., Stoddard, M., Amon, E., Brekken, T. K. A., and von Jouanne, A., 2010, "A permanent-magnet tubular linear generator for ocean wave energy conversion," *IEEE Transactions on Industry Applications*, **46** (6), pp. 2392-2400.

[69] Ackermann, B., Janssen, J. H. H., Scottek, R., and van Steen, R. I., 1992, "New Technique for Reducing Cogging Torque in a Class of Brushless DC Motors," *IEE Proceedings B on Electric Power Applications*, **139** (4), pp. 315 - 320.

[70] Pyrhönen, J., Jokinen, T., and Hrabovcová, V., 2009, *Design of Rotating Electrical Machines*, John Wiley and Sons, p. 232.

[71] Polinder, H., Mecrow, B. C., Jack, A. G., Dickinson, P., and Mueller, M. A., 2003, "Linear generators for direct-drive wave energy conversion," *Proceedings of the IEEE International Conference on Electric Machines and Drives (IEMDC-03)*, June 1 - 4, **2**, pp. 798-804.

[72] Danielsson, O., Leijon, M., and Sjostedt, E., 2005, "Detailed study of the magnetic circuit in a longitudinal flux permanent-magnet synchronous linear generator," *IEEE Transactions on Magnetics*, **41** (9), pp. 2490 - 2495.

[73] Chery, E. C., 1949, "The Duality between Interlinked Electric and Magnetic Circuits and the Formation of Transformer Equivalent Circuts," *Proc. Phys. Soc. B*, **62**, pp. 101 - 111.

[74] Polinder, H., Mueller, M. A., Scuotto, M., and Goden de Sousa Prado, M., 2007, "Linear generator systems for wave energy conversion," *Proceedings of the 7th European Wave and Tidal Energy Conference (EWTEC)*, Porto, Portugal, Sept. 11 - 14.

[75] Spooner, E., and Haydock, L., 2003, "Vernier hybrid machines," *IEEE Proceedings Electric Power Applications*, **150** (6), pp. 655-662.

[76] Liu, Z. J., Bi, C., and Low, T-S., 1997, "Analysis of iron loss in hard disk drive spindle motors," *IEEE Transactions on Magnetics*, **33** (5), pp. 4089-4091.

[77] Evans, D., 1976, "A theory for wave-power absorption by oscillating bodies," *J. Fluid Mech.*, **77**(1), pp. 1-25.

[78] Hoskin, R., and Nichols, N. K., 1986, "Optimal strategies for phase control of wave energy devices," *Proceedings of the International Symposium on Utilization of Ocean Waves-Wave to Energy Conversion*, La Jolla, California, June 16, pp. 184-199.

[79] Falnes, J., 2002, "Optimum control of oscillation of wave-energy converters," *J. Offshore Polar Eng.*, **12** (2), pp. 147-155.

[80] Bjarte-Larsson, T. and Falnes, J., 2006, "Laboratory experiment on heaving body with hydraulic power take-off and latching control," *Ocean Eng.*, **33** (7), pp. 447-477.

[81] Falcão, A. F., 2008, "Phase control through load control of oscillating-body wave energy converters with hydraulic PTO system," *Ocean Eng.*, **35** (3-4), pp. 358-366.

[82] Henriques, J. C., Falcão, A. F., Gomes, R. P., and Gato, L. M., 2012, "Latching control of an OWC spar-buoy wave energy converter in regular waves," *Proceedings of the 31st International Conference on Ocean, Offshore and Arctic Engineering (OMAE-12)*, Rio de Janeiro, Brazil, July 1-6.

[83] Valerio, D., Beirão, P., and da Costa, J. S., 2007, "Optimisation of wave energy extraction with the Archimedes Wave Swing," *Ocean Eng.*, **34**, pp. 2330-2344.

[84] Yavuz, H., Stallard, T. J., McCabe, A. P., and Aggidis, G. A., 2007, "Time series analysis-based adaptive tuning techniques for a heaving wave energy converter in irregular seas," *J. Power and Energy*, **221** (1), pp. 77-90.

[85] Clément, A.H. and Babarit, A., 2012, "Discrete control of resonant wave energy devices," *Phil. Trans. R. Soc. A*, **370**, pp. 288-314.

[86] Korde, U. A., 2002, "Latching control of deep water wave energy devices using an active reference," *Ocean Eng.*, **29**, pp. 1343-1355.

[87] Hals, J., Falnes, J., and Moan, T., 2011, "A Comparison of selected strategies for adaptive control of wave energy converters," *J. Offshore Mech. Arct. Eng.*, **133**, 031101-1.

[88] Belmont, M. R., 2010, "Increases in the average power output of wave energy converters using quiescent period predictive control," *Renewable Energy*, **35**, pp. 2812-2820.

[89] Flocard, F. and Finnigan, T. D., 2012, "Increasing power capture of a wave energy device by inertia adjustment," *Appl. Ocean Res.*, **34**, pp. 126-134.

[90] Nocedal J. and Wright S., 2006, *Numerical Optimization*, Springer, New York.

[91] Borelli, F., 2011, "Experiential Advanced Control Design I", Course MEC 231A. Lecture notes, Department of Mechanical Engineering, University of California at Berkeley, Berkeley, CA.

[92] Wâchter, A. and Biegler, L. T., 2006, "On the implementation of a primal-dual interior point filter line search algorithm for large-Scale nonlinear programming," *Mathematical Programming*, **106** (1), pp. 25-57.

[93] HSL, 2011, A collection of Fortran codes for large scale scientific computation, `http://www.hsl.rl.ac.uk`.

[94] Kelman, A., Vichik, S., and Borrelli, F., 2012, "BLOM: The Berkeley Library for Optimization Modeling and Nonlinear Model Predictive Control," Berkeley, CA, `http://www.mpclab.net/Trac/`.

[95] Faltinsen, O.M., 1990, *Sea Loads on Ships and Offshore Structures*, Cambridge University Press, Cambridge, New York.

[96] Fusco, F. and Ringwood, J. V., 2010, "Short-term wave forcasting for real-time control of wave energy converters," *IEEE Transactions on Sustainable Energy*, **1** (2), pp. 99-106.

[97] Halliday, J. R., Dorrell, D., and Wood, A., 2011, "An application of the Fast Fourier Transform to the short-term prediction of sea wave behaviour," *Renewable Energy*, **36**, pp. 1685-1692.

[98] Babarit, A., Guglielmi, M., and Clément, A. H., 2009, "Declutching control of a wave energy converter," *Ocean Eng.*, **36** (12), pp. 1015-1024.

[99] Teillant, B., Gilloteaux, J. C., and Ringwood, J. V., 2010, "Optimal damping profile for a heaving buoy wave energy converter," *Proceedings of the 8th IFAC Conference on Control Applications in Marine Systems*, Rostock, Germany, Sept. 15-17.